DEVELOPMENT OF MINIATURE, MULTILAYER, INTEGRATED, RECONFIGURABLE RF MEMS COMMUNICATION MODULE ON LIQUID CRYSTAL POLYMER (LCP) SUBSTRATE

A Dissertation
Presented to
The Academic Faculty

by

Nickolas Kingsley

In Partial Fulfillment
of the Requirements for the Degree
Doctor of Philosophy
in
Electrical and Computer Engineering

School of Electrical and Computer Engineering
Georgia Institute of Technology
May 2007

Copyright © 2007 by Nickolas Kingsley

DEVELOPMENT OF MINIATURE, MULTILAYER, INTEGRATED, RECONFIGURABLE RF MEMS COMMUNICATION MODULE ON LIQUID CRYSTAL POLYMER (LCP) SUBSTRATE

Approved by:

Dr. John Papapolymerou
Associate Professor, School of ECE
Georgia Institute of Technology, Adviser

Dr. Swapan Bhattacharya
Senior Research Scientist, School of ECE
Georgia Institute of Technology

Dr. Manos Tentzeris
Associate Professor, School of ECE
Georgia Institute of Technology

Dr. George Papaioannou
Professor, School of Sciences
University of Athens (Greece)

Dr. John Cressler
Professor, School of ECE
Georgia Institute of Technolog

Date Approved: March 30, 2007

If you're not working hard everyday, somewhere someplace someone is and when they meet you, they will beat you.

–Henry Pfingstag

Being a graduate student is like becoming all of the Seven Dwarves.
In the beginning you're Dopey and Bashful.
In the middle, you are usually sick (Sneezy), tired (Sleepy), and irritable (Grumpy).
But at the end, they call you Doc, and then you're Happy.

–Ronald T. Azuma

If we knew what it was we were doing
it would not be called research, would it?

–Albert Einstein

To my grandparents for their endless support.

To my loving wife for always leaving the light on for me.

PREFACE

When people ask me what I do for a living, I tell them that I am a microwave engineer. The problem is, to a layman, a microwave engineer is a person who designs and builds microwave ovens. People naturally make the connection between microwaves and the microwave oven (and rightfully so). The average layman knows a great deal more about microwave theory than they think. For example, there are the simple noticeable facts like microwaves are invisible. Indeed, if you look inside of a microwave oven you don't see rainbows cooking our food. Also, microwaves can be contained inside a metal box. If you ask a layman why a microwave oven has a metal mesh on the front they would note that it is necessary to keep the microwaves inside the oven. They would be absolutely correct. I bet the same layman would also note that even though microwaves can not been seen or felt, they can (and do) carry energy. How else could you cook a baked potato in 10 minutes? This is a significant amount of information that anyone born within the last 30 years probably knows and quite frankly, electromagnetic wave theory is a tough subject. I bet the general populous knows a whole lot less about other areas of science; like relativity, Brownian Motion, and the Laws of Thermodynamics.

Microwave (or millimeter-wave) engineering is an exciting field that will only become more important in the future. It's only a matter of time before we can fit a cell phone, GPS system, wireless Internet, clock radio, and whatever else you can possibly imagine into a device small enough to fit in a thimble. To make devices smaller you HAVE to go higher in frequency. As you make circuits more dense, you HAVE to worry about electromagnetic interference and cross coupling issues. You also have to worry about the usual issues of heat dissipation, power, weight, portability, reconfigurability, etc. One of my graduate professors (Dr. Doolittle - no, I'm not making this up) once said that we must never forget the three most important issues to industry: cost, cost, and cost.

The topic that I have chosen to write a dissertation on is one that I hope will set a

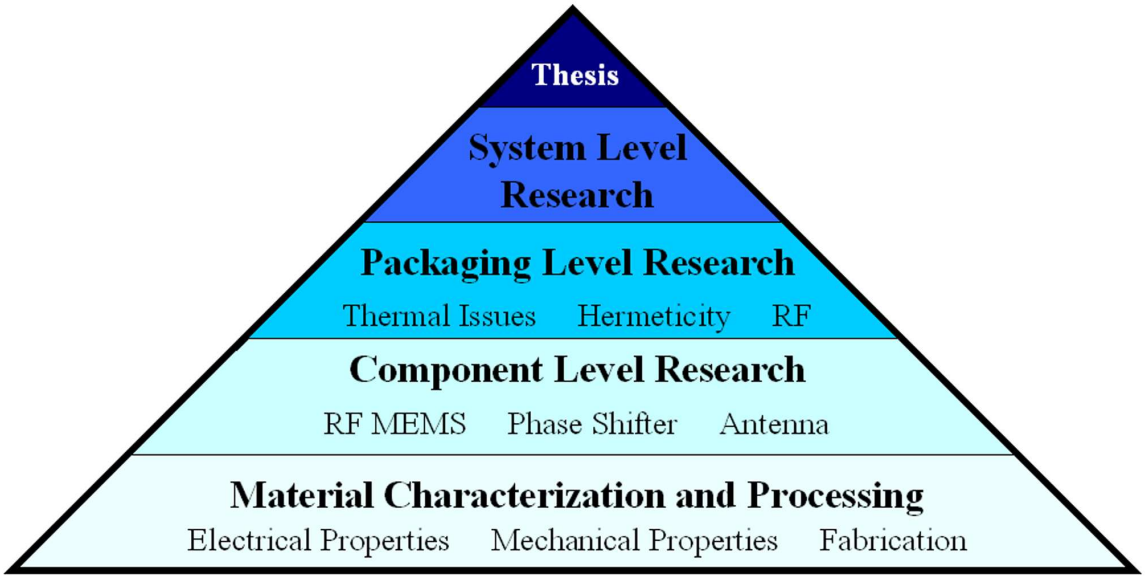

Figure 1: This research used a pyrimidal approach by starting general and building up

strong foundation for smaller, faster, lower-cost, and more complex innovations. I hope I am able to convey to you, the reader, the passion that I have for this research and for the exciting technologies that will hopefully emerge from this effort.

This research progressed in a way similar to how a pyramid is formed (as demonstrated in Figure 1). Since we are pioneering a new material, this research began with a complete study of the material and how it can be used for RF devices. Chapters 1-4 discuss this and also include a brief historical discussion. The next step was to begin making various devices on the material. Chapters 5-9 outline a number of such devices and how they furthered the state of the art. Since LCP is an excellent packaging material, at this point we were able to make our devices more robust by protecting them from the environment. Chapters 10-13 explain how we were able to do this. Finally, we were able to bring these various elements together to create a system-level device that has applications in a wide area of products. Chapters 14-17 discuss the communication modules that were assembled and tested. Several appendices have been written for projects performed that are relevant but not directly related to the scope of the topic. This thesis is organized in the most logical order for the reader, but it is also roughly in chronological order as well.

ACKNOWLEDGEMENTS

First and foremost, I want to thank my advisor, John Papapolymerou, for always pushing me to be the best and for showing me what it takes to be a successful engineer.

I would like to extend my most sincerest thanks to my colleagues at Georgia Tech: Dimitrios Anagnostou, Ramanan Bairavasubramanian, Swapan Bhattacharya, David Chung, Richard Daigler, Stephen Horst, Boyon Kim, Pete Kirby, Yuan Li, Cesar Lugo, Matt Morton, Symeon Nikolaou, Bo Pan, Dane Thompson, Guoan Wang, and Guizhen Zheng. You have been an invaluable source of knowledge and support. I'd like to thank my committee members for taking the time to study, understand, and appreciate my research.

I also want to thank Chris Evans and his staff at the GEDC for providing a world-class research facility. To Todd Whitehurst, you always stopped what you were doing to help save me from my technological crises and I do appreciate it. I also want to tip my hat to all of our administrators: Gwen Satchel, Janet Myrick, Tammy Scott, Deborah Milliner, Cathy Beam, and Joi Adams.

There are several individuals outside of GEDC that I would like to thank. I want to thank Dr. Arnaud Pothier for providing me with my first MEMS fab recipe. Many thanks to Laureen Rose for her last minute save-the-day wire bonding. I want to recognize Gary Spinner, Vinh Nguyen, Charlie Suh, Brandon Harrington, Scott Fowler, and William Kimes for doing all they could to keep the cleanroom equipment running. Many thanks to Dr. Mark Allen for allowing me to use his laser systems and to Richard Shafer for maintaining these systems and for offering helpful advice with material issues. I offer my sincerest thanks to Dr. George Ponchak with NASA Glenn for helping me measure the communication modules. I couldn't have graduated in Spring without his help.

Aside from research, there have been many people who have either made my life a little better or a little easier. I'd like to start by thanking Dr. Robert Speyer for investing countless hours into my martial arts endeavor and for pushing me to be a little stronger

and a little faster than everyone else. I want to thank Sheryl Ballenger for co-founding the Georgia Tech American Sign Language Choir with me. Many thanks to Dean Karen Boyd for the kindness she always showed me. To Tommy Klemis (owner of Junior's Grill), you served me my first meal at Georgia Tech and since then I've eaten hundreds of burger baskets and each one came with a side of fries and a smile. There are countless other directors, deans, and professors that I have had the honor of rubbing elbows with (many of which were on a first-name basis). Thank you for the favors that you have bestowed upon me.

To my friends and family, thank you, thank you, thank you. You rarely knew what the heck I was talking about (no, I don't build microwave ovens for a living) but that never stopped you from asking how my research was going. I always knew that I could overcome any obstacle because of your faith in me. To my best friends, Margie Nguyen and Fred Carlson, thanks for everything.

Lastly, I'd like to thank those who sponsored this research: NASA, the Georgia Electronic Design Center (GEDC), and the National Science Foundation (NSF). A special thanks goes out to Raytheon for providing amplifiers and support.

Me (left) with Dr. John Papapolymerou [58]

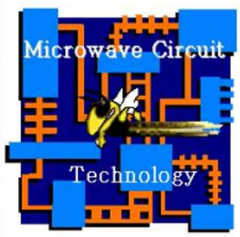

Me (left) with Dr. Dimitris Anagnostou

TABLE OF CONTENTS

LIST OF TABLES

LIST OF FIGURES

LIST OF SYMBOLS OR ABBREVIATIONS

A	area.
a	distance from the anchor that the force begins.
$\mathring{A}$	Angstrom (10^{-10}m).
AZO	aluminum doped zinc oxide.
b	length of the beam that the force is applied to.
C	capacitance.
CCVD	combustion chemical vapor deposition.
CMOS	complementary metal-oxide semiconductor.
CPW	coplanar waveguide.
CTE	coefficient of thermal expansion (ppm/K).
DARPA	Defense Advanced Research Projects Agency.
dB	decible.
DC	direct current.
δ	deflection (Greek: delta).
DMM	digital multimeter.
E	Young's modulus.
ϵ	permittivity (Greek: epsilon).
F	force.
f	frequency.
FDTD	finite-difference time-domain.
FEM	finite element method.
FET	field-effect transistor.
g	gap.
g_o	initial gap.
H	thickness (also, t).
HF	hydroflouric acid.
HT	high temperature.

HTCC high-temperature cofired ceramic.

I moment of inertia.

IC integrated circuit.

IPA isopropyl alcohol (or isopropanol).

IR infrared.

k thermal conductivity and Boltzman's constant.

κ spring constant (Greek: kappa).

k_{eff} effective spring constant.

k_m meandered spring constant.

k_{n-m} non-meandered spring constant.

KOH potassium hydroxide.

L length, inductance.

λ wavelength (Greek: lambda).

L_c distance from the end of the spring to the start of the meander.

LCP liquid crystal polymer.

LIGA Lithografie, Galvanoformung, Abformung (German for Lithography, Electroplating, and Molding).

LNA low-noise amplifier.

L_s width of a spring.

LT low temperature.

LTCC low-temperature cofired ceramic.

MEMS microelectromechanical systems.

MiRC microelectonics research center.

MMIC monolithic microwave integrated circuit.

MOM method of moments.

nH nano (10^{-9}) Henry.

ν Poisson ratio (Greek: nu).

Ω unit of impedance (Greek: Omega).

PC printed circuit.

PEC perfect electric conductor.

PECVD plasma-enhanced chemical vapor deposition.

pF pico (10^{-12}) Farad.

pH potential of hydrogen (negative 10-base log of the positive hydrogen ion concentration; measure of acidity).

PIN positive-intrinsic-negative.

ppm parts per million.

PR photoresist.

PTFE polytetrafluoroethylene (or Teflon).

q distribution of force.

R&D research and development.

RF radio frequency.

ρ resistivity (Greek: rho).

RIE reactive ion etching.

RLC resistance-inductance-capacitance.

SEM scanning electron microscope.

SOC system-on-chip.

SOP system-on-package.

SP4T single pole four throw.

t thickness (also, H).

TCE trichloroethylene.

TRL thru-reflect-line.

UWB ultra wide band.

V voltage.

w width (also, W).

x position along a beam.

SUMMARY

For this thesis, the use of Liquid Crystal Polymer (LCP) as a system-level substrate and packaging material is investigated. Early in the research, recipes for fabricating on LCP were developed. With this knowledge, RF components were able to be fabricated. These devices include filters, antennas, phase shifters, and RF MEMS switches.

To investigate the potential of using LCP as a system-level material, packaging properties and robustness were tested. This research demonstrated that LCP could be used to package something as small and delicate as an individual switch or as large as a 4" wafer. In addition, it was shown that MEMS switches could survive well over a hundred million cycles. This demonstrated that LCP could be used to create reliable, high performance systems.

The culmination of this research was used to create two variations of a communication module. The first device was fabricated on one layer and a multi-layer approach was taken for the other device. These modules needed to be low-cost, low-loss, flexible, and capable of beam steering. This technology can be used for communication, sensing, detection, and surveillance for a broad scope of applications. To this date, they are by far the most sophisticated SOP on LCP ever achieved. This technology can be further developed to include more functionality, smaller size, and even better performance.

DEVELOPMENT OF MINIATURE, MULTILAYER, INTEGRATED, RECONFIGURABLE RF MEMS COMMUNICATION MODULE ON LIQUID CRYSTAL POLYMER (LCP) SUBSTRATE

PART I

Background, Material Characterization, and Processing

by

Nickolas Kingsley

Part I

Background, Material Characterization, and Processing

Part I begins with a technical and historical background of the topic. The polymer material LCP is introduced and compared to other similar materials. A number of advancements were made in fabrication technology for processing on a flexible, thin-film material. Some of these advancements are documented in this section. This fundamental knowledge was necessary before devices could be realized. A detailed process flow for fabricating MEMS on LCP is presented.

CHAPTER I

BACKGROUND

The research being presented in this thesis has a direct application in the areas of communication, detection, and surveillance. Ever since the unfortunate events of 9-11, the war in Iraq, the war in Afghanistan, Hurricane Katrina, and countless other events there has been a push for technological advancements in these three areas. Some of the systems and products being funding by the government and private industry are:

- Satellite and navigation systems (i.e. Global Positioning System, GPS)
- Defense Systems (i.e. Patriot missile guidance and surface radar)
- Air Traffic Control and anti-collision radar
- Advanced weather monitoring
- Satellite radio and TV
- Communication devices for consumers, government officials, or military personnel

The amount of funding being invested in this research is substantial. A few examples of this investment for 2006 include [17, 69]:

$7.7 billion Missile defense

$1.3-2.5 billion Enhanced international communication

$220 million Space-based radar

$101 million Coast Guard coastal zone communication

$37 million Homeland Security network communication

$20.5 million First responder agencies

Naturally, you can't talk about communication systems without mentioning cellular phones. The last decade has seen a boom in cell phone sales and usage. To give you an idea of the rate at which cell phone usage is spreading [62]:

- Half of the world will own a cell phone by the end of 2009
- Africa alone is forecasted to add 265 million new users over the next 6 years
- There were 2.1 billion cell phone users at the end of 2005
- There will be 2.5 billion cell phone users at end of 2006
- The global wireless service industry generated $555.3 billion in 2005
- The global wireless service industry is expected to generate $800 billion in 2010

All of these areas share three requirements: small size (or low weight), high performance, and low cost. This research will bring to the table something that can help meet all of these requirements. That special something, is Liquid Crystal Polymer.

1.1 What is LCP?

LCP is an organic (comprised of only carbon, oxygen, and hydrogen atoms), thin film material. When created, it starts as a liquid polymer (a polymer is physically similar to a plastic; it is slightly different chemically) that is heated to the "liquid crystal" temperature. In this state, the molecules align into a pseudo-crystalline structure with spacial regularity. Materials that form this type of structure are incredibly strong and LCP is no exception. LCP is a versatile material because it combines the strengths of strong crystal bonds with the benefits of polymer materials (flexibility and low-cost). For these reasons, LCP has been targeted as a possible substitute for expensive semiconductor substrates in Microelectromechanical System (MEMS) devices. Current MEMS devices typically use silicon, gallium arsenide, quartz, or silicon germanium substrates. However, these materials are very expensive ($80-$200 for a single 4 inch wafer) and brittle [13]. LCP is inexpensive ($10 per square foot), flexible, light-weight, radiation resistant, chemically inert, electrically low-loss, and biocompatible. All of these qualities are desired by MEMS engineers.

LCP is a relatively young technology. It was first introduced in the late 1980s as a strong, lightweight polymer. Since then it has been used everywhere from outer space to deep ocean exploration. It is often found in recreational devices, such as tennis racket strings and sailboat sails. In the 1990s, researchers began extruding thin film LCP. Unfortunately, these films were not very strong and uniformity was an issue. Within a decade, these issues were resolved. Today the material can be made as thin as 1-mil thick and can be tailored to meet a wide range of parameters. The melting temperature, the thickness, the metal cladding, and the rate of thermal expansion are some of the parameters that can be customized. As the technology matures, the quality will improve even more and the cost of production is expected to greatly decrease [18].

1.2 Statement of Topic

The objective of this research is to realize a multilayer radio-frequency (RF) communication module with beam scanning capabilities. Careful attention will be given to minimize the size and optimize for low loss. LCP substrate will be used as the substrate and packaging material. This system should operate at or near 14GHz (Ku-band).

The module operates by receiving and amplifying an RF signal. Amplification will be performed using a low noise amplifier (LNA) chip provided by Raytheon. The signal will also be fed to a MEMS phase shifter. MEMS switches will be used since they offer excellent performance at high frequencies. The modified signal will then feed a 2x2 patch antenna array. Varying the phase shift to the patches will provide the beam scanning capability. All of the layers will be bonded together to create a System-On-Package (SOP) RF front end.

1.3 Origin and History of the Problem

Since the dawn of electronics, researchers have strived for smaller, faster, and more efficient devices. In recent years, this effort has been extended to integrate these devices into one chip (System-On-Chip, SOC) or one package (System-On-Package, SOP). This thesis will further the state-of-the-art by realizing a small, flexible, packaged, low-loss RF communication module. There were three independent topics that were investigated and then integrated for this thesis. The first topic was a study of MEMS switches for microwave devices. The second topic was the implementation of microwave devices on a flexible, organic substrate (namely, LCP). The third topic is a development of an advanced SOP device. The history of each of these topics will be discussed individually as well as a discussion of the integration of the topics.

1.3.1 RF MEMS Switch Development

Several breakthroughs have been made in the past six decades which paved the way for MEMS technology. In the early 1950s, photo fabrication was used by the Radio Corporation of America (RCA). This opened the door to quick, reliable, and repeatable fabrication. In the mid 1960s, the process of sacrificial layer etching was developed. This allowed for the realization of silicon pressure gauges, pressure sensors, and micro electrodes. In the 1970s, various sensors and micro structures were integrated and packaged. This greatly improved the robustness of these type of devices. Finally in 1982, the LIGA micromachining technology was demonstrated in Germany (the term "LIGA" comes from the German words Lithografie, Galvanoformung, Abformung meaning Lithography, Electroplating, and Molding). The LIGA technology allowed for the fabrication of high aspect ratio micro structures [25].

All of the above milestones were necessary for the development of MEMS devices. MEMS switches as we know them today were conceptualized in the late 1980s and early 1990s. The first published papers were entirely conceptual and pointed out some of the design challenges and potential uses of MEMS devices [50]. MEMS switches in particular were of great interest to RF engineers for their potential to reduce the total area, power consumption, and cost

of their devices.

MEMS were initially fabricated exclusively on silicon since integrated circuit (IC) fabrication at the time was on silicon. The material properties and fabrication processes for silicon were already well known.

Early MEMS research was funded and performed by industry leaders looking for applications in a variety of areas, including optics, transportation, aerospace, robotics, chemical analysis systems, biotechnologies, and medical engineering. Devices such as microactuators, microsensors, and microrobots were desired for a plethora of devices, such as for automobile airbags. In time, it was expected that MEMS could be used for flat panel displays, optical switches, fiber optics, and integrated sensors. It was understood that many reliability issues would have to be solved before these advanced technologies were possible. Early MEMS switches were plagued with electrical and mechanical issues, such as dielectric charging, substrate delamination, creep, and fatigue [8].

Prior to the new millennium, accurate numerical solvers were not available to MEMS designers. Research was primarily performed by fabricating, testing, and redesigning. This of course is a slow and expensive process. In December 1996, the Defense Advanced Research Projects Agency (DARPA) invested more than $17 million in government funding aimed at improving the computer-aided design technology for MEMS devices [57]. A number of useful software programs were developed from this funding, including MEMCAD (developed by MIT and Microcosm) [19], IntelliCAD (developed by IntelliSense) [11], and CAEMEMS (developed by the University of Michigan) [24].

MEMS devices quickly surpassed the RF performance of their solid-state equivalents. Even early MEMS switches had an insertion loss of 0.15 dB at 20GHz, compared to an on-state insertion loss of approximately 1 dB for a typical GaAs-FET or PIN-diode switch at the same frequency [7].

Today, many of the devices predicted in the 1990s are commercially available. MEMS switches in particular can be purchased with insertion losses as low as 0.1 dB up to 50GHz with the potential for operating more than 100 billion cycles and handling multi-watt power levels [60].

1.3.2 Microwave Devices on Organic Substates

Prior to the 1990s, multilayer structures were realized using one of the many available high-temperature cofired ceramic (HTCC) materials. These materials were typically derivatives of alumina (aluminum oxide). HTCC devices were realized by stacking layers of alumina plates and firing at approximately 1500^{o}C to bond and harden the plates. Unfortunately, this high temperature requirement eliminated the possibility of using highly conductive metals, like silver, copper, or gold (which all melt between 962–1085^{o}C) [110]. Instead, high melt, lower conductance metals like tungsten and molybdenum were used. Since high conductance metal is necessary for very high frequency devices, HTCCs were limited in their frequency range [37].

In the late 1990s, the customer-driven wireless market pushed the developers of RF hardware towards more functionality in less volume, operation at ever higher RF frequencies, and greater circuit integration. HTCCs offered excellent RF performance but they were limited to lower frequencies and only high temperature materials. In addition, these ceramics were expensive to manufacture, assemble, and test. As a solution to these problems, a ceramic-organic hybrid, known as Low Temperature Cofired Ceramic (LTCC), was created. LTCCs could be fired at 850-900^{o}C which permitted the use of high conductance metals and pastes. This in turn extended the possible frequency range to much higher frequencies [37].

LTCC allowed for multilayer, robust, high frequency, low-loss, and cost-effective systems, such as radar, sensor circuits for automotive applications (24GHz and 77GHz), telecommunication modules (28-38GHz), and high reliability aerospace applications. Its uniform material composition made it useful for many Ultra Wide Band (UWB) devices as well. LTCC is probably the current preferred packaging material, but there is a tradeoff that after firing, the ceramic shrinks in all three directions by 10-20%. This introduces an additional level of complexity to the design and manufacturing of LTCC circuits [26]. Ways of reducing or eliminating this shrinkage are being investigated [88].

In the past two decades, alternative organic substrate materials have been developed. Polytetrafluoroethylene (PTFE, or Teflon), FR4 and LCP are three examples. PTFE and

FR4 are both used as printed circuit board (PCB) materials. PTFE offers excellent RF performance but the cost is higher than the other organic alternatives. FR4, whose name is short for Flame Resistant 4, is a good substrate material for frequencies up to 10GHz [109]. LCP is a flexible substrate (unlike FR4) that has been characterized up to 110GHz as a low-loss, low-permittivity material [97]. Only in recent years has LCP been able to be manufactured cheaply, uniformly, and in thin film form. LCP is also flexible, light weight, and biocompatible. As a packaging material, LCP can be bonded to itself or most other materials at less than 300^{o}C. Since the bond temperature for LCP is much lower than LTCC, many highly temperature sensitive materials can be packaged that couldn't be packaged previously (like MEMS).

1.3.3 Multi-substrate System-on-Package Implementation

System-on-Package (SOP) technologies are widely desired for their design simplicity, lower cost, higher system function integration, better electrical performance, and various 3D packaging capabilities [99]. One limitation of HTCC, LTCC, and FR4 materials is that multilayer devices are usually monolithic (made from the same material). In the case of FR4, layers are bonded together using a laminating material such as ViaLux (by Dupont). Packaging with PTFE can be difficult due to its poor adhesion property. LCP has the advantage that it can be bonded to itself (to make an all-LCP package) or to almost any other material. This gives it the flexibility to make advanced, multilayer, multi-substrate packages. For example, LCP could be bonded to low resistivity silicon to package CMOS devices.

SOP technologies using LCP have been a popular research topic in recent years. LCP is an ideal SOP material because of its unique mechanical and electrical properties. Devices packaged in LCP have the advantage of flexibility which means they could be kept flat or attached to a contoured surface, such as the nose cone of a jet aircraft. Furthermore, since LCP is a low moisture absorbing material, it can protect very sensitive devices from atmospheric influence. This is especially important for MEMS devices which fail in humid environments. The low permittivity of LCP makes it advantageous for supporting and

Table 1: Comparison of HTCC, LTCC, FR-4, PTFE, and LCP materials

	HTCC	LTCC	FR-4	PTFE	LCP
tan δ (at $\approx$ 1GHz)	0.0002	0.0025	0.016-0.055	0.0028	0.004
CTE (ppm/^{o}C)	3.3-7	3-7	13-14	24	3-30
Bond Temp (^{o}C)	1450-1880	850-1000	N/A	343	300
ϵ_r	7-10	3.5-9	4.35-4.7	2–2.1	3.15
Moisture Absorption (%)	≈ 0	<0.1	<0.25	0.015	0.02-0.04

Sources: [12, 37, 82, 102, 103, 109]

packaging antennas as well [9].

Several material properties of the previously discussed materials are listed in Table 1. All of the materials in Table 1 are considered low-loss and are suitable for RF devices. HTCC is a powerful packaging material but it is extremely limited in what it can be used for. LTCC offers RF performance similar to PTFE and LCP at a cost higher than LCP and lower then PTFE. However, PTFE can not be package as easily as LTCC and LCP. FR4 is an excellent choice for frequencies in the single-digit gigahertz range where low-cost is critical. LCP combines all of the strengths and none of the weaknesses of the other materials. That is, it is very low-cost (like FR4), easily packaged (like LTCC), and has excellent RF performance (like HTCC and PTFE) [63]. Since LCP has great potential for future microwave and mm-wave devices, it is the chosen material for this project.

1.3.4 Technology Integration

A culmination of the previously discussed technologies would result in a multilayer, organically packaged, low-cost, low-loss, RF MEMS device. To date, this has never been done (prior to this research). This is due, in part, to material constraints. Packaging multilayer devices was challenging, expensive, and added a great deal of loss to a system. Using conventional packaging materials, like LTCC, can not be used with MEMS because of the temperature limitation. Advancements in RF integration have been made possible because of the introduction of LCP as a microwave packaging material.

CHAPTER II

LCP CHARACTERIZATION AND PROCESSING

The LCP used in this research is provided directly from the manufacturer (Rogers Corporation). Unfortunately, only a minimal amount of information is provided on the electrical and mechanical properties [18]. Dane Thompson was able to characterize the RF properties of the material up to 110GHz [97]. From his effort, we can call LCP a "low-loss" material through mm-wave frequencies. The ability to fabricate MEMS on LCP came from the efforts of Guoan Wang and this author. This chapter discusses some of the techniques developed which enabled us to fabricate on LCP.

2.1 Material preparation

Before any fabrication can commence on LCP, certain pre-fabrication steps must be performed. This includes cleaning, drying, and removing the copper cladding (optional).

2.1.1 Cleaning

When LCP is shipped from the vendor, it is packaged between layers of cardboard (both thin, white sheets and thick, corrugated sheets). This creates an enormous amount of particulate matter on the surface of the LCP. It is important to remove these contaminates before fabrication. Although a quick rinse can be done using deionized water, a better method of cleaning involves a five step process:

1. Douse liberally with trichloroethylene (TCE)
2. Douse liberally with acetone
3. Douse liberally with methanol
4. Douse liberally with isopropanol (IPA)
5. Rinse thoroughly with DI water

The order of this process is crucial. Each solvent is slightly weaker than the preceding one. This process successfully removes all dirt, dust, oils, and foreign chemicals from the surface. It also helps remove any solvent residue. The process is safe for material with and without copper cladding.

2.1.2 Copper Removal

As stated earlier, LCP comes from the vendor with copper cladding on both sides. Current layers come in thicknesses of 5 and 18 microns, although Rogers is investigating ways of making thinner layers of copper (less than 3μm). If the copper layers are not desired, as is the case when MEMS are being fabricated, then there are two methods of removing the copper.

The easiest way to remove the copper is to soak the sample in iron (III) chloride (also called ferric chloride). Aqueous $FeCl_3$ is a thick, brown liquid that is commonly used to etch copper off PC boards. Samples can be soaked in $FeCl_3$ until the metal layer is removed. To increase the etch rate, the $FeCl_3$ solution can be heated to 60^{o}C. Removing 18μm thick copper from a sample of LCP can take anywhere from 20-45 minutes, depending on the temperature and the strength of the solution.

A faster way of removing copper is to use acid. The preferred chemical is nitric acid. Full strength nitric acid can etch 18μm thick copper from a sample of LCP in a few seconds! However, etching at this rate is quite dangerous (the etch process creates hydrogen as well as a thick, brown gas). To make the process considerably safer, the acid should be diluted with water. A dilution of 1:1 acid to water is recommended although 2:1 can also be used. This level of dilution usually etches through 18μm thick copper in 40-60 seconds which is a much more controlled rate. As the copper is etched, the chemical will turn dark green. When the liquid is no longer translucent, it should be replaced with new chemicals. These two methods are compared in Table 2.

Chemical etching of any metal is very isotropic (etches in all directions). The etch angle from the vertical axis can be as much as 45^o. This can be even higher if the sample is over-etched. For 18μm thick copper, this etch profile translates to 18μm of lost metal

Table 2: Comparison of two copper etch processes

	Iron (III) Chloride ($FeCl_3$)	Nitric Acid (HNO_3)
Chemical Appearance	Thick, brown liquid	Clear liquid that turns green
NFPA 704 Rating	3-0-1	3-0-0
Strength	100%	Diluted 2:1 or 1:1 acid:water
Temperature	60^oC	Room temperature*
Etch rate (Approximate)	0.9μm/minute	20μm/minute
Quality	May leave a dark stain in some areas	Excellent

* The reaction is exothermic so the chemical will warm

per side. This means a 50μm gap will actually be 86μm after etching. This will have a profound effect on the RF performance. To minimize this effect, the thick copper layer can be removed and replaced with a thinner layer. For example, a 50μm gap with 3μm thick sputtered copper will be 56μm after etching. For this reason, it is recommended that if small features are needed, the thick copper should not be used.

2.1.3 Drying

Properly drying a sample is important to achieve the best metal adhesion. This is particularly important if evaporation or sputtering is going to be performed. Any moisture that is trapped in the surface roughness or gases that have diffused into the material will outgas and cause bumps or cracks in the metal.

Drying is usually done in an oven or on a hotplate at 120^oC for 5-10 minutes. Placing the sample in an oven with a clean aluminum foil base yields the best quality dry.

Rogers Corp. recommends that any sample that is going to be bonded should be baked for four hours [18]. This is to prevent any and all outgassing in the bonding layer during the bonding process. Engineers at Rogers Corp. are currently investigating ways to decrease this requirement.

2.2 Polishing

The polishing of LCP was never attempted prior to this research effort. Therefore, it was studied in great detail. The techniques used are discussed in the next chapter.

2.3 Mouting

There is a good reason why MEMS devices have not been fabricated on a flexible substrate prior to this research. It is very difficult to do lithography on a substrate that is not only flexible, but is prone to curling. The trick to successful fabrication on LCP is in the mounting. During this research, the fabrication technique used progressed from permanent to temporary and finally to vacuum mounting techniques.

2.3.1 Permanent Mounting

Initially, LCP layers were bonded to silicon wafers prior to fabrication. This was done by applying a thick, spin-on dielectric material and curing in an oven for many hours. This technique worked very well, but it had two main drawbacks. First, once the LCP was bonded to the silicon, it wasn't able to be removed. This prevented the possibility of making flexible devices, which was one of the main advantages for using LCP. Second, silicon is relatively expensive (especially for high resistance silicon, which is typically used for high frequency devices). Bonding a cheap material to an expensive material with a costly bonding adhesive doesn't make for a low-cost product. It was clear that a better method had to be developed.

The high cost was reduced by bonding LCP to glass microscope slides instead of silicon wafers using a cleanroom grade tape. Silicon transfer tape is clear, commercially available, and double-sided. Both glass slides and silicon transfer tape are low cost materials. However, glass slides are not flexible and the silicon transfer tape is a permanent bonding material so the lack of flexibility tradeoff remained.

2.3.2 Temporary Mounting

Developing a temporary mounting method is almost a problem in logic. That is, it was necessary to find a material that could be used as a bonding adhesive that is strong enough to withstand high temperatures, plasma processing, and strong chemicals yet could be removed easily and cleanly. In other words, it was necessary to find an invincible chemical with an Achilles heel! The answer: photoresist! The same positive photoresist that was used for lithography could be used as a bonding material. The bonding method was straight

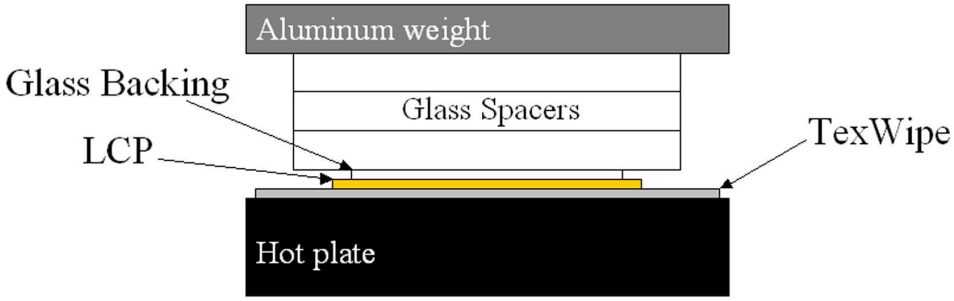

Figure 2: A temporary mounting technique for processing LCP is shown

forward. First, a relatively thick (3-4μm) layer of photoresist is spun onto a glass microscope slide. The slide is pressed against a piece of LCP with the photoresist in contact with the LCP. That sample is placed on top of a TexWipe, which is then placed on a hotplate at room temperature. Large aluminum blocks are placed on top of the sample with several thicker glass slides in between to increase the force pushing down on the sample. This stacking is demonstrated in Figure 2.

The hotplate is slowly heated to a temperature of 175^{o}C (25^{o}C hotter than the highest processing temperature). As the photoresist is heated, the solvent in the photoresist evaporates and leaves behind the sticky resin. The evaporated gas is squeezed out by the weight on top. If the weight is not heavy enough, the gas tends to collect in the middle of the glass slide to create one big bubble. If the weight is too heavy, the gas will not be able to escape so many small pockets of air will be created. Either way, the LCP will not be flat. Trial and error was used to determine the optimal weight, which seems to be about 3.5 psi. Once the temperature of the hot plate reaches 175^{o}C, the temperature is held for at least 20 minutes so that all of the solvent can evaporate. The hot plate is then allowed to cool back to room temperature. When the weight and glass spacer is removed, the glass slide is bonded flat to the LCP. Since the photoresist was cured at a temperature higher than the highest process temperature, there is no risk of degradation from heat.

When the time comes to remove the sacrificial photoresist layer from the MEMS, the sample is soaked in photoresist stripper. As the stripping agent removes the sacrificial layer, it also dissolves the bonding layer. When the sample is removed from the stripper to put in the critical point dryer, the glass backing slides off and the sample is flexible again. This

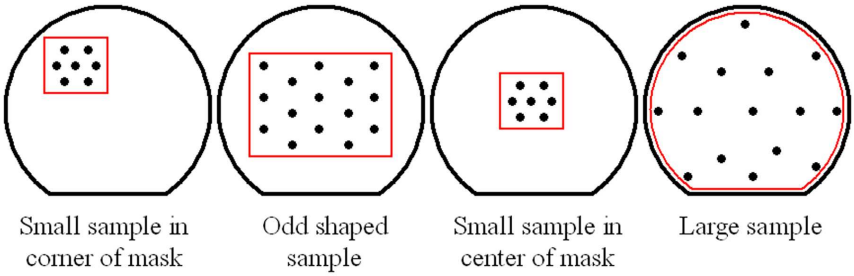

Figure 3: Various vacuum mounting wafers are shown. The holes redirect the vacuum pressure where it is needed most.

advancement allowed for the fabrication of circuits on a flexible material.

2.3.3 Vacuum Mounting

The optimal scenario is where all fabrication can be performed without the use of a backing. This would save time and money on both the small and full production scale. This was achieved by taking advantage of the vacuum system on the Karl Suss MA-6 mask aligner. The vacuum system on this machine is designed for a 4 inch diameter wafer. Most of the LCP samples processed were rectangular and much smaller than this. Several fixtures were made out of thin acrylic that were able to redirect the vacuum onto the areas needed by the sample. A picture of the fixtures is shown in Figure 3.

There was enough suction from the vacuum to hold the sample flat in place so that lithography could be done. When the samples were placed in the evaporator or sputterer, they were taped flat to the platen. When the samples were in the PECVD or RIE machines, microscope slides were laid on the edges of the samples to keep them flat. All in all, processing could be performed without the use of a backing. This is the only documented case of MEMS switch fabrication on a completely flexible substrate. Vacuum chucks can be easily implemented on a large scale so this is a low-cost solution.

2.4 Metal Adhesion to LCP

One of the earlier issues with fabricating on LCP was poor metal adhesion. After depositing a thin layer of metal, it would either peel off immediately, flake off during processing, completely delaminate during photoresist stripping, or lose adhesion during measurement

probing. A full investigation was performed to determine some guidelines for minimizing or eliminating the metal adhesion problem. Here are some of the results found:

- As long as a titanium adhesion layer is deposited, all metals stick equally well (gold, aluminum, and copper were tested). This layer is not needed when the surface is rough (more than 1μm)
- Metal that is sputtered has slightly better adhesion than metal that is evaporated.
- A titanium adhesion layer should be thicker than 200Åbut less than 600Å. The optimal thickness is around 300Å.
- LCP is a poor thermal conductor, so any heat on the sample from metalization will cause thermal stress in the metal. This can result in delamination or cracking of the metal or curling in the substrate. To minimize this, low process pressures ($< 2\mu$Torr) or cooling steps (15 minutes for every 30 minutes or 2μm) should be used.
- Before metalizing, LCP samples should be cleaned and dried as discussed earlier in the chapter.

Exhaustive chemical testing on LCP has already been performed [18]. However, metal adhesion testing to these same chemicals has not been documented. The only chemical that has effected metal adhesion is photoresist stripper, which is used to remove the sacrificial photoresist layer. This adhesion issue is worsened by the fact that it is the only chemical that requires submersion for several hours. For this reason, qualitative metal adhesion testing was performed on 3 common stripping chemicals: 1165 (by MicroChem), 1112A (by MicroChem), and acetone. Testing was done at room temperature and at 60^{o}C. The results are listed in Table 3.

From Table 3, it can be concluded that any of the listed stripping chemicals are suitable for use in fabrication. However, most of the time it is advantageous to soak MEMS samples in stripper for longer than needed to ensure that every last molecule of photoresist has been removed. Otherwise, any remaining residue will prevent the switch from deflecting properly.

Table 3: Test results for exposure to photoresist stripping chemicals to provide insight into metal adhesion issues

Chemical	Duration Until Adhesion Problems	Minimum Exposure Time for Stripping
1165 at 22^{o}C	48 hours	6-8 hours
1165 at 60^{o}C	24 hours	4-6 hours
1112A at 22^{o}C	24 hours	4-6 hours
1112A at 60^{o}C	3 hours	2-3 hours
Acetone at 22^{o}C	N/A	12-15 hours
Acetone at 60^{o}C	N/A	8-12 hours

Since the window of exposure with 1112A is so small, it is highly recommended that this chemical be avoided. Also, 1112A has a pH of 12, which makes it a strong base. LCP can degrade when exposed to a strong base, especially when heated.

Acetone does not seem to have any effect on metal adhesion (even after 100 hours), but it does evaporate quickly. Since it is much weaker than 1165 and 1112A, soaking overnight is typical. Leaving a sample in a fume hood over night has the risk of all of the acetone evaporating and the sample being ruined. With a neutral pH (7), it can definitely be used with LCP.

The third chemical, 1165, can easily be left over night at room temperature which will ensure complete photoresist removal and has no problems with delamination. Like acetone, it also has the advantage of a neutral pH. Therefore, it is the chemical of choice.

2.5 Solutions for curled LCP

LCP is flat when it comes from the vendor. It is also a thermoplastic polymer which means that it softens when heated and hardens when cooled. This ability makes it very attractive as an injection molded material. During processing, if LCP is not taped or weighted flat, it will curl. This is particularly problematic when depositing metals because of the high temperature and residual stresses that are induced in the metal. For example, a loosely placed sample of LCP in a DC sputterer will curl up into a bowl or taco shape after about 30 minutes of deposition. A wet sample with 18μm thick copper will do the same in only a few minutes if placed on a hot plate to dry. Processing on a sample that isn't flat is much

more challenging, but there are several methods for decreasing a sample's curl:

1. If the curling is due to a recently added metal layer, chances are that all of the stress is in the metal. Etch off the metal and reapply a new layer. For the new layer, make sure the sample is kept flat and is given ample time to cool after processing.

2. If kept flat, stresses in a material will sometimes relax over time. Place a curled sample between two glass slides or two pages in a cleanroom notebook overnight or for several days. This may not fix the problem entirely, but usually there is some degree of improvement.

3. Since LCP softens when heated, temperature cycling can often straighten out a sample. Place the sample on a hot plate set to any temperature less than the melting temperature (175-200^{o}C are typical values). Use glass slides or a clean metal block to keep the sample flat. Allow it to sit at temperature for 15-30 minutes and then cool SLOWLY back to room temperature. If no improvement is noticed, then the stresses are either too strong or not in the LCP. If there is some improvement, this process can be repeated until the sample is flat.

4. If none of the above techniques give satisfactory results, temporary or permanent mounting to another wafer can be used as discussed previously in this chapter.

CHAPTER III

CHEMICAL POLISHING OF LCP

It was necessary to develop and optimize a chemical mechanical polishing recipe for LCP substrate to make it adequately smooth for MEMS device fabrication. LCP is a chemically and mechanically durable material, which means that polishing is a non-trivial task. MEMS devices are very sensitive so careful attention must be given so that the polishing process does not damage the material which could hamper the MEMS operation. This chapter presents the research that was performed, the recipe that was developed, and the results that were achieved. This effort was performed in collaboration with Jerry Rung at Lapmaster International [81].

One of the issues with processing on LCP is the surface roughness. Being a polymer, LCP has a maximum surface roughness of about 1.5μm. For a MEMS device that is only 3μm tall, this is a critical problem. Silicon, for example, has an average surface roughness of 10nm, which is adequately smooth for almost all MEMS devices [20]. One solution to the surface roughness problem is to polish the surface using chemical mechanical polishing. The intention was to develop and optimize a polishing recipe for LCP that would make it smooth enough to fabricate MEMS devices on. A roughness less than 50nm was desired.

3.0.1 Polishing Theory

As the name implies, there are two components to CMP. The chemical component is used to soften the material and the mechanical component is used to grind the material away. This process is continued until the sample is sufficiently smooth or planarized. The polishing rate to smooth a sample tends to decrease exponentially as the roughness decreases. That is, it takes much longer to polish a sample from 2μm to 1μm than from 5μm to 4μm.

The sample to be polish is mounted to a fixed structure which is in contact with a rotating polishing pad. A polishing "slurry" is dripped slowly but constantly onto the

polishing pad. The pad rotates and brings the sample in contact with the slurry. The rotation speed is typically less than 60 RPM depending on the material being polished. The used slurry and the material that is removed from the sample slings off the pad due to centrifugal forces. Pressure can be applied on the sample which pushes it into the polishing pad. This will increase the polishing rate but quality may be sacrificed. Permanent damage, such as scratching, can occur as well as contamination of the sample by embedding slurry particles [13]. For this reason samples should always be rinsed thoroughly after polishing.

3.0.2 Polishing Slurry

The slurry is comprised of small particles suspended in a thick gel. The particles are usually silicon dioxide (silica), aluminum oxide (alumina), or silicon carbide crystals that are grown to a specific and consistent size. Silica and alumina crystals are usually softer (lower density) than the material that they are polishing. This prevents serious scratching from occurring. Silicon carbide is very dense and therefore is only used on hard surfaces. Diamond powder is a popular additive to polish many glasses, ceramic, various gemstones, and sapphire materials. It is much harder than silicon carbide but not quite as sharp [81].

Aside from the density of the crystals, the size of the particles is very important. Large particles (1μm to 10μm) have a fast polishing rate and are used for a rough polish (often called "lapping"). Small particles (10nm to 1μm) have a slow polishing rate but are necessary for fine polishing. The smallest particles are for giving samples a "kiss" polish, which makes the surface super shiny. The slurry is typically kept at a pH of 10 (alkaline) for non-metal polishing to keep the particles negatively charged which prevents them from collecting together. Metal polishing slurry is kept at a pH of 3 because acids are more effective at etching metals than bases. Since the particles in acidic slurry are able to attract each other, agitation must be done to maintain uniformity. Only 12-30% of slurry is actually silica or alumina particles. The rest of the material is comprised of buffering agents and other chemicals used to keep the slurry from breaking down or settling [13].

3.0.3 Chemical Mechanical Polishing Issues

Although the theory of polishing is straight forward, the act must be done carefully. A polished sample can only be as smooth as the setup allows. That is, if the sample holder is not flat and smooth, the polished sample will reflect this. Some areas will be rougher than others. If the polishing pad is not replaced often enough, it will wear down and both the polishing rate and quality will be effected. Also, if the polishing pad is not flat, there will be uneven polishing of the sample. These issues can be overcome by carefully monitoring and calibrating the polisher. Worn out parts should be replaced and used slurry should never be reused.

3.1 Polishing Hardware

A polisher is a useful tool for polishing or planarizing wafers. This is not to be confused with a lapper, which resembles a polisher in many ways, but is used for grinding down very rough surfaces. Large-scale polishers are readily available. Smaller, bench-top polishers are available for processing small quantities of samples. These are especially useful for universities and small R&D centers. The type of polisher that is best suited for a certain application depends on many factors, including:

- Type of material being processed
- Speed of plate
- Pressure on samples
- Plate material
- Size and type of abrasive
- Vehicle used
- Flatness of plate
- Feed system

- Method of charging and conditioning the plate
- and Plate temperature.

The bench-top polisher that was used in this research is the Lapmaster 15 from Lapmaster International (the number 15 comes from the size of the plate, which is 15 inches in diameter) [81]. A picture of the polisher is shown in Figure 4.

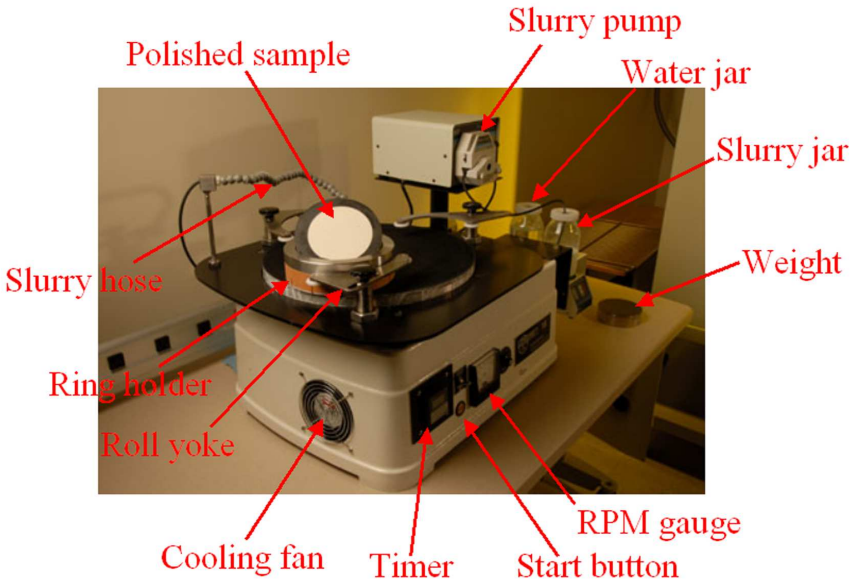

Figure 4: Lapmaster 15 polisher used for processing LCP samples [58]

This polisher utilizes a 15 inch diameter optically flat aluminum plate. A half horsepower motor turns the plate at up to 60 RPM. A large cooling fan is used to keep the motor from overheating. Three roll yokes are used to hold up to three ring holders. In each of these holders, a sample (or multiple small samples) can be held into contact with a mat attached to the plate. As the plate spins, the ring holder is able to spin inside of the roll yoke. This is to guarantee equal polishing across the sample. Four and eight pound weights are available to apply a force to the samples. Slurry is pumped out of a jar and dripped slowly onto the plate. The system is operated when the mat is saturated with slurry. Used slurry slings off the mat, under the plate, and into a waste container.

3.2 Chemical Polishing of LCP

Typically, chemicals are added to the polishing slurry that treat the surface to make it easier to polish. However, there is no known chemical that is readily available that can soften the surface of LCP. Very strong bases (KOH, for example) will dissolve LCP, but it can not be easily controlled and is not safe for use in a polishing system. The following acids and bases were tested on LCP as a possible chemical polishing agent: hydrofluoric acid, acetone, sulfuric acid, nitric acid, chromic acid, hydrochloric acid, sodium hydroxide, methanol, and ethanol [20]. None of the acids or bases had any effect on the LCP. Usually the chemical resistance of LCP is one of its greatest advantages. In this case, it's a limiting factor. The polishing of LCP must be done purely with mechanical means.

3.3 Mechanical Polishing of LCP

LCP is as mechanically durable as it is chemically resistant. Since LCP has a natural maximum roughness of about 1.5μm and a final roughness of 50nm is desired, careful selection of the slurry must be done. A silica or alumina slurry alone would not be hard enough to do the rough polish in a timely manner. A proper balance of hard particles to do the cutting and soft particles to do the polishing is needed for an optimal finish.

3.4 Polishing Recipe

With the Lapmaster 15 polisher, there are three variables that can be controlled in the polishing process: the contact force, the polishing pad spin speed, and the slurry conditions.

3.4.1 Contact Force

The contact force typically used ranges from 2 to 10 psi. Metal disks that weight 4 or 8 pounds are stacked to vary the force. For this material, 2-4 psi of pressure is applied. For a sample size with a diameter of 4 inches (12.6 square inches), this corresponds to a weight of 25-50 pounds [81].

3.4.2 Polishing Pad Spin Speed

Rotation rates can vary from 20 RPM to 500 RPM. As would be expected, the faster the rotation rate the faster the polishing rate. As long as the polishing pad remains adequately moist, no damage will be done to the sample at higher spin speeds. However, this does present a safety risk. Suppose one of the weights came loose and fell onto the platen. At 500 RPM, the weight would slide off the polisher at about 22.3 MPH. This weight would carry enough momentum to cause severe injury or damage to anything around it. For this reason, polishing is usually done at less than 60 RPM.

3.4.3 Slurry Conditions

Since we know that both hard and soft particles are needed to properly polish LCP, a special "hybrid" solution was created. The solution is comprised of three substances:

1. Alumina slurry - Americal Plus is a commercially available 1μm diameter solution that is commonly used to polish eye glass lenses. It is non-toxic as well. This will provide the soft particles.

2. Diamond - This product is monocrystalline and is produced under high temperatures and pressures to have a 0.5μm diameter. It has a multifaceted sphere-cuboid shape for strength and efficiency. It will provide the hard particles but because of its unique shape, it will not cause scratching of the surface.

3. Water - This is used to dilute the slurry.

Americal Plus is slightly acidic so the particulates will settle quickly if not agitated. For this reason, the slurry will be constantly mixed with a magnetic stirring rod. Also, the diamond particles tend to clump together when exposed to liquids. They should always be added to the solution while it is being mixed with the stirring rod. Using too much diamond will etch the material faster than the surface can be polished. In the time it takes to properly polish a 100μm sample, it may end up being 80μm thick. This can have a profound effect on the device performance. After combining all three substances, the solution should be allowed to mix for a few minutes to give the particles time to disperse evenly.

3.5 Polishing Results

As desired, a recipe for polishing LCP to within 50nm roughness was achieved. An average of 45-60 minutes is needed per four-inch sample. A before and after profilometer (surface roughness) scan is shown in Figure 5.

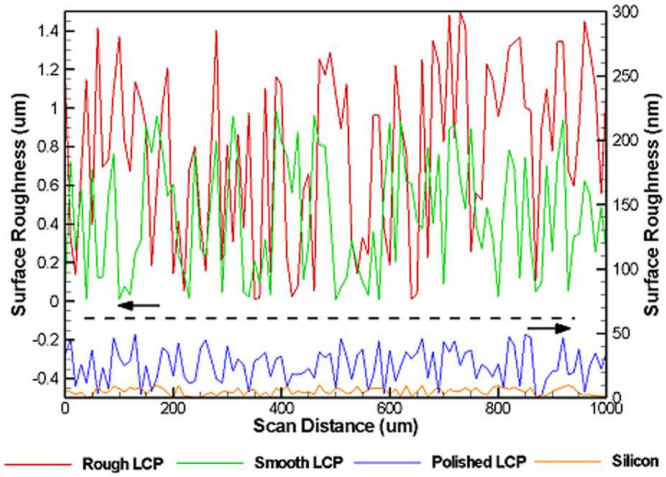

Figure 5: Before and after polishing surface roughness is shown.

"Rough LCP" is the material that comes from Rogers Corp. with the copper cladding. Once the copper is removed, the profilometer scan is performed. It has a maximum roughness of about 1.5μm. "Smooth LCP" comes from Rogers Corp. without the copper cladding. It has a maximum roughness of about 1μm. The polished LCP (which utilizes the scale on the right) has a maximum roughness of 50nm, which was the target. To compare that to a benchmark, a bare, polished silicon wafer was measured to have a roughness of less than 10nm. All four of these scans are shown in Figure 5.

The optimal polishing conditions are summarized in Table 4.

Table 4: Optimal LCP polishing conditions

Spin Speed	55 RPM
Tool Force	2-4 psi
Slurry mixture	
Water	6 oz
Alumina slurry	12 oz
Diamond powder	1 gram

CHAPTER IV

MEMS SWITCH FABRICATION STEPS

In this chapter, all of the process steps necessary to fabricate RF MEMS switches are discussed. The recipes that have been developed on the machines in the MiRC cleanroom are given in Appendix B. These steps can be used to fabricate MEMS on any material, although LCP will be used as the substrate for this example since it is the material used in this thesis. A picture of a MEMS switch fabricated on LCP is shown in Figure 6.

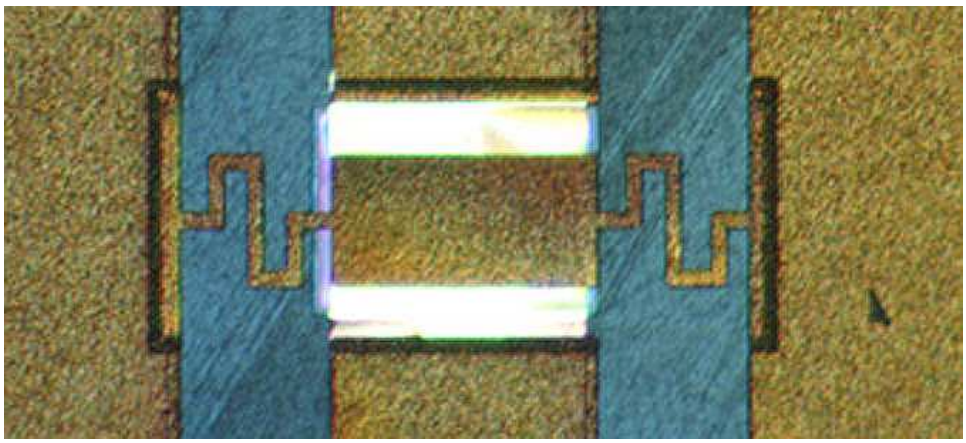

Figure 6: A picture of a MEMS switch fabricated on LCP is shown

4.1 Preparation

Before fabricating, the sample must be stripped of the copper, polished, cleaned, and dried (see the previous chapters on LCP fabrication and polishing for details). If backside metal is required, it should be sputtered on by a DC sputtering tool to a thickness of 2-3μm. Copper is recommended since it is inexpensive and can be deposited quickly.

If the device is going to be mounted to a glass slide, it should be done carefully to minimize damage to the polished surface. The easiest way to attach a glass slide is with the LCP sample upside down with the polished side laying on top of a TexWipe. The glass slide

can be aligned to the back of the sample by sight and affixed using photoresist or double-sided tape as described earlier. It is important to avoid moving the sample transversely on the TexWipe when upside down. Even though the TexWipe is soft, it can still scratch the surface. Always place the sample straight down and lift the sample straight up when the polished side is in contact with another surface. For this example, it will be assumed that vacuum mounting is used so that glass mounting is not necessary.

4.2 Fabrication Steps

In the following steps, the diagrams are not to scale. Fabrication begins with a clean, smooth, bare wafer as shown in Figure 7.

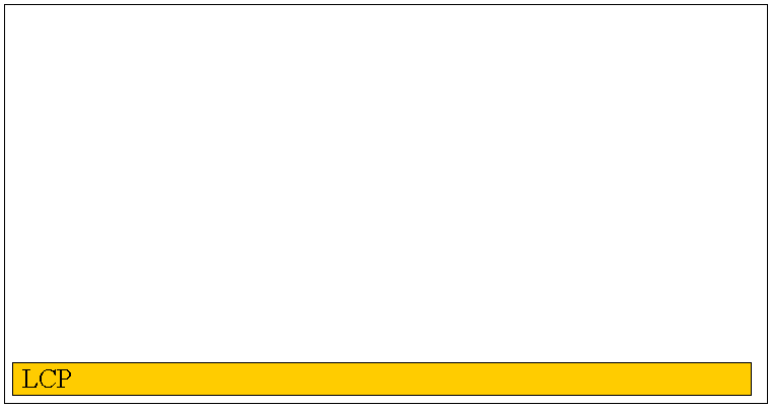

Figure 7: Fabrication starts with a clean, smooth, bare LCP wafer

A titanium-gold (250$\mathring{A}$-2500$\mathring{A}$) layer should be electron beam evaporated onto the bare wafer. The chamber pressure should always be less than 2μTorr to minimize the temperature of the sample, which will minimize substrate curling. Evaporation is used instead of sputtering because it provides a smooth, uniform metal layer. This will improve the switch reliability since the membrane will make contact with a smooth surface. Evaporation is also a low-temperature deposition process which will prevent stresses from accumulating in the signal lines. An LCP sample after metalization is shown in Figure 8.

The metal is patterned using standard hard-contact optical lithography. Positive photoresist is used with a clear field mask to apply photoresist everywhere except for where the signal lines and switch gaps are located. This is shown in Figure 9.

Figure 8: LCP sample after first metalization step is shown

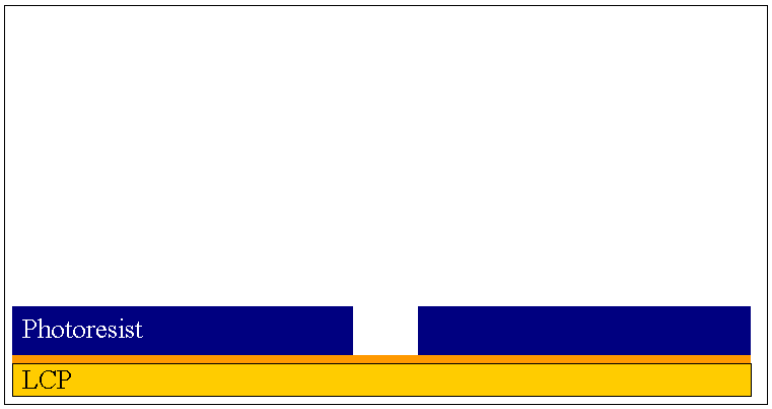

Figure 9: The seed layer is patterned with photoresist

The metal is then etched away using transcene (or gold etchent). This is shown in Figure 10.

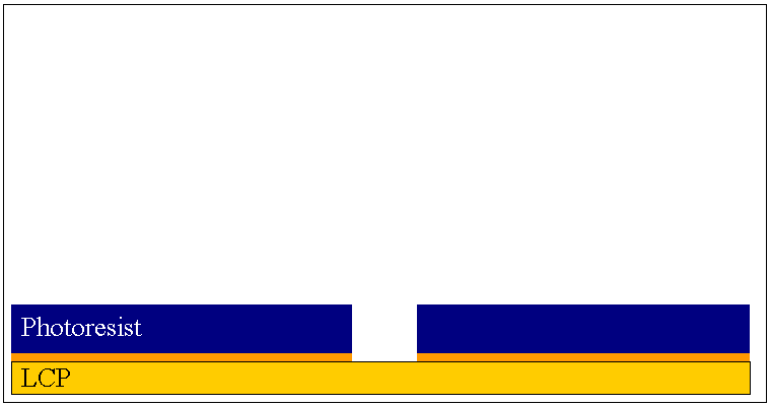

Figure 10: The metal seed layer is removed with gold etchent

The photoresist is removed using acetone and rinsed using deionized water. This is shown in Figure 11.

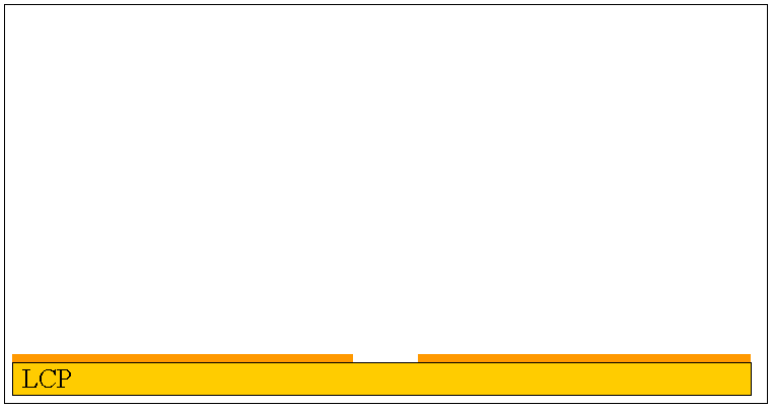

Figure 11: The first resist layer is removed with acetone

The sample is then placed in a Plasma Enhanced Chemical Vapor Deposition (PECVD) machine to deposit a 1500-3000$\mathring{A}$ (0.15-0.3μm) thick layer of silicon nitride (Si_3N_4). A PECVD is used for the deposition because it is fast and low temperature. Sputtering or thermally growing nitride would yield a much higher quality film, but the temperature is much higher than the melting point of LCP. A PECVD deposited layer of nitride tends to be "spongy" in nature, meaning it has a lot of vacancies and interstitial defects. This can worsen the dielectric charging effect since these defects can store charge.

To keep the sample flat during plasma processing, thick glass microscope slides are laid on the edges to weigh them down. The presence of the glass slides create a vertical discontinuity across the edges which effect the plasma at the discontinuity. This will result in greatly reduced deposition at those points. Since it occurs at the edges and not near the features, it's not a problem. All of the nitride at those points will be etched off anyway. The sample after nitride is deposited is shown in Figure 12.

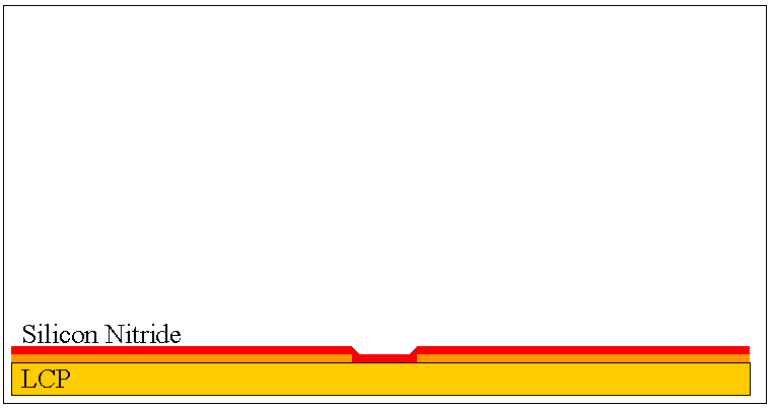

Figure 12: The sample is shown after silicon nitride deposition

Before the nitride can be etched, the areas that need to be preserved must be covered with a photoresist layer. Positive photoresist is used with a clear field mask to do this. The placement of the resist is shown in Figure 13.

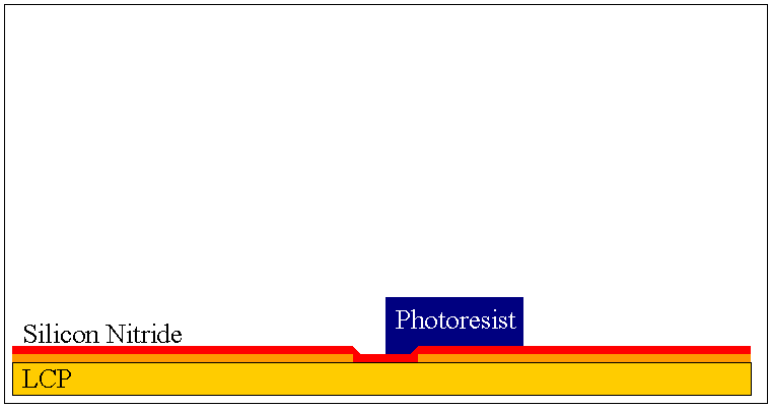

Figure 13: The nitride layer is patterned with photoresist

A Reactive Ion Etch (RIE) is used to remove the nitride layer. LCP is very sensitive to ion etching, especially if the surface is polished. The etch time should be minimized

to prevent over etching (and roughening) of the LCP. The final appearance is shown in Figure 14.

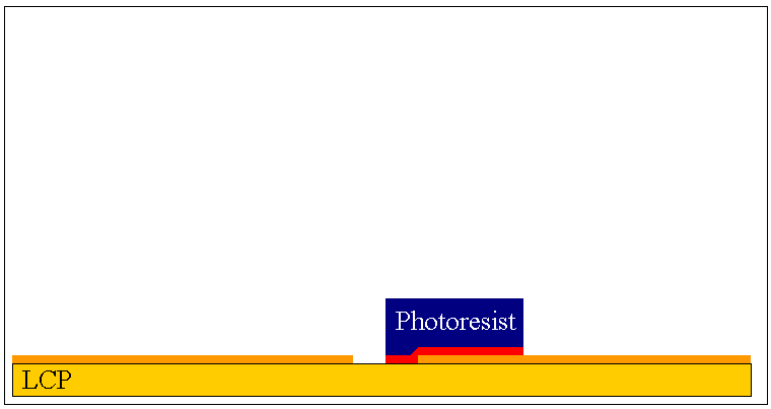

Figure 14: The nitride layer is etched using an RIE process

The photoresist can be removed with acetone. This should be done thoroughly since the RIE tends to make photoresist very hard and it can be tricky to remove. The sample after the photoresist is removed is shown in Figure 15.

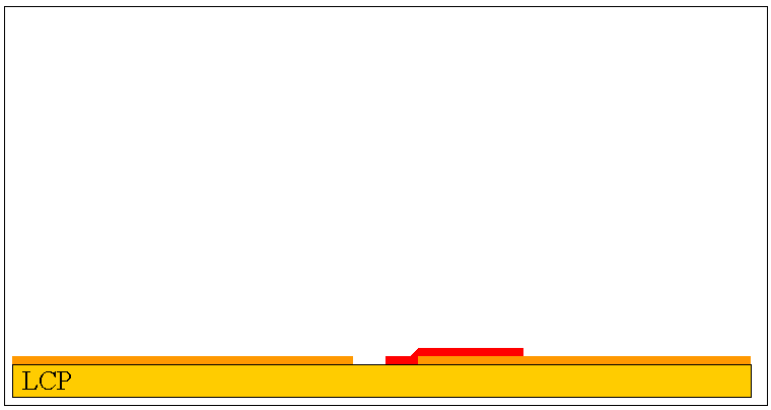

Figure 15: The second layer of photoresist is removed with copious amounts of acetone

NOTE: If the substrate material is not LCP then a short oxygen plasma can be used to remove any stubborn photoresist. Since oxygen plasma also etching LCP, it should not be used in this case.

The sacrificial layer must now be patterned using positive photoresist and a clear field mask. If the resist is not hard baked properly, it will outgas during evaporation and this

will drastically change the shape of the membrane. A hard bake can be performed using a hot plate at 140^{o}C for 10 minutes followed by a 10 minute bake in a 140^{o}C oven. The location of the sacrificial resist is shown in Figure 16.

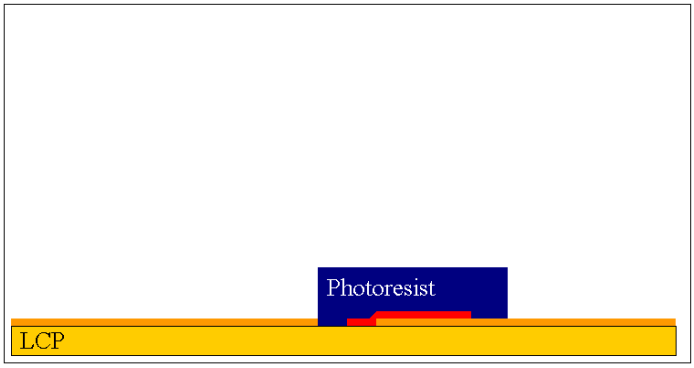

Figure 16: The sacrificial photoresist is patterned which determines the height of the switch

A titanium-gold-titanium (250$\mathring{A}$-2500$\mathring{A}$-250$\mathring{A}$) seed layer for the switch membrane should be electron beam evaporated on top of the sample. To prevent outgassing, the lowest possible chamber pressure should be used. This is typically around 1μTorr for the CVC E-beam evaporator. The seed layer deposited is shown in Figure 17.

NOTE: Since this is electron beam evaporation, the deposition should be anisotropic. However, in practice, this is not exactly the case. In Figure 17, metal coverage is shown on the side walls. There will be a small amount of deposition on the side walls, but it is much less than the deposition perpendicular to the surface.

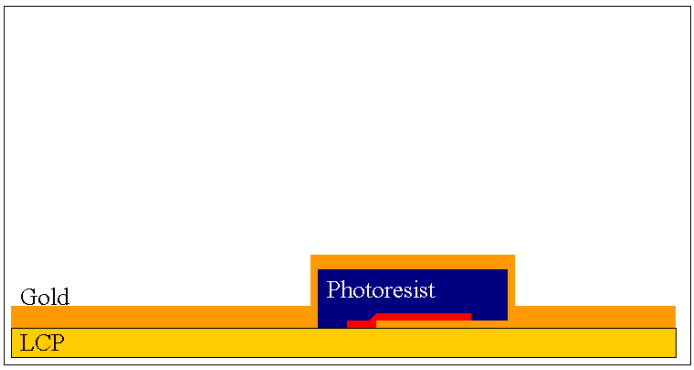

Figure 17: The top seed layer is deposited using E-beam evaporation

Photoresist must now be patterned for the membrane geometry. For this step, positive photoresist can be used with a dark field mask or negative photoresist can be used with a clear field mask. Positive photoresist is preferred because it is easier to use than negative resist. After patterning, the top titanium layer must be etched away using a 10:1 diluted solution of hydrofluoric acid (HF):water. This will not effect the gold or the resist. This is shown in Figure 18.

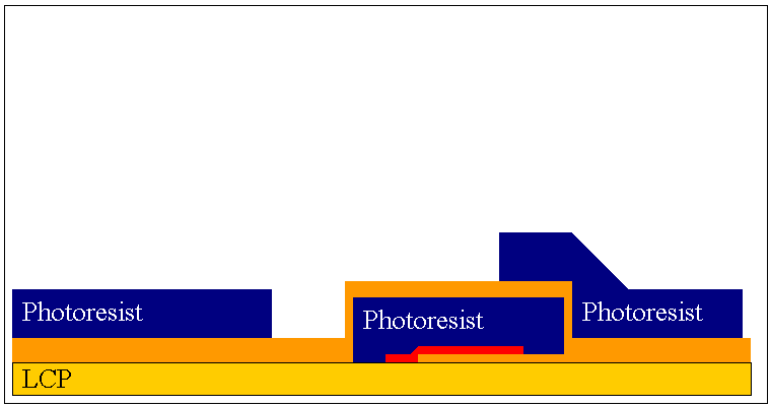

Figure 18: The membrane photoresist layer is patterned

At this point, a 2-3μm thick layer of metal must be created for the switch membrane. There are two options. The metal can be evaporated and a wet etch procedure can be used to remove the unwanted metal. This is typically done using aluminum or gold. However, evaporating a layer this thick can take 2.5 hours which will significantly heat the sample and can cause problems. The other option is to electroplate, which is the preferred option. Even though electroplating is messy, dangerous work (gold plating solution is cyanide based) it is the best way to make a well defined membrane geometry with a controllable thickness. The process of electroplating is described in Appendix B. A current of 6-15 mA is typically used which can take 30-60 minutes to complete. The elecroplated sample is shown in Figure 19.

Removing the photoresist can not be done using acetone. Exposing the sample to acetone will also dissolve the sacrificial layer, which will damage the switch membrane. The best way to remove the resist is to expose and develop. The switch metal prevents the photoresist under it from being exposed. Since the resist has not been exposed, it is not effected by the developer. This step is shown in Figure 20.

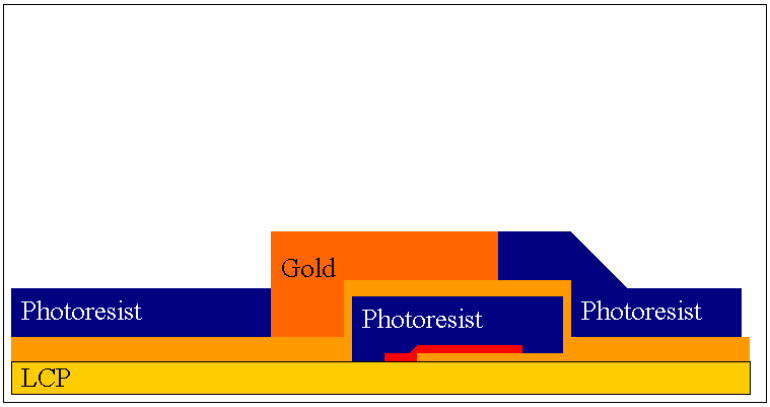

Figure 19: The sample is electroplated with 2-3μm of gold to form the membrane

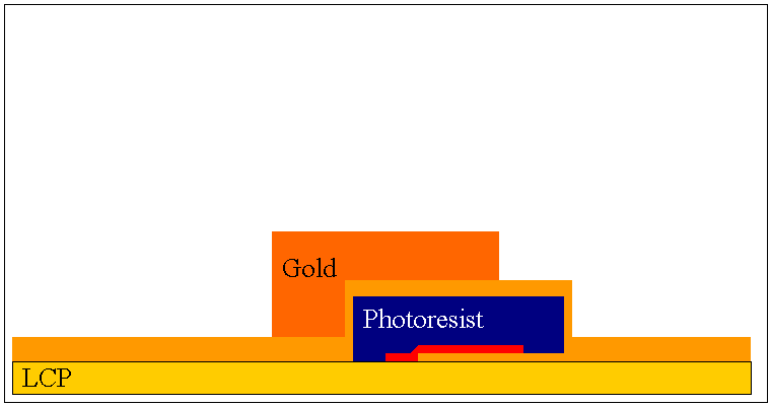

Figure 20: The top photoresist layer is removed by exposing and developing away the material

The seed layer that was evaporated for the switch membrane must now be removed. Since the signal lines and switch membrane are much thicker than the seed layer, the seed layer can be etched without greatly effecting the other metal layer. Removing the seed layer requires exposure to titanium etchent then gold etchent and then titanium etchent. Titanium etchent does not etch gold so it can be left in the solution for longer than needed. Usually 10-12 seconds is enough though. The gold etching should be done as quickly as possible. The sample should be checked every 10-20 seconds to see if the gold has etched completely. A final exposure to titanium etchent should return the sample back to the usually LCP color. Checking the sample in the microscope throughout this etching process is a good idea. By this point, many hours have been invested in the fabrication process. A distracted fabricator can easily ruin a week's worth of work in seconds. The sample after

metal etching is shown in Figure 21.

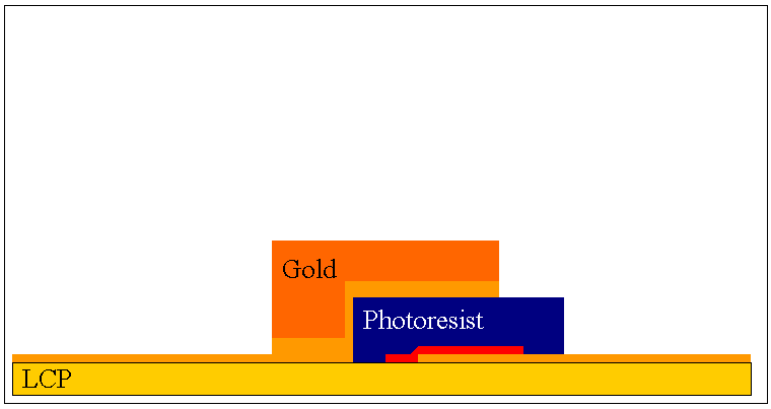

Figure 21: The top seed layer is removed using a titanium-gold-titanium wet etch

The sample should now be soaked in photoresist stripper to dissolve the sacrificial photoresist layer. The guidelines for doing this on LCP was discussed in Chapter 2. The sample becomes very delicate during this step so it should be handled with great care. After stripping is complete, the sample should be soaked in deionized water for 2 minutes to remove the stripper. Afterwards, it should be placed in IPA. Samples can be stored in IPA for up to a week, as long as the samples are not disturbed and the IPA doesn't fully evaporate. From the IPA, it should go directly into a critical point dryer. This machine is capable of drying the sample without the switches being pulled down from water tension. A picture of the switch after fabrication is complete is shown in Figure 22.

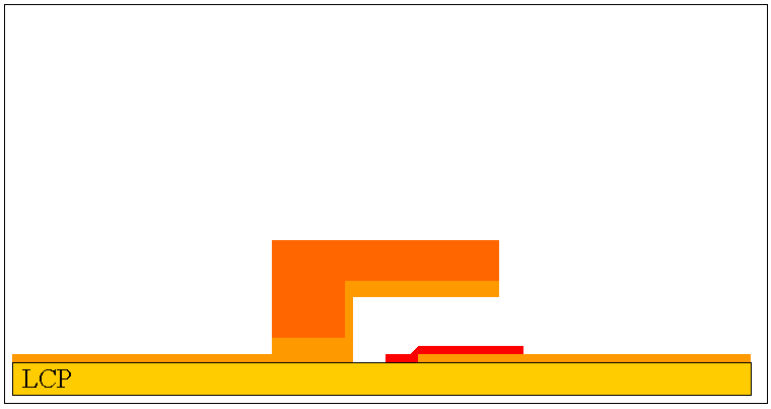

Figure 22: After fabrication is complete, the membrane is suspended over the substrate

From experience, fabricating MEMS on an empty stomach, when feeling rushed, or when

over tired will usually results in careless mistakes and time being wasted. This is the pace that is recommended:

Day 1 Laser cut and clean the samples. Polish.

Day 2 Backside and topside metalization. If mounting is going to be done, this is a good time.

Day 3 Pattern and etch the first metal layer. Deposit, pattern, and etch the nitride layer.

Day 4 Pattern and hard bake the sacrificial layer. Deposit the bridge seed layer. Pattern and electroplate the bridge membranes. Soak in photoresist stripper (overnight)

Day 5 Dry the switches and measure

Day 4 will be the most rigorous fab day, but for the optimal results, once the sacrificial layer has been formed it's best to finish the fabrication as quickly as possible. Aging photoresist will outgas and compress, forming compression lines on the surface. This will induce stress in the metal layer and will often cause curling in the membrane.

DEVELOPMENT OF MINIATURE, MULTILAYER, INTEGRATED, RECONFIGURABLE RF MEMS COMMUNICATION MODULE ON LIQUID CRYSTAL POLYMER (LCP) SUBSTRATE

PART II

Component Level Research

by

Nickolas Kingsley

Part II

Component Level Research

In Part I, a fundamental level of knowledge was presented. In this section, that knowledge is used to create RF devices on LCP. The most challenging component to fabricate was the RF MEMS switch. A thorough analysis of MEMS switch design, simulation, and testing is given. Phase shifters and planar antennas were the first devices to be integrated with MEMS switches. These devices are described in this section.

CHAPTER V

NOVEL TECHNIQUE FOR CALCULATING MEMS PULL DOWN VOLTAGE

RF MEMS switches are useful for providing low-loss switching elements in high frequency devices. Since these devices contain a mechanical and an electrical component to their operation, predicting their performance is not trivial. Computational analysis can be extremely complicated due to the large number of variables that need to be incorporated. Using a multi-physics simulation tool seems like the only solution, but most simulators are optimized for only one engineering realm (i.e. mechanics or electronics). Combining different engineering realms into one simulated model will usually compromise the accuracy of the results. Often simulators cannot properly model a multi-realm device at all. This chapter offers a solution to this problem by proposing a technique for combining computational analysis with simulation to determine the pull-down voltage and RF characteristics of a MEMS switch. Measurement results agree closely with the simulated results using this technique.

5.1 Switch Operation

The switches being considered are double-supported, capacitive type. The switch works by deflecting the beam towards the bottom metal layer and causing an RF short circuit. The inductive regions behave like springs and make it easier to deflect the beam. A spring constant can be determined which evaluates the amount of force necessary to deflect the beam a given distance. Changing the shape or dimensions of the inductive region will increase or decrease the spring constant. The capacitive regions are responsible for creating an electrostatic force between the DC biased beam and the metal layer below it. This force is responsible for decreasing the "gap" between the metal layers. Changing the gap length, height, or the area of the capacitive region will increase or decrease the electrostatic force

necessary to deflect the beam. Across the capacitive region, the charge density in the metal should be uniform. Otherwise, the beam will not deflect parallel to the bottom metal layer. Any skewing of the beam caused by fabrication misalignment or non-symmetric inductive regions will result in a smaller capacitance and a poor RF short circuit. As long as the switch is adequately thick (2-3 skin depths), made from a high-quality, highly conductive metal (aluminum or gold, usually), and properly aligned (to equalize the fringing electric fields on all sides) charge density in the metal will be uniform. MEMS switches that are not deflecting uniformly are usually caused by fabrication misalignment, non-uniform metal thickness, or contaminants in the capacitive region metal. The latter two issues prevent the charge density from being uniform by hampering the flow of electrons in the metal and can be rectified by altering the fabrication recipe.

Electrically, the inductive and capacitive regions behave as their name implies. Changes in these regions will change the RF performance of the switch. The dielectric layer provides high capacitance when the switch is in the down state and is used to prevent stiction between the two metal layers. A very thin layer ($2000\mathring{A}$) of silicon nitride is typically used and generally has a negligible effect on the mechanics of the switch. That is, the bending of the beam is not directly effected by the presence of the silicon nitride. However, electrons can accumulate in this thin layer which can build up a large enough charge to effect the electrostatic actuation of the switch. Dielectric charging is especially pronounced in silicon nitride layers that are deposited using Plasma Enhanced Chemical Vapor Deposition (PECVD) because of the large number of atomic defects generated from the plasma. Charging effects can be greatly reduced by properly grounding the silicon nitride to prevent electron accumulation. This can be improved further by thermally growing the dielectric layer instead of using PECVD, if the substrate material can handle the high temperature [14]. Modeling MEMS switches for optimal electrical and mechanical performance can be a daunting task and is often substituted with a less accurate method. For instance, MEMS switches are often designed for optimal electrical properties (such as a low RC time constant [87]) or optimal mechanical properties (such as a low actuation voltage [70]). There are four popular inductive region configurations [100]. These designs, labeled 1-4, are shown in Figure 23.

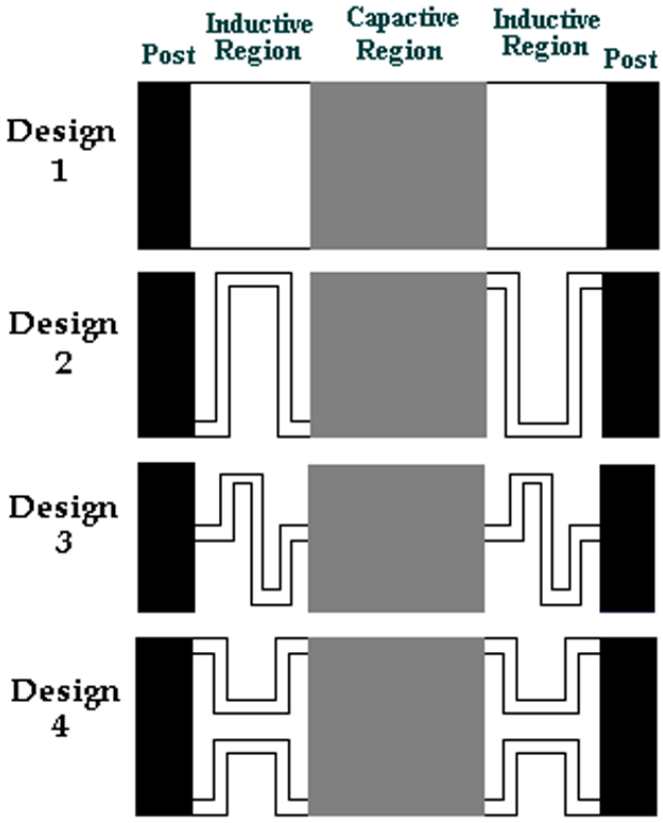

Figure 23: Four different popular MEMS switch geometries [44]

Deriving the equations for predicting MEMS switch performance that utilize these inductive and capacitive regions is difficult. Very general equations can be investigated but the results can only be used as rough estimates [61, 87]. Those who have tried predicting MEMS switch behavior using only theory often report a discrepancy upwards of a factor of ten between predicted and measurement results [72]. Certainly design optimization can not be done this way. Using simulation software is the only way to take into account most of the idiosyncrasies of device performance. However, it is not always possible, or effective, to use a simulator to predict mechanical performance due to an electrostatic force. RF MEMS switch feature sizes are often on the order of $\lambda/1000$ or smaller. This is much smaller than the typical element size of a Finite Element Method (FEM) or Finite-Difference Time-Domain (FDTD) simulator, whose typical element sizes are $\lambda/20$ to $\lambda/10$, although simulations with small feature sizes are still possible with these methods [10]. A Method of Moments (MOM) simulator could be used to model the small feature sizes, but if the switch is being simulated with other devices (i.e. filters or antennas) or on a multilayer substrate then an FEM simulator would be more accurate because of the improved cell size. Clearly there is a trade off. Alternatively, hybrid simulators have been investigated which attempt to utilize the advantages of both types of simulation. No matter which type of simulator is used, when devices with small feature sizes (i.e. RF MEMS switches) are simulated in a complex environment (i.e. when surrounded by an electric field) assumptions must be made within the simulator and results will be compromised [101]. Often, when multiple physical realms are involved in a problem, the optimal solution method is to use a simulator to solve the problem in the more complicated realm and to combine those results manually with theory from the simpler realm. For the RF MEMS switch, we are combining a mechanical beam dynamics problem with an electrostatic problem. The theory that deals with the electrostatics of a capacitive region is well known and straightforward, whereas the dynamics of a beam with complicated springs is much more difficult to solve. Solving the problem in one simulation that couples the two physical realms does not always give the most accurate results because of assumptions and simplifications used in the simulator.

Instead, the proposed method models an RF MEMS switch by simulating first in an optimized FEM mechanical simulator then calculating the pull-down voltage by using simple electrostatic equations.

5.2 Mechanical Analysis of RF MEMS Switches

Equations for predicting the bending of cantilever and doubly-supported beams have been around for decades [73]. Unfortunately, applying simplistic equations to complex MEMS devices can be cumbersome. The two most important mechanical features of a MEMS switch are the pull-down voltage and the deflection. Both of these quantities can be calculated by treating the MEMS switch as a mechanical spring. In order to calculate the pull-down voltage, one must equate the force pulling down on the beam by the electrostatic force between the metal layers

$$f_{down} = \frac{\epsilon A V^2}{2g^2} \tag{1}$$

and the force pushing up from the spring (Hooke's Law) [85]

$$f_{up} = -\kappa(g_o - g). \tag{2}$$

For these equations, ϵ is the permittivity, A is the area, V is the voltage, κ is the spring constant, g_o is the initial gap, and g is the evaluated gap. We can use these simple, spatially independent equations since we know the charge density (and therefore the force) is uniform across the capacitive region. It has been well documented that for parallel plate electrostatic actuation, when the gap reduces to 2/3 of the original gap, the beam becomes unstable and experiences a "pull-in" effect [85]. That is, the MEMS switch does not deflect over the entire gap according to the formula in (1). Instead, when the gap reaches a certain threshold, namely 2/3 the original gap, the switch will snap down. Magnets experience the same effect. As two magnets of opposite polarity are brought closer together the attractive force is barely noticeable until they reach a certain distance apart. At this point they snap together and the force between them is great. Equating (1) and (2) where the gap is 2/3 the original gap and solving for the pull down voltage gives

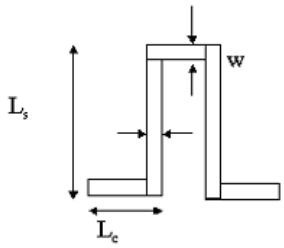

Figure 24: Illustration of dimensions for Eqn. 5 [44]

$$V_{PI} = \sqrt{\frac{8kg_o^3}{27\epsilon A}}. \tag{3}$$

The maximum deflection can also be calculated from the spring constant by the equation [73]

$$\delta = \frac{-F}{k} \tag{4}$$

where δ is the deflection, F is the force pushing down on the spring (in Newtons) and k is the spring constant. The values for the permittivity, area, and gap can be designed for and implemented in fabrication. The only two unknowns for a given MEMS switch are the spring constant and the downward force. The spring constant can be derived for a meandered line by the equation [100]:

$$k_m = \frac{Ew\left(t/L_c\right)^3}{1 + \frac{L_s}{L_c}\left(\left(\frac{L_s}{L_c}\right)^2 + 12\frac{1+\nu}{1+(\frac{w}{t})^2}\right)} \tag{5}$$

where w is the width of the meander, t is the thickness of the metal, ν is the Poisson's ratio of the metal, L_s is the overall width of the spring, and L_c is the distance from the end of the spring to the start of the meander. These dimensions are illustrated in Figure 24.

For a non-meandered spring, the spring constant is given by [27]

$$k_{non-m} = \frac{32EWH^3}{L^3} \tag{6}$$

where E is the Young's Modulus, W is the width, H is the thickness, and L is the length. The effective spring constant, k_{eff}, for the entire MEMS switch can be determined

by combining the simple spring equations in a fashion similar to capacitors. That is, springs in parallel add directly and springs in series add as the inverse of the sum of the reciprocals. Therefore, the effective spring constants for the four switch designs presented in this chapter are:

Design 1

$$k_{eff} = \frac{32EWH^3}{L^3} \tag{7}$$

Design 2

$$\frac{1}{k_{eff}} = \frac{1}{k_m} + \frac{1}{k_{n-m}} + \frac{1}{k_m} \tag{8}$$

$$\therefore k_{eff} = \frac{k_m k_{n-m}}{k_m + 2k_{n-m}} \tag{9}$$

Design 3

$$\frac{1}{k_{eff}} = \frac{1}{k_m} + \frac{1}{k_m} + \frac{1}{k_{n-m}} + \frac{1}{k_m} + \frac{1}{k_m} \tag{10}$$

$$\therefore k_{eff} = \frac{k_m k_{n-m}}{k_m + 4k_{n-m}} \tag{11}$$

Design 4

$$\frac{1}{k_{eff}} = \frac{1}{2k_m} + \frac{1}{k_{n-m}} + \frac{1}{2k_m} \tag{12}$$

$$\therefore k_{eff} = \frac{k_m k_{n-m}}{k_m + k_{n-m}} \tag{13}$$

where k_m is the meandered spring constant given by (5) and k_{n-m} is the non-meandered spring constant given by (6). Substituting k_{eff} from (7)-(13) into (3) for k will give the theoretical pull down voltages.

5.3 Mechanical Simulation of RF MEMS

Before any complex mechanical simulations are performed, it is necessary to validate the model. Careful attention must be given to material properties, boundary conditions, and the applied forces. One way to validate a simulation model is to compare simulated values with theoretical values for a simple case. If the results agree, more complicated configurations can be simulated and the results can be trusted.

5.3.1 Verification of Simulation Tool

The FEMLAB 3.0 static structural mechanics module from Comsol was used for the mechanical simulations. FEMLAB is a multiphysics simulation tool, which is commonly used in industry and university settings [16]. The 3D MEMS switch structure with non-meandered springs (Design 1) was simulated with a uniform force pushing down on the center capacitive region. The theoretical deflection profile can be determined by taking advantage of spring superposition. This procedure is demonstrated in Figure 25 for the distribution of force, q.

The deflection equation for a uniformly actuated beam is given by [73]

$$\delta(x) = \frac{x^2(L^2 - 2Lx + x^2)q}{2EWH^3} \tag{14}$$

where x is the position along the beam, L is the length of the beam, and q is the force applied per length. These parameters are exemplified in Figure 26.

The deflection equation for a partially actuated beam is given by [85]:

$$\delta = \begin{cases} -\frac{qbx^2}{12EI}3L+3a-2x & for\ 0 \le x \le a \\ -\frac{q}{24EI}x^4-4Lx^3+6L^2x^2-4a^3x+a^4 & for\ a \le x \le L \end{cases} \tag{15}$$

where a is the distance from the anchor that the force begins, b is the length of the beam that the force is applied to, and I is the moment of inertia given by [27]:

$$I = \frac{HW^3}{12} \tag{16}$$

where H is the thickness and W is the width of the beam. Figure 27 shows a plot of the

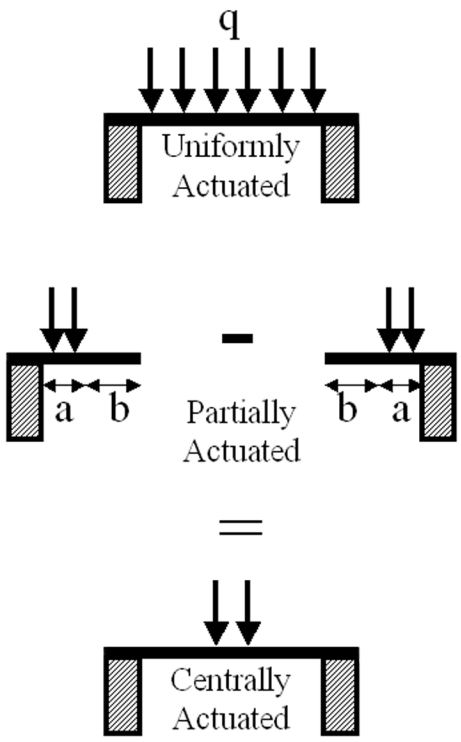

Figure 25: The procedure for spring superposition is shown [44]

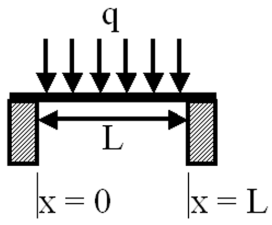

Figure 26: Illustration of dimensions for Eqn. 14 [44]

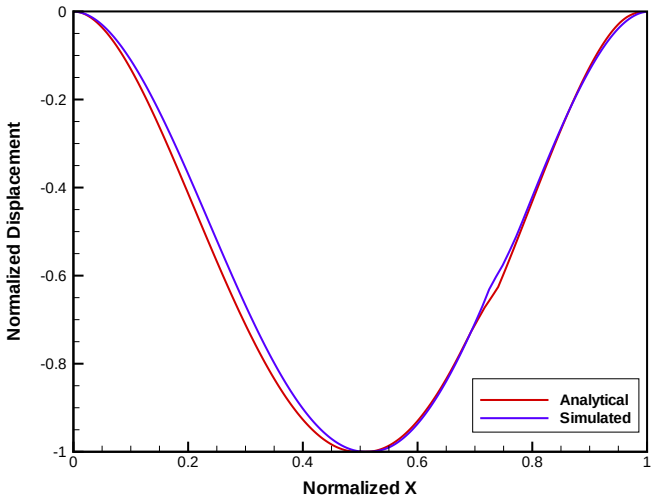

Figure 27: Comparison of simulated and analytical displacement of non-meandered switch [44]

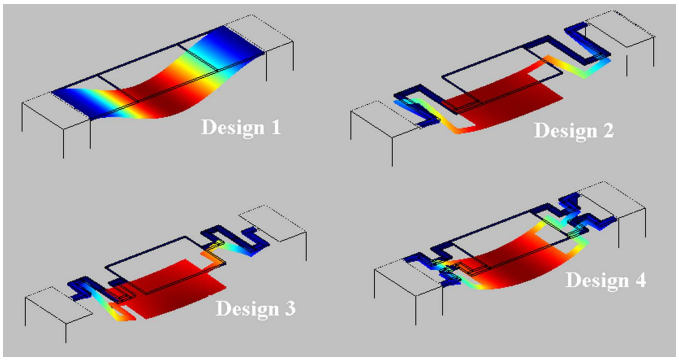

Figure 28: 3D deflection profile of RF MEMS switches [44]

deflection given by FEMLAB and the results from the superposition of (14) and (15). The average error across the Normalized X axis is 1.4% and the maximum error is 4.8%.

Since the simulation results agree closely with the analytical results, it is safe to assume that the simulator will be reasonably accurate for the more complicated spring configurations. The simulated deflection profile of the four switch designs is shown in Figure 28.

5.3.2 Deriving Pull-down Voltage from Simulation

Using FEMLAB, it is easy to determine the force necessary to deflect the MEMS switch a desired distance. Ideally, it is necessary to deflect the MEMS switch the same distance as the gap between the beam and the metal layer below it (usually 1.5-3μm). The equation that relates force to pull-down voltage in terms of the gap is given by [73]

$$V_{PI} = \sqrt{\frac{2g^2F}{\epsilon}} \tag{17}$$

where F is the force per area. This equation is derived from the pull-down voltage in (3), where F incorporates the spring constant. Doing a unit analysis between (3) and (17) will result in the same outcome, volts. Changing the force per area acting on the capacitive region until the deflection matches the gap will determine the force. Although a guess-and-check method is necessary to determine the value, this can be performed quickly using interpolation since force and deflection are linearly related. This force can then be used in (17) to calculate the pull-down voltage.

5.4 Electrical Simulation of RF MEMS

In addition to the mechanical performance of MEMS switches, it is important to evaluate the RF characteristics. The springs exhibit an inductance, the actuation region exhibits a capacitance, and the metal beam exhibits a resistance. All together, the beam behaves like a series RLC circuit. These values can be calculated within an order of magnitude by using fundamental RLC equations. The resistance can be calculated using [75]:

$$R = \frac{\rho L}{HW} \tag{18}$$

where ρ is the metal resistivity and L is the length of the beam. The capacitance can be calculated using [75]:

$$C = \frac{\epsilon A}{g}. \tag{19}$$

Knowing the resonant frequency from measurements, the inductance can be calculated using [75]:

$$L = \frac{1000}{4\pi^2 C f^2} \tag{20}$$

where f is the resonant frequency given in GHz, C is given in pF, and L is calculated in nH. Papers have been published which investigate elaborate circuit models for MEMS

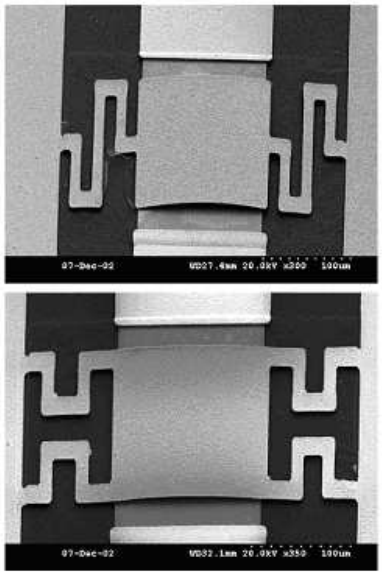

Figure 29: SEM photos of fabricated switches (designs 3 and 4) [44]

switches [65, 77]. However, if results within an order of magnitude are suitable, these simple equations are more than adequate.

5.5 Measurements

All four switch designs were fabricated and measured to determine the actual pull-down voltage and resonant frequency. This effort was performed by Guoan Wang. Scanning electron microscope (SEM) pictures of two of the switches are shown in Figure 29. Measurements were taken with Thru-Reflect Line (TRL) calibration to deembed the cable and connector losses.

5.6 Results

Results for the mechanical and electrical characteristics of the four spring designs are presented in the following sections. Measurement results were taken for each design. The measured pull-down voltage is within 5V of the minimum pull-down voltage. Voltage ramping must be done quickly to minimize charge accumulation in the underlying dielectric region.

Table 5: Comparison of theoretical, simulated, and measured V_{PI} [44]

Design	Theoretical	Simulated	Measured	Avg Error	Avg % Error
1	117.135V	127.5V	100V	13.75V	11.97%
2	40.547V	38.4V	35V	3.85V	10.14%
3	31.875V	27.8V	30V	2.98V	9.97%
4	69.050V	72.8V	70V	2.35V	3.33%

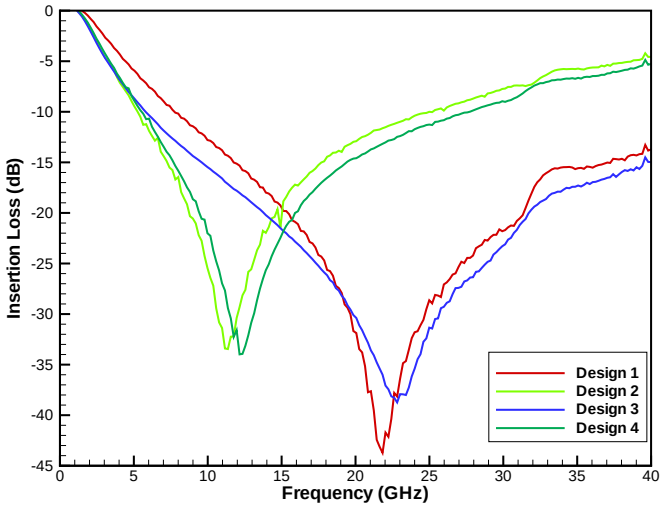

Figure 30: Measured response of MEMS switches to determine the resonant frequency [44]

5.6.1 Comparison of Mechanical Analysis

Table 5 displays the comparison between the purely theoretical, the simulated method presented in this chapter, and the measured pull-down voltage.

The measurement results agree closely with the theoretical and simulated results. The average error is within the measurement ramping tolerance (5V). The theoretical results are generally within 5-8% of the simulated values. There is a small discrepancy between simulated and theoretical values due to simulator meshing tolerances.

5.6.2 Comparison of Electrical Analysis

The switches were measured to determine the resonance frequency. This is shown in Figure 30.

Using the measured resonance frequency and the capacitance calculated from (19), the

Table 6: Calculated capacitance, inductance, and resistance for the four switch geometries [44]

Design	Resonant Frequency	C	L	R
1	22.8175GHz	2.2pF	22pH	0.3Ω
2	11.3625GHz	2.9pF	65pH	0.6Ω
3	12.1525GHz	2.8pF	60pH	0.5Ω
4	21.83GHz	1.9pF	28pH	0.2Ω

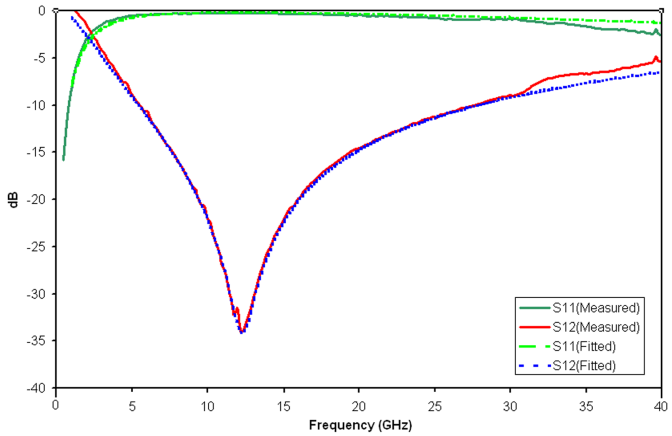

Figure 31: RLC circuit vs. measurement results for one of the switches [44]

inductance can be determined by (20). The resistance can be calculated from (18). Table 6 shows the resonance frequency values and the calculated capacitance, inductance, and resistance.

The measurement results were compared to a series RLC circuit with the same values as Table 6 to verify the model. One such comparison is shown in Figure 31. These results agree very closely with each other. Therefore, the electrical model is satisfactory.

CHAPTER VI

RF MEMS SWITCH LIFETIME TESTING

Before a technology becomes appropriate for consumer and military applications, it is important to determine its lifetime. If a device only lasts two month in the field, it is not going to be well liked by its purchasers. In this case, the limiting factor for device lifetime is the MEMS switch. Since it is a mechanical device, it is effected by fatigue, creep, fracture, and other mechanical issues. It is also an electrical device and can be adversely effected by electrostatic charging effects. MEMS switches have been documented that can reliably cycle over 500 billion times [59]. This is a great achievement for MEMS technologies.

Unfortunately, lifetime testing is a time consuming process. At a cycling rate of 1000Hz, it would take almost 16 years to cycle 500 billion times! Commercial testing is usually performed between 10-20kHz, which would still take up to 1.5 years to complete. This is not something that can be attempted in a university setting where equipment is shared among many students. Instead, a more manageable goal of at least 100 million is attempted.

Previous papers have demonstrated pull-down voltage and losses versus switching cycle [28, 111]. It has been well documented that a switch lifetime increases with a decrease in the actuation voltage. It has also been shown that the isolation improves, the insertion loss worsens, and the minimum actuation voltage decreases over time.

For this research, we intend to demonstrate two things that have never been documented:

1. Demonstrate that MEMS switches fabricated on LCP can survive at least 100 million cycles

2. Demonstrate the activation (fall) and release (rise) time of the switch over its lifetime

6.1 Testing Setup

The testing setup was inspired by the system used by Harvey Newman with the Naval Research Laboratory [67]. The output of the MEMS switch is fed to an Agilent crystal

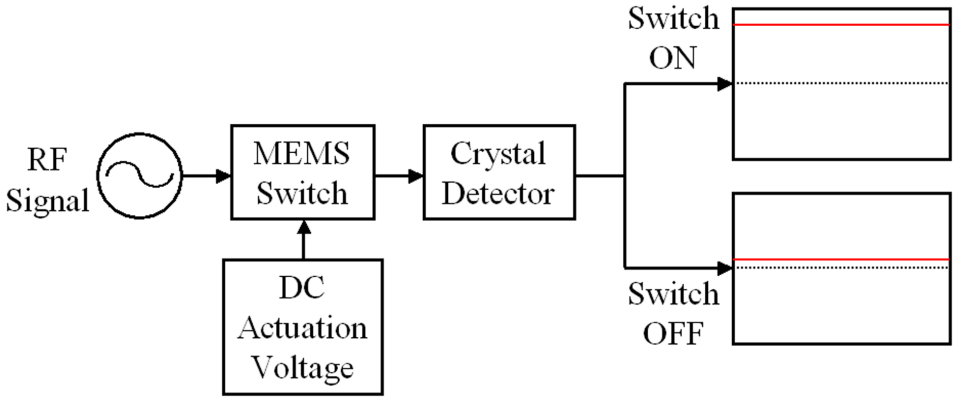

Figure 32: The MEMS switch lifetime test setup is shown. The output voltage of the crystal detector is high when the switch is "on" and low when the switch is "off".

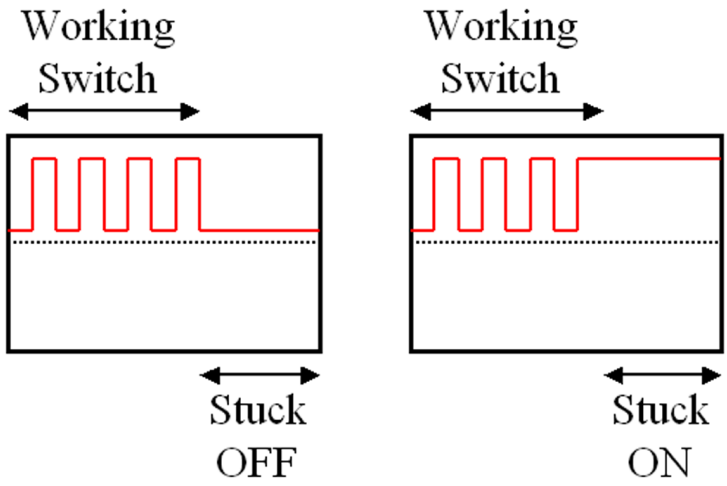

Figure 33: The voltage output of the crystal detector while a test is being performed is shown. When the square wave becomes flat, it can be determined if the switch is stuck "on" or "off".

detector, which acts as a signal summer. When the switch is "on" and the RF signal passes through, the crystal detector sums the RF signal and outputs a high DC voltage. When the switch is "off", the detector has little or no output voltage. This is demonstrated in Figure 32.

As long as the switch is toggling on and off, the output from the crystal detector should be a square wave. If the switch ever flat lines, then that is an indication that the switch is stuck in the on or off state. This is demonstrated in Figure 33.

A LabView program was written by Matt Morton that automates the measurements.

The user specifies the toggling frequency, the actuation voltage, and how often measurements should be taken. The third parameter is necessary because measurements can not be taken fast enough to keep up with the toggling frequency. In addition, handling a data file with billions of data points would be cumbersome. Instead, the switch is toggled a set number of times (in this case 50,000). Then, the switch is toggled while an oscilloscope measures the rise and fall times. These times as well as the output voltage from the crystal detector are saved to the hard drive. This entire process only takes a few seconds. Finally, the oscilloscope is disabled and toggling resumes. When the output from the crystal detector no longer toggles (that is, the "on" and "off" state voltages are less than the set threshold) the test is ended and the results are automatically sent to the user via E-mail. Status updates can also be E-mailed to the user at a set time interview (once a day, once a week, etc).

6.2 Time to Failure

Ideally, the switch would either fully operate or completely stop. This would represent the situation shown in Figure 33. Unfortunately, lifetime testing isn't so black and white. Over time, the switch is going to wear down. It's possible that the switch could become stuck in the up or down state, but a more likely scenario is that the switch will start to partially actuate. At this point, the switch is no longer toggling even though it is technically moving. To compensate for this, testing is stopped when the output of the crystal detector reaches 2/3 of the initial value.

Since the "off" state isolation and "on" state insertion loss vary from switch to switch, the output voltage from the crystal detector will vary as well. For one particular switch, the difference in the output voltage between the "on" and "off" states was around 90mV. The failure threshold voltage was therefore set to 60mV. This voltage versus the cycle is shown in Figure 34.

The output voltage is quite smooth up to 35 million cycles. After that it becomes more variable but the average doesn't change. At 128 million cycles, the output suddenly drops by 5mV. It maintains a new average value of 85mV until it reaches 153 million cycles. At

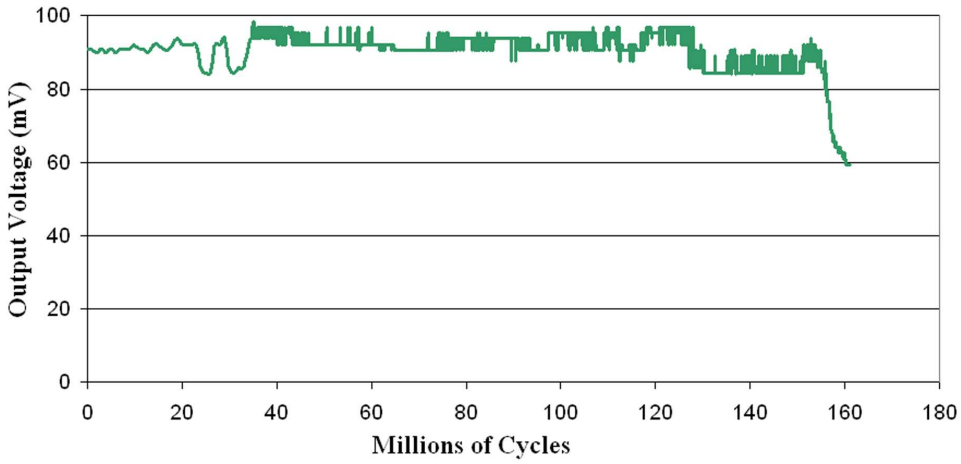

Figure 34: The difference in the measured output voltage from the crystal detector between the "on" and "off" states is shown versus switch cycle.

that point, the performance degrades quickly and it reaches the 60mV threshold voltage after 161,018,000 cycles. The switch was able to greatly exceed our goal of 100 million cycles.

6.3 Activation and Release Time Over the Lifetime

To date, the change in performance of the rise and fall times over the lifetime of an RF MEMS switch has not been published. This evaluation can be very important if timing is critical in a system. The activation (fall) and release (rise) times for the same switch depicted in Figure 34 is shown in Figure 35.

The events noted in the previous section for the crystal detector output also have significance in this figure. The switching times are very consistent up to 35 million cycles. After that, the switching times are more variable and the average value is also changing. The activation time is taking longer and the release time is taking less time. At 128 million cycles, both lines decrease by about 10%. The release time steadily decreases until the failure point. The activation time increases exponentially until 153 million cycles. At that point, it decreases rapidly until 161,018,000 when the switch fails.

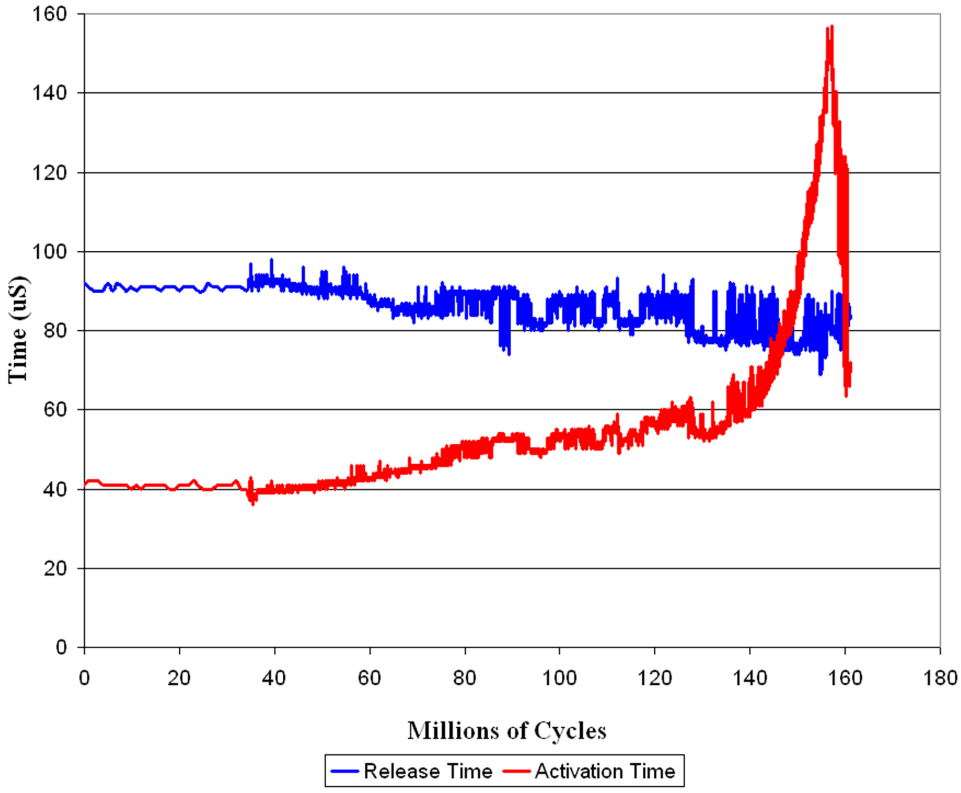

Figure 35: The activation (fall) and release (rise) time is shown versus switch cycle.

6.4 Failure Mechanisms

There are a variety of reasons for why switches fail. These can be grouped into environmental, electrical, and mechanical contributors.

6.4.1 Environmental Contributors

Switches that are not packaged (like this one) can succumb to environmental effects. The best place to test the lifetime of a switch would be in a clean, dry environment with little air circulation. Unfortunately this is difficult to achieve in a university setting. Measurement labs are bustling places with constant air conditioning to keep the measurement equipment cool. Packaging devices in a hermetic enclosure is best, but any kind of covering would help.

An abrupt failure could be caused by a stiff breeze, particulate matter, or from vibrations. A more gradual failure could be caused by moisture buildup on the dielectric film and metal layers. Moisture causes surface tension which will cause the membrane to be held down longer than desired. This would increase the release time but have little effect on the activation time. As the moisture collects, it's likely that the switch will become stuck in the DOWN state. In a worst case scenario, the moisture could short out the switch causing a large surge of current and possibly destroying the test setup.

6.4.2 Electrical Contributors

Direct contact between the ground and the DC voltage source is not only disastrous to the switch but can also cause significant damage to the rest of the system. The sudden surge of current can cause delamination of the signal lines and charring of the substrate surface. This can happen if the dielectric layer is not sufficient to prevent direct contact between the metal layers. Alternatively, if these layers are misaligned, the dielectric may not be in the right place to prevent contact. If this happens, the switch will blow immediately and no cycling will occur.

One of the most widely researched lifetime limiters is dielectric charging. During the deposition step, pin holes develop in the material which are capable of storing electrostatic

charge. This charge naturally dissipates into the substrate but it can take time. If the switch is held down for extended periods, the dielectric may not be able to discharge fast enough. The static buildup can become large enough to hold the switch down even after the bias has been removed. Eventually the static will discharge and the switch will operate normally. This can take milliseconds to hours depending on the bias voltage, the amount of charging, and the electron mobility of the substrate material.

The effect of dielectric charging on the activation and release time of a switch is similar to that of the moisture stiction. The activation time will remain relatively uneffected but the release time will increase.

6.4.3 Mechanical Contributors

Mechanically speaking, an RF MEMS switch is little more than a metal beam exposed to cyclic loading. When cyclic stresses are applied to a material, even though the stresses do not cause plastic deformation, the material may experience a degradation in performance. Metal fatigue is the progressive, localized, and permanent structural damage that occurs when a material is subjected to cyclic or fluctuating strains at nominal stresses that have maximum values less than the static yield strength of the material [107]. Another issue is creep, which is the tendency of a material to move or to deform permanently to relieve stresses. High levels of stress can lead to fracture, which would almost certainly prevent movement in a MEMS switch.

The stresses that result from cyclic loading can lead to strain. Eventually this effect can lead to strain hardening, which is an increase in mechanical strength due to plastic deformation. At low temperature, these defects do not anneal out of the material, but instead build up as the material is worked. This increases its strength and decreases its ductility [108]. The change in performance of a switch experiencing strain hardening is not as consistent as the previous contributors. The change would resemble that of a stress-strain curve, like the one shown in Figure 36. There is a linear (elastic) regime where a device would ideally be used. This transitions into the yielding regime where the device elongates with little or no additional stress. The next regime is where strain hardening occurs. Once

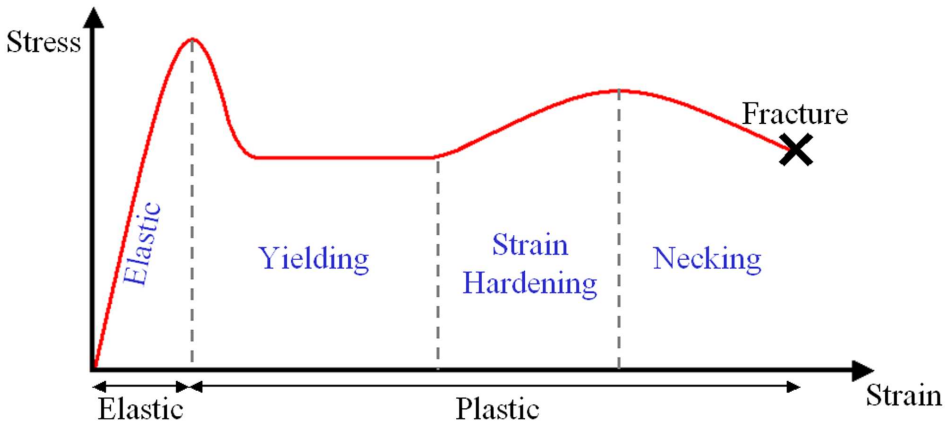

Figure 36: A typical stress-strain curve is shown. The exact shape varies from material to material. This figure is not to scale.

the ultimate strength is reached, necking occurs and this leads to fracture.

6.5 Failure Analysis

From Figures 34 and 35, some conclusions can be made as to what might have caused the switch to fail.

Since the release time decreased over time, it is likely that environmental and dielectric charging effects did not have a significant effect on the lifetime. Since the switch was capable of well over 100 million cycles, we can rule out electrical shorting. However, there is a striking resemblance between the curve in Figure 36 and the measured data in Figures 34 and 35. Figure 37 shows the normalized measured data compared to the stress-strain curve.

It seems likely that strain hardening was the reason that this switch failed. The switch operated in the elastic regime until it reached 35 million cycles. This is denoted by the smooth line to that point. It experienced yielding for 30 million cycles after that. This is determined from the randomness in the data, but an overall consistent average. Between 65 and 153 million cycles, the activation time increases and the release time decreases. Both of these effects are the result of a stiffer membrane. This is the strain hardening effect. At 128 million cycles, something happens that causes an exponential degradation in performance. This was most likely caused by some type of metal fatigue or creep. After 153 million cycles, necking occurs which results in severe strain occurring in the membrane. Within 10 million

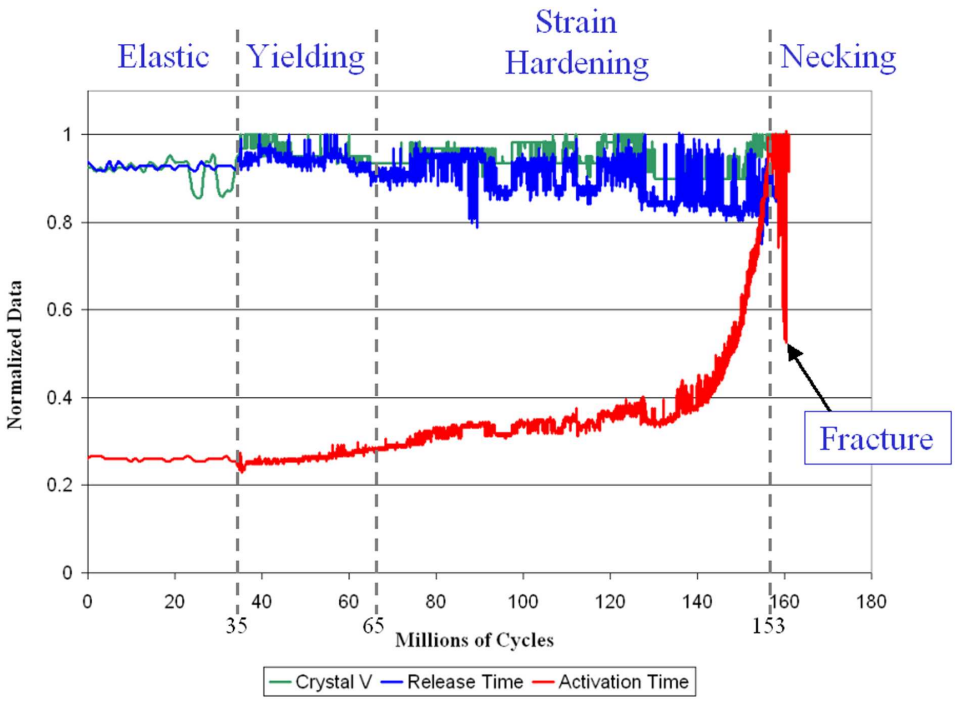

Figure 37: The data from Figures 34 and 35 are normalized and matched to the curve in Figure 36. Strain hardening is the most likely reason for the failure of this switch.

cycles, the switch is no longer performing well enough to be considering a working device.

CHAPTER VII

TRADITIONAL PHASE SHIFTER DESIGN

The first device that was designed on LCP was a phase shifter at 14GHz. One and two bit MEMS microstrip phase shifters were realized on 100μm thick LCP layers. This chapter presents the background, theory, and design of a simple MEMS phase shifter on LCP.

7.1 Introduction

Phase shifters are an integral part of microwave devices. Likewise, the design and application of phase shifters have been well documented. To date, MEMS phase shifters have been designed and realized on silicon [40, 41, 47–49, 54, 78], GaAs [52, 89], glass [34, 35], and quartz [79, 80]. Multibit phase shifters have applications in almost all microwave devices, but are most commonly used in phased antenna arrays. MEMS phase shifters have been of particular interest in recent years due to the RF isolation, size, and cost benefits associated with using MEMS switches. PIN diodes, FETs, and other solid state switches are typically lossier, consume more power, and have more distortion at high frequencies than MEMS switches. In addition, microwave devices on non-semiconductor substrates have been explored due to their low-cost, low-loss, and near-hermetic nature [97]. This effort resulted in the first integration of MEMS phase shifters and a flexible, organic substrate.

For simplicity, a switched-line design was implemented as shown in Figure 38. By splitting a signal into a reference path with a length of one wavelength (or an integer multiple of the wavelength) and a second path that adds or subtracts a fraction of a wavelength, a net phase shift was achieved. For example, if a phase shift of 90^o is desired, $90^o/360^o$ or 1/4 of a wavelength would be the difference in length between the phased path and the reference path. Mathematically, this is represented by Equation 21 where $\Delta\Phi$ is the phase difference in degrees, λ is the wavelength, and l is the line length.

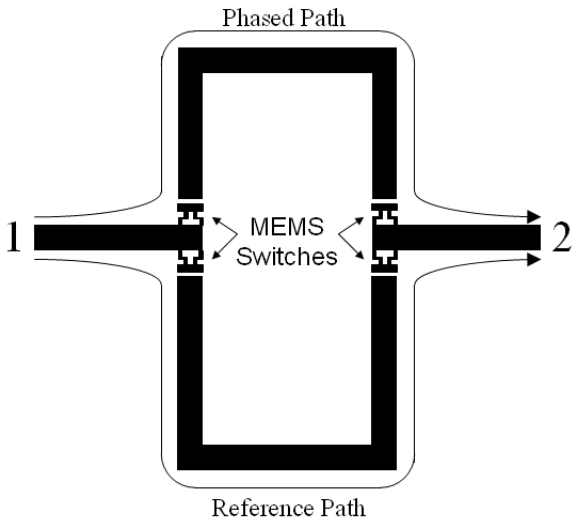

Figure 38: Implementation of switched-line MEMS phase shifter [43]

$$\Delta\Phi = \frac{360}{\lambda} \times (l_{phased\ path} - l_{reference\ path}) \tag{21}$$

Using this method, one-bit phase shifters were designed at 14GHz and fabricated with phase shifts of 0^o, 22.5^o, 45^o, and 90^o. The reference path (0^o) has a length of one wavelength (1.361 cm) and the 22.5^o, 45^o, and 90^o phased paths have lengths of $15/16\lambda$ (1.276 cm), $7/8\lambda$ (1.191 cm), and $3/4\lambda$ (1.021 cm) respectively. In addition, the 45^o and 90^o phase shifters were cascaded in series to obtain a two-bit phase shifter. The possible phase shifts with this device are 0^o, 45^o, 90^o, and 135^o. MEMS switches are ideal for switched-line topologies because of the excellent isolation they can provide.

In order to apply the necessary bias voltage to actuate the MEMS switches, radial stubs were designed and placed on each of the two signal paths. A fabricated one-bit phase shifter with radial stubs is shown in Figure 39. When a DC voltage is applied to the radial stub, electrostatic force pulls the switch (which is grounded) towards the signal line. A layer of silicon nitride deposited over the signal line prevents switch metal to signal line metal contact. Therefore, no DC current can flow but the capacitance between the switch and the signal line is large enough for RF energy to pass through.

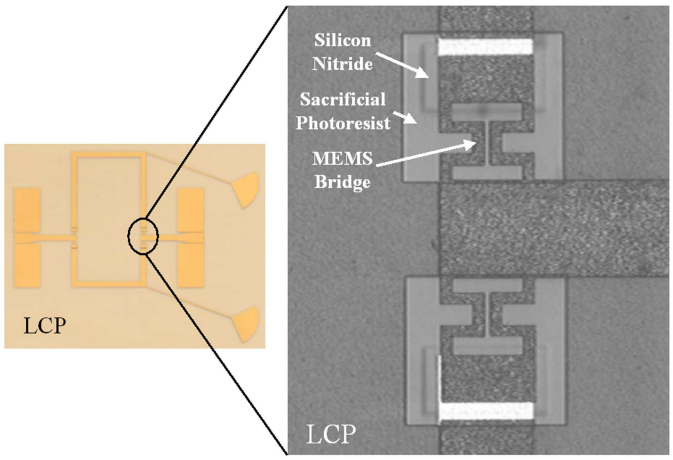

Figure 39: Fabricated one-bit MEMS phase shifter on LCP [43]

7.2 Measurement

Measurement results were taken using DC probes to apply the switch bias voltage. TRL calibration was performed to remove the connector and cable losses. The transmission line loss over the frequency range 12-16GHz varies from 0.35-0.40 dB/cm. At 14GHz, the line loss is 0.375 dB/cm. Given that the line lengths vary from 1.021cm to 1.361cm, it is expected that 0.38 dB to 0.51 dB of line loss will be present per bit. The MEMS switch loss varies slightly from switch to switch due to fabrication tolerances. However, the loss ranges from 0.08 dB to 0.16 dB per switch. These values are typical for MEMS switches in the down (actuated) state at this frequency.

Measurement results are very good for the one-bit MEMS phase shifters. The average return loss is 19.0 dB and the average insertion loss is 0.59 dB. The phase error is less than 1.38^o from the desired phase shift for all frequencies. These results are shown in Figures 40 and 41 centered around the design frequency.

Measurement results for the two-bit MEMS phase shifters are also very good. The average return loss is 22.5 dB at the design frequency. The average insertion loss is 0.98 dB per bit. The average phase error is only 1.26^o. These results are shown in Figures 42 and 43 centered around the design frequency.

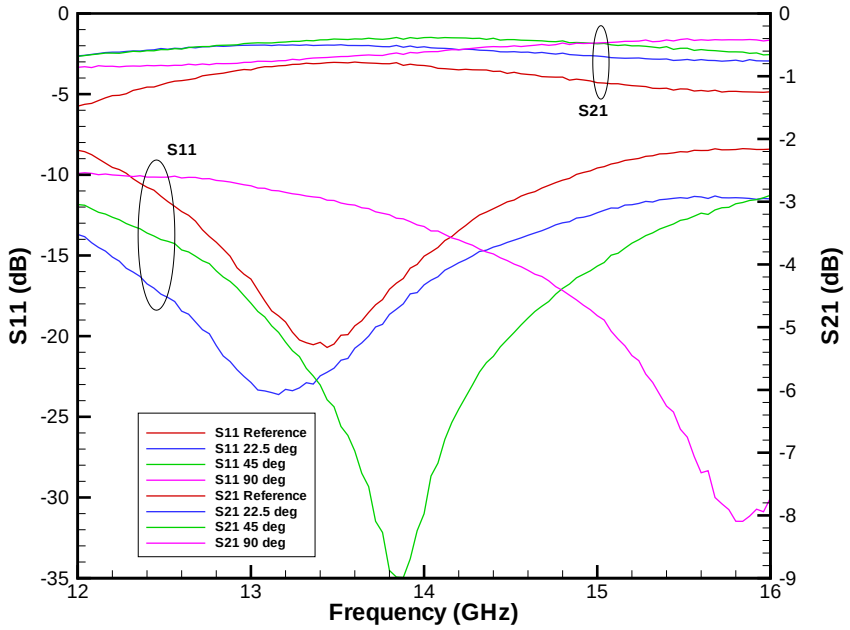

Figure 40: Loss measurement results of 1-bit MEMS phase shifters [43]

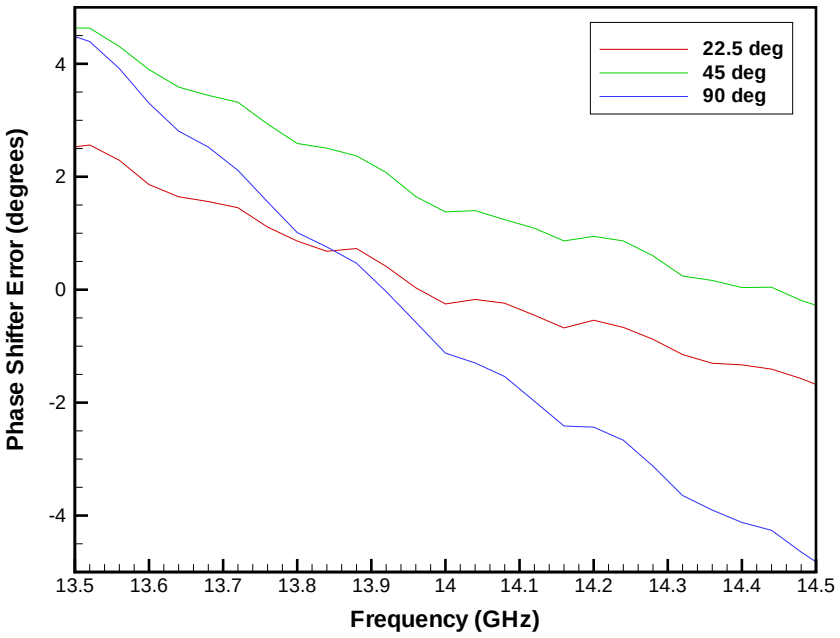

Figure 41: Phase error measurement results of 1-bit MEMS phase shifters [43]

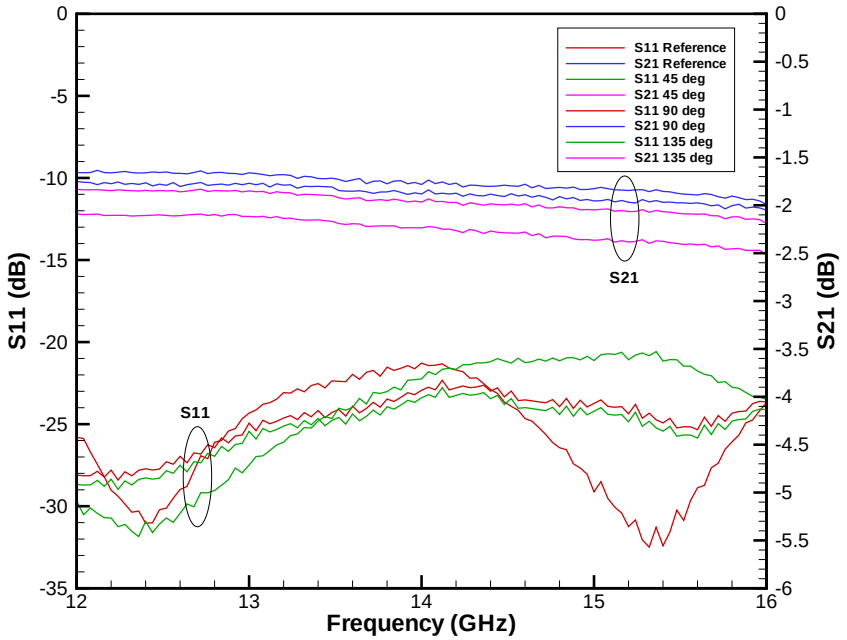

Figure 42: Loss measurement results of 2-bit MEMS phase shifter [43]

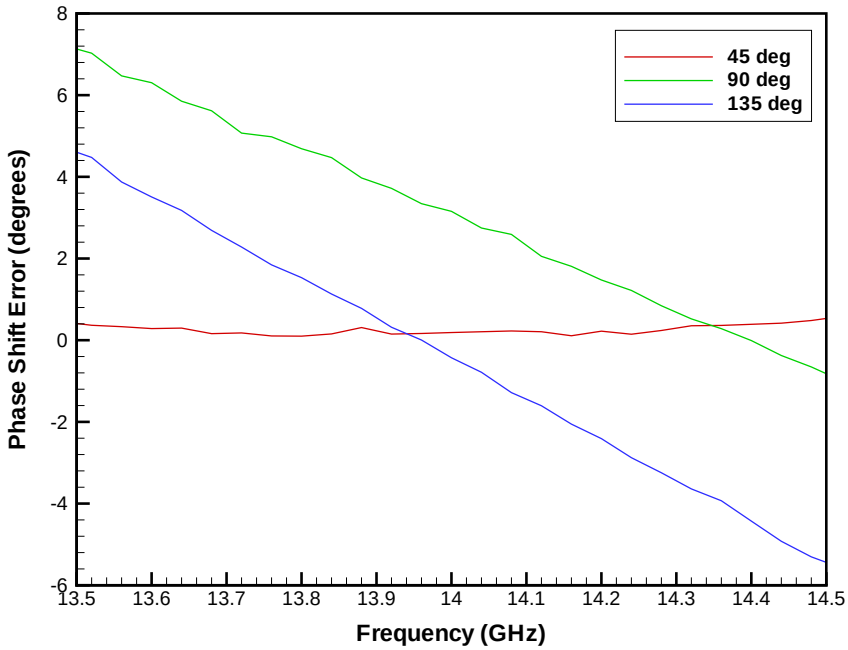

Figure 43: Phase error measurement results of 2-bit MEMS phase shifter [43]

CHAPTER VIII

FOUR-BIT REDUCED SIZE MEMS PHASE SHIFTER

The previous chapter focused on the first ever documented MEMS phase shifter on a flexible, organic substrate. However, due to the low ϵ_r of LCP, the microstrip design was quite large compared to the state-of-the-art. It was necessary to redesign the phase shifter for small size, low loss, and optimal performance.

8.1 4-bit MEMS Phase Shifter on LCP

To improve on the original design, a four-bit MEMS phase shifter was optimized at 14GHz for small size and exceptional performance. The improved geometry of the reduced size phase shifter was 2.8 times smaller than a traditional switched-line phase shifter and was much less lossy. For the four-bit phase shifter, the worst case return loss was greater than 19.7 dB and the average insertion loss was less than 0.96 dB (0.24 dB/bit or 280^o/dB) at 14GHz. The average phase error at 14GHz was only 3.96^o. The way that this was achieved is discussed here.

8.1.1 General Phase Shifter Design

The LCP material used has a thickness of 100μm, a permittivity (ϵ_r) of 3.1, and a tan δ of 0.004 [97]. The phase shifter has phase shifts between 0^o and 337.5^o in 22.5^o increments (16 cases). Traditional microstrip theory was used to design the phase shifter [75]. A layout of the final four-bit phase shifter is shown in Figure 44.

8.1.2 Reduced-size Methodology

Switched-line phase shifters are widely used because they are straight-forward to design, fabricate, and integrate with other microwave devices. Unfortunately, the overall size of the switched-line geometry is comparable to the wavelength for each bit. Since multibit phase shifters are usually desired, this can result in a phase shifter that is much larger than the

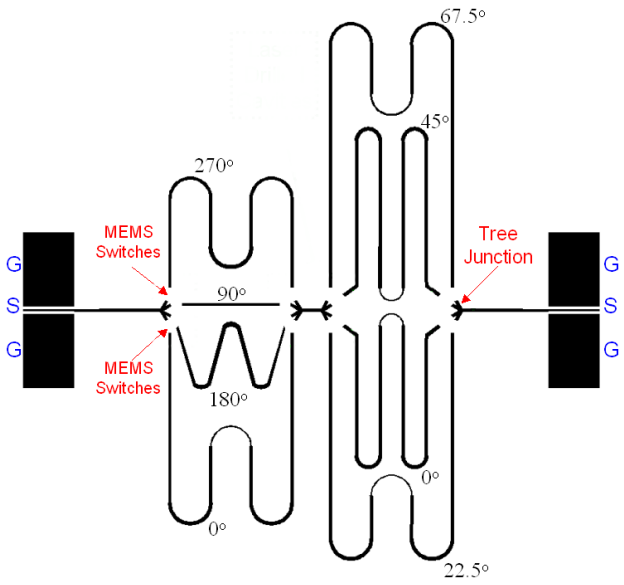

Figure 44: Top view of the 4-bit series-shunt RF MEMS phase shifter [42]

other microwave components in an RF system. For this reason, a number of changes were made to the traditional layout presented in [43] to decrease the size. These design changes are detailed in this chapter. By incorporating these layout changes, the overall area was reduced by a factor of 2.8. The length was reduced by a factor of four. In addition to the size reduction, the signal line length and number of MEMS switches traversed compared to a traditional implementation were each reduced by a factor of two. This results in half the line loss and half the switch loss by using this implementation. A size comparison of the modified layout compared to a traditional layout is shown in Figure 45.

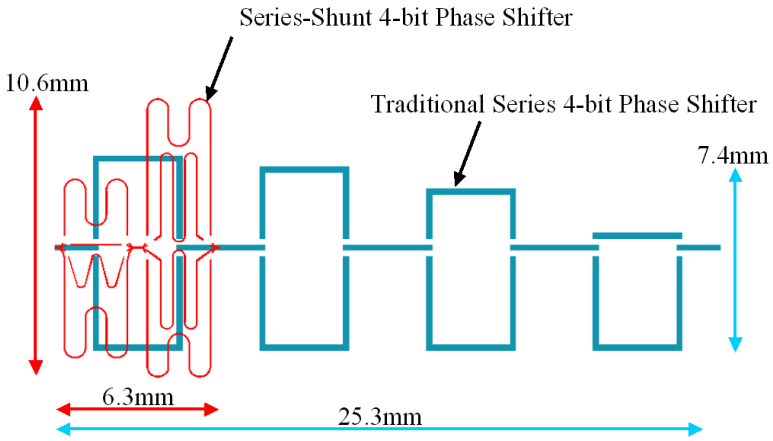

Figure 45: Size comparison of 4-bit series-shunt design with traditional series switched-line phase shifter on LCP at 14GHz [42]

8.1.2.1 Series-Shunt Modification

Instead of cascading four one-bit phase shifters in series (as demonstrated in Figure 45), four shunt phased paths were cascaded with another four shunt phased paths (hence the series-shunt distinction). The final series-shunt phase shifter was shown in Figure 44. In order to generate all sixteen possible cases, a 0^o reference path must occur in every series portion of the phase shifter. In addition, the 0^o, 90^o, 180^o, and 270^o phased paths must be in one section and the 0^o, 22.5^o, 45^o, and 67.5^o phased paths must be in another section to create all 16 cases. In order to make this feasible for really short phased paths (like the 22.5^o case) and really long phased paths (like the 270^o case), the shortest phased paths were elongated by a wavelength. This is why the smallest phase shifts have longer line lengths than the largest phase shifts.

This series-shunt technique was previously published by the University of Michigan and Rockwell Scientific using Single Pole Four Throw (SP4T) MEMS switches [78, 90]. The switches used here are SP4T as well, but they are implemented differently than in [90]. For example, via holes were omitted which add an unnecessary level of complexity to the design and fabrication. The switches presented here offer the same loss performance without the use of vias.

Previous works that claim "small", "reduced", or "miniature" size multibit phase shifters

always use high dielectric materials, such as silicon or GaAs, that have permittivities between 11 and 13 [89]. This is because the wavelength of a microstrip line is inversely related to the square root of the permittivity. Microstrip phase shifters on high dielectric materials will always be much smaller than those on low dielectric materials.

8.1.2.2 High Impedance Modification

Instead of using the standard 50Ω input impedance, 100Ω was used. By making this change, the signal line width decreased from 240μm to 65μm. This allowed for more signal lines to be placed in less area. In practice, high impedance patch antenna arrays which would utilize this type of phase shifter are common [5]. However, a 50Ω to 100Ω transition could be added for integration with other standard microwave components.

8.1.2.3 Curled Signal Line Modification

Instead of using the traditional rectangular phased paths, the lines were curled inward to minimize the overall area (as shown in Figures 44 and 45). Careful attention was given to minimize coupling between the signal lines. A full wave HP-ADS Momentum (method of moments) simulation was performed to determine the amount of coupling that would result between two 65μm wide, 2.5mm long signal lines at 14GHz. These results are shown in Figure 46.

Most of the distancing between signal lines used in the layout is 300-400μm, which corresponds to 5.8-3.6% coupled power. However, in some areas, distances as small as 150μm were necessary. The lines in these areas were placed at oblique angles to each other to minimize the coupling.

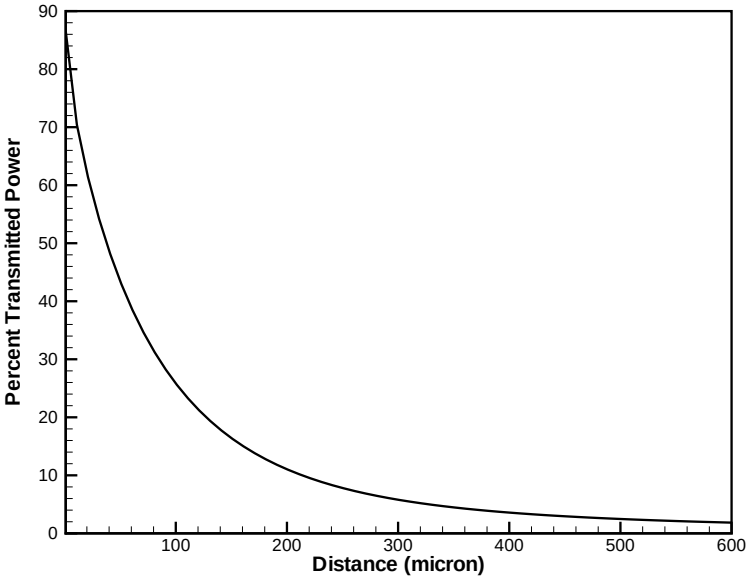

Figure 46: Percentage of power transmitted between coupled signal lines for a given spacing at 14GHz [42]

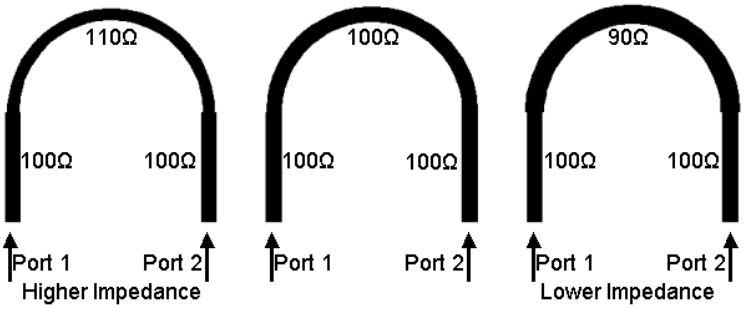

Figure 47: Demonstration of iterative approach for impedance matching. Higher impedance lines are made narrower and lower impedance lines are made wider [42]

8.1.2.4 Impedance Matching

Since curved microstrip lines are being used to reduce the size, impedance matching must be done to compensate for the additional parasitic impedance. Instead of using additional matching devices, such as stubs [90], all impedance matching was handled through the signal lines themselves. Lines that require a higher impedance match were made thinner and lines that require a lower impedance match were made wider. This was performed in a full-wave simulator using an iterative method as demonstrated in Figure 47.

Since the arcs are the shortest part of the signal line, they were used to do the impedance matching. The center case in Figure 47 uses a curved line with the device characteristic

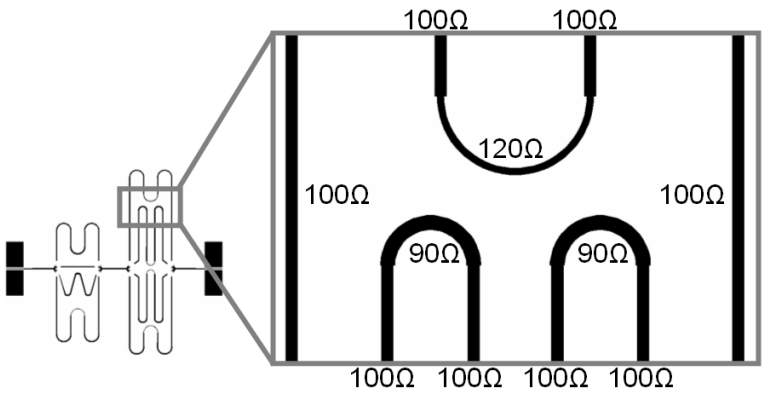

Figure 48: Optimal impedance values for a section of the 4-bit series-shunt phase shifter [42]

impedance (100Ω). The leftmost case has a slightly higher impedance and the rightmost case has a slightly lower impedance. The impedance was varied until the lowest insertion loss was achieved. The overall size of the circuit does not change by using this method of impedance matching. The optimized impedance values for a section of the phase shifter are shown in Figure 48.

8.1.3 Tree-Junction Design

To simplify the design and fabrication process, all of the MEMS switches are SP4T. Since one signal must be split among four different phased paths, a four-way Y-junction (or tree-junction) was designed. The geometry of the tree-junction used is shown in Figure 49.

Each of the four output stubs are the same width as those of the other signal lines and are $\lambda/65$ long at the design frequency (or 220μm). This is sufficiently small to prevent RF energy from entering the stubs that are associated with non-activated MEMS switches (that is, in the up state). Using longer lines increases the amount of leakage power into these stubs. Using shorter stubs forces the layout to be too dense. The $\lambda/65$ length is optimal for this particular layout. However, a good rule of thumb is to use line lengths less than $\lambda/25$ to avoid excessive leakage power. Fine tuning can be done using a full-wave simulator.

Each stub is placed at 30^o or 60^o off the main axis. These values can vary, but symmetry across the main axis is necessary for symmetric distribution of power. Very wide angles can be used with very short stubs to prevent layout crowding (as in this case). Alternatively, very narrow angles can be used with long stubs to keep the layout small. To demonstrate

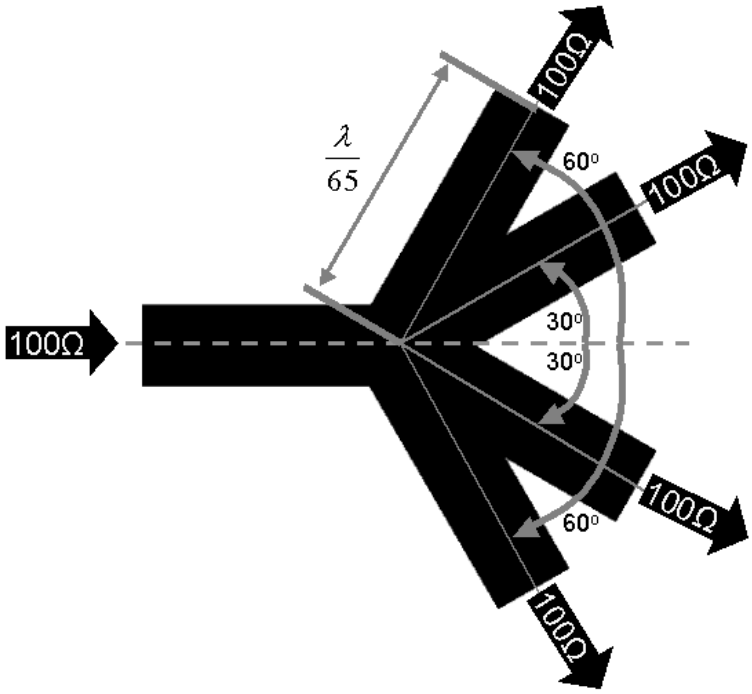

Figure 49: Design geometry for the tree-junction [42]

that the angle can vary without greatly effecting the performance, a full wave simulation was run with one stub that varies the bend angle from 0^o to 90^o. The results are shown in Figure 50.

For all angles between 0^o to 90^o, the effect of the bend is negligible. The additional phase increase from the bend discontinuity is 0.39^o and 0.66^o for the 30^o and 60^o bends, respectively. The additional insertion loss is too small to measure.

8.1.4 Simulation Results

A full-wave simulation was performed using HP-ADS Momentum for the 4-bit phase shifter. The design was optimized for low-loss and a phase error less than three degrees. S11 and S21 simulation results for four of the sixteen possible phase shifts are shown in Figure 51.

As expected, the phased paths with the longest lengths have more insertion loss than the shorter phased paths. The 67.5 degree configuration has the longest signal line length and the 90 degree configuration has the shortest signal line length in the system. The MEMS switch and metal losses were not modeled in these simulations. Therefore, it is expected that the insertion losses shown in Figure 51 will be much less than the measured results.

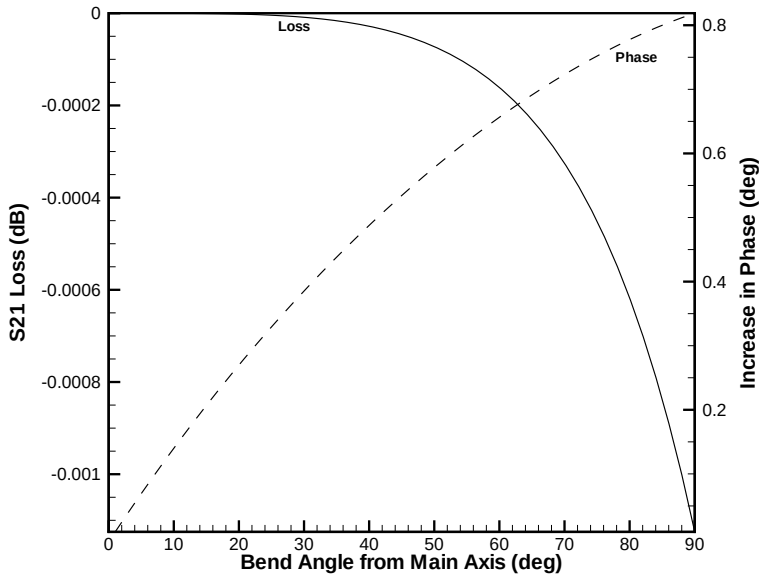

Figure 50: S21 Loss and phase data for one stub of the tree-junction versus the bend angle from the main axis . The simulation loss is negligible [42]

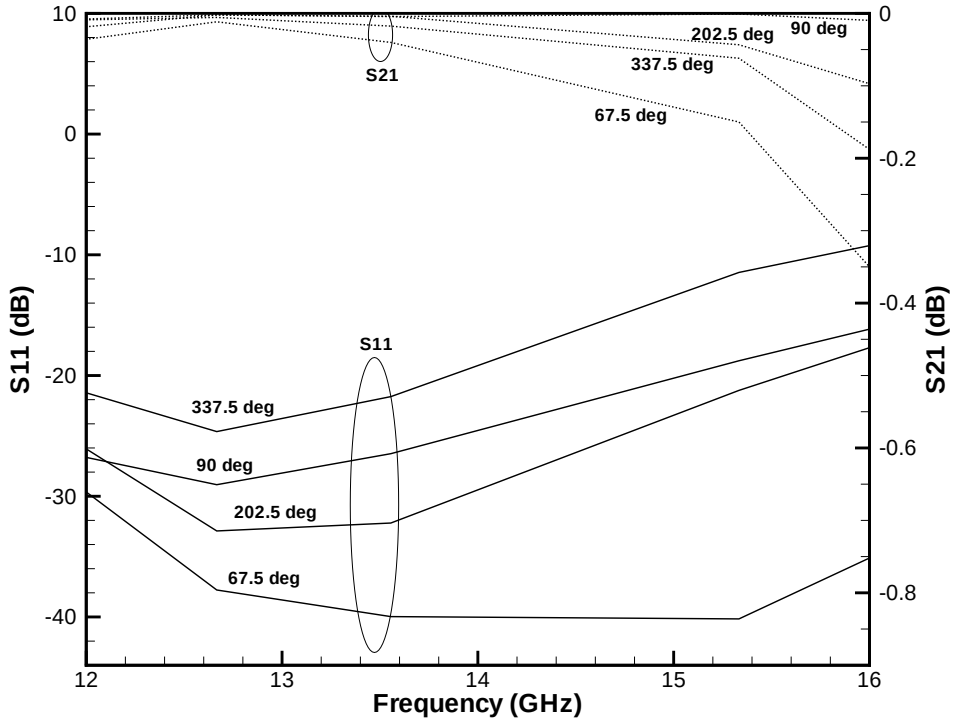

Figure 51: Full-wave simulation results for four of the sixteen possible phased paths [42]

8.1.5 Measurement Results

Measurement results were taken using high impedance DC probes to apply the switch bias voltage. TRL calibration was performed on wafer to remove the connector and cable losses.

The loss measurement results for the four-bit MEMS phase shifter are shown in Figure 52. This method of tabulating all 32 data lines was first demonstrated by this author in [42]. Most papers plot the data without labeling each line.

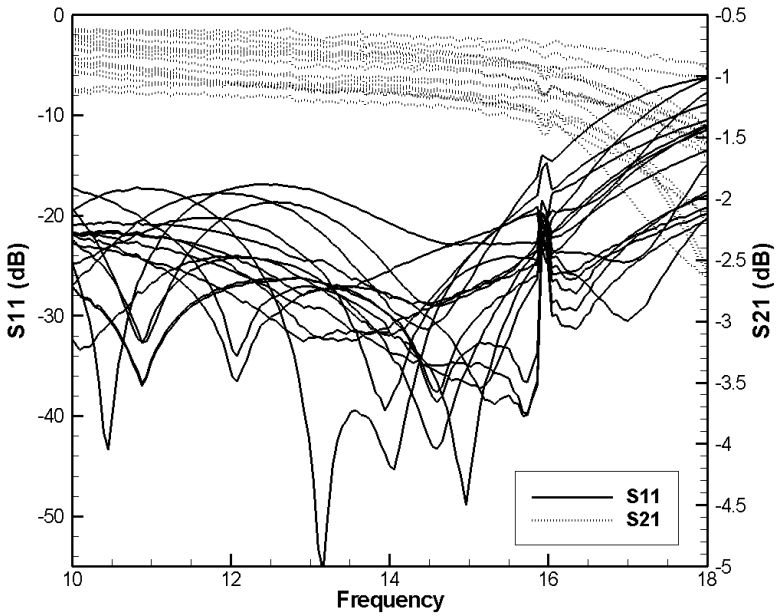

Most Lossy	
S11	**S21**
337.5	67.5
270	22.5
292.5	315
90	45
247.5	0
315	337.5
135	270
225	292.5
202.5	247.5
0	225
180	202.5
112.5	180
45	157.5
67.5	135
157.5	112.5
22.5	90
Least Lossy	

Figure 52: Measured loss of unpackaged phase shifter. The order of the lines is listed from most lossy to least lossy at 14GHz [42]

The phase error measurement results are shown in Figure 53. Table 7 summarizes the measurement results.

Table 7: Measurement results for the 4-bit series-shunt MEMS phase shifter [42]

	Worst Case	Average	Best Case
S11	-20.8 dB	-30.9 dB	-45.0 dB
S21	-1.22 dB	-0.95 dB	-0.66 dB
Phase Error	8.25^o	3.96^o	0.34^o

The loss data is exceptional. With an average 4-bit S21 less than 1 dB, these loss results

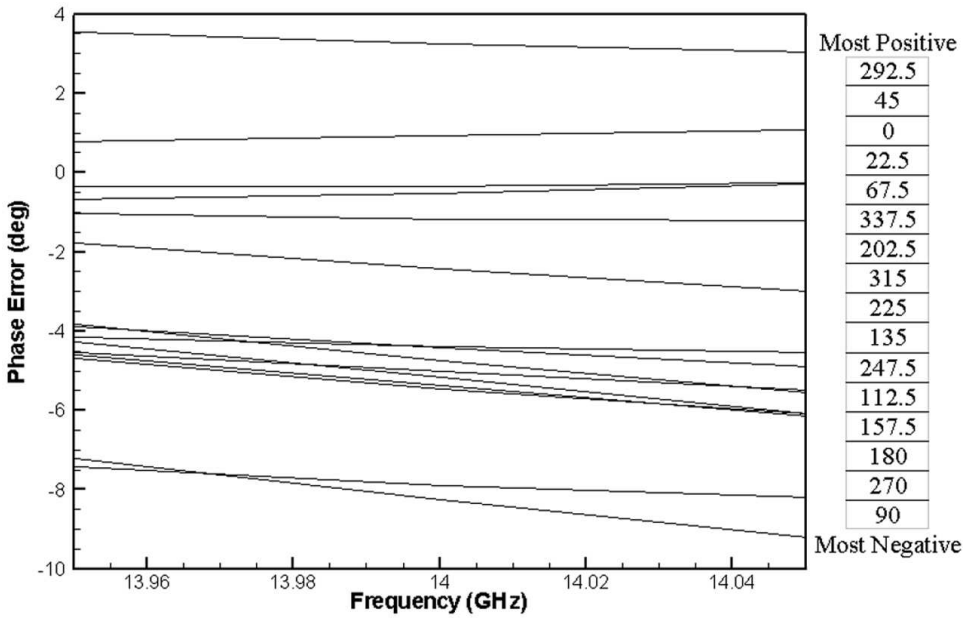

Figure 53: Measured phase error of unpackaged phase shifter. The order of the lines is listed from most positive to most negative at 14GHz [42]

are some of the best ever published (for this typology). The phase error, however, is slightly higher than expected. A typical rule of thumb is that phase errors should be less than 5^o. On average, this requirement was met. However, the two longest phased paths experienced higher coupling than expected. Even though the loss wasn't largely effected, the phase was. Even the worst case phase error is still respectable (and better than many other papers report). Improvements could be made to reduce these phase errors if necessary.

CHAPTER IX

RF MEMS SEQUENTIALLY-RECONFIGURABLE SIERPINSKI ANTENNA WITHOUT DC BIAS LINES

In this chapter, MEMS switches are used to sequentially activate and deactivate parts of a multiband antenna. The implementation of such a concept allows for the direct actuation of the electrostatic MEMS switches through the RF signal path, therefore eliminating the need for DC bias lines. This reconfigurable antenna operates at several different frequencies between 2.4-18GHz while maintaining its radiation characteristics. It is also the first integrated RF MEMS reconfigurable antenna on a flexible organic polymer substrate for multiband antenna applications. Simulation and measurement results are presented to validate the proposed concept.

9.1 Introduction

RF MEMS switches have been successfully used to reconfigure self-similar antennas on silicon to enhance their multiband performance [3]. In this work, RF MEMS switches are used to sequentially activate and deactivate parts of a CPW-fed Sierpinski gasket monopole antenna. The antenna has inherent multiband performance due to its resemblance to a 3-iteration Sierpinski gasket-type radiating element [76].

The concept of having sequentially-actuated antenna parts is shown in Figure 54. Regardless of the applied voltage, the triangular element that is closest to the RF/DC input is always active (Figure 55, State 1). When no DC voltage is applied, this radiates at the highest frequency. When a low DC voltage is applied to the signal line, the first set of MEMS switches actuate and this activates the second level of triangular elements (Figure 55, State 2). This antenna radiates at a lower frequency. The low voltage is also present at the edges of the next set of switches, but it is not high enough to actuate them. When a higher DC voltage is applied, the first set of MEMS switches remain 'ON' while the second set of

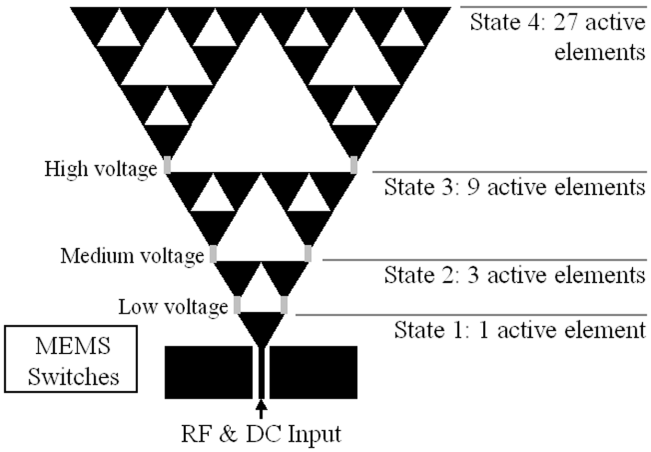

Figure 54: Illustration of MEMS reconfigurable Sierpinski antenna [45]

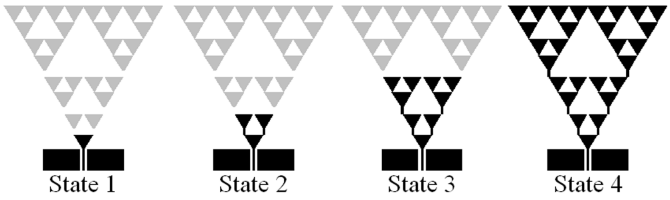

Figure 55: The four different reconfigurable antenna states: State 1 has no voltage applied, State 2 has a low voltage applied, State 3 has a medium voltage applied, and State 4 has a high voltage applied [45]

switches actuate (Figure 55, State 3). This activates the next iteration, consisting of six additional elements. Again, this higher voltage is present at the next set of switches, but the electrostatic force created is not sufficient for activation. Finally, when the voltage is increased to its highest value, the first two sets of switches remain 'ON' while the remaining set of switches actuates (Figure 55, State 4). In a way, the voltage cascades from one state to the next like a sequence of overflowing buckets. The four different states are illustrated in Figure 55, where all of the activated regions for different voltages are dark in color.

This biasing technique allows for direct actuation of the electrostatic MEMS switches without the need for DC bias lines. Elimination of the bias lines is highly advantageous because they can significantly distort the radiation patterns and they can introduce additional unwanted resonances.

The coplanar waveguide feed was chosen to facilitate the measurement setup. This reconfigurable antenna operates at four different principle frequencies. For each of these

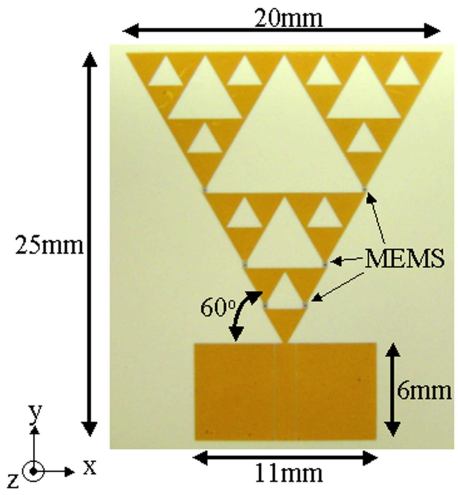

Figure 56: Fabricated antenna with MEMS switches is shown [45]

frequencies, the antenna maintains its multiband performance. The antenna and switch designs, along with the simulation and measurement results, are presented.

9.2 Antenna Design

To date, Sierpinski gasket antennas have been fabricated on many different, rigid substrates with low-permittivity (such as CuClad) and high-permittivity (such as silicon). In this work, LCP was chosen as the substrate.

With respect to the geometry, the antenna elements have a 60^o flare angle, and maintain the resonant structure's self-similarity with a log-periodicity of $\delta = 2$. The antenna is fed through a 6mm long CPW transmission line with a 50μm gap, a 1.3mm signal conductor width, and a 1.2μm thick aluminum layer. A picture of the fabricated antenna is shown in Figure 56. The overall size of the antenna, including the feed, is 20mm $\times$ 25mm.

The antenna was simulated using IE3D [36], a Method of Moments electromagnetic solver. The simulated return loss is shown in Figure 57. The switches were modeled in two ways. First, they were simplified down to a 200μm $\times$ 400μm gap in the "OFF" state and by a metal pad of the same size in the "ON" state. Those results were compared to a simulation that included the MEMS geometry in the "OFF" and "ON" states. The difference in the results between the two simulations was minor which indicates that the isolation provided by the MEMS was adequate.

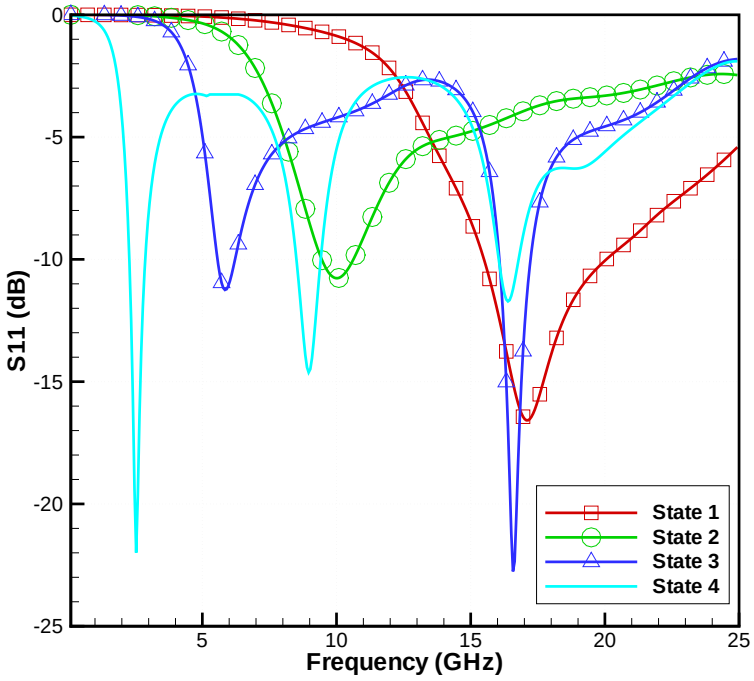

Figure 57: Simulated return loss for all four states of the Sierpinski antenna [45]

It was verified that the antenna has a different first resonant frequency for each of the four states. Since the antenna is self-similar with a log-periodicity of 2, each time the antenna transitions to the next state the frequency should be halved. That is, the resonant frequency of State 2 should be half that of State 1. The simulated zy-plane (φ=90^o) patterns for the four states are shown in Figure 58. These patterns are as expected for a monopole antenna. The simulated radiation pattern for the xz-plane (φ=0^o) is shown in Figure 59 and it shows the expected omni-directional pattern in that plane.

9.3 MEMS Switch Integration

The placement of the RF MEMS switches was illustrated in Figure 54. In order to bias the switches for electrostatic actuation, the MEMS need to have an applied voltage. A metal pad beneath the switch should be present to attract the charged metal. The metal pad must be placed under a thin dielectric material (such as silicon nitride) to prevent direct metal bridge to metal pad contact. Otherwise, no charge will develop and the switch will not actuate. Traditionally, the actuation voltage is applied via a DC bias line. However, in order to prevent RF leakage into the DC path, careful attention needs to be given to the

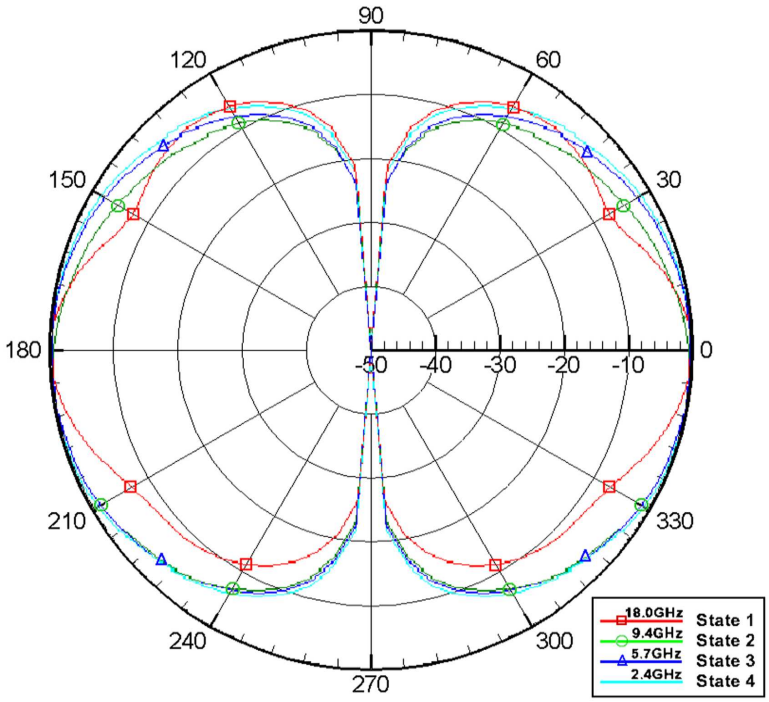

Figure 58: Simulated radiation pattern for φ=90^o (zy-plane) for all four states of the Sierpinski antenna [45]

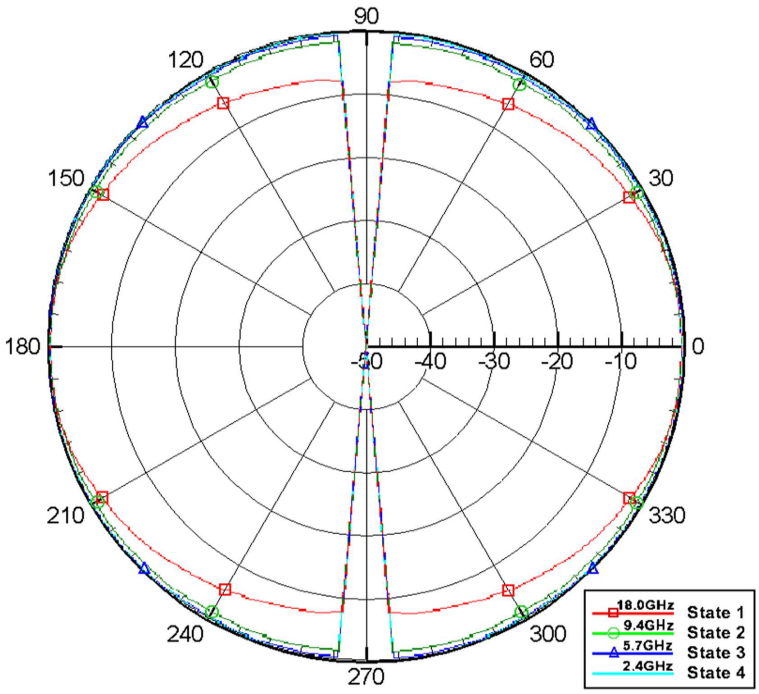

Figure 59: Simulated radiation pattern for φ=0^o (xz-plane) for all four states of the Sierpinski antenna

DC bias lines themselves. This can be implemented in different ways:

a) By using a quarter-wavelength transmission line connected to a quarter-wavelength open-circuit radial stub. Alternatively, a half-wavelength transmission line without a radial stub can be used with a reduced bandwidth. Each MEMS switch would require a different DC bias line and for this antenna that would require six lengthy metal lines being added. This would have a pronounced effect on the antenna performance. Therefore, this solution is not advisable.

b) High-resistance lines have been investigated to provide a wider bandwidth alternative [22]. Aluminum doped Zinc Oxide (AZO) is one such example, used for biasing in [3]. Thin-films of this kind are generally deposited using Combustion Chemical Vapor Deposition (CCVD), which uses very high temperatures. This is not a problem for materials like silicon, but it is much higher than the melting point of the organic substrate ($\approx 315^{o}$C) used in this work. At the moment, very high resistivity materials that can be deposited at low temperature are not widely available but are under investigation [33].

The proposed alternative to these approaches is to eliminate the need for DC bias lines. Instead, the biasing is handled through the antenna structure itself. Here, the DC voltage and the RF signal are both applied to the antenna through the same signal conductor of the CPW feed line. The antenna reconfigurability is made possible by using MEMS switches of varying actuation voltages. This can be easily implemented by using three different switch geometries with different spring constants. This is demonstrated in Figure 60. The MEMS switches used are single-supported (cantilever) and ohmic. This is necessary to implement the DC voltage cascading effect since capacitive switches do not pass DC. They have an "ON" state resistance of 1.7 ohms. The "OFF" state capacitance is approximately 35 fF.

The only trade-off to using this technology is in the MEMS lifetime. Since there are no grounded DC bias lines, there is no direct path for the electrostatic charge to travel. Instead, it will need to naturally dissipate into the substrate. This is typically not a problem unless the switches will remain "ON" for very long durations. For an application that requires a constantly reconfigured antenna this should not be a limiting factor.

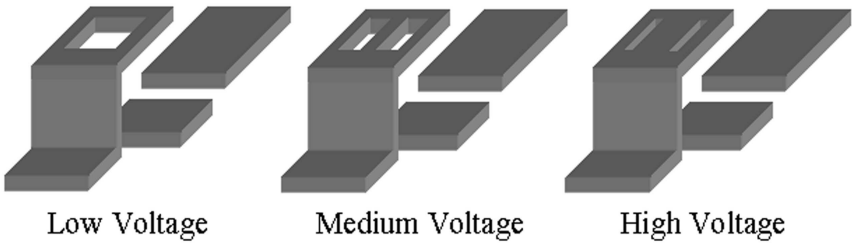

Figure 60: Example of MEMS switch geometries. Low voltage switches have a lower spring constant than high voltage switches. The electrically floating metal pad is also shown [45]

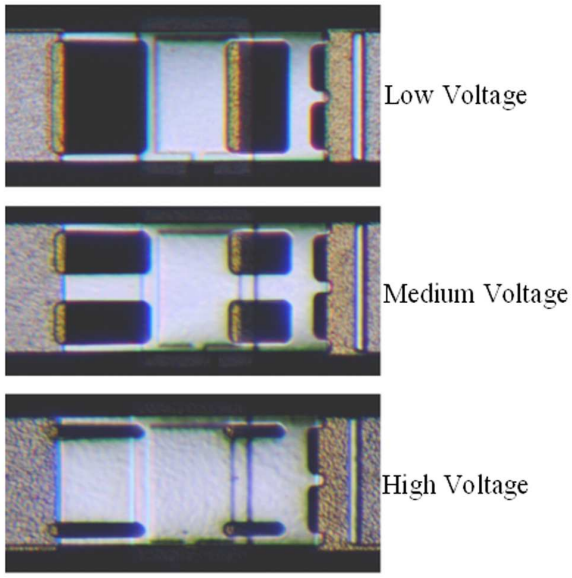

Figure 61: The low, medium, and high voltage MEMS switches are shown. They should resemble the switch geometries shown in Figure 60 [45]

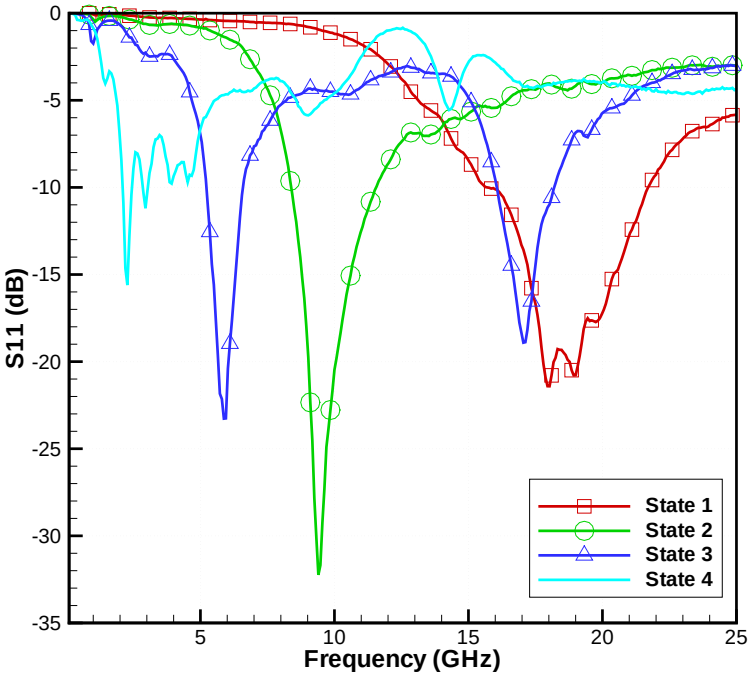

Figure 62: Measured return loss for all four states of the Sierpinski antenna [45]

9.4 Measurement Results

The switches after fabrication are shown in Figure 61. The return loss measurements were taken with an Agilent 8510C vector network analyzer using 850μm pitch GSG RF probes. Pattern measurements were taken using an Agilent 8530 vector network analyzer with the antenna inside an anechoic chamber. End-launch gold SMA connectors were hand-soldered onto the antenna for pattern measurements. These connectors have a maximum operating frequency of 18GHz, which coincides with the highest principle frequency of the antenna when no voltage is applied. Since the gap in the CPW lines is 50μm wide to achieve 50Ω for our chosen signal line width, manual soldering of the connector pin may not always result in a smooth transition. This can cause undesired ripple in the measurements at higher frequencies.

The return loss measurement results are shown in Figure 62. The resonant frequencies roughly halve as the antenna increases in size. These measurement results are summarized in Table 8 and agree well with the simulated values shown in Figure 57.

The measured normalized patterns are shown in Figures 63 and 64. Some ripple can be

Table 8: Tabulated antenna measurement results for all four states. The actuation voltage and measured resonances are given.

	Voltage	f_1	f_2	f_3
State 1	0V	18.0GHz	>30GHz	>30GHz
State 2	20V	9.4GHz	>30GHz	>30GHz
State 3	30V	5.7GHz	17.5GHz	>30GHz
State 4	40V	2.4GHz	9.0GHz	14.3GHz

Table 9: Simulated antenna efficiency with ideal and ohmic switches.

State	Frequency	Ideal Switch	Ohmic Switch	Difference
1	18GHz	94.07%	94.07%	0.00%
2	9.4GHz	89.18%	88.56%	0.62%
3	5.7GHz	87.65%	85.83%	1.82%
4	2.4GHz	84.43%	81.68%	2.75%

noticed in State 1 of the antenna due to mismatch from the coaxial SMA connector. The measured patterns agree well with the simulated ones shown in Figure 58. For clarity, these plots are not superimposed.

9.5 Efficiency Considerations

As stated previously, this reconfigurability would not be possible without ohmic switches. Since the RF signal is propagating through a resistive device, this is going to create additional loss in the antenna. The extra loss will effect the antenna's efficiency. Each switch has an on-state resistance of about 1.7Ω. Simulations were performed using IE3D to calculate the efficiency of the antenna with ideal switches and switches with a 1.7Ω resistance. The metal lines were simulated as 1.5μm thick aluminum and the LCP had a loss tangent of 0.003. The results of those simulations are shown in Table 9.

It has been previously documented that Sierpinski antennas have high efficiencies. The range varies from 77-95% although most antennas are in the high 80s [4, 51, 98]. The simulated efficiencies for this antenna are well within this range of typical values. As

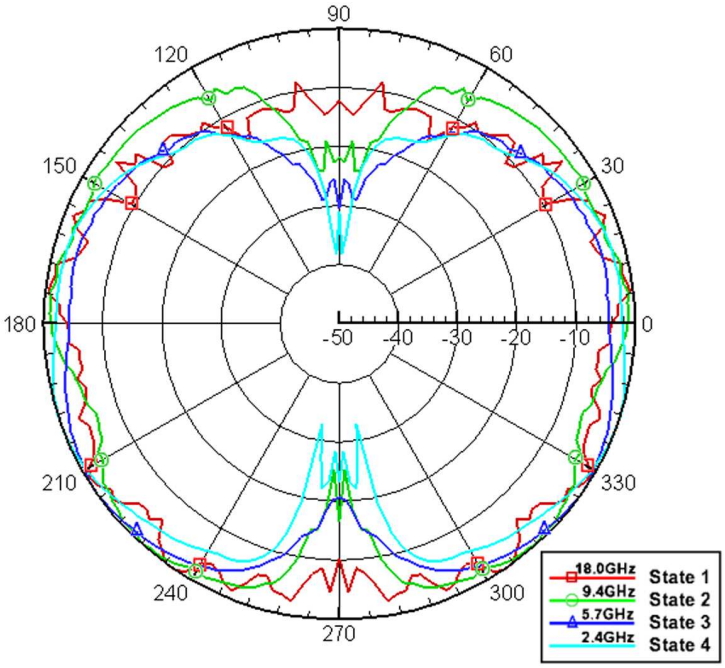

Figure 63: Measured radiation pattern φ=90^o (zy-plane) for all four states of the Sierpinski antenna [45]

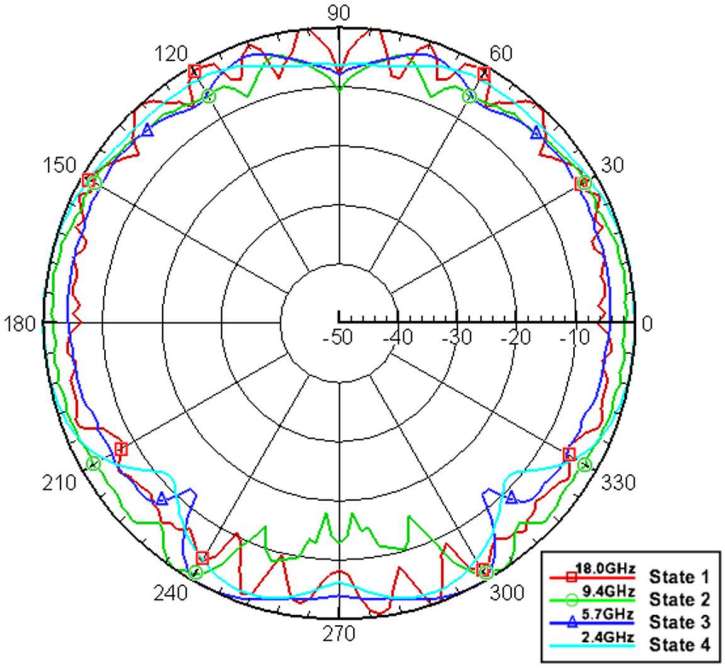

Figure 64: Measured radiation pattern φ=0^o (xz-plane) for all four states of the Sierpinski antenna

expected, the efficiency decrease is more substantial when there are a greater number of switches actuated (fewer actuated switches translates to less resistive loss). In the case where all switches are "OFF" (State 1), there is no loss in efficiency from the switches. This is expected. For all states, the added loss from the switches is less than 3%, which is minimal.

DEVELOPMENT OF MINIATURE, MULTILAYER, INTEGRATED, RECONFIGURABLE RF MEMS COMMUNICATION MODULE ON LIQUID CRYSTAL POLYMER (LCP) SUBSTRATE

PART III

Packaging Level Research

by

Nickolas Kingsley

Part III

Packaging Level Research

In Part II, various RF components were realized on LCP. In order to make these devices more robust, they need to be packaged. The process for packaging devices in LCP is presented in this section. A comparison of various packaging methods is made. The results for successfully packaged MEMS switches and phase shifters are presented. A thorough analysis of the packaging hermeticity was also performed.

CHAPTER X

THERMAL EFFECTS ON MEMS SWITCHES

One of the goals for this research is to embed a MEMS switch between layers of LCP. Ideally, the layers of LCP will be bonded using thermocompression at around 300^{o}C and up to 60 psi tool pressure. Before this type of bonding could be attempted on layers of LCP, the effect of the temperature on the MEMS had to be studied. It was important to determine whether or not a MEMS switch can survive the bonding process. This work was performed with the assistance of Dane Thompson.

10.1 Temperature Effect on Membranes

When most materials are heated, they expand. When they are cooled, they contract. The amount of expansion is determined by the material and is quantified by the coefficient of thermal expansion (CTE) of a material. The change in length can be calculated by:

$$\Delta L = L\Delta T * \alpha \tag{22}$$

where ΔL is the change in length, L is the original length, ΔT is the change in temperature, and α is the CTE. Note that the units on α are inverse temperature (1/K or K^{-1}). Since these values are usually very small, the numbers are typically divided by one million and are quoted as ppm/K. A list of CTE values for popular MEMS materials is shown in Table 10.

Switch membranes are usually comprised of titanium and gold or aluminum. Whenever you have materials bonded together of different CTE, any change in temperature will cause a mismatch in expansion (or contraction) and stresses will be induced. If the object is in the form of a beam, any expansion will cause buckling. Any buckling in a switch membrane will cause a change in the RF and mechanical properties of the switch. In the worst case, the switch may be permanently stuck in the up or down state.

Table 10: Table of CTE values for popular MEMS materials and substrates [110]

Material	CTE (ppm/K)
Titanium	8.6
Gold	14.2
Aluminum	23.1
Silicon	2.6
LCP	3-30
Copper	16.5

Note: The CTE of LCP is usually around 17 to match copper

Furthermore, there is also thermal mismatch between the switch and the substrate. If the signal lines are heated, they may delaminate from the substrate. Alternatively, the signal lines could crack causing a capacitance in the signal path. The same could happen to the switch.

It is expected that the switches will curl as the temperature is increased. However, as long as the amount of expansion is within the elastic regime of the material, the switch should return to the steady-state when cooled. Otherwise, plastic deformation will occur if the switches expand too much.

10.2 Experiment Procedure and Results

Double-supported (air-bridge type) MEMS switches were fabricated on one inch square samples of LCP. Each sample contained four different switch typologies (shown in Figure 65). All heating was performed using a conventional hot plate in a fume hood in a cleanroom environment. The heating and cooling rates were the same as that used by the Karl Suss Bonder (since ultimately that is what this testing was for).

The samples of switches were placed on the hot plate and heated to 290^{o}C. This temperature was chosen because it is the melting temperature of the bond ply material. If the switches can not withstand this temperature, then they can not withstand thermal bonding.

Three dimensions were evaluated before and after heat exposure: the maximum height of the bridge from the substrate, the gap between the bridge and the substrate, and the height

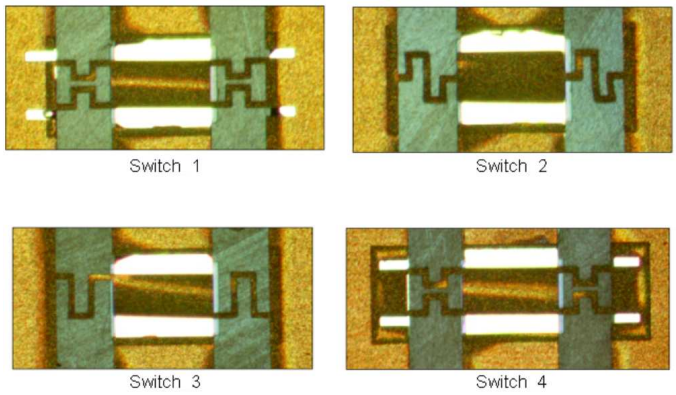

Figure 65: The four MEMS switch membrane designs tested for heat exposure

of the curl on the bridge. Measurements were taken using a Veeco optical profilometer. A 3D image of each of the four switch geometries before and after heat exposure is shown in Figures 66 through 69.

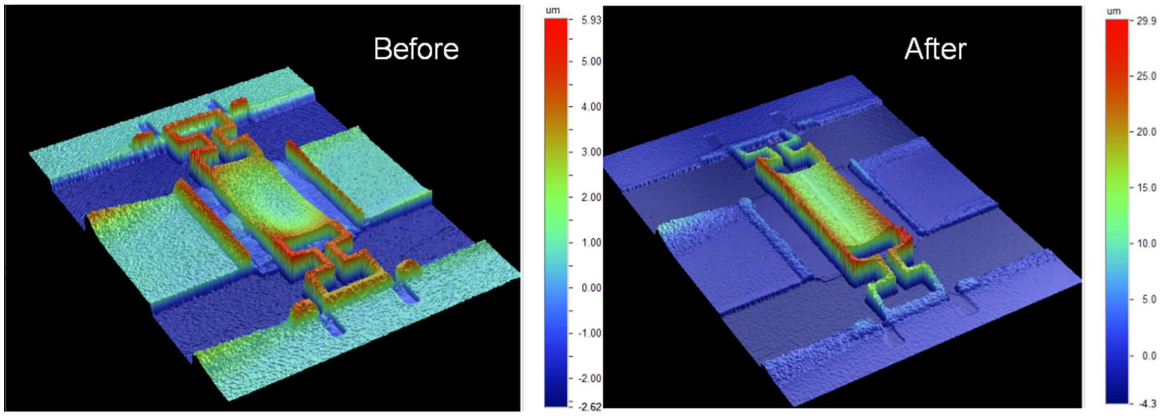

Figure 66: Deflection of switch design 1 before and after heat exposure. This switch curled 9.5μm as a result of the temperature change

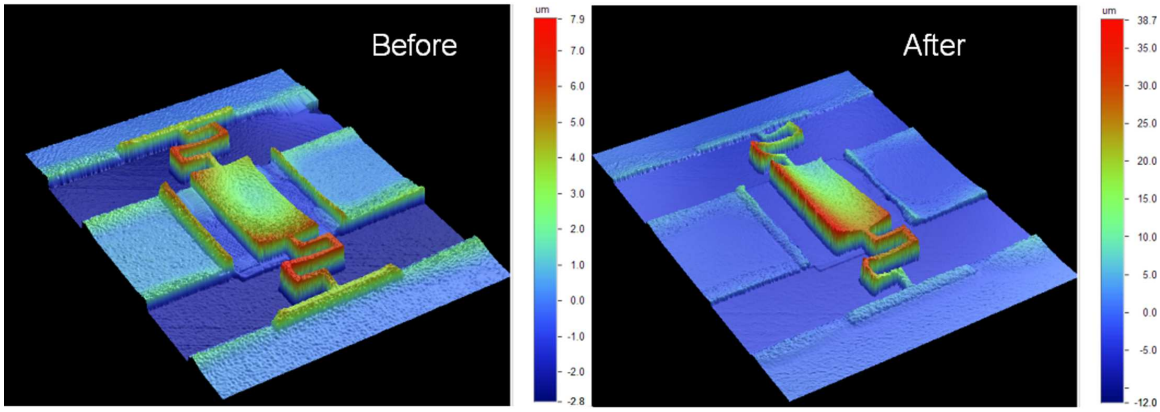

Figure 67: Deflection of switch design 2 before and after heat exposure. This switch curled 15.5μm as a result of the temperature change

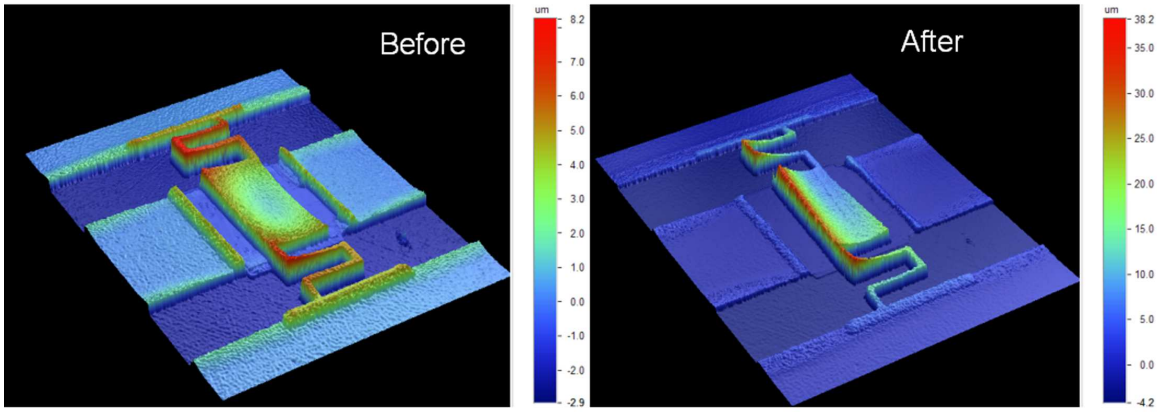

Figure 68: Deflection of switch design 3 before and after heat exposure. This switch curled 19.1μm as a result of the temperature change

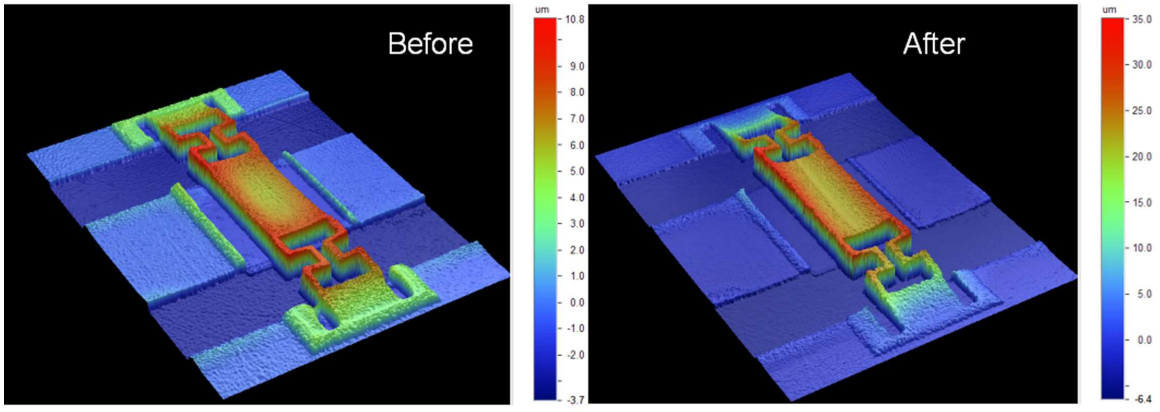

Figure 69: Deflection of switch design 4 before and after heat exposure. This switch curled 6.9μm as a result of the temperature change

The change in geometry from the heat exposure is summarized in Table 11. It seems clear that the effect of 290^{o}C heat exposure on a MEMS switch is extreme. With an average gap of 18.3μm after exposure, the switches have no chance of deflecting with a reasonable amount of voltage. For this reason, thermocompression bonding can not be used to package RF MEMS switches.

Table 11: Switch geometry before and after heat exposure is given

	Switch 1	Switch 2	Switch 3	Switch 4
Max Height (before)	8.5	10.7	11.1	14.5
Max Height (after)	34.2	50.7	42.4	41.4
Gap (before)	1.8	2.9	2.4	7.8
Gap (after)	15.0	20.0	11.9	26.3
Curl (before)	1.5	2.0	3.1	2.2
Curl (after)	11.0	17.5	23.0	9.1

All units are in microns

10.3 Determining the Highest Process Temperature for RF MEMS Switches

Even though the MEMS can not survive a 290^{o}C exposure, it's important to determine the highest temperature that the MEMS can withstand. This temperature varies with the materials used and the switch geometry. Stiffer switches can withstand higher temperatures but they also have higher actuation voltages. Through trial and error, it was determined that for these materials and geometries, the maximum temperature that can be used before substantial curling occurs is 200^{o}C. The deflection for a switch before testing, at 200^{o}C, and at 290^{o}C is shown in Figure 86. The data is summarized in Table 12.

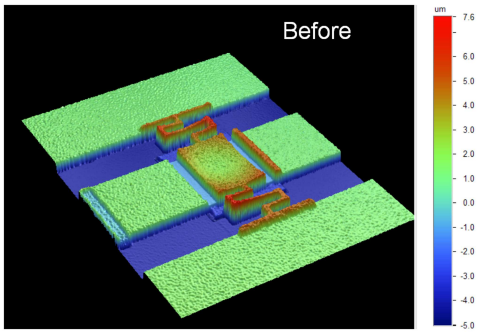

(a) Before heat exposure

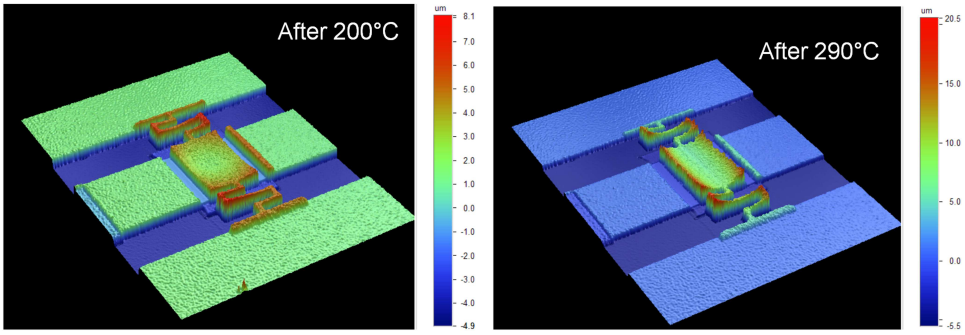

(b) After 200°C heat exposure

(c) After 290°C heat exposure

Figure 70: RF MEMS switch deflection before and after various heat exposures. The highest temperature that the MEMS can be exposed to and still operate is 200°C

Table 12: The switch geometry over various temperatures

	Height Range	Gap	Membrane Curl
Before	12.6	2.9	1.2
200°C	14.0	2.9	1.5
290°C	26.0	8.0	8.3

All units are in microns

CHAPTER XI

LCP BONDING METHODS AND ANALYSIS

MEMS are highly-sensitive by nature. Often, metal bridges or cantilever beams are suspended a few microns above a substrate layer and deviations less than a micron can drastically change the performance. For these devices, air-born particles, air flowing over the surface, moisture, and temperature changes can effect the performance and possibly cause damage to the device. For these reasons, it is essential to package MEMS to protect them from the environment.

LCP has a relatively low melting point compared to other RF packaging materials. This can be both a blessing and a curse. It's too low for many of the exotic bonding materials to be plasma deposited. It's too high to be melted before MEMS have problems. Therefore, a number of different bonding techniques were investigated. The tradeoffs are explored in this chapter.

11.1 Bonding Methods

There are four proposed methods for bonding LCP: epoxy bonding, ultrasonic bonding, thermocompression bonding, and localized ring bonding. These methods are described below.

11.1.1 Epoxy Bonding

The most economical method for bonding LCP is epoxy bonding. In this method, multiple layers are literally "glued" together with a commercially available adhesive. Several of these adhesive materials are available in spray (i.e. Super 77^{TM} by $3M^{TM}$ [1]), spin-on (i.e. Elmer's ProBond® [38]), or roll-on (i.e. double sided tape). There are three challenges to using these methods. First, they must be applied carefully. Any residue that is indirectly exposed to the devices can alter the performance. Second, most epoxies outgas as they cure or dry. This can weaken the package integrity and also harm the devices. Finally,

since these layers can be tens or hundreds of microns thick, their RF performance should be taken into account. It's nearly impossible to ensure uniform distribution of material across a sample, which can be problematic. Some devices may experience more loss than others. Quality control, reliability, and repeatability are not always achievable with this method.

11.1.2 Ultrasonic Bonding

Ultrasonic bonding (or welding) has been around since about the 1960s for joining plastics and metals. In this method, high-frequency low-amplitude ultrasonic acoustic vibrations (20-40kHz) are used to weld objects together. The materials heat up and melt due to absorption of vibration energy. This technique is particularly useful for joining dissimilar materials or chemically sensitive devices since no adhesives are used. Unfortunately, this method is not suitable for small, localized packages. Instead, it can only be used for global edge bonds. In addition, the effects of the ultrasonic waves on the MEMS could be problematic since MEMS switches have a mechanical resonance in the kHz range. Since this method requires expensive machinery and can only be used for edge bonding, it was not investigated [104].

11.1.3 Thermocompression Bonding

Thermocompression bonding is implemented by pressing together multiple layers under vacuum and heated to the melting point of a bonding material. In the case of LCP, the temperature used is adequate to melt the middle bond ply but not the outer core layer. This prevents any circuits that are fabricated on the core layer from being damaged. Other packaging materials, like silicon, may use a metal interface to provide a bonding medium. Adding a metal interface can have a profound effect on the RF performance and has the risk of creating shorts. Direct LCP to LCP bonding eliminates these problems and provides a low-loss, low-cost package.

Even though it has been shown that thermocompression bonding is not suitable for MEMS, it is still the preferred method for bonding LCP in general. Countless other RF devices can survive the high temperature and benefit from the packaging method. Before attempting to perform thermocompression bonding on samples of LCP, simulations were

Table 13: LCP material properties [18]

Property	Symbol	Value
Young's Modulus	E	16 GPa
Poisson's Ratio	ν	0.3
Density	ρ	1400 $\frac{kg}{m^3}$
Thermal Conductivity	k	0.5 $\frac{W}{mK}$
Relative Permittivity	ϵ_r	3.1

done to gain insight on the process. It was very important to analyze the integrity of a micromachined cavity throughout the bonding process. These simulations were performed using a multiphysics simulator.

For the all-LCP package, two 100μm thick layers of LCP provide the substrate and the superstrate that the microwave device will be packaged between. In the top layer, cavities will be created that are large enough to encapsulate the device that is being packaged. Specifically, a 50μm tall cavity that has a width of 1.5mm will be used although larger cavities are also possible.

11.1.3.1 Multiphysics Simulation

FEMLAB 3.1 multiphysics simulator by COMSOL [16] was used to simulate the thermo-compression bonding environment. This was done using two separate 2D simulations. The static, plane stress, structural mechanics module was used to simulate the bonding pressure and the steady-state, conduction, heat transfer module was used to simulate the transfer of heat to the cavity. Since a mechanical model is being used, the appropriate physical constants must be entered for LCP. These values are shown in Table 13.

Bonding Pressure Simulation Ideally, if the bonding material is infinitely strong then no amount of pressure pushing the substrate layer and the superstrate layer together would effect the devices within the package. That is, packaging materials that have a large Young's Modulus, like silicon, would experience very little deflection in the superstrate layer above the cavity. However, since LCP is a flexible material with a relatively low Young's Modulus,

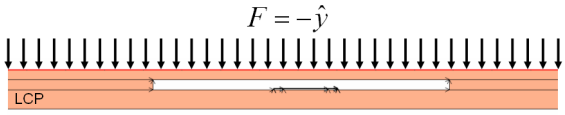

Figure 71: The force used in the thermocompression simulation is equally distributed across the surface in the -ŷ direction

it is expected that some deflection will occur. This simulation will predict the extent of that deflection.

The pressure used for thermocompressive bonding is usually 5-40 pounds per square inch (psi). This force is distributed equally along the surface of the package. This force was entered as a boundary edge load in the negative ŷ direction along the top of the superstrate. This is demonstrated in Figure 71.

The simulated deflection of the superstrate for 875.6 N/m (5.0 lbf/in) force was 5.6nm, which is negligible compared to the 50μm tall cavity. To test the durability of the package, the force was increased until the deflection was large enough to crush the device. The deflections for three different forces are shown in Figure 72 and are tabulated in Table 14.

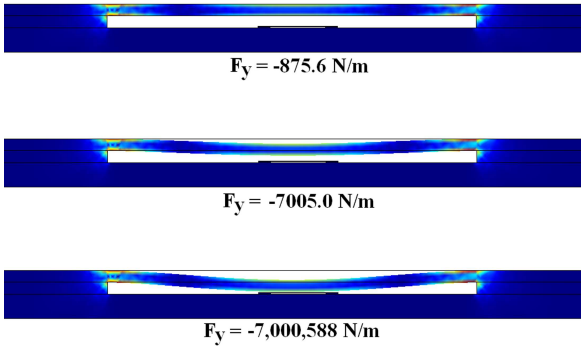

Figure 72: The deflection in the package due to bonding pressure is shown. The force is increased until failure.

Since the package deflection is much less than the height of the cavity, the bonding pressure should not be an issue.

Heat Transfer Simulation LCP, like most polymers, is a terrible thermal conductor. It is about 17 times more conductive than air but it pales in comparison to semiconductors. Silicon, for example, is almost 300 times more conductive than LCP [110]. That means it

Table 14: The deflection of the superstrate due to bonding pressure is shown. The simulator estimates that a 1" sample can survive almost 20 tons of weight

Pressure (N/m)	Pressure (lbf/in)	Maximum Deflection
875.6	5.0	5.6nm
2626.9	15.0	16.9nm
7005.0	40.0	45nm
7,000,588	39,974	44.8μm

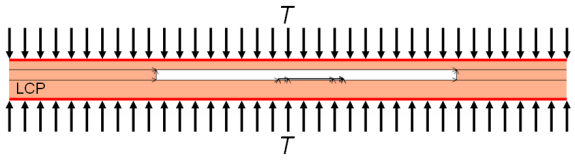

Figure 73: The temperature used in the thermocompression simulation is equally distributed across the top and bottom surfaces

would take a lot more energy to heat up a sample of LCP than it would for a sample of silicon. Since layers of LCP need to be bonded using heat, it is important to study how quickly and efficiently heat can spread through LCP.

The low-melting temperature LCP melts at 290^{o}C, which is the bonding temperature (using a higher temperature has no benefit). The high-melting temperature LCP melts at 315^{o}C so bonding should not be done above that temperature. The bonding machine operates by heating the sample from both sides (top and bottom) evenly and equally. For the simulation, a temperature boundary condition was associated with the top of the superstrate and the bottom of the substrate. This is shown in Figure 73.

Since the package is only 200μm thick, the steady-state temperature throughout the package is equal to the temperature applied by the bonding machine. It is important to investigate how long it will take to reach the steady-state. To determine this duration, the transient analysis module was used. It was demonstrated that the temperature reaches equilibrium within 2 seconds of applying the bonding temperature. The results for five time increments are shown in Figure 74.

As expected, it takes longer for the cavity of air to heat up than the surrounding LCP.

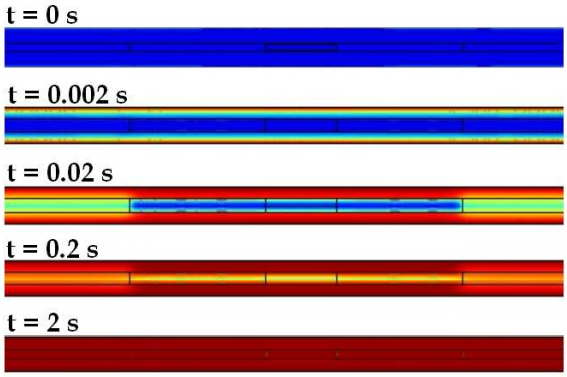

Figure 74: The temperature distribution is shown over time. It takes almost two seconds for an all-LCP sample to reach the melting temperature during bonding

This is because the thermal conductivity of LCP is approximately 17 times larger than that of air. However, even though the cavity is much larger than the microwave device, it is not large enough to provide thermal insulation from the bonding heat.

Both simulations predicted that thermocompression bonding can be used with LCP to create sufficiently strong cavities to protect microwave devices. As stated before, this only holds true for devices that can withstand the 290^{o}C bonding temperature. For other devices, a localized bonding method was investigated.

11.1.4 Localized Ring Bonding

Thermocompression bonding is the best way to bond LCP, but in order for the MEMS to survive the bonding process, the heat must be isolated from the MEMS. A method for implementing localized heating of LCP was proposed by Matt Morton. Some preliminary investigations were performed by Dane Thompson. Their original design is shown in Figure 75. The equipment for localized ring bonding is shown in Figure 76.

The layers are first stacked as demonstrated in Figure 75. The stack is then placed between two glass slides. This is to keep them flat and to thermally isolate them from the rest of the setup. A manual press is used to press out any air between the LCP layers. A pulsed DC current is generated by a current source and passed through a ring of 18μm thick copper surrounding the MEMS device. Since the copper ring has a small resistance, the metal will heat causing the LCP around it to melt (resistive heating). Since there is a

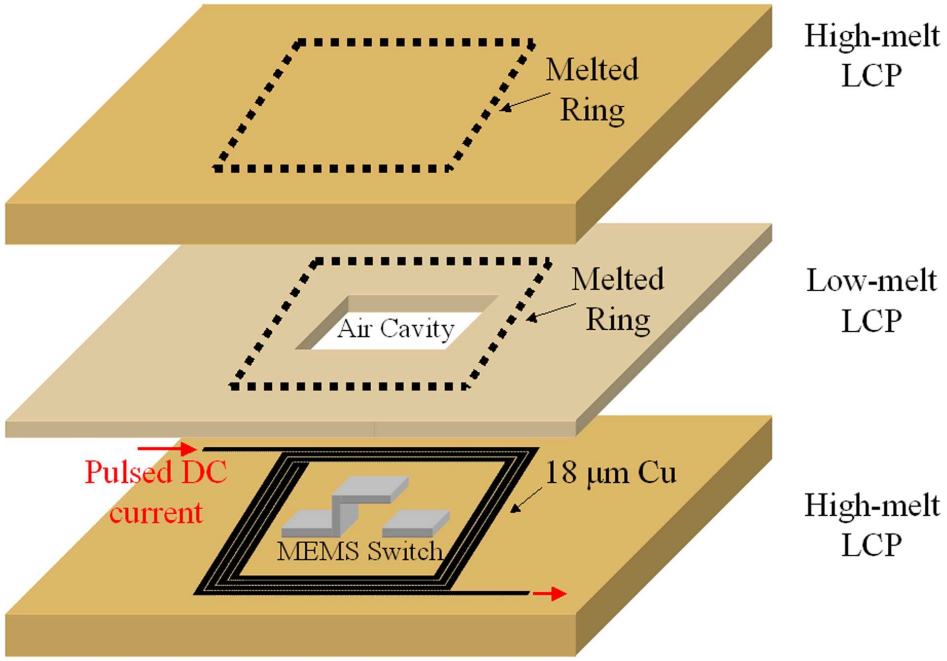

Figure 75: Localized ring bond method proposed by Matt Morton and Dane Thompson. In this method, a copper ring is placed on the same layer as the switch to be packaged

ring of metal in proximity of RF devices, the electrical effects would have to be taken into account.

Through experimentation, Mr. Morton and Mr. Thompson were able to show that this method could be used to melt layers of LCP. However, only straight segments of metal were used as heating elements. The use of a ring was proposed but not investigated. Since neither researcher was knowledgeable in MEMS, the technology was passed on to this author to show that a MEMS switch could be packaged.

11.2 Analysis of Localized Ring Bonding

At the time, only an experimental approach was taken to analyze this bonding method. It was determined that a heat transfer analysis should be performed to attain a theoretical background on the topic. The FEMLAB 3.1 multiphysics simulator by COMSOL [16] was used to simulate the ring bonding environment. The same physical properties shown in Table 13 were used in these simulations. The steady-state, conduction, heat transfer module was used to simulate the transfer of heat to the MEMS switch. Two-dimensional

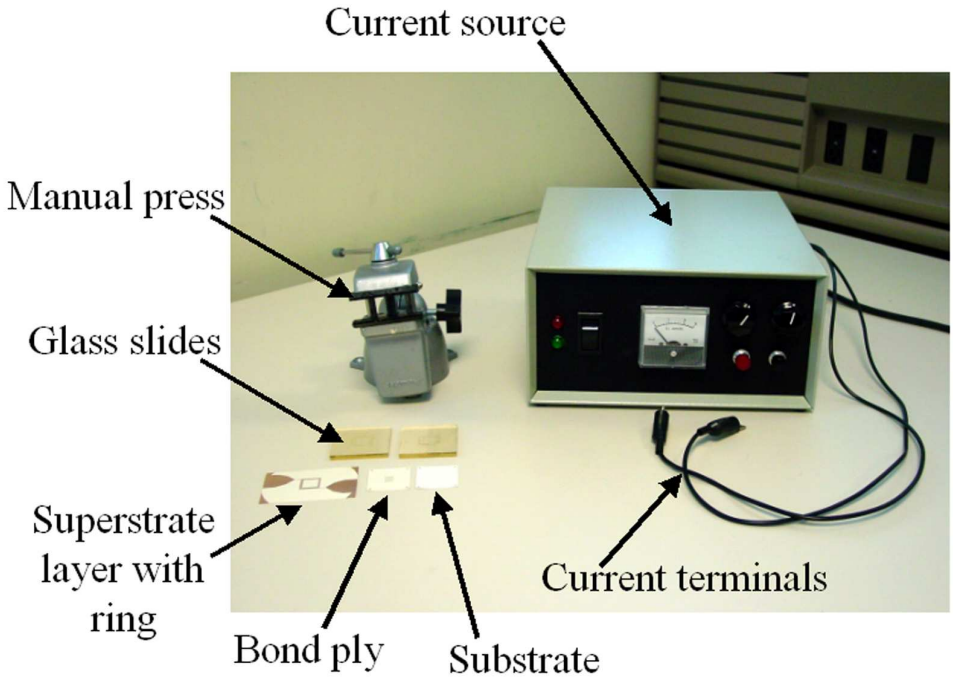

Figure 76: The equipment used to perform localized ring bonding is shown. The current source was designed and built by Matt Morton

simulations were performed from the top and side perspectives. The impact of the bonding process on the MEMS switch was investigated.

For the first simulation, the entire ring is simulated with enough room around the borders to show the lateral spread of heat. A perfect thermal insulating boundary condition is used at the extremities to provide a reference point at room temperature (22^oC). The copper lines are set to 300^oC and the package is allowed to reach the steady-state. The results from this simulation are shown in Figure 77.

As expected, the heat spreads very well between the copper traces but does not extend much laterally. This is desired since it is important that the high temperature does not reach the switch.

For the second simulation, a cross section of one side of the ring is simulated with enough depth to show the vertical spread of heat. Again, a perfect thermal insulating boundary condition is used at the extremities to provide a reference point. The copper lines are heated to 300^oC and the package is allowed to reach the steady-state. The results from this simulation are shown in Figure 78.

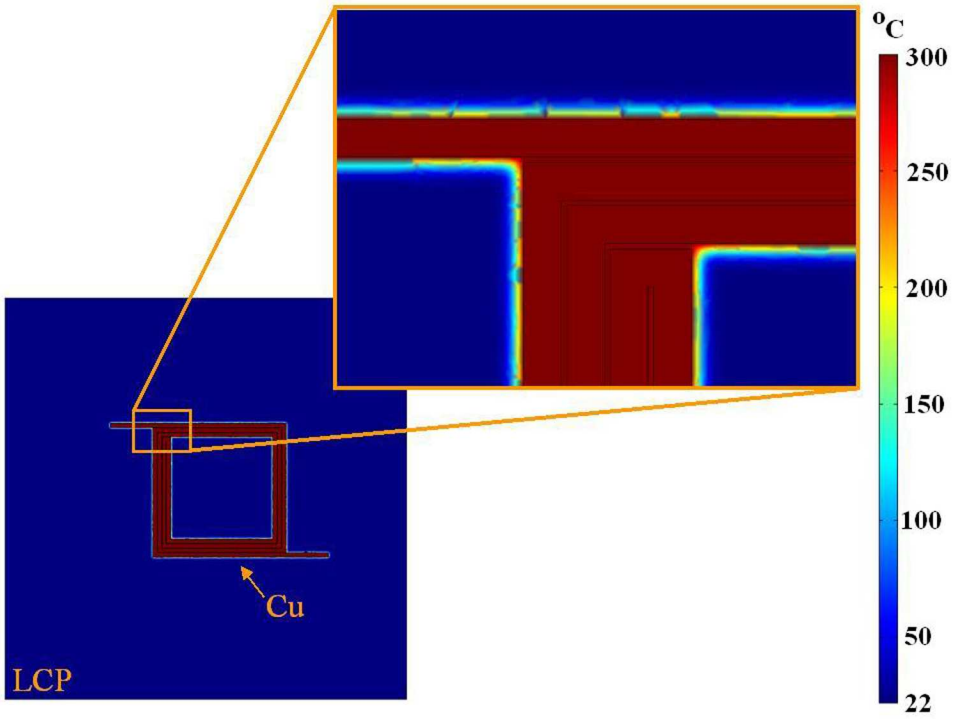

Figure 77: Simulated temperature distribution of the ring bond viewed from the top of the package [64]

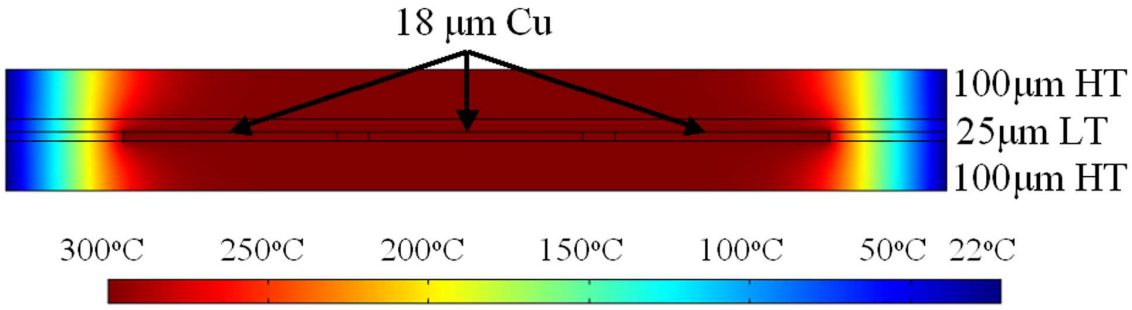

Figure 78: Simulated temperature distribution of the ring bond viewed from the side of the package is shown. There are two layers of 100μm thick high temperature (HT) LCP and one layer of 25μm thick low temperature (LT) LCP [64]

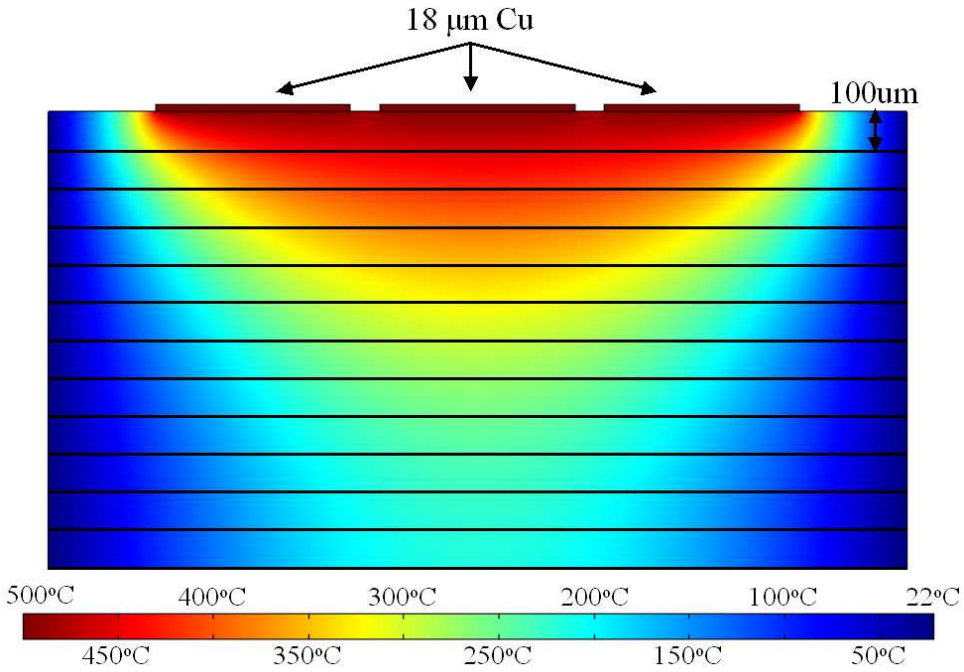

Figure 79: Simulated temperature distribution viewed from the side of the package with a ring temperature of 500^{o}C. The LCP is divided into 100μm thick sections.

This simulation verified the earlier experimental results that this method can be used to melt layers of LCP. The question remained of how many layers of LCP could be melted at one time. It would be beneficial if several layers could be processed individually and then bonded all at once. For this simulation, the temperature was increased to 500^{o}C since this is the highest temperate that can be safely used before approaching the flash temperature of LCP [18]. The results are shown in Figure 79.

LCP will not melt below 290^{o}C. If the maximum temperature of 500^{o}C is used, the maximum height of melting is 600μm. At temperatures higher than this, the LCP will boil and the package will be destroyed. For the standard 300^{o}C process temperature, there is approximately 200μm of vertical bonding. This is significant because standard LCP packages use a 25μm thick bond ply and a 100μm thick core layer. The combination of the two is less than the 300^{o}C melting height which means that the ring does not need to be located inside the package as expected by Mr. Morton and Mr. Thompson. Instead, the ring can be placed on top of the package and there will still be enough vertical spread to sufficiently melt the LCP layers. The final bonding methodology is shown in Figure 80.

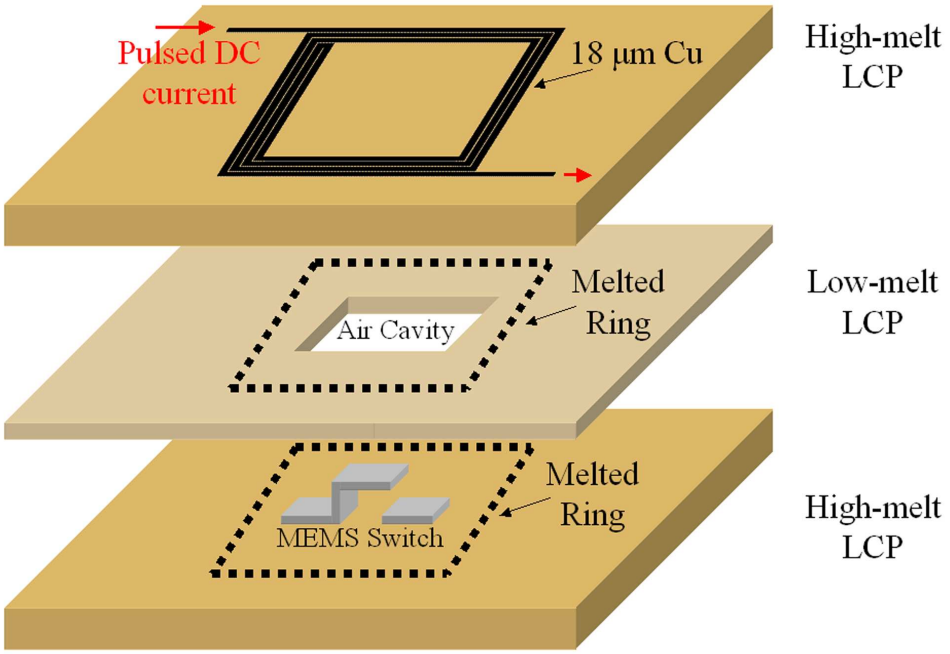

Figure 80: The improved bonding method brings the metal ring outside of the package for easy removal after bonding.

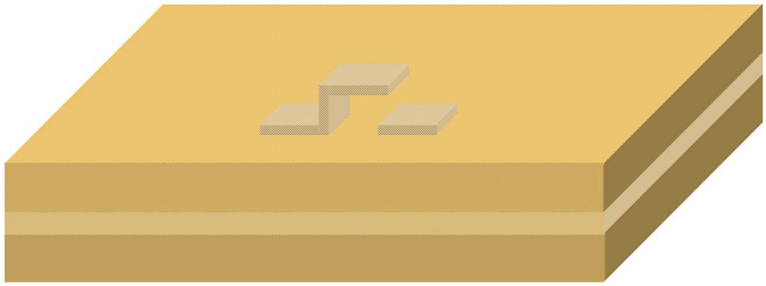

Figure 81: After ring bonding, the MEMS switch is packaged inside of an air cavity. The copper ring is removed to eliminate the effects of the metal.

Bringing the metal ring outside of the package is beneficial since the copper layers can be removed after bonding using a chemical etchent. This eliminates the RF coupling issues and the package no longer requires a feeding transition. An example of a fully packaged MEMS switch is shown in Figure 81.

CHAPTER XII

HERMETICITY TESTING OF LCP PACKAGED MEMS SWITCHES

RF MEMS switches, like all MEMS devices, are extremely sensitive to humidity and therefore must be packaged. Ideally, all MEMS devices would be protected by perfectly hermetic packages which could prevent all moisture from reaching the devices. Such a package can be realized by using metal or ceramic caps, but these methods are very costly and effect the RF performance.

Recently, polymer materials that claim "near-hermetic" packaging performance have been investigated to provide a low-cost solution to MEMS packaging [95]. Many published papers claim that these polymers are ideal for packaging MEMS devices because they can provide adequate moisture protection and can be bonded to the substrate at low temperatures; both of which are necessary for RF MEMS switches [18]. Several papers have demonstrated excellent water resistance from polymer packaged devices [94, 96]. Unfortunately, few papers have tested moisture resistance, which is a much more aggressive test. Moisture testing (or steam testing) is used because steam particles can pass through holes and cracks in the material that water droplets can not. Moisture resistance has commonly been tested by embedding humidity sensors [29] or by performing weight gain analysis [39, 92, 93]. The results from these tests are compared to an accepted standard to determine whether the packaging method passes or fails. The standards used are often written for microelecronic devices, which MEMS are a sub-category of, but they were not written with MEMS in mind. It is possible that a package may pass an industry or military standard but may not be suitable for MEMS devices.

To test for hermeticity, MEMS switches are packaged in LCP and subjected to two humidity conditions. According to the manufacturer, LCP has a "water absorption" of 0.04% [18]. S-parameter results are shown before and after testing to determine the effects

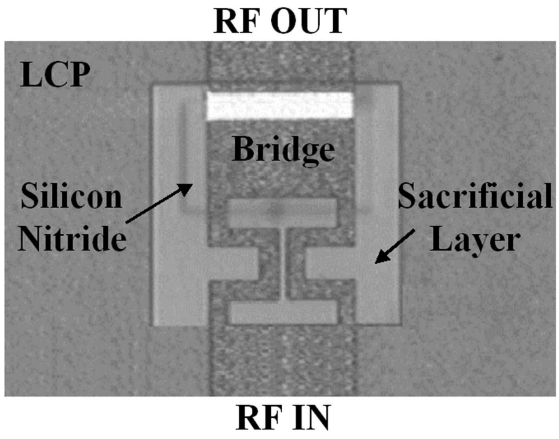

Figure 82: The fabricated MEMS switch is shown. The sacrificial layer is removed to facilitate the suspended bridge.

of the moisture exposure. The lifetime of an LCP packaged switch is extrapolated for jungle, ambient, and desert-like conditions.

12.1 LCP Packaging of MEMS Switches

The MEMS switches used in this work are fabricated directly on the LCP material. Single-supported, capacitive-type switches were used although the experimentation and results are applicable for ohmic and double-supported switches as well. These switches were designed to work at 30V actuation. The fabricated MEMS switch is shown in Figure 82.

Since the MEMS switches will be contained in a package entirely made of LCP, there are two possible sources of moisture: through the LCP material and through the seal. Four sample configurations were investigated:

1. Global lamination with an air-filled cavity (no MEMS switch)
2. Global lamination with an air-filled cavity and 18μm thick copper on the top and bottom (no MEMS switch)
3. Localized ring bond with an air-filled cavity and MEMS switch
4. Epoxy bonding with an air-filled cavity and MEMS switch

These configurations are shown in Figure 83. For Configurations 1 and 2, global thermocompression bonding was performed. For this bonding, the layers are heated to the

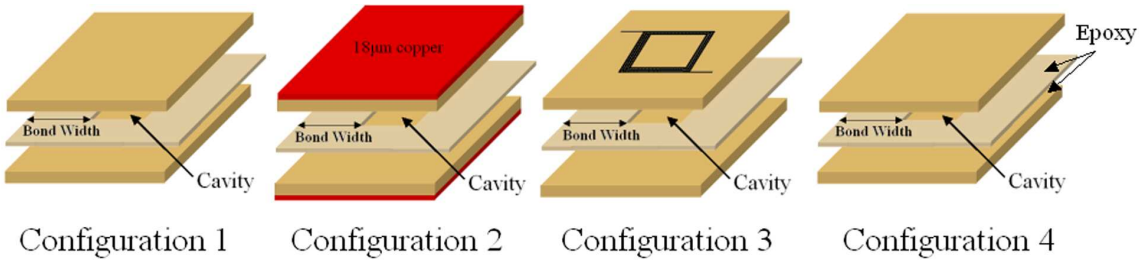

Figure 83: The four sample configurations for hermeticity testing are shown. A cavity is formed by bonding two layers of high-melt LCP to a layer of low-melt LCP with a hole cut in the material. The bond width dimension is shown [46]

melting temperature over the course of 10 minutes. They are then held under compression for 45 minutes. The sample is continually held under compression until it cools to room temperature. Since this process is slow, the molecules have time to arrange in the same crystal-like state as they did before melting [18]. Even though RF MEMS switches can not survive this process, it does represent the best-case scenario that can be achieved with direct LCP to LCP bonding. Bond widths of 2mm, 5mm, and 10mm were tested.

For Configuration 3, a seal around the MEMS switch was formed using resistive heating of thin copper lines [94].The layers of LCP are heated to the molten state in less than 5 seconds. They are then held in place for 30 seconds to ensure that uniform melting has occurred. The temperature is allowed to cool down to room temperature over the course of 5 minutes. Since this process is quick, the heat from the bonded areas do not effect the MEMS switches. The bond width is approximately 2mm.

For Configuration 4, Super 77^{TM} by $3M^{TM}$ [1] was used to glue the layers together. The adhesive was sprayed onto both sides of the bond ply as uniformly as possible. The layers were stacked and bonded as quickly as possible. The epoxy was allowed to dry over night as recommended by the manufacturer.

To provide the best possible bond quality and consistency across samples, several precautions were taken. First, all of the samples were plasma cleaned prior to bonding to remove any trace amounts of dust, dirt, oils, or other impurities. Second, all processing was performed in a class 10 cleanroom environment. Third, all cavities are of the same size (2cm $\times$ 2cm $\times$ 50μm or 0.02cm^3). Finally, all samples were processed at the same time in

a low-humidity environment.

12.2 Hermeticity Standards and Tests

One of the most commonly used hermeticity standards is Military Standard 883G, Method 1014.12. This standard is intended to determine the seal quality of microelectronic devices with designed internal cavities. For this method, a sample is weighed before and after moisture exposure. The test fails if the weight gain is more than 1.0mg for a cavity volume less than 0.01cm^3 or 2.0mg for a cavity volume greater than 0.01cm^3 [68].

There are three commonly used leak tests. Immersion testing is used to determine gross leaks. Helium and humidity tests are used to find fine leaks. These tests will be discussed below.

12.2.1 Immersion Testing

Packages can be completed submerged in water (or another liquid) for many hours. Standard durations range from 24 hours to several months. The temperature of the liquid can also change depending on the standard, but 60^{o}C to 100^{o}C (boiling for water) are typical. Also, some standards require additives being added to the liquid to make the test more rigorous. Salt is typically used as a corrosive agent. Methanol is often added as a solvent [68].

This test is typically used to find large cracks and leaks. Since liquids (especially water) tend to have a strong surface tension, the liquid may not enter into the package even though small holes are present. For this reason, fine leak testing is often performed if this test passes.

Configurations 3 and 4 were subjected to a 24 hour, 60^{o}C water immersion testing. The S-parameter measurement results of Configuration 3 before and after immersion are shown in Figures 84 and 85. Since these are double-supported (air-bridge) type switches, there should be total reflection when the switch is down (actuated) and total transmission when the switch is up (non-activated). It has been determined that Configuration 3 passed the immersion test.

Configuration 4 did not pass the immersion test. The epoxy dissolved in the water and caused delamination of the layers. Since it failed the gross leak test, no further testing will

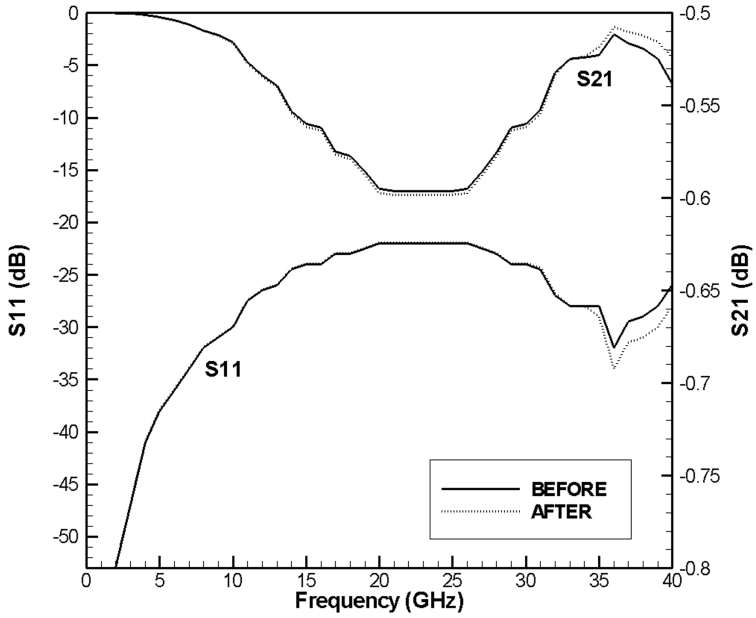

Figure 84: Measurement results of the MEMS switch packaged by Configuration 3 before and after hermeticity testing in UP (non-actuated) state. Since there was a negligible change in the performance, this configuration passed the immersion test [46]

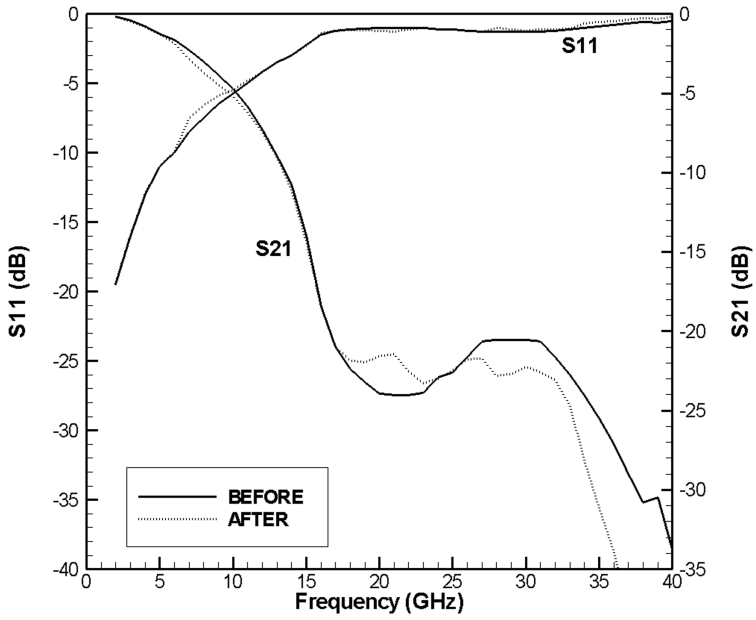

Figure 85: Measurement results of the MEMS switch packaged by Configuration 3 before and after hermeticity testing in DOWN (actuated) state. Since there was a negligible change in the performance, this configuration passed the immersion test [46]

be performed. Epoxy bonding is not a suitable method for hermetically packaging MEMS devices.

12.2.2 Helium Leak Testing

Helium leak testing is one of the most rigorous tests used for microelectronic devices. The device is first subjected to a helium rich environment. Any leaks in the package will allow helium to flow into the cavity. The package is removed from the helium environment and a mass spectrometer helium leak detector is used to determine how much (if any) helium entered the package [86].

Unfortunately, organic materials naturally absorb helium. Whenever an organic package is subjected to a helium leak test, it always results in a failure. Since LCP is an organic material, helium leak testing can not be done [86]. Papers that report helium leak testing being performed on LCP have to metalize the package in order for it to pass. However, these results are misleading since metal packages are hermetic by definition and any material packaged in metal should pass the helium leak test. Complete metalization of a device is not always possible for RF applications. For these reasons, many papers that use polymer packages use weight gain analysis instead of helium leak tests [39, 92, 93].

12.2.3 Humidity (Moisture) Testing

If helium leak testing can not be performed, but a more rigorous test than immersion testing is required, humidity testing is used. In this test, the package is subjected to temperatures and humidity levels higher than those found in ambient conditions (typically 25^oC and 50% relative humidity). An acceleration factor (AF) can be calculated using the two-stress Eyring model [23] quantified by [31]:

$$AF = \frac{(RH^{-3}e^{E_a/kT})operating\ conditions}{(RH^{-3}e^{E_a/kT})accelerated\ conditions} \tag{23}$$

In Equation 23, RH is the relative humidity, E_a is the activation energy (usually 0.9 eV), k is Boltzmann's constant (8.617×10^{-5} eV/K), and T is the absolute temperature (K). Table 15 shows the acceleration factor and 1 hour equivalence for five commonly used temperatures and relative humidities.

Table 15: The acceleration factor (AF) and 1 hour equivalence are given for five temperatures (T) and relative humidities (RH) with respect to ambient conditions

Classification	T/RH	AF	1 Hour Equivalent in Ambient
Desert	$45^oC/10\%$	0.0724	4.34 minutes
Ambient	$25^oC/50\%$	1	1 hour
Jungle	$35^oC/85\%$	15.3	15.3 hours (0.638 days)
	$85^oC/85\%$	1738.1	72.4 days (0.198 years)
	$100^oC/100\%$	9319.5	380.7 days (1.042 years)

12.3 Hermeticity Testing Performed

Before and after testing, all samples were baked for one hour at 100^oC on a hot plate. This step is necessary to remove any surface moisture that will not compromise the integrity of the package but can skew the weight measurements. Precautions were taken to protect the samples from dirt and oils. All measurements were taken with a scale that has five digits of precision and is enclosed to eliminate the effects of room pressure changes (this is required by [68]). According to Military Standard 883G, Method 1014.12, a cavity with a volume of $0.02cm^3$ can pass the seal leak test with less than 2mg of weight gain.

12.3.1 $100^oC/100\%$ Relative Humidity

To evaluate long duration exposures to the elements (up to 10 years), a test was performed at 100^oC and 100% relative humidity for 1, 5, and 10 hours. The measured weight gain from this test is shown in Table 16.

A visual inspection of the MEMS in Configuration 3 showed that the switches had been effected by moisture. Measurement results confirmed that the switches did not survive the test and were stuck in the DOWN state.

There are two samples that gained a great deal more moisture weight than the others (Configuration 1, 10mm, 10 hour and Configuration 2, 10mm, 1 hour). A visual inspection did not find any indication of why these samples leaked profusely. Since LCP is a polymer, defects in the material are always possible and can not be avoided.

Table 16: The weight gain measured for Configurations 1-3 at 100^{o}C and 100% relative humidity are shown. At this temperature and humidity, one hour of testing is equivalent to one year in ambient conditions. There are only two sets of data for Configuration 3 because only 2mm ring bond widths were tested and a 10 hour test was not performed due to the obvious failure after 5 hours

Bond Width/Duration	Configuration 1	Configuration 2	Configuration 3
2mm/1 hour	0.3mg	0.1mg	5.5mg
2mm/5 hour	0.3mg	0.5mg	8.2mg
2mm/10 hour	0.8mg	0.2mg	Not tested
5mm/1 hour	0.4mg	0.7mg	Not tested
5mm/5 hour	0.5mg	0.2mg	Not tested
5mm/10 hour	0.4mg	0.1mg	Not tested
10mm/1 hour	0.5mg	1.5mg	Not tested
10mm/5 hour	0.6mg	0.3mg	Not tested
10mm/10 hour	6.4mg	0.3mg	Not tested

12.3.2 85^{o}C/85% Relative Humidity

To evaluate the short term effects of moisture, a second test was performed on Configurations 1 and 3 at 85^{o}C and 85% relative humidity for 30, 50, and 70 minutes. This test has roughly one-fifth the acceleration factor of the 100^{o}C/100% test. The weight gain from this test is shown in Table 17. Since the weight gain was less than 2mg, all tests passed the Military Standard.

The post-test S-parameter measurement results for the Configuration 3 switches are shown in Figure 86. The 30 minute switch was able to actuate without problems at 30V (Figure 86(a)). The 50 minute switch had deformed enough that it was only able to move a fraction of a micron at 100V. Only a slight change in the response was measured (Figure 86(b)). The 70 minute switch was unable to move at all (Figure 86(c)).

Since the 30 minute switch survived the moisture exposure, a comparison can be made in the S-parameter measurements before and after testing. These results are shown in Figure 87. This comparison confirms that there was no degradation in the performance due to the moisture exposure.

Table 17: The weight gain measured under 85^{o}C and 85% relative humidity conditions. All samples have a 2mm bond width. All samples passed the Military Standard

Sample	Weight Gain	Switch worked after testing?
Configuration 1 - 30 minutes	0.1mg	N/A
Configuration 1 - 50 minutes	0.1mg	N/A
Configuration 1 - 70 minutes	0.1mg	N/A
Configuration 3 - 30 minutes	0.1mg	YES
Configuration 3 - 50 minutes	0.2mg	NO
Configuration 3 - 70 minutes	0.2mg	NO

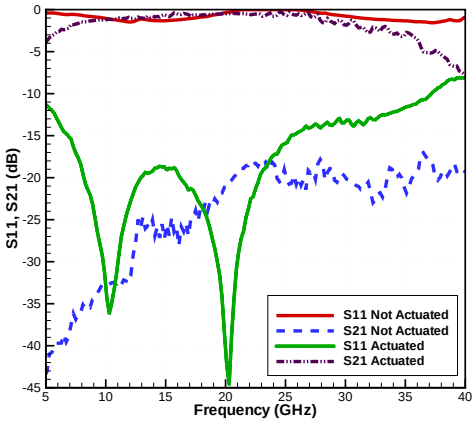

(a) 30 minute exposure

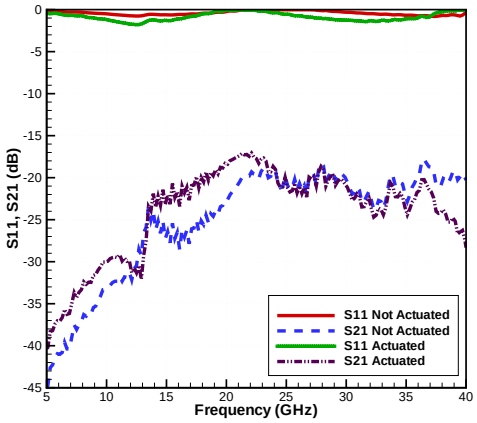

(b) 50 minute exposure

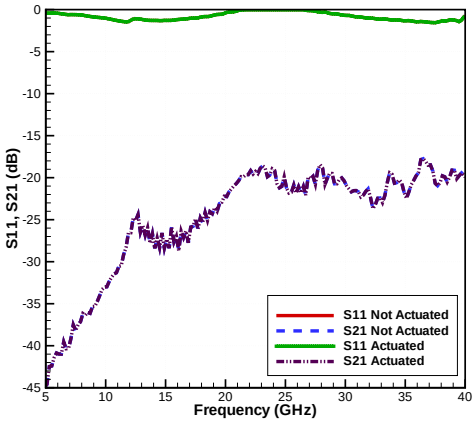

(c) 70 minute exposure

Figure 86: S11 and S21 measurement results for the Configuration 3 MEMS switch at multiple duration exposures to the 85^{o}C/85% moisture test condition. Measurement 86(a) shows a working switch with a 30V actuation. Measurement 86(b) shows a non-working switch with some movement at 100V. Measurement 86(c) shows a switch stuck in the not actuated (UP) state [46]

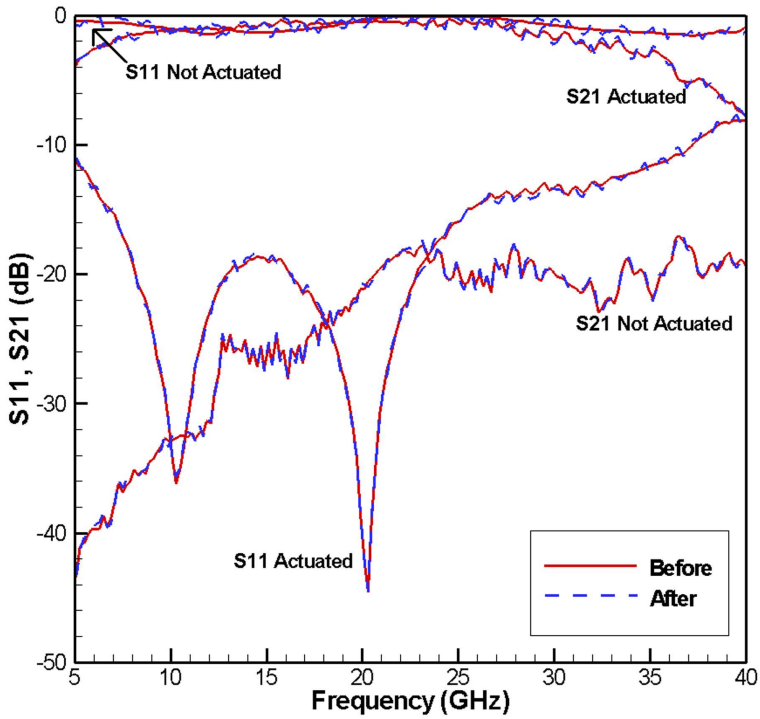

Figure 87: The S-parameter measurement results are shown for the working 30 minute Configuration 3 switch before and after moisture exposure. Less than 0.1 dB and 0.5 dB difference were measured between the S21 and S11 results, respectively. This is within the tolerance for measurement error. There is no degradation in performance caused by the moisture [46]

12.4 Results & Discussion

From the data in Table 16, several conclusions can be made:

- All packaged cavities resulted in at least 0.1mg of weight gained.
- The presence of the 18μm thick copper had very little effect (less than 10% improvement) on the amount of weight gained. This suggests that most of the leakage is through the seal, not the material.
- Most of the weight gain occurs within the first hour of testing.
- The bond width has a negligible effect on the rate or amount of weight gained
- For some cases, as the duration is increased, the weight gain decreases. This demonstrates the inconsistency with polymer materials.
- Of the 18 globally laminated samples in Configurations 1 and 2, only one test failed the Military Standard. Both locally bonded samples in Configuration 3 failed.

The data in Table 17 supports these conclusions as well. This work has also shown that passing the Military Standard for seal quality does not guarantee that the package is suitable for MEMS switches. All of the cases shown in Table 17 passed the standard but only one switch actually survived. If 0.1mg of weight gain is the actual amount of moisture that the switch can tolerate for this cavity size, then the data in Table 16 suggests that even the best-case bonding effort is not suitable for reliable MEMS packaging. Sixteen of the eighteen samples gained more than 0.1mg of moisture weight.

Aside from measurement data, a visual analysis can also provide an indication of the damage that has occurred from moisture exposure. The metal bridge membrane is relatively unaffected by low levels of moisture. As the humidity level within a cavity is increased, the edges of the membrane begin to curl. This is demonstrated in Figure 88. Effectively, this strengthens the bridge in the axis of motion. This type of curling was seen in the switches exposed to the 85^{o}C/85% condition for 50 minutes and 70 minutes. This is why the membrane did not actuate even at very high voltages. The curling was less severe in the

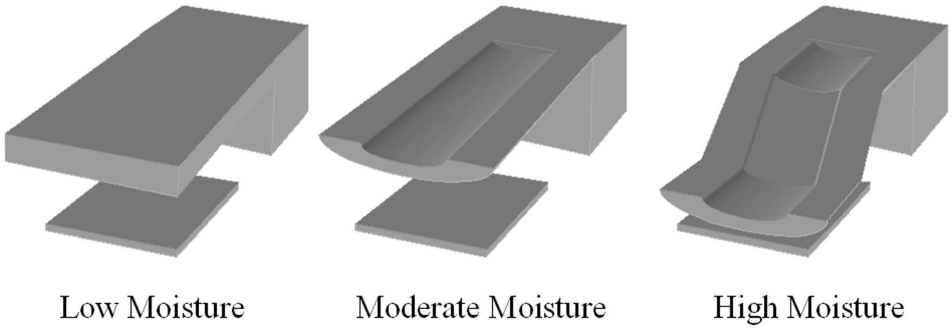

Figure 88: The short (low moisture) and long term (high moisture) effects of moisture are demonstrated. Low moisture levels have little or no effect on the switch membrane (left image). As the moisture level increases, curling occurs (middle image). If the moisture level is high enough, the membrane will be pulled down by surface tension (right image) [46]

50 minute sample which is why it was able to deflect slightly. Both of these samples were stuck in the UP state. As the humidity level increases further, moisture begins to collect on the metal membrane and the signal line beneath it. If the humidity level increases high enough, the surface tension in this moisture will pull the switch down. This effect was seen in the switches exposed to the 100^{o}C/100% condition. These switches were stuck in the DOWN state.

Using the acceleration factors shown in Table 15, it can be extrapolated that an LCP packaged MEMS switch should survive 7-10 hours in jungle conditions, 5-7 weeks in ambient conditions, or 1.4-1.8 years in desert conditions. Metalizing both sides of the LCP package does not provide a sufficient amount of protection. In order to properly protect an enclosed MEMS device, all sides will need to be covered in metal or another material that is better suited for repelling moisture.

CHAPTER XIII

PACKAGED MEMS PHASE SHIFTER

In Chapter 8, a 4-bit reduced-size MEMS phase shifter was introduced. In Chapter 11, various methods for packaging with LCP were discussed. In this chapter, the two topics are combined by packaging the 4-bit MEMS phase shifter in LCP.

13.1 Laser Micromachining

LCP layers can be laser micromachined to create cavities. Cutting through LCP with a 60 watt CO_2 laser is very straight forward. The smallest feature size capable with a CO_2 laser is 200μm because of the ablation process. The molecules that are being ablated are heated with the laser until they break apart. This is a very dirty process since it often leaves the cut edges charred (CO_2 lasers are often called "hot" lasers). For this reason, an oxygen plasma process was developed which can easily remove the carbon residue from the LCP. That recipe is given in Appendix B. The ablation recipe used for LCP and Teflon (which was used in the bonding process) is given in Table 18.

Table 18: CO_2 laser ablation recipe for micromachining LCP and Teflon

Material	Power (W)	Percent Speed
1 mil LCP (bond ply)	6 (10%)	50
4 mil LCP (core)	12 (20%)	50
Teflon	24 (40%)	10

13.2 Packaged MEMS Switches and Phase Shifter

The dielectric discontinuity between LCP and air is much smaller than the discontinuity between a high permittivity material (silicon, for example) and air. It was determined in [95] that the LCP-air discontinuity is small enough that an LCP superstrate layer can be added with a minimal effect on the device performance. Using LCP as a packaging material has many advantages over other materials for this reason.

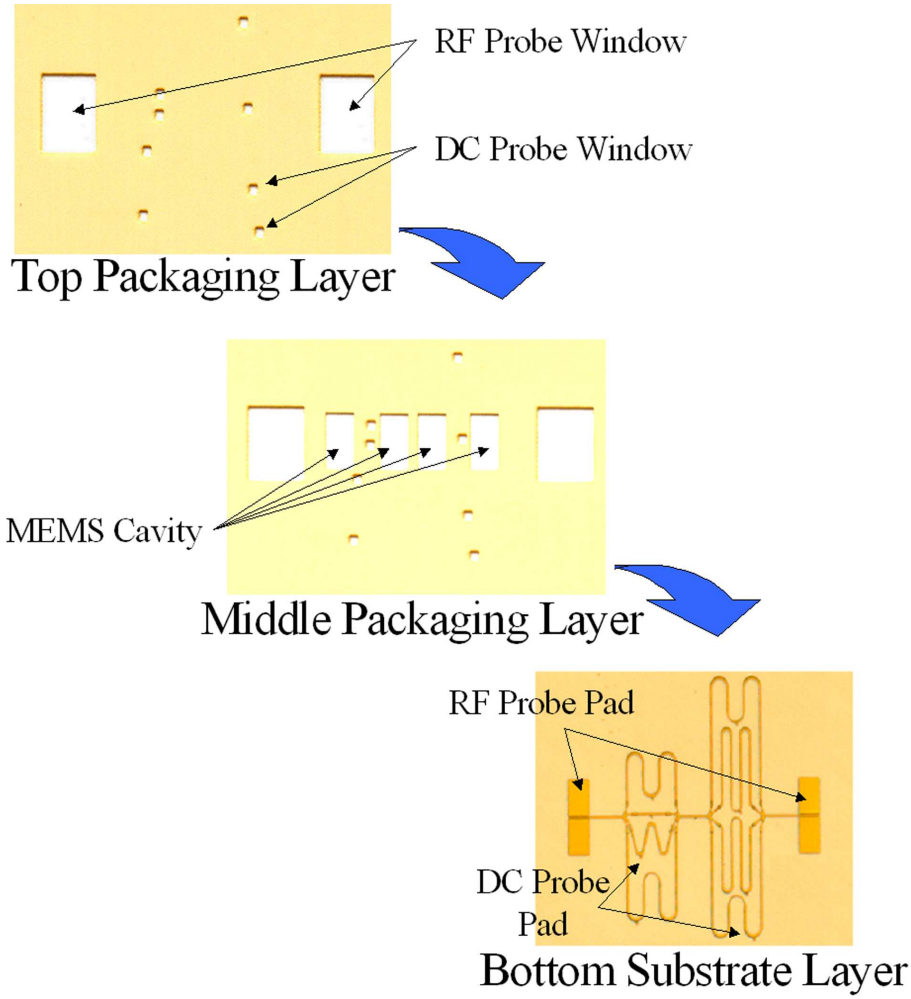

Figure 89: The three LCP layers are shown with the laser micromachined windows and cavities. The top packaging layer is bonded to the bottom substrate layer with the middle packaging layer in between

Two methods were used for packaging the phase shifter: tension and epoxy bonding. Tension bonding was achieved by stretching a piece of LCP over the devices to be tested. It was held down in tension using scotch tape. This is not a practical method of packaging but it does give a good estimate of the results that could be achieved using thermocompression bonding (without MEMS). Epoxy bonding was realized by gluing the packaging layer on top of the substrate layer using a spray adhesive.

The method used to package the phase shifters is shown in Figure 89. The phase shifter signal lines and MEMS switches are fabricated on the bottom substrate layer. A piece of 25μm thick LCP bond ply (middle packaging layer) is placed on top of the fabricated

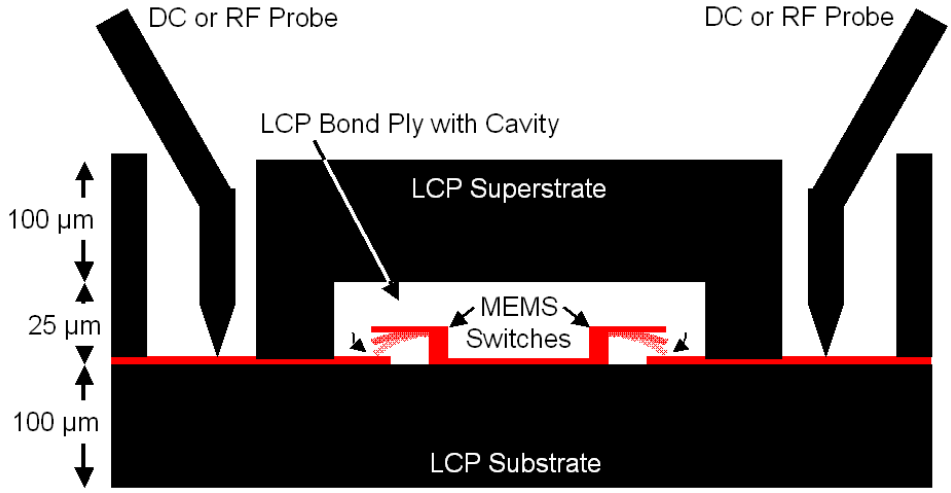

Figure 90: Side view of packaged MEMS switches at tree-junction. The MEMS switches are protected by an air cavity between the superstrate and substrate layers [42]

substrate. This layer is electrically the same as the thicker 100μm material. To prevent the MEMS switches from being damaged by the superstrate layer, cavities were laser-micromachined to expose each of the MEMS devices using a CO_2 laser. These cavities align with the switches on the substrate layer to create an opening large enough and tall enough to prevent contact between the switches and the cavity walls. Above these two layers of LCP, a top packaging (superstrate) layer of 100μm thick LCP is stacked to complete the package. A side view of the laser drilled cavities and packaged MEMS switches is shown in Figure 90.

In order to access the metal signal lines from outside the package with DC or RF probes, windows over the bias pads were laser etched in the middle and top layers to allow direct contact. The DC bias pads were connected to a voltage source through a high impedance DC probe. Since the DC probe is of a much higher impedance than the signal lines, very little RF power is leaked into the DC probe. The placement of the windows and cavities is demonstrated in Figure 91.

13.2.1 Tension Bonding

The first method investigated was tension bonding. The packaging layers were held on top of the substrate layer using scotch tape under tension. The goal was to get an estimate

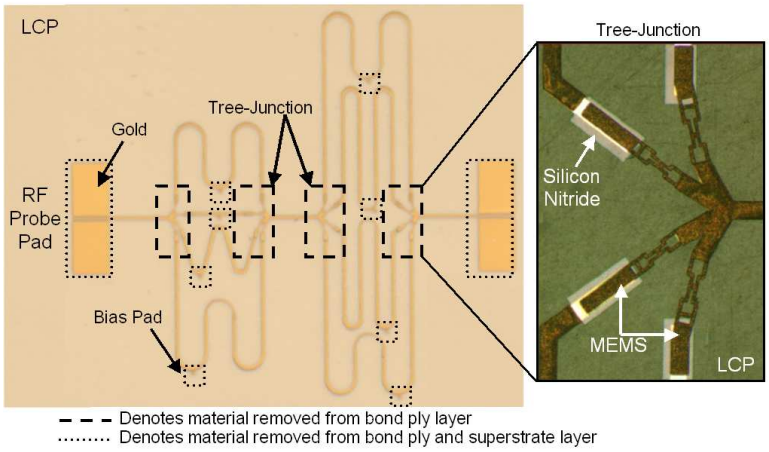

Figure 91: A picture of a fabricated MEMS phase shifter is shown. The location of the micromachined cavities and windows are highlighted [42]

of how much loss would occur from the presence of the additional LCP layers. This work was presented in [95]. As expected, the effect on the device performance from the package was negligible. This method does not provide a viable bonding technique since it provides no protection from the elements. It does provide a benchmark for the lowest possible loss. Any measurements taken with other bonding techniques can be compared to these results to determine the amount of loss added from the bonding.

13.2.2 Epoxy Bonding

The second method investigated was epoxy bonding. The goal was to find a more practical way of bonding LCP layers at a low temperature. The spray adhesive used for epoxy bonding is Super 77^{TM} by $3M^{TM}$ [1]. The thickness of the epoxy is approximately 100μm, which is about the same thickness as the substrate layer. The permittivity of the material is unknown. A comparison of the measured loss for a tension and epoxy bonded MEMS switch is shown in Figure 92. The average variation in S11 and S21 is 3.69 dB and 0.087 dB, respectively at 14GHz. Adding the epoxy to the metal lines must have effected the impedance which caused the additional S11 mismatch. The material itself is either electrically low-loss or thin enough so that the loss isn't significant.

An epoxy bonded 4-bit MEMS phase shifter and MEMS switch sample is shown in Figure 93. A closer view of the cavities in the epoxy bonded package is shown in Figure 94.

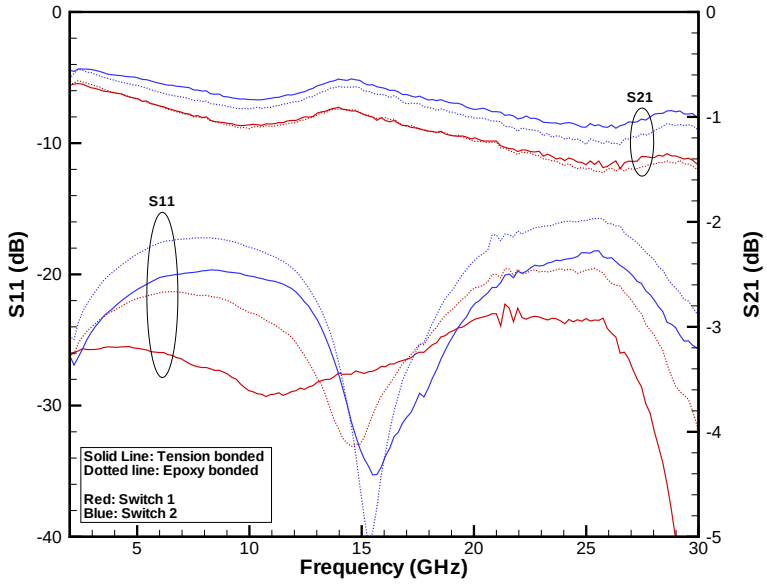

Figure 92: Measurement results for MEMS switches bonded using tension or epoxy bonding. The presence of the epoxy adds a minimal amount of insertion loss

Notice that the epoxy residue does not extend to the center of the window, which is where the MEMS switch would be located. The epoxy should have little or no effect on the mechanical operation of the switch.

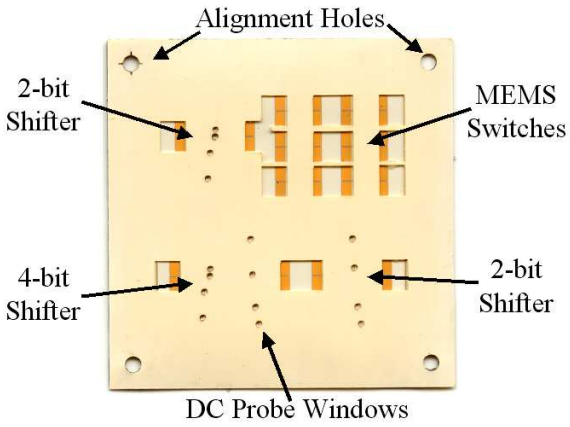

Figure 93: Epoxy bonded phase shifter with DC and RF probe windows shown [42]

The loss measurement results with the top superstrate layer (epoxy bonded) are shown in Figure 95. The worst case S11 is -19.7 dB and the average S21 is -0.96 dB at 14GHz. This is a per-bit insertion loss of only 0.240 dB. The phase error measurement results are shown in Figure 96. The average phase error at 14GHz is 6.57 degrees.

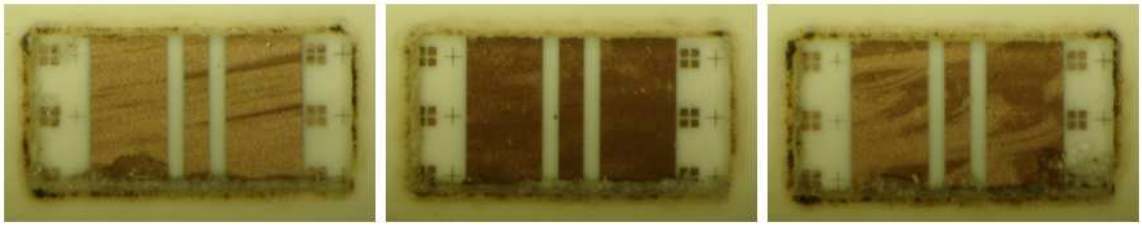

Figure 94: Close up view of epoxy bonded cavities. The epoxy stays at the edges of the cavity and does not flow towards the location of the switch

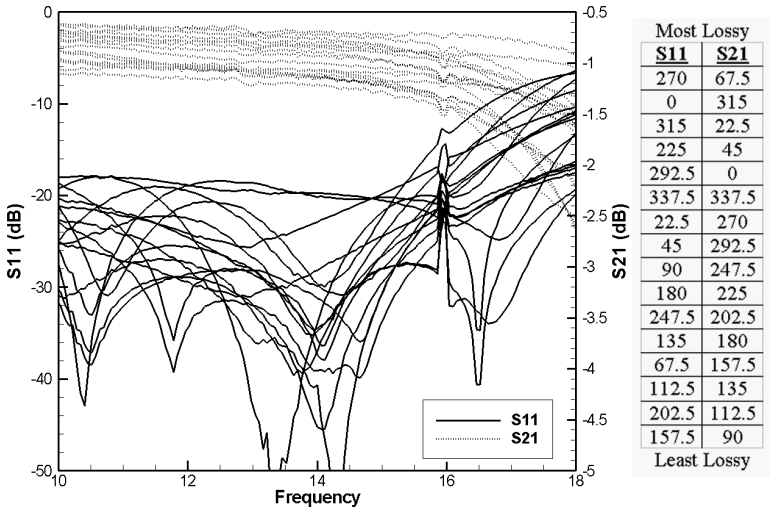

Most Lossy	
S11	**S21**
270	67.5
0	315
315	22.5
225	45
292.5	0
337.5	337.5
22.5	270
45	292.5
90	247.5
180	225
247.5	202.5
135	180
67.5	157.5
112.5	135
202.5	112.5
157.5	90
Least Lossy	

Figure 95: Measured loss of epoxy-bonded 4-bit MEMS phase shifter. The order of the lines is listed from most lossy to least lossy at 14GHz [42]

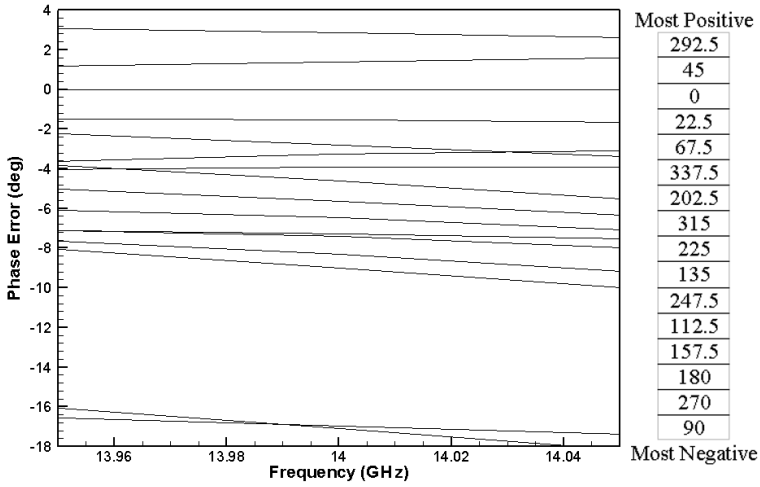

Most Positive
292.5
45
0
22.5
67.5
337.5
202.5
315
225
135
247.5
112.5
157.5
180
270
90
Most Negative

Figure 96: Measured phase error of epoxy-bonded 4-bit MEMS phase shifter. The order of the lines is listed from most positive to most negative at 14GHz [42]

It was originally shown in [95] that packaging MEMS switches in LCP had a negligible effect on the loss. This was tested again with the packaged phase shifter. The addition of the packaging layers added only 0.013 dB on average to the insertion loss. This variation is practically negligible. The variation in the phase was measured to be 3.16 degrees on average at the design frequency. This can be taken into account by simulating the phase shifter with the packaging layer in place.

To demonstrate the mechanical strength of the package, a 15 pound per square inch (psi) force was applied to the top of the package. This test is necessary to show that the cavities can protect the MEMS switches from compression. A loss and phase comparison of the phase shifter without the package, with the package, and with the package after being subjected to the weight is shown in Figure 97. For brevity, only the shortest (0^o) and longest (337.5^o) phased paths are shown.

The addition of the weight creates compressive stresses in the LCP around the cavity discontinuities. These stresses extend to the signal line metal which causes small deflections in the MEMS switches. Any changes in the MEMS switch geometry will change the switch capacitance which accounts for the very small variation in the loss and phase. Increasing the size or rounding the shape of the cavities would decrease the compressive stresses in the LCP. This would decrease the effect of the weight and would allow for more weight to be applied.

As expected, adding the superstrate layer to package the phase shifter had a minimal effect on the performance. The best case, worst case, and average results are summarized in Table 19 [42].

This work represented the first MEMS phase shifter implemented in an all-organic, flexible package. This is one of the smallest and lowest loss designs ever published at this frequency. The phase error is higher than expected, but this could be compensated for in a second revision. The industry standard requires that most phase errors are within 5^o of the target although some radar systems have been known to operate with twice that. It seems certain that this technology furthered the state-of-the-art for phase shifters and flexible packaging. A demonstration of the flexibility is shown in Figure 98.

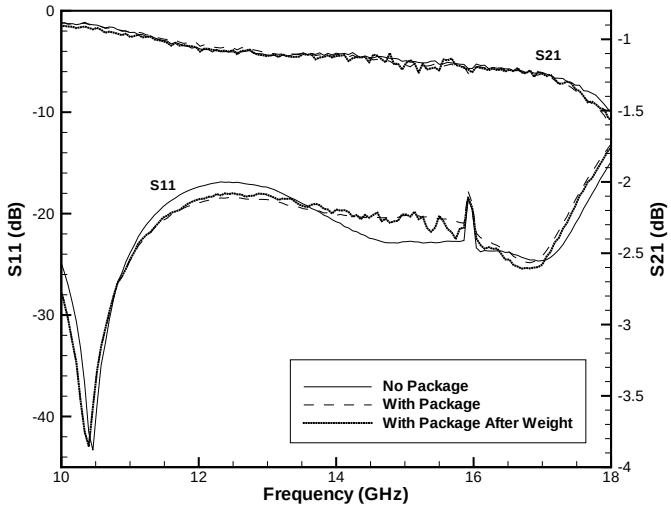

(a) Loss measurement of 0^o case

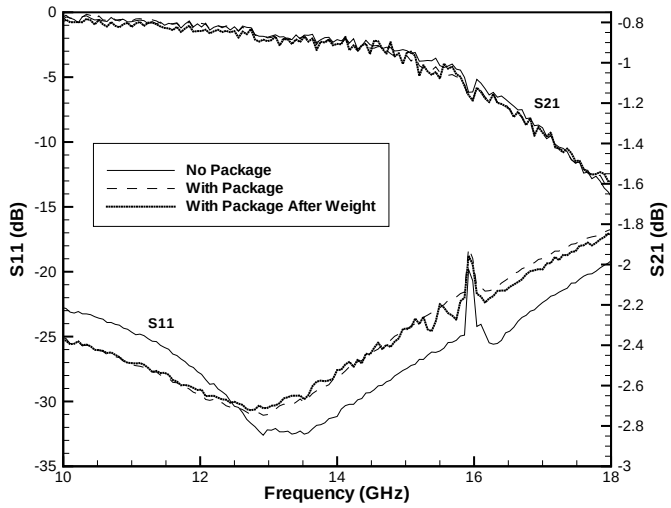

(b) Loss measurement of 337.5^o case

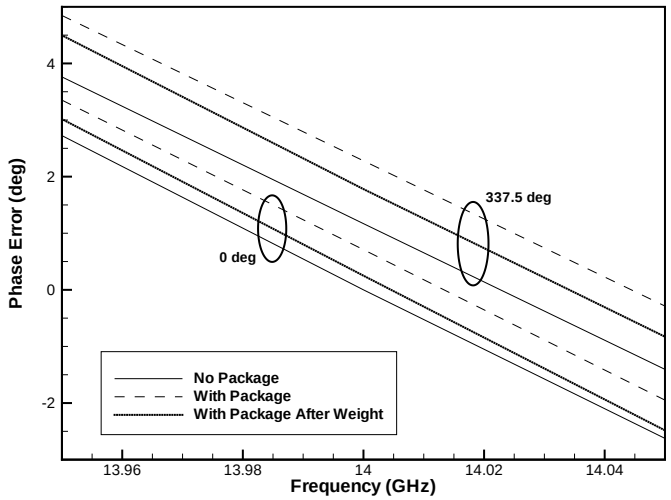

(c) Phase error measurement of 0^o and 337.5^o cases

Figure 97: Comparison of the 4-bit MEMS phase shifter without a package, with a package, and with a package after applying 15 psi of force for the 0^o and 337.5^o cases (all with epoxy-bonding) [42]

Table 19: Measurement results for unpackaged and epoxy-bonded (packaged) 4-bit MEMS phase shifter [42]

	Worst Case	Average	Best Case
Unpackaged S11	-20.8 dB	-30.9 dB	-45.0 dB
Unpackaged S21	-1.22 dB	-0.95 dB	-0.66 dB
Packaged S11	-19.7 dB	-32.5 dB	-45.3 dB
Packaged S21	-1.21 dB	-0.96 dB	-0.69 dB
Unpackaged Phase Error	8.25^o	3.96^o	0.34^o
Packaged Phase Error	17.07^o	6.57^o	1.38^o
S21 Loss Variation	0.045 dB	0.013 dB	0.0022 dB
S21 Phase Variation	9.77^o	3.16^o	0.27^o

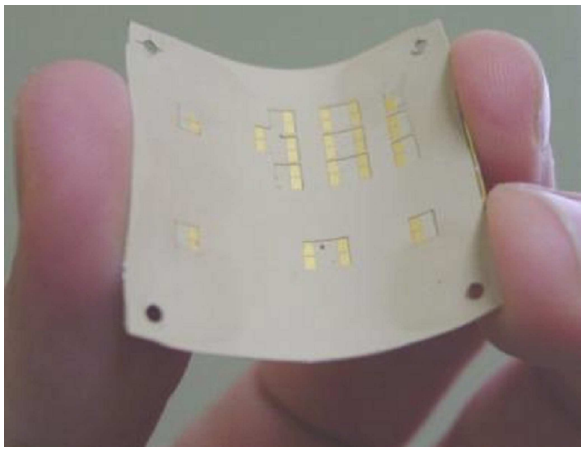

Figure 98: The flexibility of the packaged MEMS phase shifter is shown.

DEVELOPMENT OF MINIATURE, MULTILAYER, INTEGRATED, RECONFIGURABLE RF MEMS COMMUNICATION MODULE ON LIQUID CRYSTAL POLYMER (LCP) SUBSTRATE

PART IV

System Level Research

by

Nickolas Kingsley

Part IV

System Level Research

In Part III, several RF components were packaged in LCP. At this point, all of the necessary steps have been taken to proceed to the system-level. A MMIC amplifier (LNA), MEMS phase shifter, and 2x2 patch antenna array will be integrated to create an RF communication module. This module will be implemented in single and multi-layer configurations. The significance of this work will be addressed.

CHAPTER XIV

COMMUNICATION MODULE COMPONENTS

Before the communication module can be assembled, each component must be individually designed and optimized. In this chapter, the four main components of the communication module are discussed: the aperture, the patch antenna array, the phase shifter, and the monolithic microwave integrated circuit (MMIC).

14.1 Aperture Design

In order to implement a multilayer device, the RF signal needs to propagate down to a lower layer and then propagate back up to the top layer. This is usually done using metalized vias or coupling.

Metalized vias are lower loss than any of the various coupling methods, but they are challenging to implement precisely. In the case of LCP, a via hole would need to be created using a drill press or laser. The via could then be filled with silver epoxy, electroplating, or sputtering. This process is time consuming and costly.

Coupling does have a higher loss than vias but they are easy to make and the dimensions can be controlled precisely. Since the RF signal needs to propagate through a ground plane, aperture coupling was chosen to transmit the data between layers. Some guides were published in [74] for designing aperture couples. The slot dimensions should be kept as small as possible while still getting a good impedance match. The amount of overlap between the signal lines determines the resonant frequency of the aperture (the resonant frequency is inversely proportional to the length of the overlap). ADS Momentum was used to optimize the slot dimensions and overlap length. These values are given in Table 20. The final design is shown in Figure 99.

Since alignment of multilayered devices on LCP is never perfect, a study was performed

Table 20: Optimized dimensions for aperture coupling on 100μm thick LCP

Dimension	Length	Length/wavelength
Slot width	813μm	$^1/_{18}\lambda$
Slot length	2.91mm	$^1/_5\lambda$
Overlap length	2.43mm	$^1/_6\lambda$

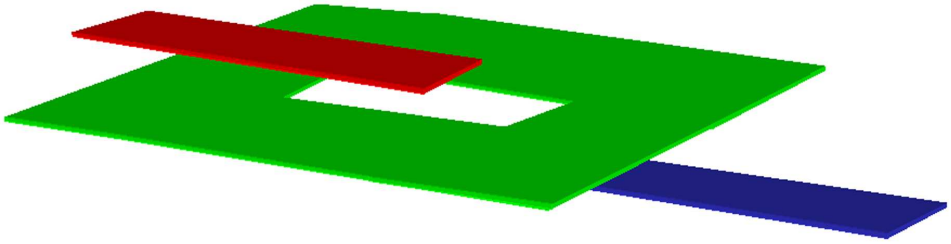

(a) Perspective view

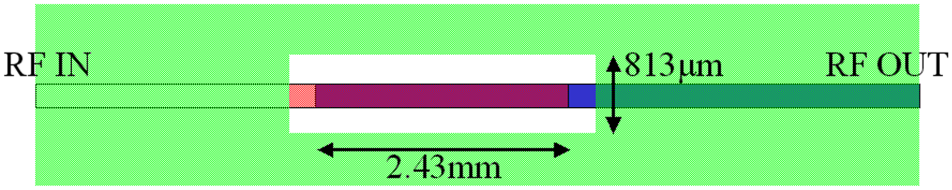

(b) Top view

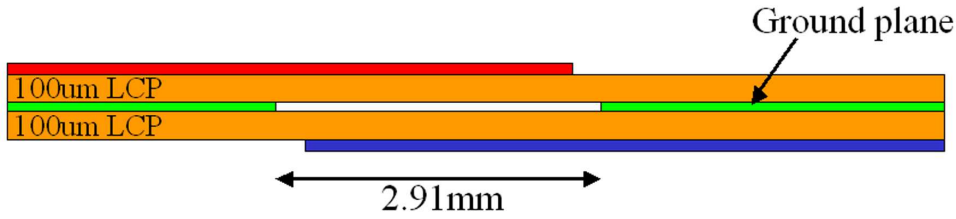

(c) Side view

Figure 99: Layout of aperture coupling. The red layer is on top, the blue layer is on bottom, and the green layer is the ground plane

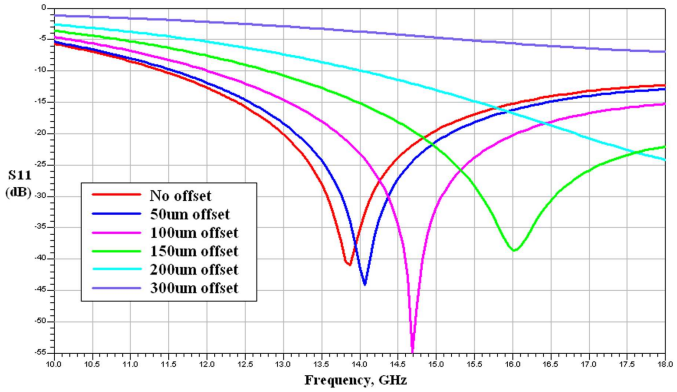

(a) S11 (dB)

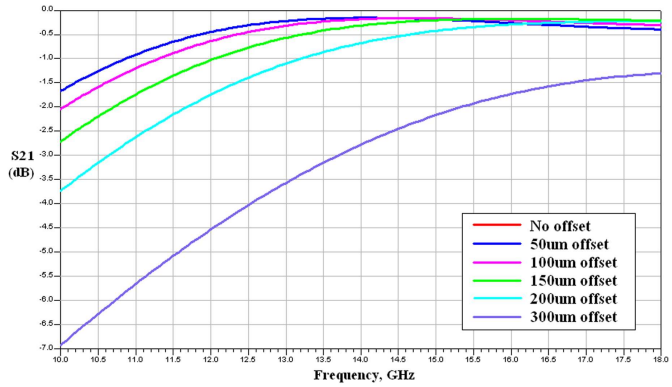

(b) S21 (dB)

Figure 100: Study of S11 and S21 for different degrees of misalignment in the aperture

to determine the amount of loss that would result for a given misalignment. The transmission line at port 1 is moved up to 300μm away from the center. These results are shown in Figure 100. The aperture can operate with a reasonable amount of loss with up to 200μm of misalignment.

14.2 Patch Antenna Array Design

The purpose of this thesis is to create a communication module capable of beam steering. To do this, an antenna array will be fed with different phases. Since this device is to provide a proof of concept, a 2x2 antenna array will be implemented. This technology can be scaled to a much larger array.

Table 21: The patch antenna dimensions calculated using Equations 24-27.

Parameter	Value
W	7.620mm
ε_{reff}	2.881
ΔL	49.616μm
L	6.209mm

14.2.1 Single Patch Design

The antenna geometry was designed using the procedure given in [6]. First, the width (W) of the patch is calculated by Equation 24, where f_r is the resonant frequency and ε_r is the dielectric constant of the substrate.

$$W = \frac{1}{2f_r\sqrt{\mu_o\varepsilon_o}}\sqrt{\frac{2}{\varepsilon_r+1}} \tag{24}$$

Second, the effective dielectric constant (ε_{reff}) is calculated by Equation 25 where h is the substrate height and W is the width calculated in Equation 24.

$$\varepsilon_{reff} = \frac{\varepsilon_r+1}{2} + \frac{\varepsilon_r-1}{2}\left[1+12\frac{h}{W}\right]^{-1/2} \tag{25}$$

Third, the extension of the length (ΔL) is calculated using Equation 26.

$$\Delta L = 0.412h\frac{(\varepsilon_{reff}+0.3)\left(\frac{W}{h}+0.264\right)}{(\varepsilon_{reff}-0.258)\left(\frac{W}{h}+0.8\right)} \tag{26}$$

Finally, the patch length (L) can be calculated using Equation 27.

$$L = \frac{1}{2f_r\sqrt{\varepsilon_{reff}}\sqrt{\mu_o\varepsilon_o}} - 2\Delta L \tag{27}$$

Table 21 shows these values for 100μm thick LCP with an ε_r of 2.95.

The geometry suggested by Table 21 was entered into an ADS Momentum simulation. The length was tuned to resonate at 14.0GHz. The recessed microstrip feed length was

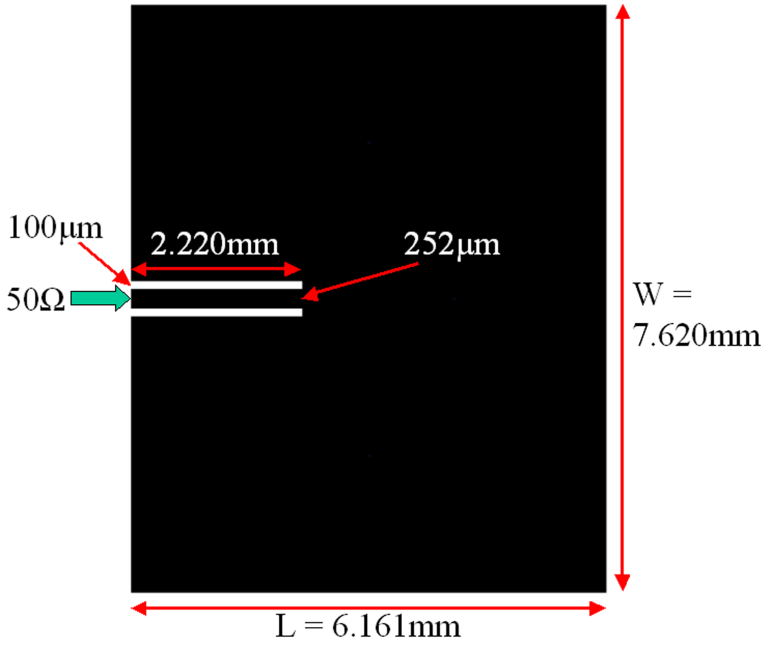

Figure 101: The final patch antenna geometry optimized using a full-wave simulator to resonate at 14GHz with a 50Ω input impedance

increased until an input impedance of 50Ω was achieved. The final layout with dimensions is shown in Figure 101.

The simulated S11 and pattern plots for the patch antenna are shown in Figures 102 and 103.

14.2.2 2x2 Patch Array

The 2x2 patch array was arranged to minimize the distance between the patches. This is to make the array as small as possible and to minimize the side lobes. The layout is shown in Figure 104.

A 50Ω impedance was maintained throughout the feed network by using quarter wave transformers. The individual transmission line impedances are labeled in blue. The simulated S11 and pattern plots for the 2x2 antenna array are shown in Figures 105 and 106.

As the number of elements is doubled, an additional 3 dB of directivity is expected. Since four radiating elements are being used, an additional 6 dB is expected. Since the directivity increased from 6.94 dB to 12.49 dB, this was confirmed.

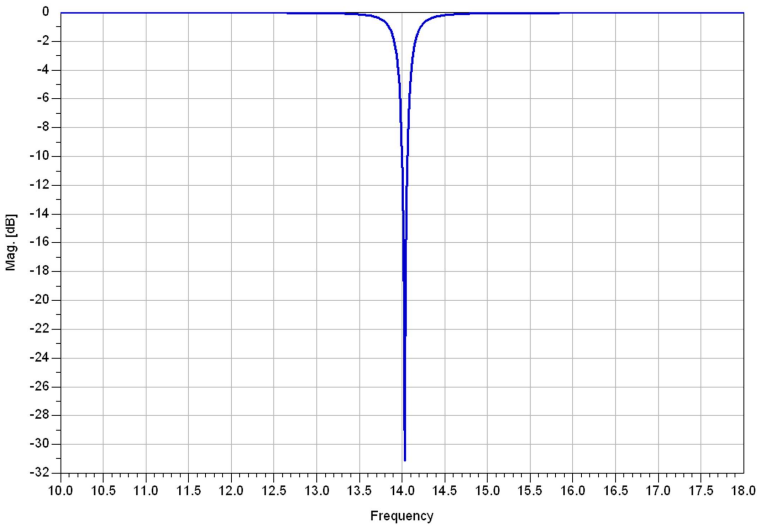

Figure 102: The patch antenna S11 simulation. The antenna has been tuned to resonate at 14.0GHz

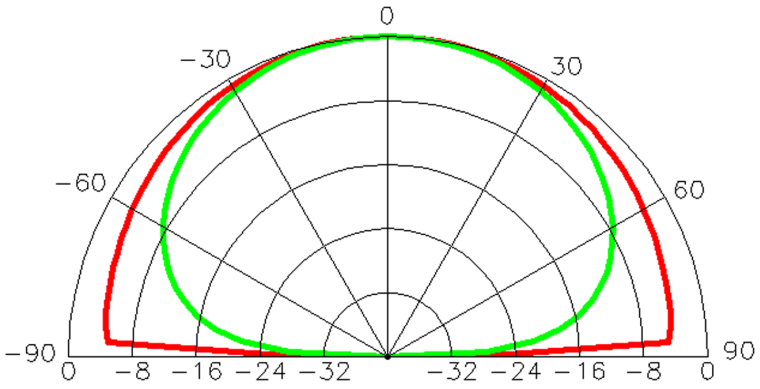

Figure 103: The patch antenna pattern simulation. The red plot is for E-co and the green plot is for H-co. The directivity is 6.94 dB.

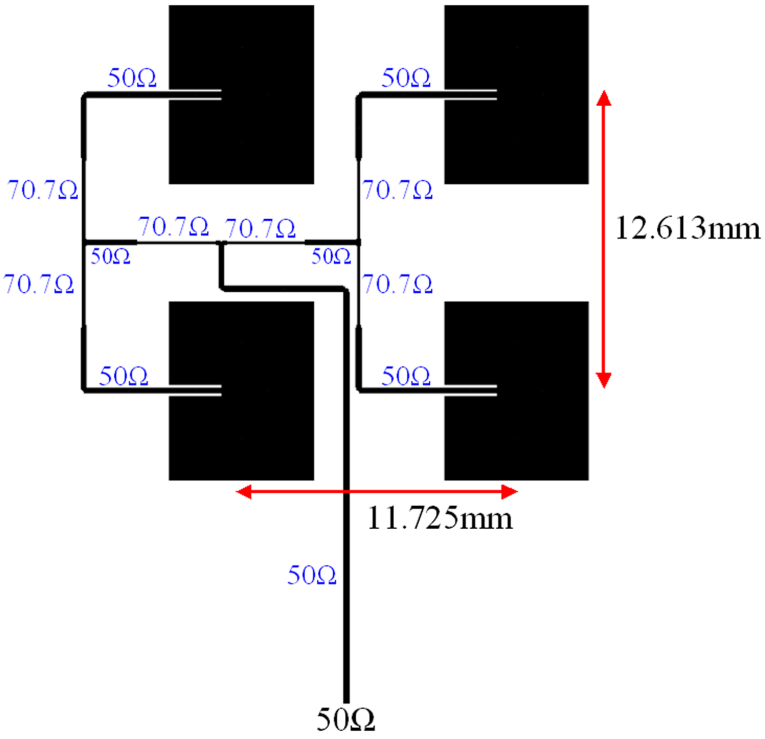

Figure 104: The 2x2 patch antenna array with a 50Ω input impedance. The distances between the patches are labeled. The feed network impedances are labeled in blue.

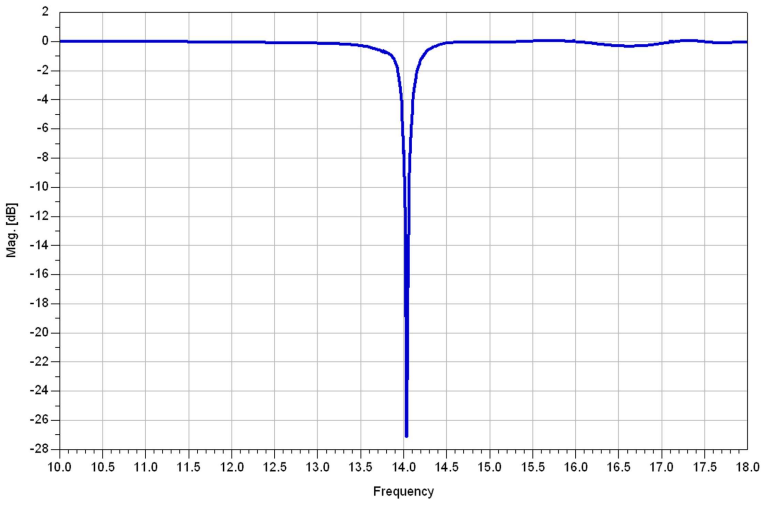

Figure 105: The 2x2 antenna array S11 simulation

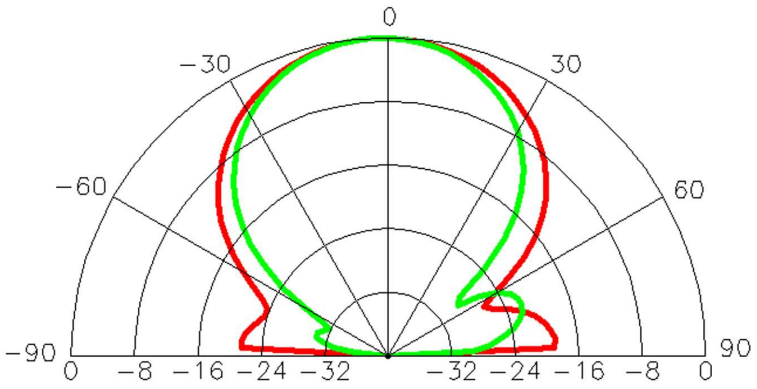

Figure 106: The 2x2 antenna array pattern simulation. The red plot is for E-co and the green plot is for H-co. The directivity is 12.49 dB.

14.3 Phase Shifter Design

There is a correlation between phase shift, degree of beam steering, and the side lobe level. As the phase shift is increased, the amount of beam steering increases but the side lobe level also increases. There are algorithms for decreasing the side lobe level by using amplitude modification, but that is outside the scope of this research. It was decided that a phase shift of 30^o would be implemented since this will result in several degrees of beam steering with minimal side lobe level increase.

The wavelength of a microstrip line on 100μm thick LCP at 14GHz is approximately 13.9mm. In order to get the desired phase shift, a length difference of $30^o/360^o$ or $1/12^{th}$ of a wavelength (1.16mm) was needed. The design was optimized using Momentum and the final layout is shown in Figure 107. The simulated phase shifter performance is shown in Figure 108.

14.4 Phased Array Design

The phase shifter shown in Figure 107 was integrated into the 2x2 antenna array shown in Figure 104. Since everything was designed for 50Ω, integration was straight forward. The resulting phased array is shown in Figure 109.

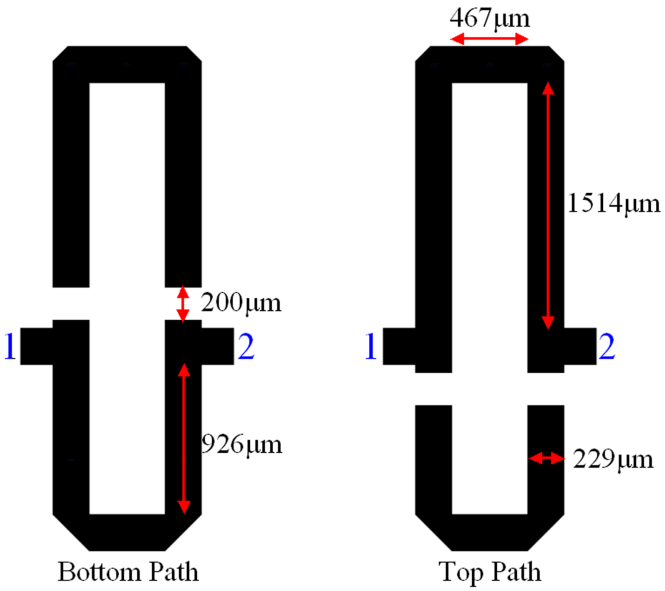

Figure 107: Layout of phase shifter with all dimensions labeled. Port 1 and 2 are labeled in blue.

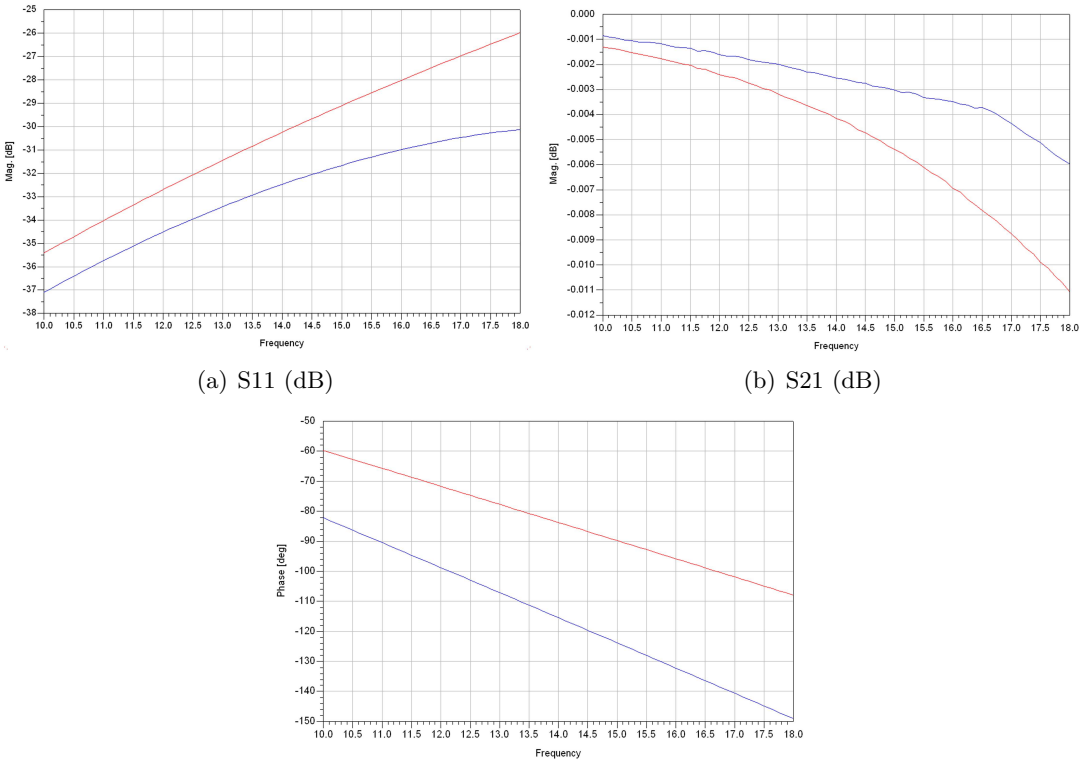

(a) S11 (dB)

(b) S21 (dB)

(c) S21 phase (degrees)

Figure 108: Simulated phase shifter performance. The red plot is for the bottom path (Figure 107 left) and the blue plot is for the top path (Figure 107 right).

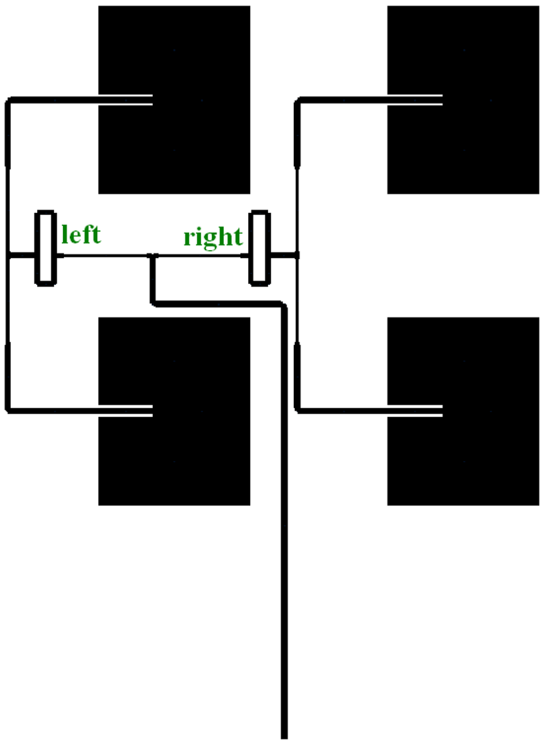

Figure 109: The 2x2 antenna array with phase shifters.

To implement the beam steering, the phase shifters can be set to one of three states:

1. Both phases can be the same (either 0^o or 30^o) – Beam is not steered
2. The left phase shifter is 0^o and the right phase shifter is 30^o – Beam is steered left (-θ direction)
3. The left phase shifter is 30^o and the right phase shifter is 0^o – Beam is steered right (+θ direction)

14.4.1 Simulation Results

The simulated S11 results for these three states are shown in Figure 110. The simulated radiation patterns are shown in Figures 111, 112, and 113.

The degree of beam steering is detailed in Figure 114.

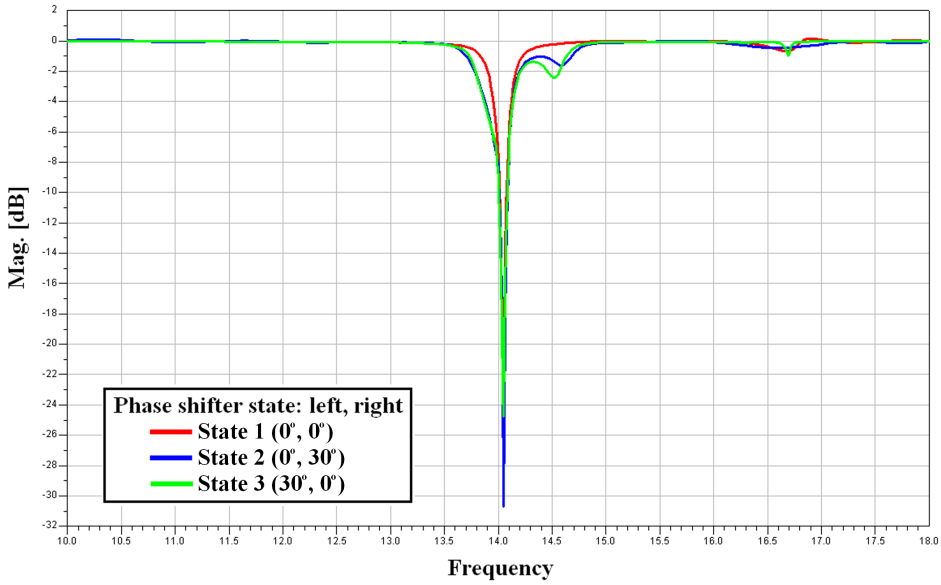

Figure 110: The 2x2 antenna array with phase shifter S11 simulations. State 1 is shown in red, State 2 is shown in blue, and State 3 is shown in green.

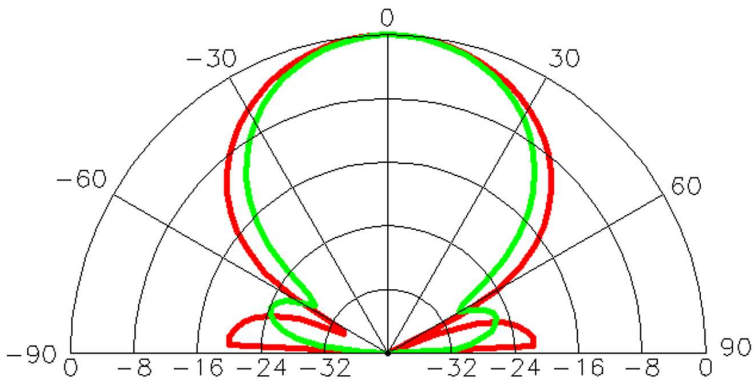

Figure 111: The 2x2 antenna array with phase shifter (State 1) pattern simulation. The red plot is for E-co and the green plot is for H-co. The directivity is 12.58 dB and the angle of maximum radiation is $\theta = 0.00^o$.

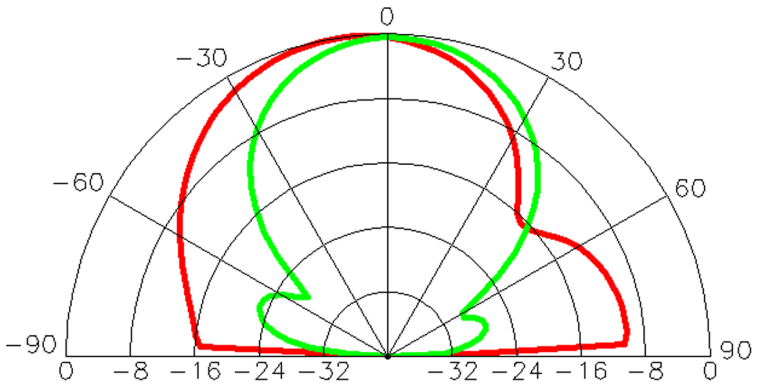

Figure 112: The 2x2 antenna array with phase shifter (State 2) pattern simulation. The red plot is for E-co and the green plot is for H-co. The directivity is 12.22 dB and the angle of maximum radiation is θ= -9.00^o.

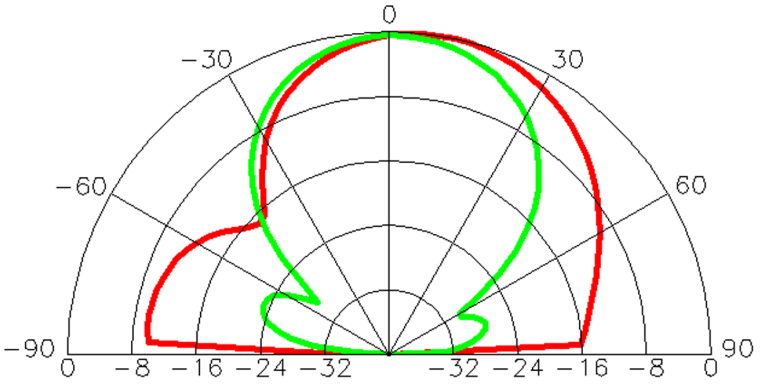

Figure 113: The 2x2 antenna array with phase shifter (State 3) pattern simulation. The red plot is for E-co and the green plot is for H-co. The directivity is 12.18 dB and the angle of maximum radiation is θ= 6.00^o.

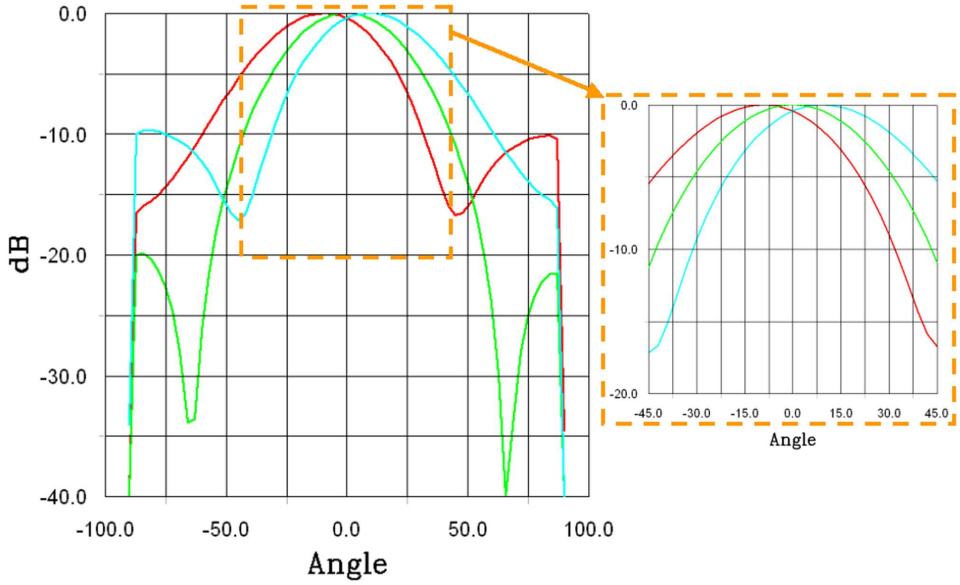

Figure 114: The radiation patterns from Figures 111 to 113 are superimposed and the degree of beam steering is shown. The beam can steer left by 9^o and right by 6^o.

14.5 MMIC Design

To provide amplification of the RF signal, the Raytheon LN167-00 30 dB low-noise amplifier (LNA) was used. Since this LNA was designed to work at 50Ω, no additional matching networks were needed. To prevent oscillation, a 100pF and a 10,000pF off-chip capacitor were added between the DC bias and ground pads. The chip can be driven with up to 2.5V and 66mA of DC current.

CHAPTER XV

COMMUNICATION MODULE INTEGRATION

The communication module was created in two configurations: a single-layer implementation and a multi-layer implementation. The two configurations are pictured in Figure 115.

The single layer implementation offers design and fabrication simplicity. However, as functionality is added, the size of the module will increase. The multi-layer implementation is more challenging to design and fabricate, but the overall size can be kept small. More functionality can be added by increasing the height and keeping the footprint size constant. This configuration has the disadvantage of being higher loss (since there are vias or aperture coupling) and less flexible (since it is thicker). The procedure that was used to assemble these modules is described in this chapter.

15.1 Single-layer Implementation

The layout of the single-layer implementation is shown in Figure 116. The module operates by receiving an RF signal at 14GHz. The signal is amplified by an LNA and then fed to a pair of one-bit MEMS phase shifters. If the phase shifters are in-phase, the antenna array radiates perpendicular to the substrate. If the phase shifters are out of phase, the radiation

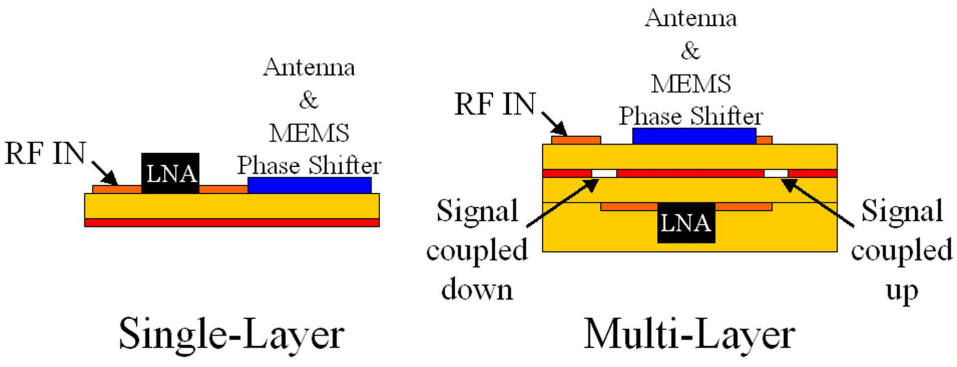

Figure 115: Side view comparison of single and multi-layer implementations of the communications module. The multi-layer implementation uses the same components as the single-layer implementation but it is smaller in size.

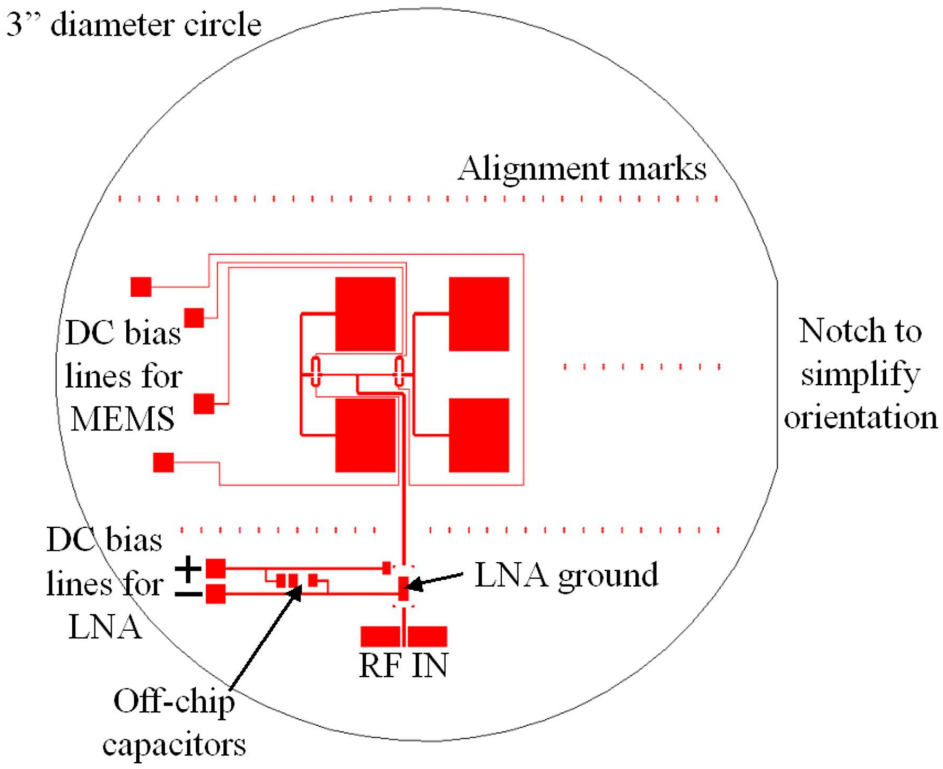

Figure 116: Layout of single layer communication module. The 2x2 patch antenna array, MEMS phase shifters, bias lines, and LNA pads are shown.

is steered left or right depending on which phased path is longer.

The module is fabricated on a 3 inch diameter circle that is precisely cut using a CO_2 laser. A notch is etched on one side which helps keeps the device aligned during fabrication. The circular shape was chosen because it tends to have less issues with surface wave edge effects. The size was chosen because it is the largest size sample that can be processed with either the MJB-3 or MA-6 mask aligners.

Three rows of alignment marks were placed to facilitate the alignment between layers. All of the antennas and MEMS bridges were plated with 1.5μm thick gold. The DC bias lines for the RF MEMS switches were evaporated with the first seed layer and were not plated. With a width of 15μm and a thickness of 2000$\mathring{A}$, these lines have an impedance of over 380Ω. This high impedance will reduce the amount of RF energy that propagates down the DC path.

Since performing optical lithography with the LNA on-wafer is not possible, it was

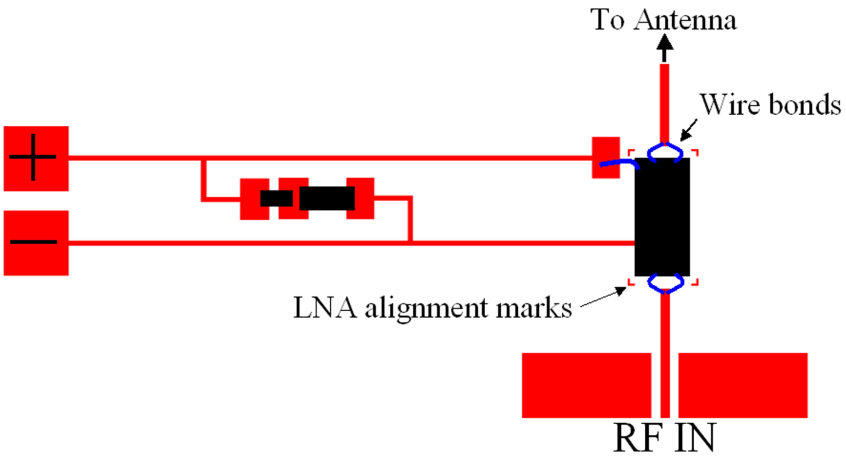

Figure 117: The LNA was integrated by centering it between the corner alignment marks. Five wire bonds (shown in blue) were added to connect the LNA to the DC bias and to the RF signal lines.

decided that the LNA would be integrated after the MEMS switches were released. The LNA ground and bias pads were added at the same time as the MEMS to prevent any additional process steps. Once the MEMS were released, the LNA and off-chip capacitors were mounted onto the module using silver epoxy. Alignment marks were added to help place the chip squarely between the signal lines. The epoxy was cured for 2 hours at 100^{o}C to harden the connection and increase the conductivity of the epoxy. It was shown in Chapter 10 that this temperature has a negligible effect on the MEMS switches. Finally, wire bonds were added to connect the LNA to the DC bias and RF signal lines. The placement of the wire bonds is shown in Figure 117. The fabricated communication module is shown in Figure 118.

15.2 Multi-layer Implementation

Implementing the multilayer configuration is much more challenging than the single layer configuration because this approach requires multi-substrate alignment, device packaging, substrate bonding, fabrication on two sides of a substrate, and some method for transmitting the data across layers.

The final layout for the multilayer module is shown in Figure 119. The module operates by receiving an RF signal at 14GHz. The signal is transmitted to a lower level by aperture

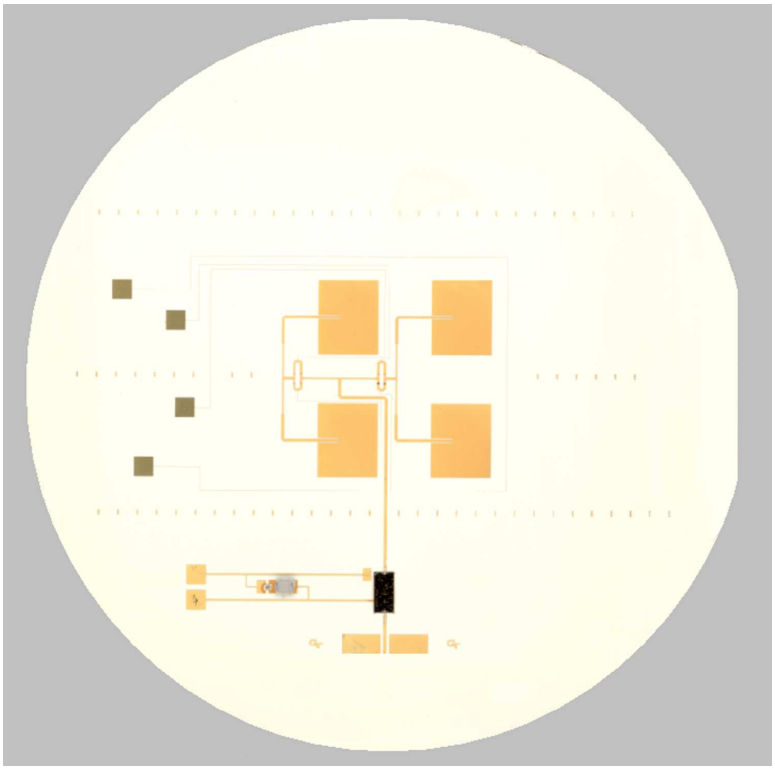

Figure 118: The fabricated single-layer communication module is shown.

coupling. There is an LNA on that layer that amplifies the signal. Another aperture transmits the signal back up to the top layer. Just like with the single-layer module, a pair of one-bit MEMS phase shifters are used to change the phase and steer the beam.

The substrate material was cut into the same size and shape as the previous implementation. The notch on the side of the wafer was particularly useful in this design because it is easy to get the samples turned around when fabricating on the top and bottom side of a substrate. To aid in the alignment of the substrate layers, four $1/16^{th}$ inch (1.5875mm) diameter holes were laser cut in the corners of the substrate.

The top substrate (left side of Figure 119) was fabricated in the same way as the single-layer approach without the LNA. The same alignment marks were used to align the MEMS layers. On the backside of the top substrate, the metal layer is etched to provide the window for aperture coupling. This is done by patterning with photoresist and etching using nitric acid (this process is described in Appendix B).

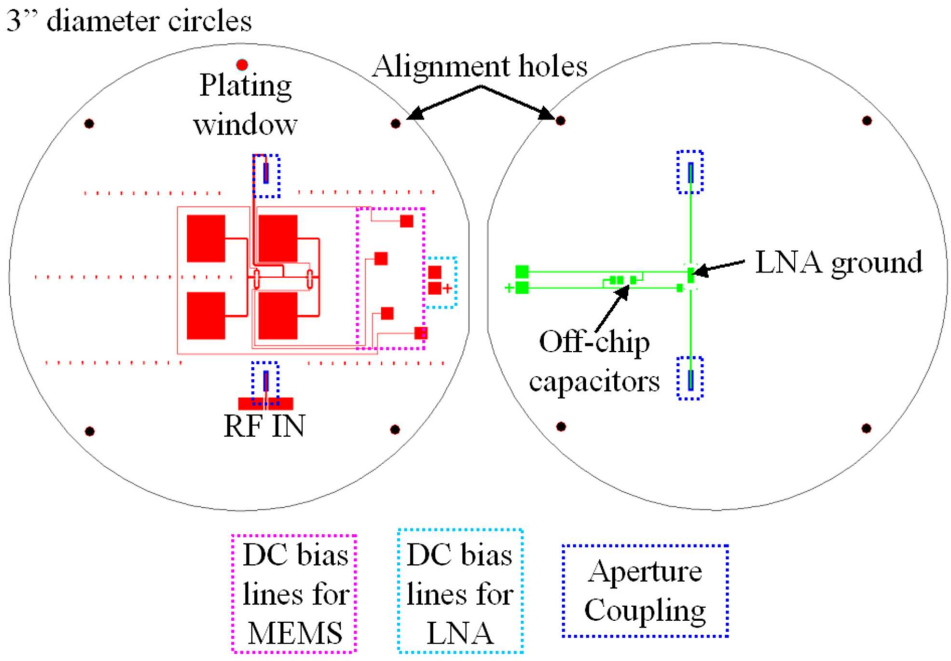

Figure 119: Layout of multi-layer communication module. The 2x2 patch antenna array, MEMS phase shifters, bias lines, and LNA pads are shown.

The bottom substrate (right side of Figure 119) has its features fabricated on the back-side on the substrate (notice the notch is now on the left). Doing it this way improved the aperture coupling by bringing the signal lines as close together as possible.

The final fabrication stack-up is shown in Figure 120. There are four main layers. The top layer has the RF input, MEMS phase shifters, and phased array. The bottom layer has the LNA and off-chip capacitors. The LNA package layer has laser micromachined cavities which protect the LNA, wire bonds, and off-chip capacitors. It also provides a window for accessing the LNA DC bias pads. The LNA cap layer covers the cavities to protect the components inside. The DC bias for the LNA can be brought to the top layer for probing with a bond wire or double-sided conductive tape.

There are two ways that the module could be assembled:

1. The LNA can be attached to the bottom layer, packaged, and then bonded to the top layer before fabricating the MEMS switches.

2. The MEMS can be fabricated on the top layer and the LNA can be packaged separately. Bonding can occur after all layers have been fabricated.

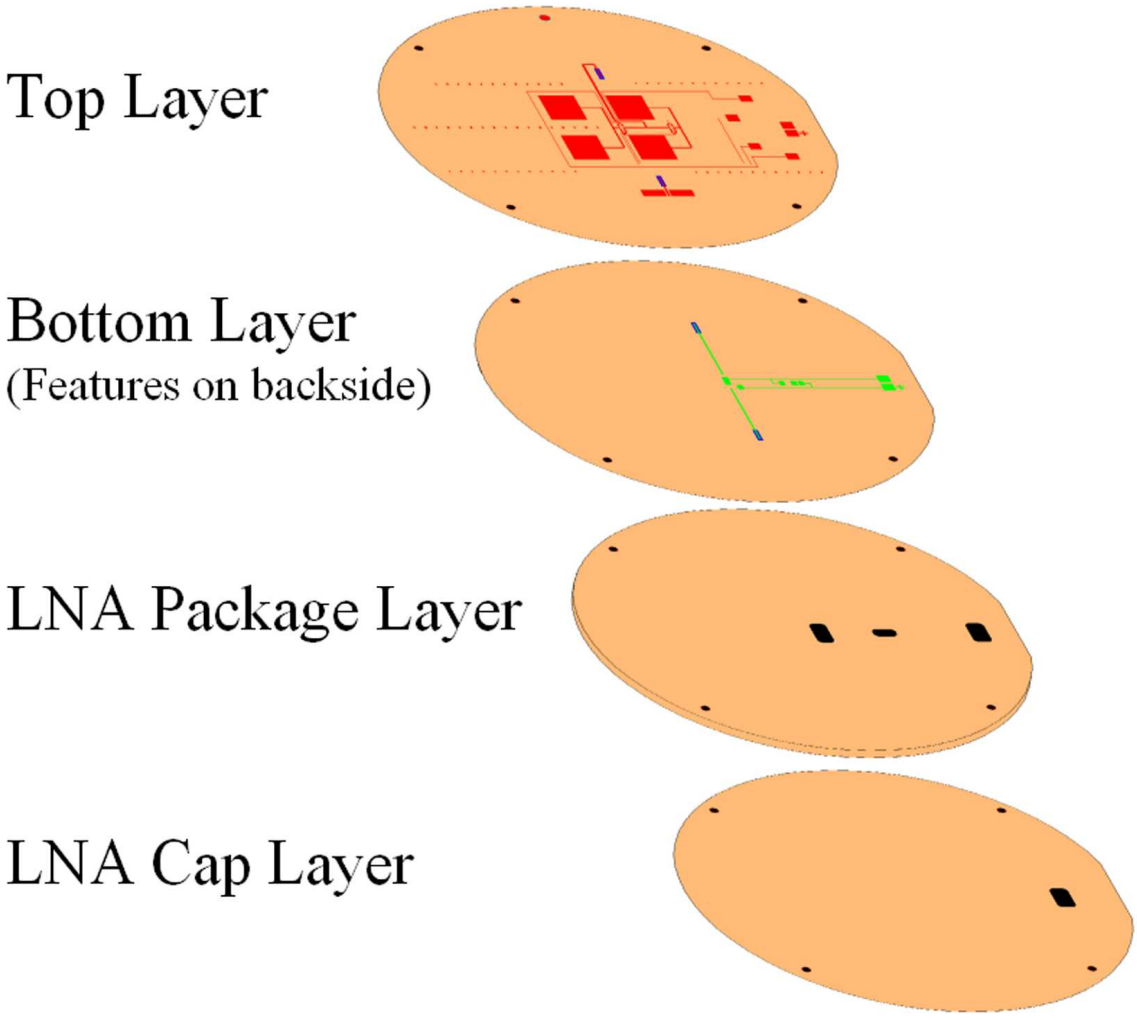

Figure 120: Stack-up of multi-layer communication module. The features shown on the Bottom Layer are actually on the backside. The cavities in the LNA package layer line up to protect the chip, wire bonds, capacitors, and to open a window for DC probing.

Method 1 has the advantage of taking care of the "dirty" processing first. Attaching the LNA with solder or silver epoxy can be messy. Since this process is done by hand, the samples are prone to scratching and other handling defects. As the samples are cured, the material is subjected to toxic outgas and environmental contaminants. By doing this part of the process first, the sample could be cleaned and polished right before MEMS fabrication. This method would probably result in cleaner samples with a better switch yield.

Unfortunately, in order for this method to work, the LNA, bond wires, and capacitors must be packaged inside of the LCP. These components must be properly protected from the acids and solvents used during MEMS fabrication. In Chapter 12, it was presented that LCP does not provide a good barrier against moisture. Therefore, this method can not be used.

Method 2 does require that the layers are bonded after the MEMS are fabricated. This does present the handling issues discussed previously but careful planning can minimize the effect. For this method to work, all of the layers are fabricated independently and bonded together last. Three bonding techniques were discussed in this thesis: thermocompression, localized ring, and epoxy. Unfortunately, none of these methods can be exclusively used to bond the layers. The MEMS switches and LNA can not survive thermocompression bonding (see Chapter 10). Localized ring bonding can not penetrate through the 1.3mm thick LNA package layer (see Chapter 11). Epoxy bonding over 20 layers would be very messy and difficult to control (see Chapter 11). Therefore, a combination of techniques will be used. To bond the thick LNA package layer, thermocompression bonding will be used. The top and bottom layers will be bonded using epoxy bonding since it has been proven to be an easy, low-loss packaging method (see Chapter 13). The LNA cap layer will also be bonded using epoxy.

The fabricated multi-layer communication module is shown in Figure 121.

15.3 Comparison of Technologies

The single and multi-layer implementations both perform the same function (beam steering at 14GHz). However, there are three main differences: size, loss, and degree of expandability.

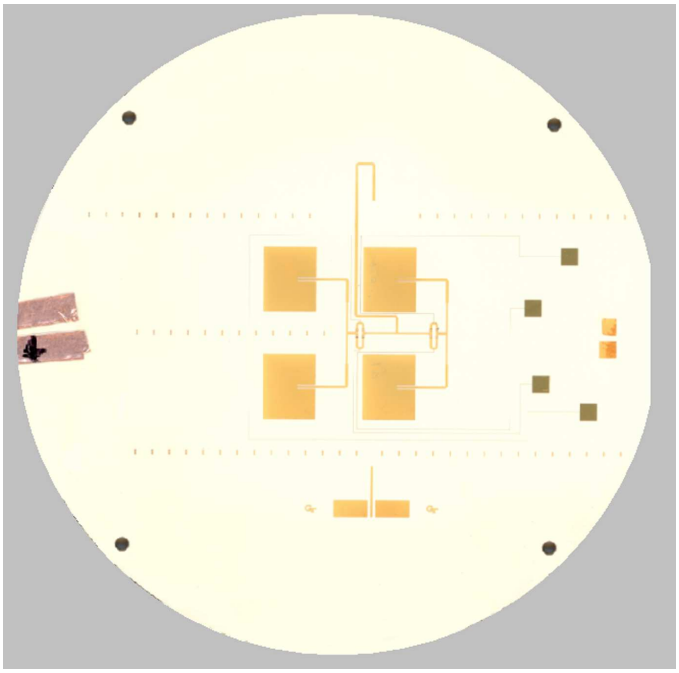

(a) Top view

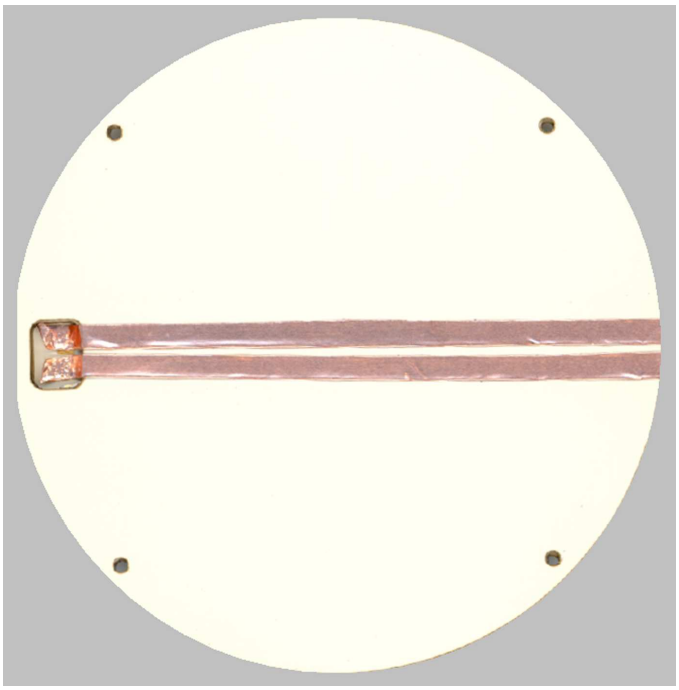

(b) Bottom view

Figure 121: The fabricated multi-layer communication module is shown. In order to probe the LNA from the top of the substrate, double side conductive copper tape was used to extend the DC pad to the top side.

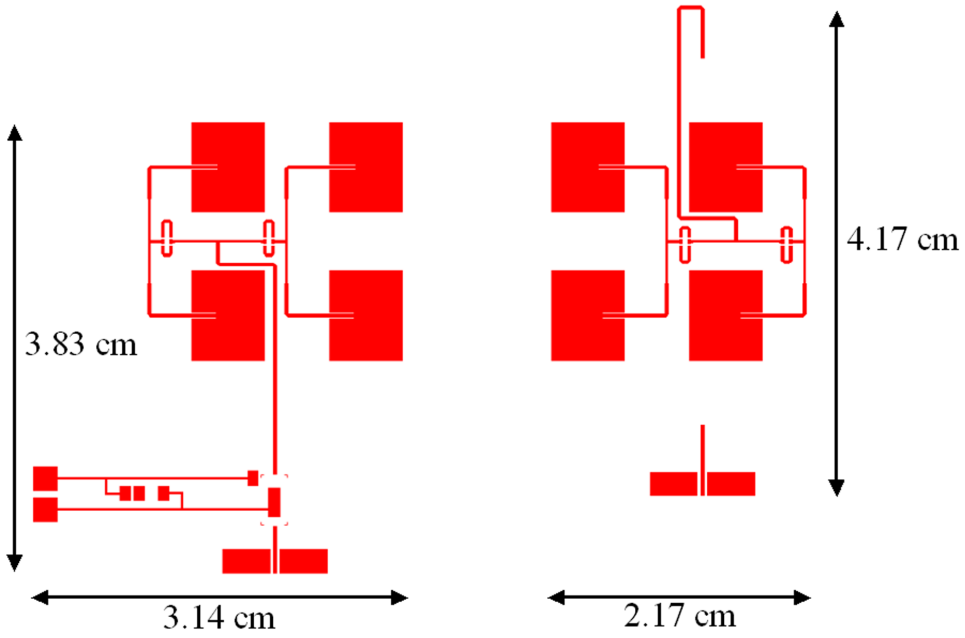

Figure 122: The size of the two implementations is shown to scale. The multi-layer configuration (on the right) is 25% smaller than the single layer configuration (on the left).

15.3.1 Size Comparison

For both implementations, the phase shifters and 2x2 antenna array are identical. The size difference comes from the LNA being on a different layer. The size of the two implementations is compared in Figure 122.

The multi-layer configuration is 25% smaller by moving the LNA to a lower layer. Since these designs were intended to serve as a prototype, the modules were made as small as possible while maintaining proper distance between components to reduce coupling. Each design could certainly be made smaller.

15.3.2 Loss Comparison

The multi-layer configuration is inherently lossier than the single-layer because it has a longer RF signal length and uses aperture coupling. The line loss can be minimized by using thick, highly conductive metal. Fortunately, LCP is a low-loss substrate. The aperture coupling loss can be minimized by properly simulating the device and having good alignment accuracy during fabrication.

15.3.3 Degree of Expandability

Ideally, this research should set the foundation for bigger and better communication modules on LCP. As more components and functionality are added, the size will inherently grow. In the single-layer case, this means a larger area. For the multi-layer case, the area can be kept constant and the height can increase. In this case, adding another few hundred microns of thickness can add another 9 square centimeters of area. Aside from making devices smaller, this will also lower cost since circuit real estate can be expensive.

Another advantage to the multi-layer implementation is that the antenna is shielded from the other components in the system. The metal ground plane below the patch antennas is capable of preventing radiation from the other system components to effect the radiation pattern. This is not the case with the single-layer implementation.

CHAPTER XVI

COMMUNICATION MODULE TESTING

Before pattern measurements were taken, the antenna array (with hard-wire switches), the LNA (by itself), and the communication modules were measured at Georgia Tech. This was to verify that the components and system were operating as expected.

Pattern measurements were taken with the help of Dr. George Ponchak at NASA Glenn in Cleveland, Ohio. The samples were carried by hand on board the flight from Atlanta to Cleveland in an air-tight container surrounded by bubble wrap. All of these measurement results are presented in this chapter.

16.1 Antenna Array Return Loss Measurements

The 2x2 antenna array with hard-wired phase shifters was measured using 800μm pitch GSG RF probes. TRL calibration was performed to remove the cable and connector losses. The measured results are shown in Figure 123.

The resonant frequency and 10 dB return loss bandwidth are given in Table 22. There is good agreement between the simulated and measured data. Having a lower measured bandwidth is not uncommon with these type of antennas [21].

16.2 LNA Measurement Results

The LNA was mounted to an LCP sample using the same setup as with the modules. The measured performance of the Raytheon LN167-00 LNA by itself on LCP is shown in Figure 124. The gain for two different bias currents is shown. A higher bias current results in a higher gain.

16.3 Pattern Measurement Setup

The single and multi-layer communication modules were measured at NASA Glenn using a far field range. A collection of measurement images is shown in Figure 125.

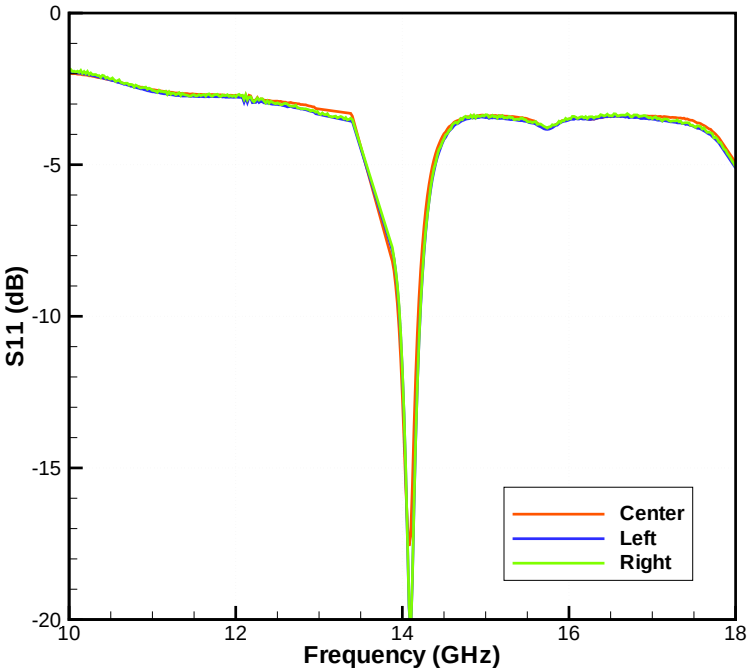

(a) Measured data only

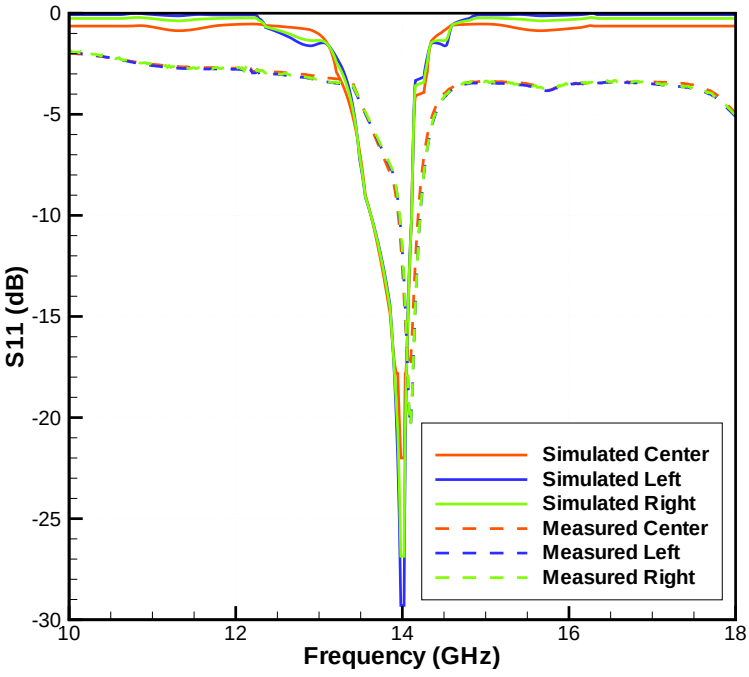

(b) Simulated and measured data

Figure 123: The measured hard-wired antenna array return loss is compared to the simulation results. The results show good agreement.

Table 22: The resonant frequency and 10 dB return loss bandwidth of the simulated and measured antenna array with hard-wire switches

	Resonant Frequency	10 dB Return Loss Bandwidth	Percent Bandwidth
Simulated Left	14.00GHz	487MHz	3.48%
Measured Left	14.10GHz	248MHz	1.76%
Simulated Center	14.00GHz	489MHz	3.49%
Measured Center	14.05GHz	240MHz	1.71%
Simulated Right	14.00GHz	488MHz	3.49%
Measured Right	14.10GHz	245MHz	1.74%

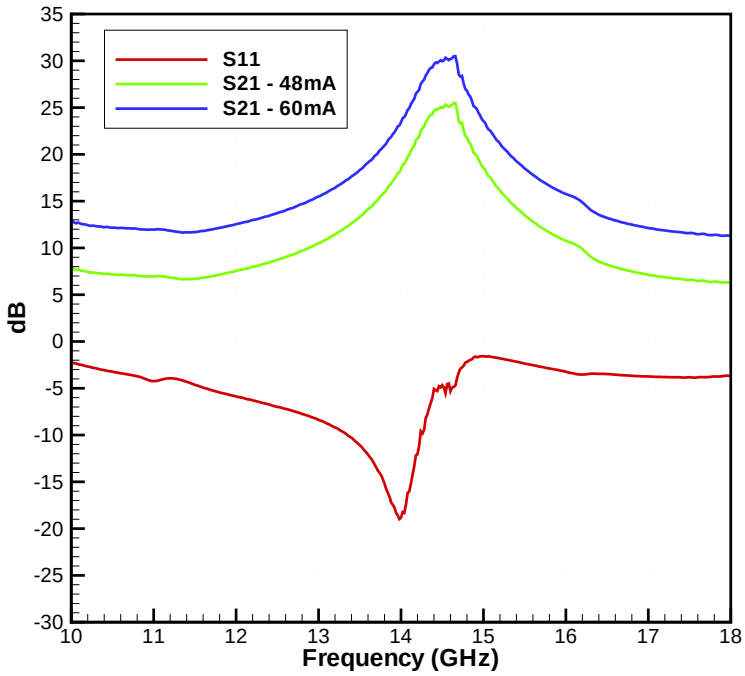

Figure 124: The measured performance of the Raytheon LNA mounted to an LCP sample is shown. The gain increases with the bias current. The S11 does not change with different loads on the output port. These measurements include the loss from the wire bonds

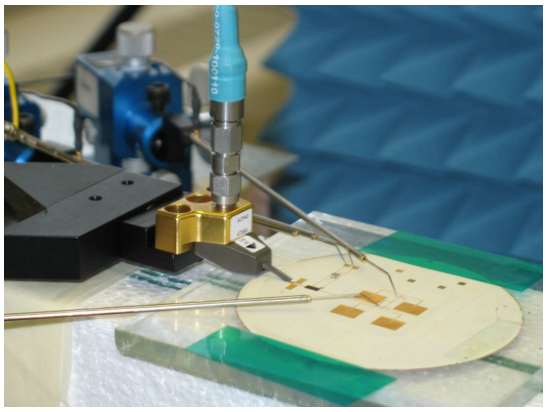

(a) The sample is shown with 4 DC probes and the RF probe

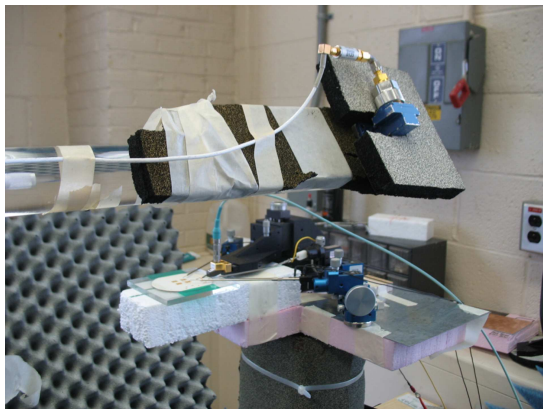

(b) The receiving antenna that rotates 180^o around the sample is shown.

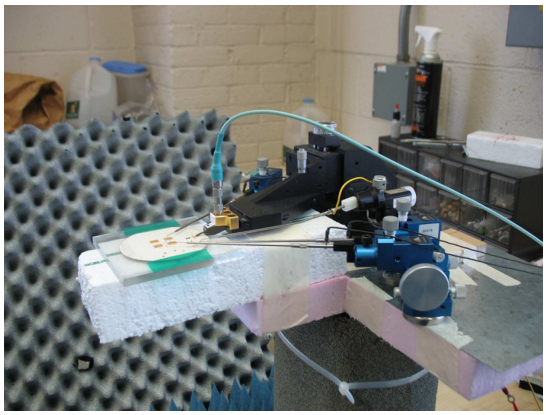

(c) The left side of the setup is shown. The probe positioners and metal plates are sources of scattered radiation.

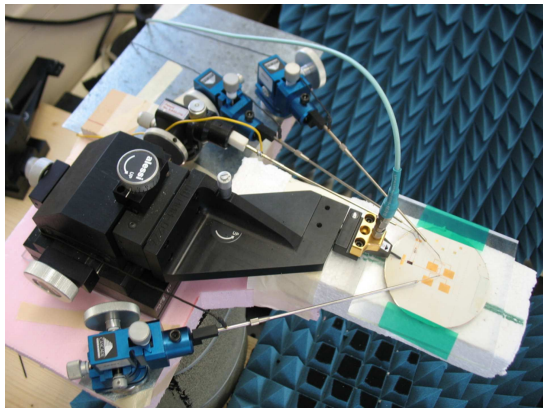

(d) The setup is shown from above.

Figure 125: The radiation pattern measurement setup is shown.

Two DC probe positioners were used to apply the 2V bias voltage and ground to the LNA. Two additional DC probe positioners were used to apply the actuation voltage to each phased path (the switches were grounded by a floating ground). It was intended that the bias voltages would be applied to the bias pads, but unfortunately micro cracks in the thin, narrow lines prevented this. Instead, the bias was applied directly to the phase shifters. This caused some noise and a small dimple to appear in the pattern. The same 800μm pitch GSG RF probe was used to feed the antenna. An HP sweep oscillator was used to provide the 14.05GHz signal. A crystal detector was used to convert the received power into a measurable voltage. Multiplying this value by 10 log gave the pattern in decibel units.

16.4 Single-Layer Module Measurements

Since the single-layer module is very thin, it was mounted to a glass slide using spray epoxy before measuring. Otherwise, it was very difficult to probe the material without puncturing it. The glass slide was under the metal ground plane so it should have had a negligible effect on the pattern. This was shown in Figure 125(a).

16.4.1 Return Loss Measurements

This LNA was designed to operate equally well regardless of the load on the output port [55]. Therefore, the performance of the antenna is not a factor when measuring the return loss of the module. The return loss is shown in Figure 126, which is nearly identical to that of the return loss shown in Figure 124.

16.4.2 Radiation Pattern Measurements

The measured E-plane co-pol and cross-pol results are shown in Figure 127. The cross-pol level is more than 10 dB less than the co-pol level over most of the half-space. It was expected that the cross-pol level would be higher than desired due to the measurement setup. From the images in Figure 125, many sources of scattering can be found. Some of the largest contributors to the high cross-pol are the DC probes, the probe positioners, and the large steel plate that everything is mounted to.

The raw data was normalized and smoothed using a MATLAB 3rd order moving average

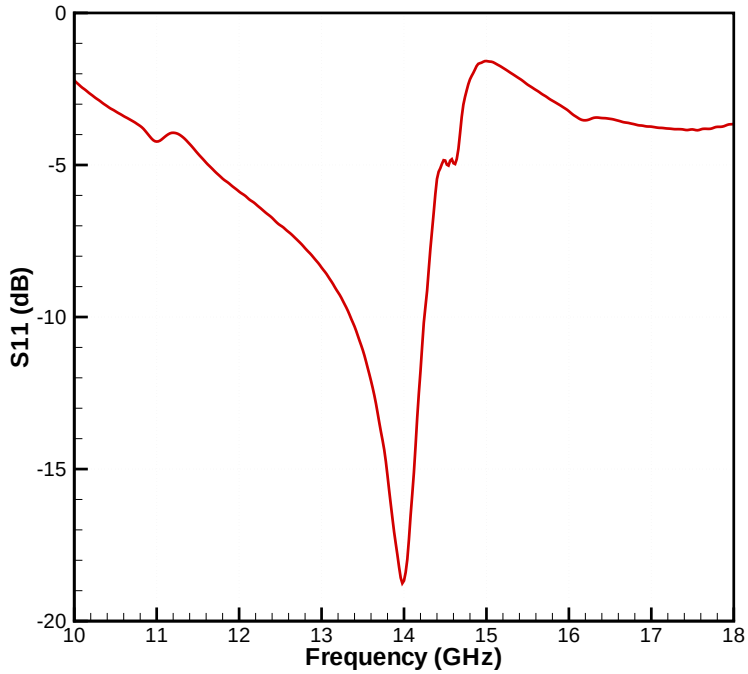

Figure 126: The measured return loss for the single-layer module. It is nearly identical to the response measured by the LNA alone (Figure 124).

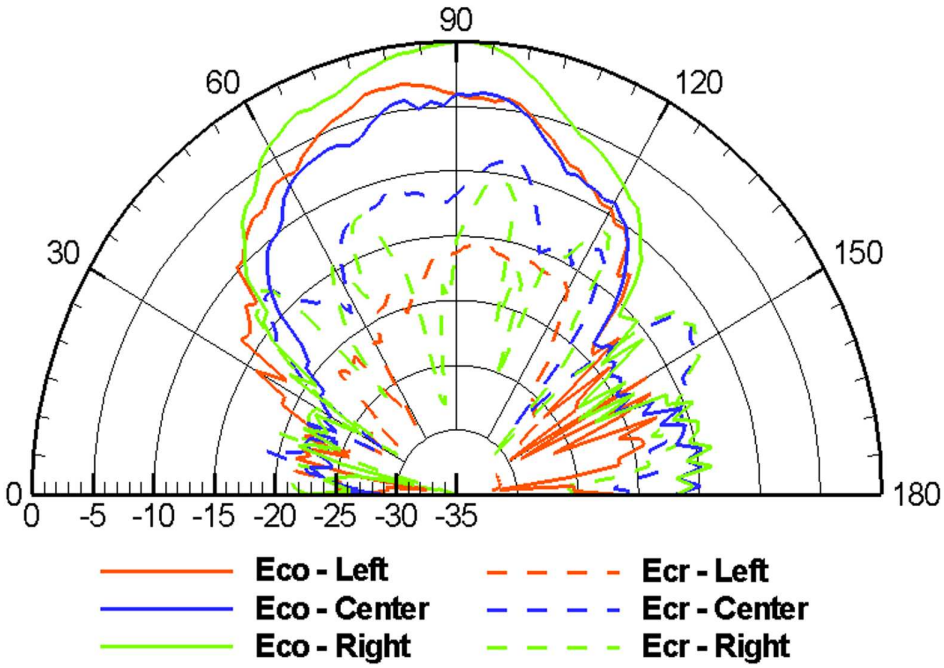

Figure 127: The measured E-plane co-pol and cross-pol are compared for the single-layer module.

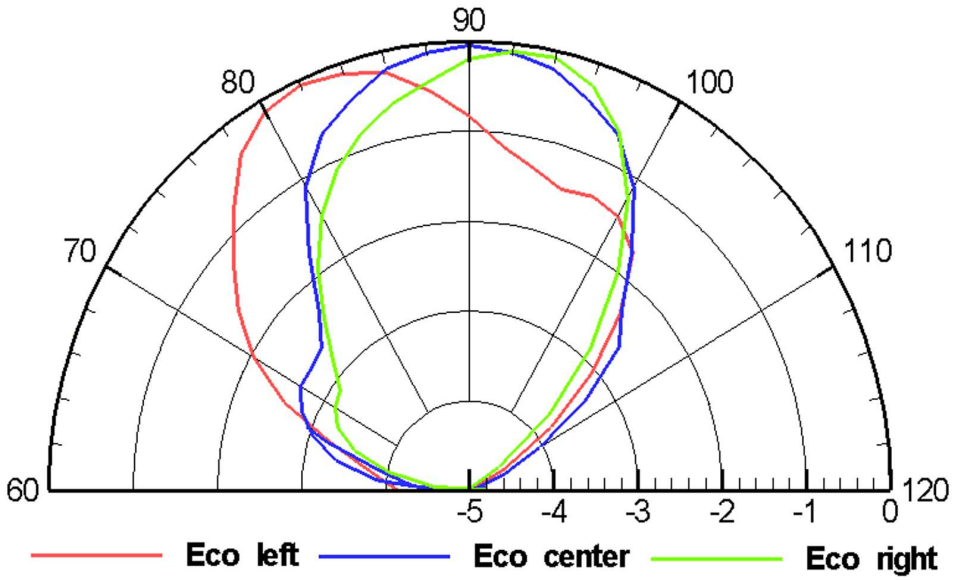

Figure 128: The degree of beam steering for the single-layer module is emphasized. The beam can be steered left by 8^o and right by 4^o. The beam is centered perpendicular to the antenna.

Table 23: Comparison of the simulated and measured -10 dB pattern beam width. There is good agreement between the results.

Sim. Left	Meas. Left	Sim. Center	Meas. Center	Sim. Right	Meas. Right
89^o	90^o	86^o	86^o	91^o	81^o

filter to remove some of the noise in the pattern. These results are shown in Figure 128. The beam is able to sweep from -8^o to +4^o. These results agree well with the simulated results which predicted a sweep from -9^o to +6^o. The shape of the beam matches well with the one shown in Figures 111, 112, and 113. A comparison of the -10 dB pattern beam width is made in Table 23.

Due to time constraints and MEMS fatigue, H-plane measurements were not taken.

16.5 Multi-Layer Module Measurements

Unlike the single-layer module, the multi-layer device is rigid and does not need to be mounted. The module was measured in the same fashion as the single-layer device.

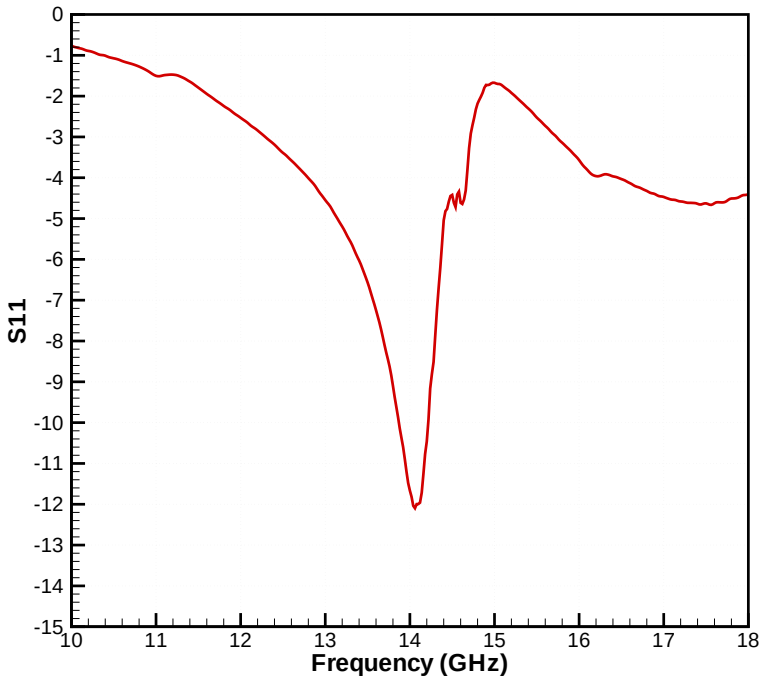

Figure 129: The measured return loss for the multi-layer module. It is similar to the response measured by the LNA alone (Figure 124) but it's lossier. This loss is from the first aperture.

16.5.1 Return Loss Measurements

Unlike the single-layer module, this implementation will not have a return loss identical to the LNA. Since the LNA is after the first coupled aperture, the return loss will be different. The measured return loss is shown in Figure 129.

The additional loss is due to the first aperture. With a return loss of 12 dB, 6.3% of the power is reflected back into the source.

16.5.2 Radiation Pattern Measurements

The measured E-plane co-pol results are shown in Figure 130(a). The raw data was normalized and smoothed using a MATLAB 5th order moving average filter to remove most of the noise in the pattern. These results are shown in Figure 130(b).

Figure 131 emphasizes the beam steering shown in Figure 130(b). The beam is able to sweep from -4^o to +8^o. The beam is centered slightly off center. This is likely due to the MATLAB filtering.

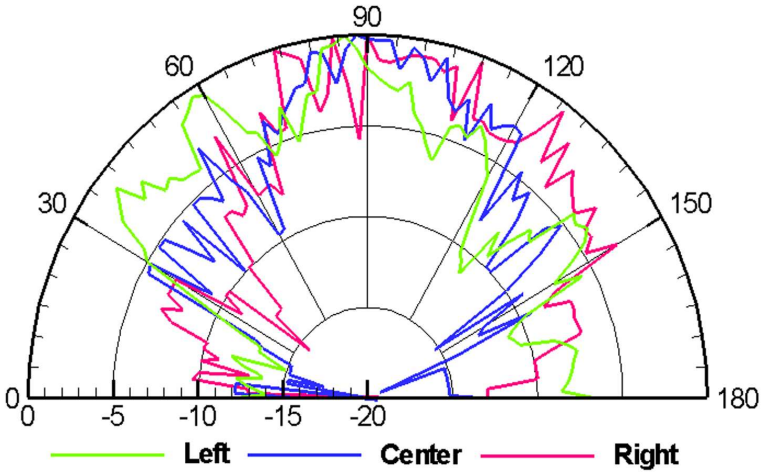

(a) Raw data

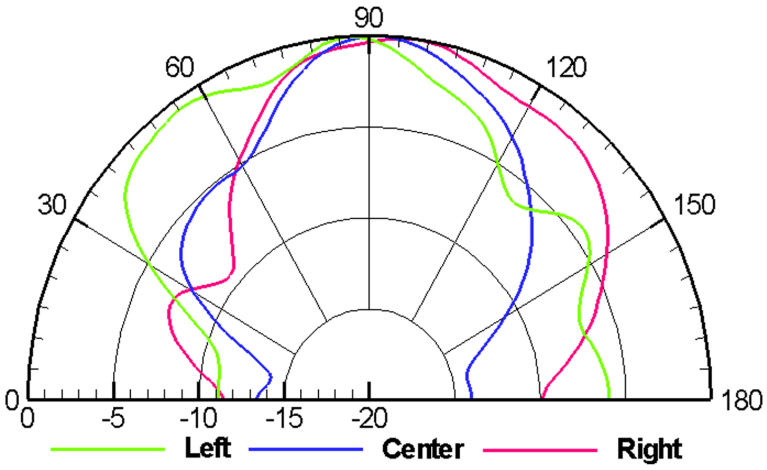

(b) Filtered data

Figure 130: The measured E-plane co-pol for the multi-layer module. The filtered data was calculated using a 5th order moving average filter in MATLAB.

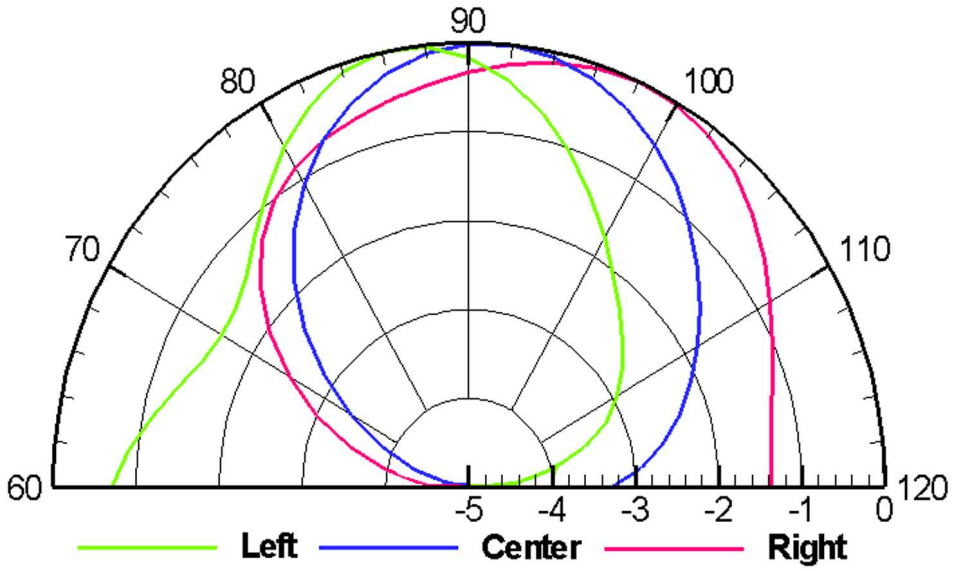

Figure 131: The degree of beam steering is emphasized for the multi-layer module. The beam can be steered left by 4^o and right by 8^o.

It is expected that this module should have more loss than the single-layer implementation. Therefore, less energy is fed to the antenna which explains the noisy pattern. This is explained further in the next section.

Due to time constraints and MEMS fatigue, the E-cross and H-plane measurements were not taken.

16.6 Measured Gain

The directivity of an antenna is not related to the level of input power. In addition, the efficiency of an antenna is not related to the level of input power. Therefore, since the gain of an antenna is equal to the product of the directivity and the efficiency, the gain is not related to the input power. It almost seems counter intuitive, but adding an LNA to an antenna does not change the gain of the antenna. Instead, it increases the power radiated so that a lower input power can be used or the antenna can transmit further.

The gain was measured using a comparative method. The raw pattern data was compared to the measured data for a 10 dB gain horn antenna. The difference was added to 10 dB to calculate the gain of the module. The power level was adjusted so that the gain horn received the same amount of input power as the 2x2 antenna array.

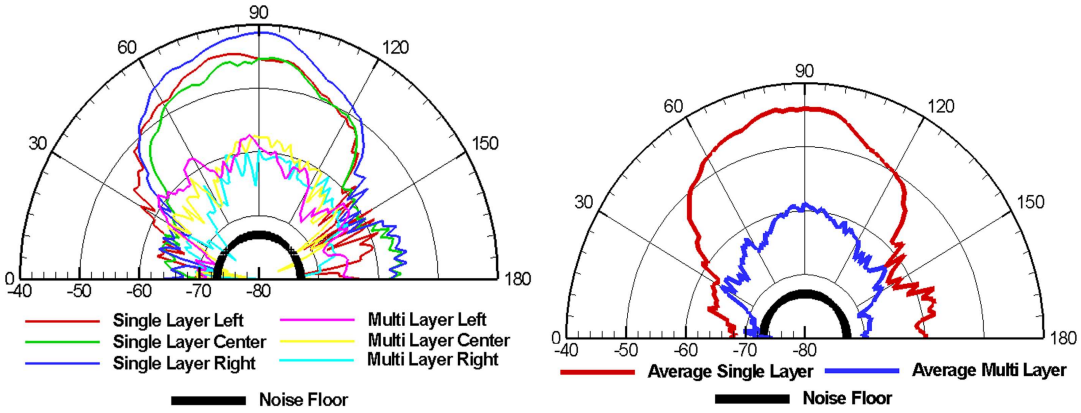

(a) Raw single and multi-layer module radiation pattern data

(b) Average single and multi-layer module radiation pattern data

Figure 132: The radiation pattern data before normalization (raw). The noise floor for this measurement setup is approximately -73dB.

All of the radiation pattern plots presented have been normalized in order to properly compare the different states. The measured raw data is shown in Figure 132(a). The left, center, and right configuration data is averaged for each device and is shown in Figure 132(b).

According to Dr. George Ponchak, who provided the measurement setup, it is typical to measure radiation pattern data in the -40 dB range when the input power to a typical planar antenna is +6 dBm. Since these antennas were fed with -15 dBm (recommended by the designers [55]) and the measured pattern data was in the -44 dB range, it can be concluded that the LNA was amplifying the signal as expected.

The procedure for calculating the gain is shown in Table 24. The calculated and simulated values both agree that the gain is approximately 7.75 dB. The simulated value matches closely to the measured value because the substrate, metal, and switch losses were included in the simulation.

16.7 Single-layer Module Loss Analysis

ADS Momentum simulations show that if the substrate and metal were lossless, the gain would be equal to the directivity. This makes sense since the efficiency would be 100% and the gain is equal to the product of the efficiency and the directivity. The simulated

Table 24: Gain calculation for the single-layer module. Values are taken in the direction of maximum radiation. The simulated and measured values agree very well.

Antenna Parameter	Value
Measured power for single-layer module	-43.97 dB
Measured power for gain horn	-41.72 dB
Difference in measured power	2.25 dB
Measured gain	10 - 2.25 = 7.75 dB
Simulated gain without MEMS	8.30 dB
Simulator discrepancy	0.55 dB (7%)
Simulated gain with MEMS	7.5 dB
Simulator discrepancy	0.25 dB (3.2%)

directivity for this module is 12.63 dB, which is expected for a four element array. Since the measured gain was 7.75 dB, this calculates to an estimated 4.88 dB of loss for the module. Most of the loss comes from substrate and metal losses. This was demonstrated in the previous section since the simulated (with substrate and metal losses) and measured gains were nearly identical.

The measured loss of a transmission line on 100μm thick LCP is 0.375 dB/cm. The total feed network length is 10.04cm. This gives a line loss of 3.77 dB. Of that, 0.34 dB is from the phase shifters. There is an additional 0.20 dB of loss from each MEMS switch. Since there are four switches activated at any given time, that equates to 0.80 dB of added loss. In total, the are 4.57 dB of loss from the MEMS and line length. There is 0.31 dB of additional loss that is unaccountable. This is a minimal margin of error.

If it can be assumed that the simulated directivity is close to the actual directivity then it is possible to estimate the efficiency of the module. Since the simulated gain agrees well with the measured gain, this assumption is reasonable. The measured gain (7.75 dB) divided by the simulated directivity (12.63 dB) results in an estimated efficiency of 61.3%. This is less than desired since similar papers without switches report efficiencies of 77-80% [21]. Removing the loss from the MEMS, the efficiency would be approximately 70.2%. The efficiency could be improved by redesigning the feed network to reduce the line length.

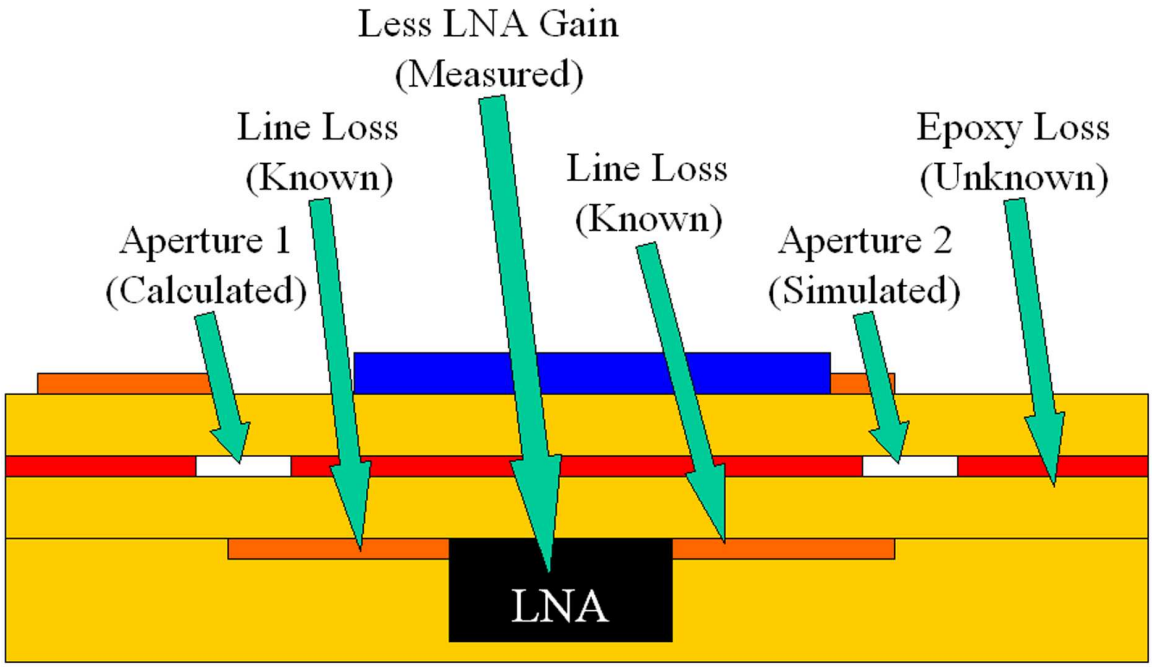

Figure 133: The sources of additional loss in the multilayer module are identified

16.8 Multi-layer Module Loss Analysis

It was shown in Figure 132 that the multi-layer configuration is 14 dB above the noise floor and the single-layer configuration is 30 dB above the noise floor in the direction of maximum radiation. Since the multi-layer measurements are near the noise floor, the patterns are not as clean as the single-layer case. The receiving waveguide is picking up a considerable amount of scattering and noise.

It is important to determine where this additional 16 dB of loss is coming from. If there is 16 dB less power radiated in the multi-layer module, then there must be 16 dB less power being fed to the antenna. Since the MEMS, phase shifters, and antenna array are identical for the two module configurations, the loss must be occurring outside of the array. Sources of the additional loss are shown in Figure 133 and are investigated below.

16.8.1 Aperture 1 Loss

The loss due to aperture 1 can be calculated precisely by comparing the return loss measurements from the single and multi-layer modules. The only difference between the modules from a return loss point of view is the first aperture. To make the comparison, a model

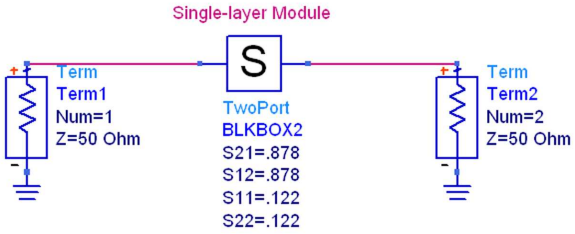

Figure 134: The ADS schematic model for the single-layer module return loss.

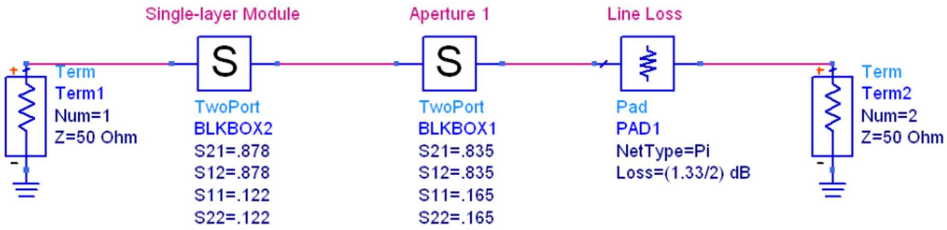

Figure 135: The ADS schematic model used to calculate the loss from the first aperture.

is made that represents the measured return loss of the single-layer module (Figure 126). This is shown in Figure 134.

A second simulation is run that represents the additional loss in the multi-layer module. The setup is shown in Figure 135. The model from Figure 134 is cascaded with the first aperture model and a signal line loss model. The model for the first aperture is varied until the simulated response matches the measured response from Figure 129. It was found that 16.5% of the power was reflected from aperture 1.

16.8.2 Additional Line Loss

The multi-layer module has 3.5398cm of additional line length than the single-layer module (half before and half after the LNA). As stated before, the line loss is 0.375 dB/cm. This equates to 1.327 dB of additional line loss.

16.8.3 Actual LNA Amplification

Each LNA tested ran at a slightly different current for a given voltage. It was shown in Figure 124 that the gain is proportional to the bias current. The single layer module had a 52mA current which translates to a gain of 19.97 dB. The multi-layer module had a 48mA current which translates to a gain of 18.30 dB. Therefore, the multi-layer device had 1.67 dB

Table 25: The simulated return loss and percent power reflected is shown for aperture 2 as the epoxy gap is increased

Air gap	Simulated Return Loss	Power Reflected
0μm	35.2 dB	0.030%
10μm	22.0 dB	0.630%
25μm	15.6 dB	2.75%
50μm	11.1 dB	7.76%
100μm	2.1 dB	61.7%
150μm	0.5 dB	89.1%

less gain than the single-layer device.

16.8.4 Aperture 2 Loss

Unfortunately, the loss in aperture 2 can not be directly measured as with aperture 1. Instead, the loss will be determined by simulation.

Variations in the substrate thickness can have a profound effect on the impedance mismatch. For the multi-layer module, since the bottom layer is epoxy bonded to the top layer (as shown in Figure 120), an air gap is formed in the aperture. Applying an even coating of spray epoxy everywhere is nearly impossible to within the tolerance that is needed. The simulated return loss and percent power reflected for a range of gap values is shown in Table 25.

The epoxy gap was measured to a thickness between 100-120μm with a micrometer. This results in approximately 32.8% power transmitted. This does not include the loss from the epoxy itself.

16.8.5 Epoxy Loss

The only unknown factor from Figure 133 is the loss due to the epoxy. The loss tangent of the epoxy is unknown. If all of the loss components are combined into a simulation, the epoxy loss can be varied until the insertion loss is 16 dB. The setup for this simulation is shown in Figure 136.

When the epoxy loss is 2.248 dB, the S21 is -16 dB. If the loss tangent of the gap in

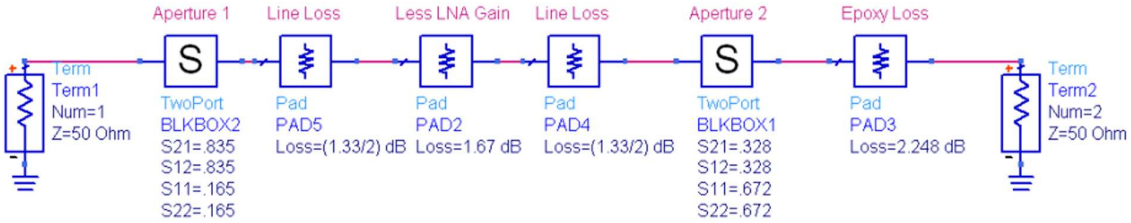

Figure 136: The simulated loss in the multi-layer module. Each loss component is known except for the epoxy loss. This value can be varied until the S21 is -16 dB. The final amount of loss due to the epoxy is 2.248 dB.

the simulation for aperture 2 is varied until the S21 is -2.248 dB, the resulting loss tangent is 0.0996. This value is reasonable since the epoxy is resin based, which has a loss tangent between 0.06-0.16. All of the additional losses in the multi-layer module are accounted for.

16.8.6 Method to Reduce Loss

To eliminate this problem, the bottom layer would need to be thermocompression bonded to the top layer before the MEMS are fabricated. Then, the MEMS could be fabricated and packaged. Packaging the MEMS is essential because in order to attach the LNA to the module, it needs to be flipped over. If the switches are not packaged, they will be crushed. The LNA packaging layer could still be epoxy bonded since the coupling does not propagate in that direction.

16.9 Analysis of Beam Steering

The single-layer module is capable of steering left by 8^o and right by 4^o. The multi-layer module is capable of steering left by 4^o and right by 8^o. The directions "left" and "right" are given with respect to the RF probe feed. Therefore, the multi-layer antenna is fed in the opposite direction as the single layer antenna. This can be seen in Figure 122. The amount of beam steering is the same whether we use a single or multi-layer implementation.

These communication modules are capable of steering a total of 12^o. If the device is used on a satellite in geostationary orbit, this would give a scanning length of over 4,700 miles. This distance could easily cover the continental United States and possibly Hawaii, as shown in Figure 137. A ground based RADAR system scanning the skies for aircraft flying at a

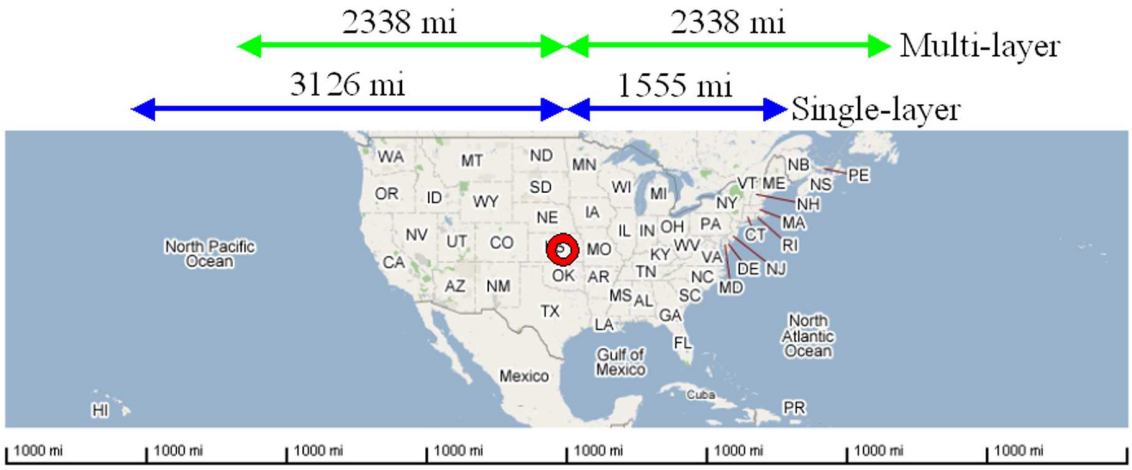

Figure 137: The amount of area that can be scanned from geostationary orbit (22,240 miles above the Earth) with this amount of beam steering is shown [30].

typical 30,000 feet could scan 6,377 feet of sky. This is more than the length of 26 Boeing 777-300 [106]. The Northrop Grumman B-2 Spirit stealth bomber can cruise at an altitude of 50,000 feet. This module could scan 10,628 feet of sky at that height. That is the equivalent length of 154 B-2 bombers [105].

CHAPTER XVII

COMPARISON TO STATE OF THE ART

Many excellent papers have been published by other researchers that suggested the possibility of making fully integrated communication modules on LCP. Work has been done to prove that various antennas, filters, and integration schemes can be implemented on this material [91]. Previous works have thoroughly documented the "potential" that LCP has for packaging RF MEMS devices and integrating them into WLAN systems [83]. Previous works have even gone so far as to publish the concept of integrating an amplifier and antenna on LCP [66]. However, for the first time, the expression "has the potential" can be replaced with "has been implemented". This is a big step towards taking this technology to a consumer market.

Since this research represents the first fully operational communication module on a flexible, organic substrate, it's difficult to compare this technology to any competition directly. Finding rival technologies is further complicated by the fact that few commercially available wireless systems operate at frequencies this high. 14GHz (Ku band) signals are typically only used for satellite communication systems. Typical RF devices at this frequency are made on semiconductor substrates (such as silicon or GaAs) and are not widely available. There are currently no consumer based electronic systems at this frequency. Devices on semiconductor substrates have the benefit of tighter fabrication tolerances, higher power, and are well established technologies. Some advantages for using LCP over semiconductors are:

1. Low-cost material
2. Flexibility
3. Ideal for multilayer systems
4. Great for antennas

5. Easy to package with

Although RF communication modules are not commercially available on LCP specifically, devices are available on similar materials. Parallax, Inc. and Semtech offer low-cost RF modules on PCB (an organic material). However, these devices operate at 433.92MHz (UHF). The overall size is typically 1 x 4 inches [71, 84]. Aerocomm offers a small, easy to use RF module at 2.4GHz. The substrate material is not given, but it is likely PCB as well. The module is 1.65 x 2.65 x 0.2 inches. It has a range of about 0.5 miles [2].

The communication modules developed here were designed at 14GHz for atmospheric precipitation monitoring. Rain attenuation is high at this frequency. However, they could be scaled to operate at any frequency, including X-band (8-12GHz) for RADAR applications.

There are a number of technologies that could come from this research. Three examples of possible future systems are given here.

17.1 Wearable Antenna System

Soldiers on the front line rely on hand-held devices or large portable antennas to communicate with each other and the command center. These devices can be cumbersome to transport easily. Large antennas are also easy to target. Since LCP is flexible, light-weight, and thin-film, it could be sewn directly into the uniform of a soldier. This is shown in Figure 138.

In addition, sensors could be integrated directly onto the material. This could relay important vital signs back to the soldier or to the command center. Everything could be automated and hands-free.

17.2 Portable Radar System

Currently, when a radar system needs to be deployed into a military area, it is flown in and dropped or trucked in. This is a challenging endeavor since this process can be easily detected. Alternatively, soldiers can often covertly sneak their way into a military zone. Bringing a radar system with them is not practical due to the size and weight of a typical system.

Figure 138: A wearable antenna system is shown. The communication device is sewn directly into the soldiers uniform. Potential areas for integration are outlined in pink. The areas in orange denote convenient areas to place sensors to detect vital signs.

However, LCP could change this. An entire system can be made on LCP, rolled-up tightly, stored in canisters, and unrolled when on location. A typical device is shown in Figure 139.

Furthermore, several of these devices could be tiled together on location to make a large radar system. This process can happen quickly and would be much harder to detect.

17.3 Space Deployable Satellites

Deploying a satellite into space is expensive because of the weight of most systems. The size of the satellite is limited by the size of the rocket or shuttle payload. One way of improving on both of these limitations is to make the antenna portion of the satellite out of LCP. Since LCP is light-weight, this will make it cheaper to deploy. Since the antenna can be rolled-up, a smaller rocket can be used or a larger antenna can be used. This process is shown in Figure 140.

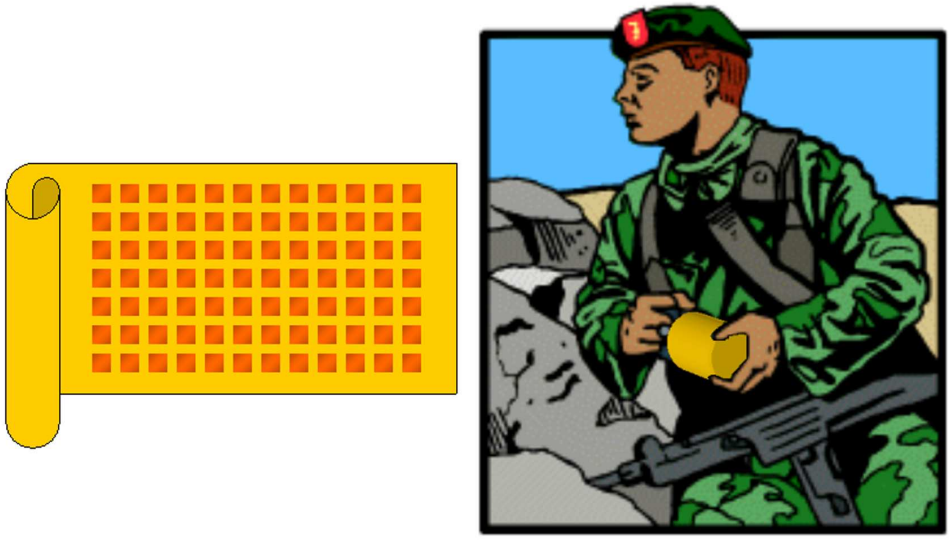

Figure 139: A portable radar system is shown. The system can be rolled up and safely stored when not in use.

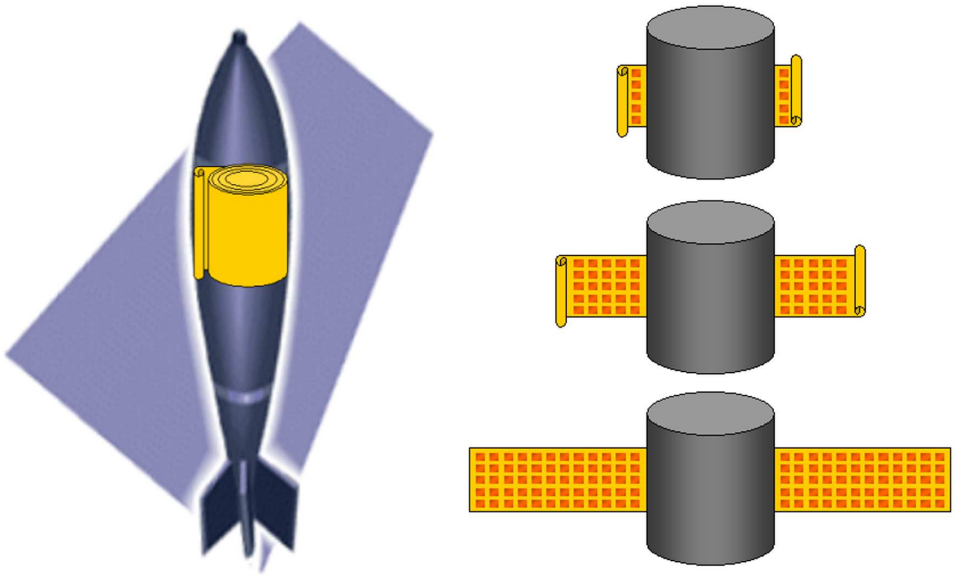

Figure 140: A new way of deploying large satellites in space is shown. For this method, the antenna array can be rolled up and placed inside the payload of a rocket or space shuttle. It can then be unrolled in space.

CHAPTER XVIII

CONCLUSION

For this thesis, we were able to take a material that was relatively unknown in the RF world and do things with it that others had only talked about. The concept of RF MEMS on a thin-film, flexible substrate was completely unheard of. We were able to master this skill and many others in only a few short years.

Early in the research, we were able to develop processes that were truly "out of the box". Recipes for fabricating on silicon were well established but polymers are a different story. A great deal of time was spent understanding the material and its quirks. With this knowledge, we were able to start fabricating microwave devices, such as filters, antennas, phase shifters, and of course, RF MEMS switches on LCP. Many papers were published along the way to document our successes.

Before the technology could go system-level, packaging and robustness had to be tested. This research demonstrated that LCP could be used to package something as small and delicate as an individual switch or as large as a 4" wafer. In addition, it was shown that MEMS switches could survive well into the hundreds of million cycles. LCP could, in fact, be used to create reliable, high performance systems.

The culmination of this research was used to create two variations of a communication module. These communication modules are by far the most sophisticated SOP on LCP achieved to date. At the moment, researchers at this and other universities are still trying to put single components on LCP. This research demonstrates the first, complete system on a flexible, organic polymer. As promised, it is low-cost, low-loss, miniature, flexible, and capable of beam steering. These modules can be customized to meet almost any size, frequency, and performance needed.

The following technical contributions were made from this research:

LCP processing:

- Plasma processes were developed for etching LCP, removing laser residue, and treating the surface for enhanced stiction
- Polishing process was developed for reducing the surface roughness of LCP from 2-5μm to 10nm
- Mounting techniques were developed for performing high accuracy lithography on a curled wafer
- Metal adhesion issues on LCP were studied and several solutions were found
- The process flow for fabricating MEMS on LCP with a near 100% yield was developed
- The thermocompression process for LCP lamination and packaging was established

New algorithms and testing:

- A new technique for predicting the pull down voltage of a MEMS switch was presented with unprecedented accuracy
- The lifetime of a MEMS switch on LCP was tested and analyzed to over 160 million cycles
- Hermeticity testing of various LCP packaging techniques was presented

Components and packaging with LCP:

- The first MEMS phase shifter on a flexible, organic material was presented
- The smallest and lowest-loss switched-line multi-bit MEMS phase shifter ever reported was demonstrated on LCP
- The first packaged MEMS phase shifter was documented
- A MEMS reconfigurable Sierpinski antenna was presented that eliminated the need for DC bias lines

- A localized, low-temperature method for packaging devices in LCP was demonstrated

Systems on LCP:

- A single-layer communication module was created for low-loss, low-cost, and flexible applications
- A multi-layer communication module was created for greater functionality in a small area.

The use of LCP in RF applications is still a relatively new field. It will take many more years before modules like these can be properly tested and expanded to include all of the necessary functionality of a real transmit/receive module. This research has established the foundation for this future work.

CHAPTER XIX

ACCOLADES AND INVENTION DISCLOSURES

The following accolades have been awarded since enrolling at Georgia Tech (in chronological order). A listing of invention disclosures filed and positions held are also presented.

19.1 Accolades Received and Positions Held

1. 1998-2002 PepsiCo Scholarship Award Recipient (outstanding student award)
2. 2001 Compaq Armada Award Recipient (coop student of the year)
3. 2002 Georgia Tech President's Undergraduate Research Award Recipient
4. 2003-2004 President of Georgia Tech Tae Kwon Do Club (2nd degree brown belt)
5. 2005 Trainer of the Year awarded by Georgia Tech Microelectronics Research Center (2nd place)
6. 2005 Mentor for Mount Zion High School teachers
7. 2005-2006 Mentor for Georgia Tech undergraduate students
8. March 2006 Georgia Tech Packaging Research Center Industry Advisory Board Poster Competition Winner (2nd place)
9. 2006 School of ECE Student Project Expo Award Winner (2nd place)
10. September 2006 Georgia Tech Packaging Research Center Industry Advisory Board Poster Competition Winner
11. 2006 Georgia Tech Graduate Research Symposium Award Winner (2nd place) for the College of Engineering
12. 2006 Trainer of the Year awarded by Georgia Tech Microelectronics Research Center

19.2 Invention Disclosures

1. D. Thompson, N. Kingsley, G. Wang, E. Tentzeris and J. Papapolymerou, "RF MEMS Switches on Liquid Crystal Polymer (LCP) Packaged with a Thin-Film Laser Micromachined LCP superstrate," submission of the invention for patent protection to U.S. Patent and Trademark Office on 1/18/2005 (provisional patent application).

2. R. Bairavasubramanian, D. Thompson, N. Kingsley, G. Wang, G. DeJean, R.L. Li, E. Tentzeris and J. Papapolymerou, "Scannable Antenna Arrays with Microwave Components and Electronic/Electromechanical Switching Elements on Single/Multilayer Liquid Crystal Polymer Substrates," submission of the invention for patent protection to U.S. Patent and Trademark Office on 6/29/2005 (provisional patent application).

3. D. Thompson, N. Kingsley, M. Morton, M. Tentzeris, and J. Papapolymerou, "Localized Bonding Technique for Near-Hermetic Packaging of RF MEMS Devices on Flexible, Organic Substrate", submission of the invention for patent protection to U.S. Patent and Trademark Office on 5/18/2006 (provisional patent application).

4. N. Kingsley and J. Papapolymerou, "Multivoltage RF MEMS Switch Systems", submission of the invention for patent protection to U.S. Patent and Trademark Office on 11/16/2006 (provisional patent application).

CHAPTER XX

PUBLICATIONS TO DATE

The following publications have been accepted and/or published to a peer-reviewed conference or journal (listed in chronological order):

20.1 Book Chapter

1. Nickolas Kingsley and John Papapolymerou, "Comprehensive Microsystems," Chapter title "RF MEMS Devices and Systems," Elsevier Limited.

20.2 Journal Publications

1. Il Kwon Kim, Nickolas Kingsley, Matt Morton, Ramanan Bairavasubramanian, John Papapolymerou, Manos M. Tentzeris, and Jong-Gwan Yook, "Fractal Shaped Microstrip Coupled Line Bandpass Filters For Suppression Of 2nd Harmonic," IEEE Transactions on Microwave Theory and Technique, Vol. 53, No. 9, pp. 2943-2948, Sept. 2005.

2. Nickolas Kingsley, Guoan Wang, John Papapolymerou, "Comparative Study of Analytical and Simulated Doubly-Supported RF MEMS Switches for Mechanical and Electrical Performance," Applied Computational Electromagnetics Society Journal, Vol. 21, No. 1, pp. 9-15, March 2006.

3. Nickolas Kingsley and John Papapolymerou, "Organic 'Wafer-Scale' Packaged Miniature Four-Bit RF MEMS Phase Shifter," IEEE Transactions on Microwave Theory and Technique, Vol. 54, No. 3, March 2006.

4. Il Kwon Kim, Nickolas Kingsley, Matthew A. Morton, Stephane Pinel, John Papapolymerou, Manos M. Tentzeris, Joy Laskar, and Jong-Gwan Yook, "Koch Fractal Shape Microstrip Bandpass Filters on High Resistivity Silicon for the Suppression of

the 2^{nd} Harmonic," Journal of the Korea Electromagnetic Engineering Society, Vol. 6, No. 4, Dec. 2006.

5. Nickolas Kingsley, Swapan Bhattacharya, and John Papapolymerou, "Moisture Lifetime Testing of RF MEMS Switches Packaged in Liquid Crystal Polymer", IEEE Transactions on Components, Packaging, and Manufacturing Technology, Submitted Jan. 3, 2007.

6. Nickolas Kingsley, Dimitrios E. Anagnostou, and John Papapolymerou, "RF MEMS Sequentially-Reconfigurable Sierpinski Antenna on a Flexible, Organic Substrate Without the Need for DC Bias Lines," IEEE Journal of MEMS, Submitted Jan. 22, 2007.

7. Communication module with George Ponchak to MTT or AP Transaction. To be submitted prior to defense.

20.3 Conference Publications

1. Dane Thompson, Nickolas Kingsley, Gerald DeJean, Vasilis Iliopoulos, RongLin Li, George E. Ponchak, Manos Tentzeris and John Papapolymerou, "Development of Lightweight Dual Frequency/Polarized Microstrip Antenna Arrays on Organic Substrates," Third NASA Earth Science Technology Conference, College Park, MD, June 23-26, 2003.

2. N.D. Kingsley, P. Kirby, G. Ponchak, and J. Papapolymerou, "14GHz MEMS 4-bit Phase Shifter on Silicon," 2004 Topical Meeting on Silicon Monolithic Integrated Circuits in RF Systems, pp. 326-328, September 2004.

3. Dane Thompson, Nickolas Kingsley, Guoan Wang, John Papapolymerou, and Manos M. Tentzeris, "RF Characteristics of Thin Film Liquid Crystal Polymer (LCP) Packages for RF MEMS and MMIC Integration," Presented at the 2005 IEEE MTT-S International Microwave Symposium in Long Beach, CA, June 11-17, 2005.

4. Nickolas Kingsley, Guoan Wang, and John Papapolymerou, "14 GHz Microstrip

MEMS Phase Shifters on Flexible, Organic Substrate," Presented at the 35th European Microwave Conference in Paris, France, October 4-6, 2005.

5. Il Kwon Kim, Nickolas Kingsley, Matt Morton, John Papapolymerou, Manos M. Tentzeris, and Jong-Gwan Yook, "Fractal shape microstrip band pass filter on High Resistivity Silicon for Suppression 2nd Harmonics," Presented at the 35th European Microwave Conference, Paris, France, October 4-6, 2005.

6. Nickolas Kingsley and John Papapolymerou, "Multibit MEMS Phase Shifter on Flexible, Organic Substrate for Microwave Antenna Systems," 15th IST Mobile & Wireless Communications Summit, Myconos, Greece, 4-8 June 2006.

7. Dimitrios E. Anagnostou, Ramanan Bairavasubramanian, Gerald DeJean, Guoan Wang, Nickolas Kingsley, Manos Tentzeris, and John Papapolymerou, "Development of a Dual-Frequency, Dual-Polarization, Flexible and Deployable Antenna Array for Weather Applications," 15th IST Mobile & Wireless Communications Summit, Myconos, Greece, 4-8 June 2006.

8. Ramanan Bairavasubramanian, Nickolas Kingsley, Gerald DeJean, Guoan Wang, Dimitrios E. Anagnostou, Manos Tentzeris, and John Papapolymerou, "Recent Developments on Lightweight, Flexible, Dual Polarization/Frequency Phased Arrays using RF MEMS Switches on LCP Multilayer Substrates for Remote Sensing of Precipitation," Sixth Annual NASA Earth Science Technology Conference, College Park, MD, June 27-29 2006.

9. Matthew A. Morton, Nickolas Kingsley, and John Papapolymerou, "Low Cost Method for Localized Packaging of Temperature Sensitive Capacitive RF MEMS Switches in Liquid Crystal Polymer," 2007 IEEE MTT-S International Microwave Symposium in Honolulu, HI, June 3-8, 2007.

APPENDIX A

14GHZ MEMS FOUR-BIT PHASE SHIFTER ON HIGH RESISTIVITY SILICON

This appendix is devoted to the second research project I had at Georgia Tech (the first was an investigation of a wireless chip-to-chip interconnect system). I needed to design a 4-bit MEMS phase shifter on high resistance silicon substrate (this was before my research group began work on LCP). Unfortunately, we were not able to get good measurement results from this project before it was set aside to work on an improved design on LCP. The results were published at the 2004 Topical Meeting on Silicon Monolithic Integrated Circuits in RF Systems conference [41]. That paper is reproduced here (unabridged). A commentary is given at the end of the Appendix to explain some of the shortcomings.

For this project, we wanted to realize a coplanar waveguide (CPW) MEMS phase shifter that was to be simulated, fabricated, and measured at 14GHz on 400μm thick high-resistivity silicon ($\epsilon_r = 11.7$). Simulated results using a full wave simulator predicted a return loss better than 19 dB and insertion loss better than 0.1 dB for a one bit phase shifter using perfectly conducting lines (PEC). Measurement results for the single MEMS switch were shown to have 22 dB return loss and 0.095 dB insertion loss in the UP (not activated) state and 0.83 dB return loss and 14.5 dB insertion loss in the DOWN (activated) state. The phase shifters demonstrated accurate phase shifts, but higher than expected loss.

A.1 Introduction

MEMS are quickly becoming a low-cost, high-performance replacement for solid-state switches (FETs, PIN diodes, etc.). Multi-bit phase shifters have been around for several years and have a common application in phased array antenna systems. The combination of the two technologies is the purpose for this project. Furthermore, a phase shift step size of 22.5^o is desired, which requires a 4-bit phase shifter. Most current phase shifters max at 3-bits,

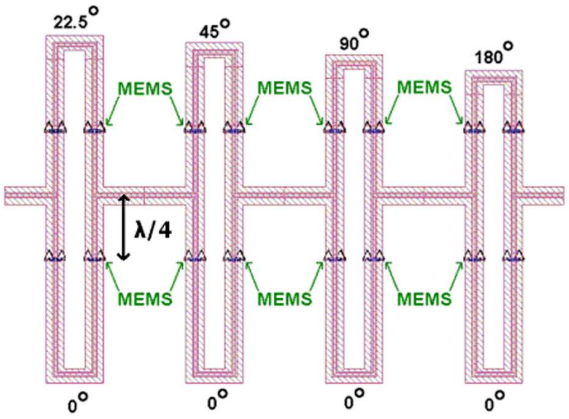

Figure 141: Layout of 4-bit phase shifter [41]

although 4-bit shifters have been published on other substrates (i.e. glass, GaAs), using solid-state switches (i.e. JFETs, PIN diodes), and using other transmission line types (i.e. microstrip) [32,53,56]. This project is the first 4-bit on silicon using MEMS switches, which furthers the state of the art. Measurement results of the single MEMS switch and of the 1-bit shifters, which are simply cascaded to achieve a 4-bit shifter, are presented in this paper.

A.2 Circuit Design and Fabrication

A.2.1 Circuit Design

To achieve a 4-bit phase shifter, four 1-bit phase shifters must be designed. These four shifters share a common reference line length and have a relative phase difference of 22.5^o, 45^o, 90^o, and 180^o. There are sixteen possible states ranging from 0^o to 337.5^o with 22.5^o steps. Each 1-bit shifter requires two sets of two cantilever MEMS switches, which are spaced $\lambda/4$ from the T-junction. This is shown as a 4-bit cascaded configuration in Figure 141.

Each set of MEMS is either in an UP (no activation) or DOWN (activation) state. When in the DOWN state, the MEMS bridge shorts the signal line to ground and effectively creates an RF open circuit. This causes the signal to flow through the opposing path. By choosing the set of MEMS to activate, the signal can be driven through the reference path or the delay path. A thin silicon nitride (Si_3N_4) layer is used to reduce stiction between the bridge

Table 26: Simulation results for one-bit phase shifter (using Sonnet full-wave simulator) [41]

Expected Phase	Magnitude S11	Magnitude S21	Phase S21	Phase Error
22.5	-19.06 dB	-0.094 dB	21.363^o	1.137^o
45	-24.485 dB	-0.074 dB	52.518^o	7.518^o
90	-25.465 dB	-0.021 dB	88.171^o	1.829^o
180	-20.773 dB	-0.077 dB	178.332^o	1.668^o

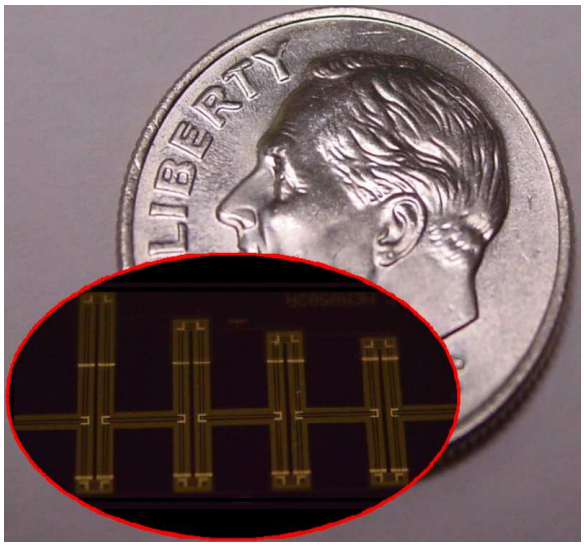

Figure 142: Size comparison of 4-bit phase shifter to a United States dime [41]

and metal layer and also to isolate the DC activation voltage. Simulation results for the 1-bit phase shifter are summarized in Table 26.

The size of the 4-bit phase shifter is approximately 16.5mm by 8mm. This is comparable to the size of a U.S. dime, as shown in Figure 142.

A.2.2 Fabrication

Preliminary fabrication of the MEMS switches, the 1 bit, and the 4-bit phase shifters has been completed. A detailed look at the cantilever MEMS switch and T-junction air bridge is shown in Figures 143 and 144.

A.3 Measurements

The measurement results for the MEMS switch in the UP state are shown in Figure 145. Measurement results for the MEMS switch in the DOWN state are shown in Figure 146.

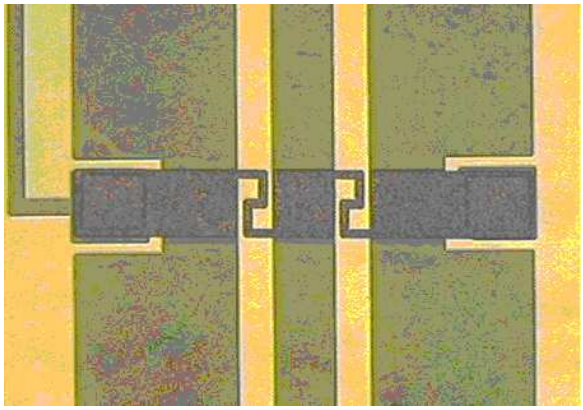

Figure 143: Single capacitive MEMS switch fabricated on high resistivity silicon [41]

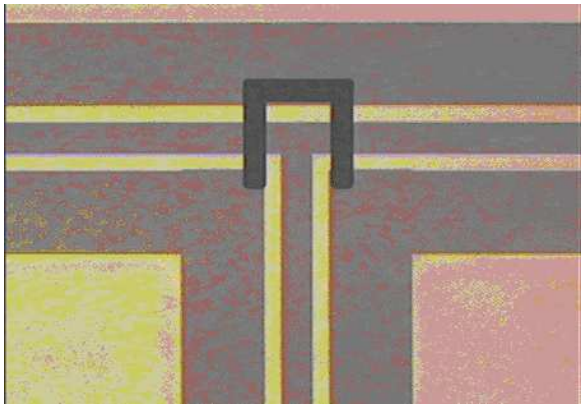

Figure 144: An air bridge T-junction is used to cancel slot line modes [41]

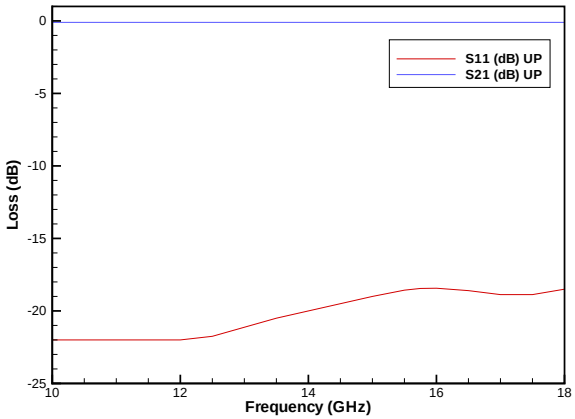

Figure 145: Measured results for a MEMS switch in the UP state [41]

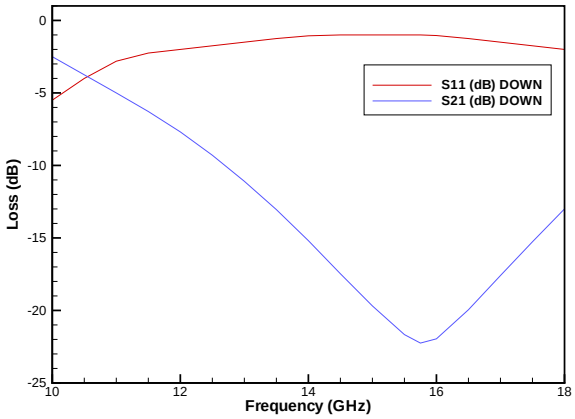

Figure 146: Measured results for a MEMS switch in the DOWN state [41]

Table 27: Measurement results for one-bit phase shifter [41]

Expected Phase	Magnitude S11	Phase S21	Phase Error
22.5	-5.1257 dB	25.697^o	3.197^o
45	-16.35 dB	54.906^o	9.906^o
90	-10.787 dB	95.101^o	5.101^o
180	-10.886 dB	177.88^o	2.120^o

The loss associated with MEMS switches is far less than the loss exhibited by their solid state counterparts (such as pin diodes, which can exhibit several dB of loss). The measurement results for the 1-bit phase shifter are summarized in Table 27.

It is expected that the more bits in a phase shifter, the greater the overall loss will be. This is due mostly to metal and substrate losses. Even though the overall length of the 4-bit phase shifter is about 16.5mm, the signal path length ranges from 36.5mm (for the 0^o case) to 46.1 m (for the 337.5^o case). Using TRL calibration, 0.8-1.2 dB/cm loss was observed over the frequency range. This adds 3 to 5 dB of loss alone. Adding several more decibels of loss from the switches would not be acceptable, which is why the low-loss and high isolation characteristics of MEMS switches makes them ideal for multi-bit phase shifters. Expected measured results for the 4-bit phase shifter have been extrapolated and summarized in Table 28.

The measured phase shifts are generally within a few degrees of the simulated values. The loss is greater than expected which is likely caused by slot line modes propagating

Table 28: Sample of extrapolated results for four-bit phase shifter [41]

Expected Phase	Magnitude S21
0^o	-3.718 dB
90^o	-3.922 dB
180^o	-4.122 dB
270^o	-4.327 dB
337.5^o	-4.487 dB

through the coplanar waveguide. These modes are not being fully canceling out by the air bridges. As the fabrication process is optimized, these slot line modes will be greatly reduced while maintaining a desired phase shift. In addition, a greater yield on the MEMS switches will be achieved and measurement results for the 4-bit shifter, which requires 16 working MEMS switches to measure, will be presented.

A.4 Future Work

Thus far, working 1-bit phase shifters at 22.5^o, 45^o, 90^o, and 180^o have been achieved. Attention will be given to improving the return and insertion loss. Optimization of the fabrication process will allow for measurement of the 4-bit phase shifter.

A.5 Commentary

Hopefully it is obvious to the reader why this is an appendix and not a chapter in the thesis. The concept has merit, which is why it published, but the results were not acceptable. There are several reasons why these phase shifters failed:

1. Simulator error: These simulations were performed using Sonnet, which is very slow compared to other full-wave simulation tools. This is particularly true for CPW structures. Therefore, to save time, a large mesh was used which gave inaccurate results.

2. Design flaws: I did not have a clear understanding of current flow through a waveguide structure. I did not properly shape the design to minimize the insertion loss. Also, many more air bridges were needed to properly tie together the grounds.

3. Fabrication difficulty: Since this was the first project that I was asked to fabricate, it was expected that mistakes would be made. Expecting a novice user to fabricate MEMS with good yield (all 16 switches had to work to have a working 4-bit phase shifter) was a bit much.

4. Ground air-bridge lesson: To save time and a mask, the MEMS switches and the air-bridge grounds were fabricated together. This is a big problem. Since the air-bridges and the switch membranes were the same height and thickness, whenever the switches actuated, so did the bridges! In order to get the measurement results presented in this paper, wire bonds were used to connect the ground lines. This could have been fixed by making one additional mask and plating the ground bridges much taller than the MEMS posts.

APPENDIX B

CLEANROOM & LASER LAB EQUIPMENT AND RECIPES

Many new recipes were developed by me in the MiRC cleanroom and shared among my group members. Those recipes are given in this appendix.

B.1 Chemical processing

The following chemicals were used in the fabrication of MEMS. Comments for each chemical are given.

351 Photoresist developer for SC 1827 and 1813 (by MicroChem Corp). This chemical is diluted with water by a factor of 3 before using.

Developing time after diluting	20-40 seconds

354 Photoresist developer for SC 1827 and 1813 (by MicroChem Corp)

Developing time	30-60 seconds

1112A Photoresist stripper (by MicroChem Corp)

1165 Photoresist stripper (by MicroChem Corp)

Acetone Solvent (by Brenntag)

Aluminum Etchant Aluminum Etchant (by Brenntag)

Deionized (DI) water Rinses away chemicals and particles (by Brenntag)

Ferric chloride Copper etchant (by MC Chemicals). Also called Iron (III) Chloride

Etch rate	0.9μm/minute

Gold etchant Gold etchant (by Transene)

Etch rate	0.4μm/minute

Isopropanol Used by Tousimis Super Critical Dryer (by Brenntag)

Methanol Solvent (by Brenntag)

Nitric Acid Used to etch copper (by Brenntag)

NR7-1500P Negative photoresist (by Futurrex)

Potassium Aurocyanide Gold plating solution (by Technic)

R/Flex 3850 Laminate LCP material for packaging and substrate uses (by Rogers Corporation)

RD6 Photoresist developer for NR7-1500P (by Futurrex)

SC 1827 Positive photoresist (by Shipley)

SC 1813 Positive photoresist (by Shipley)

Trichloroethylene, TCE Solvent (by Brenntag)

Hydroflouric acid, HF Used to etch titanium (by Brenntag). This chemical is diluted with water by a factor of 10 before using.

Etch rate	0.3μm/minute

B.2 Lithography

Lithography is one of the most challenging aspects of the fabrication process because it introduces plenty of opportunities for user error. Any misalignment can have a significant impact on the operation of the device. The following machines were used for lithography:

CEE 100CB Spinner Spin coats wafers with photoresist (see Figure 147)

Karl Suss MA-6 Mask Aligner Aligns and exposes wafers to optical masks (see Figure 148)

Figure 147: CEE 100CB Spinner [15]

Figure 148: Karl Suss MA-6 [15]

Karl Suss MJB-3 Mask Aligner Aligns and exposes wafers to optical masks (see Figure 149)

Figure 149: Karl Suss MJB-3 [15]

B.3 Deposition

The following machines are used to deposit materials:

CVC DC Sputterer Deposits metal (see Figure 150 and Table 29)

Figure 150: CVC DC Sputterer [15]

Table 29: DC Sputterer recipe for metal deposition

Metal	Percent Power	Deposition Rate
Aluminum	40	5.9Å/second
Copper	40	11.4Å/second
Gold	7	4.3Å/second
Titanium	7	0.52Å/second

Note: All values represent the rotostrate rotating at about 9-12 RPM (dial setting of "4")

CVC E-Beam Evaporator Deposits metal (see Figure 151 and Table 30)

Table 30: E-beam recipe for metal deposition

Metal	Deposition Rate
Aluminum	1.5-3.0Å/second
Copper	3.0Å/second
Gold	1.5-3.0Å/second
Titanium	1.0-1.5Å/second

Unaxis PECVD Deposits thin dielectric films (see Figure 152 and Table 31)

Figure 151: CVC Electron Beam Evaporator [15]

Figure 152: Unaxis PECVD [15]

Table 31: Unaxis PECVD recipe for Silicon Nitride deposition on LCP. The standard temperature for other substrate materials is 250^{o}C [15]

Temperature	150^{o}C
Gasses	SiH_4 (5% in He) - 200 sccm, NH_3 - 8 sccm, He - 560 sccm, N_2 - 150 sccm
Pressure	900 mTorr
Power	30 W
Deposition Rate	100$\mathring{A}$/minute

B.4 Etching

The following machine is used to plasma etch materials:

Plasma-Therm RIE Etches thin dielectric layers and removes laser residue (see Figure 153, Table 32, and Table 33)

Figure 153: Plasma-Therm RIE [15]

Table 32: RIE recipes for Silicon Nitride etching [15]

Temperature	25^oC	25^o
Gasses	SF_6 - 33 sccm, O_2 - 7 sccm	CHF_3 - 45 sccm, O_2 - 5 sccm
Pressure	75 mTorr	40 mTorr
Power	85 W	200 W
Etch Rate	$1000\mathring{A}$/minute	$450\mathring{A}$/minute

Table 33: RIE recipe for LCP and laser residue etching

Temperature	25^oC
Gasses	O_2 - 50 sccm
Pressure	200 mTorr
Power	200 W
Etch Rate	3-4 minutes/micron

A sample of LCP that was cut using a CO_2 laser (recipe given in Table 18) and plasma cleaned with the recipe in Table 33 is shown in Figure 154.

B.5 Metrology

The following machines are used to scan the surface of the sample:

Nanospec Profilometer Measures the thickness of dielectric films optically (see Figure 155)

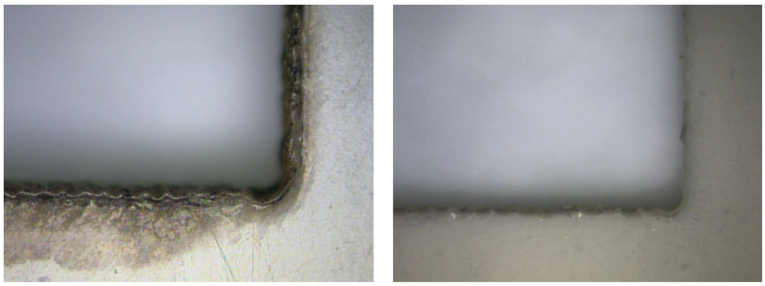

Figure 154: Laser residue on an LCP sample before and after cleaning with RIE plasma

Figure 155: Nanospec profilometer [15]

Tencor KLA Profilometer Measures surface roughness mechanically (see Figure 156)

Figure 156: Tencor KLA Profilometer [15]

Wyko Optical Profilometer Measures surface roughness optically (see Figure 157)

Figure 157: Wyco optical profilometer [15]

B.6 Bonding

The Karl Suss SB-6 substrate bonder (shown in Figure 158) was used to perform thermo-compression bonding. This machines uses temperature and pressure to force a chemical-mechanical bond to form between the LCP layers. In this bonder there are four variables to set: temperature, tool force, pressure, and duration.

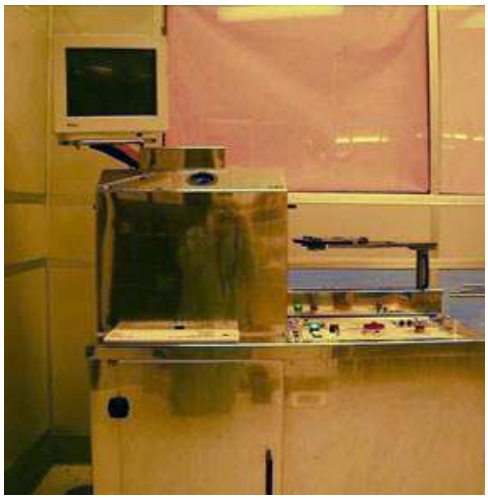

Figure 158: Karl Suss bonder [15]

B.6.1 Temperature

The temperature should be set to the melting point of the bond ply material, which is around 290-295^{o}C. A lower temperature will have no effect on the material. A temperature higher than the melting point may cause reflow which will damage the devices.

B.6.2 Tool force

This parameter is probably the least sensitive of all. It really only varies with sample size. Figure 159 shows some recommended tool force values. An improper tool force can lead to delamination.

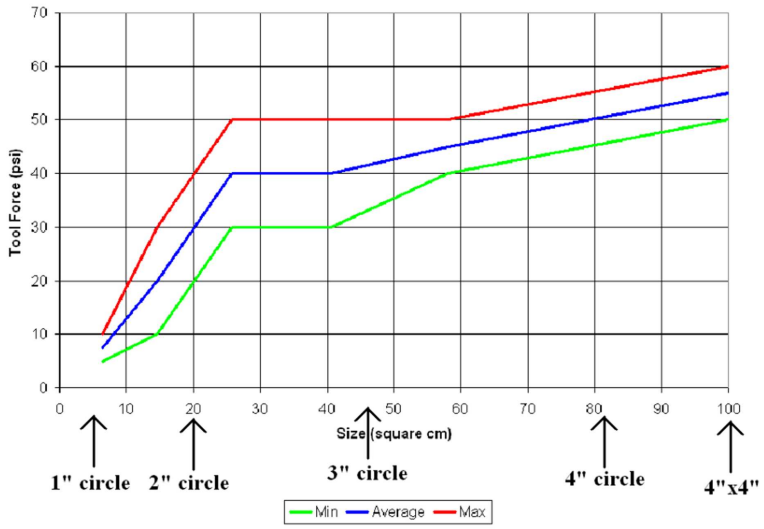

Figure 159: Tool force recommendation for Karl Suss bonder

B.6.3 Pressure

The bonder has two chamber pressure settings, vacuum and atmosphere (called "purge"). The vacuum setting is usually between 4-6 microtorr and atmosphere is around 1 torr (1 atm is 760 torr). Packaging can be done at either setting successfully. If MEMS are being packaged, many experts argue that bonding should be done at atmosphere because the air inside the cavity will help dampen the movement of the MEMS.

B.6.4 Duration

A typical run lasts for 20-45 minute under stable pressure and temperature. Less time can be used, but this can lead to delamination of the layers. Longer runs do not pose any known issues.

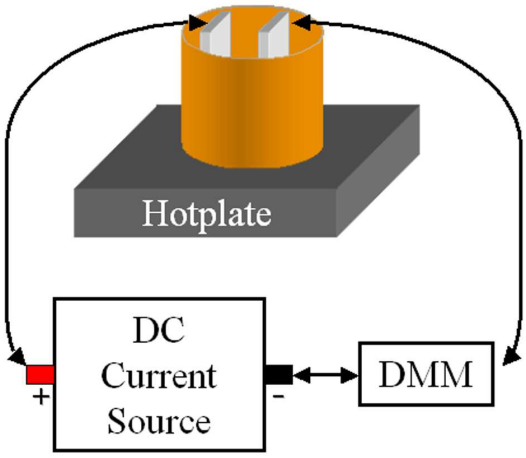

Figure 160: Gold electroplating station setup

B.7 Electroplating

Electroplating can be used to grow thick layers of metal. For this research, we only electroplated gold since that is one of the best metals for MEMS. The layout of our electroplating set-up is shown in Figure 160.

The deposition rate depends on many factors, including:

- The temperature of the solution
- The amount of gold in the solution
- The plating area
- The current level

In order to get good uniformity across the sample, a magnetic stirring rod should constantly mix the solution at 200 RPM. The plating temperature is set to 55^{o}C, which was determined by the manufacturer. Note that this is the temperature of the solution, not the hot plate. As the gold depletes from the solution, it will turn from clear to dark gold. The current level is set by the user and it should be a good compromise between slow enough to have good quality but fast enough to process in a timely manner. The current can be monitored using a digital multimeter (DMM). Some current settings and their respective deposition rates are shown in Table 34 for a typical sample size.

Table 34: Gold eletroplating deposition rates

Current (mA)	Deposition Rate
8	170 $\mathring{A}$/minute
10	215 $\mathring{A}$/minute
12	260 $\mathring{A}$/minute
15	330 $\mathring{A}$/minute

Note: Solution is heated to 55^{o}C and the rate shown is for a two square inch sample with about 25% plating area

Typically, 6-8mA of current was used. The thickness was measured every 15-20 minutes to prevent depositing too much gold. Plating too quickly can lead to metal delamination.

B.8 Miscellaneous

The following machines are used to perform a variety of tasks:

Olympus Video Microscope Takes digital images with high resolution

Tousimis Super Critical Dryer Dries MEMS devices at the super critical point to prevent damage from surface tension (see Figure 161)

Figure 161: Tousimis Super Critical Dryer [15]

B.9 Laser Micromachining

There are three laser systems that were available to us from Dr. Mark Allen's laser lab. They are the CO_2, excimer, and infrared (IR) lasers.

	CO_2	Excimer	Infrared
Wavelength	10.6μm	248nm	1048 or 523nm
Spot size	200μm	20μm	40μm
Ablation type	hot	cold	hot
Focal type	point	projection	point
Stop layer	anodized aluminum	ceramic	glass
Pros	quick and easy to use	can drill vias; small spot size	can cut metal
Cons	large spot size	difficult to use	long warm-up

Table 35: Comparison of the CO_2, Excimer, and Infrared lasers

The most versatile laser is the CO_2 laser. It can cut through pretty much everything except thick metals ($> 5\mu$m), glass, and semiconductors. Fortunately it cuts though LCP like a hot knife through butter. Since you can import a dxf file directly into the laser software, it is a very easy laser to use. Unfortunately, the smallest feature it can burn is 200μm, which is too large for some of our applications. Also, since it is an ablation process, it is very difficult to do depth controlled cutting.

The excimer laser has the smallest spot size of the three lasers. It can burn holes as small as 20μm. Since the output is pulsed, it is possible to make depth controlled cuts. This makes it perfect for making vias. One nice feature about the excimer laser is that it uses a projection beam. The laser beam is magnified by 4-10x and projected onto a fixture (usually made of brass) that will shape the beam. The beam is then demagnified so that it is back to the original size, but maintains the shape defined by the fixture. This is very convenient for cutting odd shaped cavities and vias very quickly.

As far as this thesis is concerned, the IR laser is only useful for two applications: cutting copper cladded LCP and cutting the brass plates used by the excimer laser. Since copper cladded LCP is not used as a substrate for MEMS samples, the IR laser was rarely used for this application. However, the IR laser was used quite often to cut brass plates since it is the only way to do so reliably. The IR system has an accuracy of 1μm which allows for excellent control of the features being ablated by the excimer laser.

A summary of the three lasers is shown in Table 35.

The CO_2 laser cutting recipe used for LCP and Teflon (which was used in the bonding process) was given in Table 18.

APPENDIX C

QUICK START GUIDE TO MAKING MEMS

This appendix is devoted to the inspired grad student that is anxious to get started in MEMS fabrication. These are all the bare-bones steps from start to finish for fabricating MEMS on LCP. Detailed recipes for each of these steps were presented in Chapter 4 of the thesis.

This recipe was first established with assistance from Dr. Arnaud Pothier on November 26, 2003. It has gone through a number of revisions since then.

1. Remove the copper cladding from LCP using nitric acid or iron (III) chloride
2. Laser cut LCP using CO_2 laser
3. Plasma clean laser residue using RIE (nki_poly: 4-8 minutes/side)
4. Polish LCP using Lapmaster polisher
5. (optional) Sputter 2.2μm Copper on backside using DC Sputterer (2000 seconds)
6. E-beam: Ti (250$\mathring{A}$) / Au (2500$\mathring{A}$)
7. (optional) Mount the sample to a glass slide
8. Spin PR 1827 (5 secs @ 500RPM, 40 secs @ 3000RPM): Use Conductor Layer Mask
   a. Bake at 120^{o}C for 2 minutes
   b. Expose
   c. Develop (354)
9. Gold Etchent: Soak for about 20 seconds
10. Dilute HF: Etch Ti (8-10 seconds)
11. Acetone: Remove PR

12. Dry Circuits thoroughly using hot plate or oven (2-3 minutes at 120^{o}C)

13. Unaxis PECVD: Deposit Si_3N_4 (gwa_sin150: 20-30 minutes)

14. Spin PR 1827 (5 secs @ 500RPM, 40 secs @ 3000RPM): Use Nitride Mask
    a. Bake at 120^{o}C for 2 minutes
    b. Expose
    c. Develop (354)

15. RIE: Etch Si_3N_4 in right chamber (nki_nit: 10-15 minutes)

16. Acetone: Remove remaining PR

17. Spin PR 1827 (5 secs @ 500RPM, 40 secs @ 4000RPM) or 1813 for thinner layer (5 secs @ 500RPM, 40 secs @ 3000RPM): Use Sacrificial Layer Mask
    a. Bake at 120^{o}C for 2 minutes
    b. Expose
    c. Develop (354)
    d. Bake at 140^{o}C for 10 minutes on a hotplate followed by another 10 minutes in an oven at 140^{o}C

18. E-beam: Ti (250$\mathring{A}$) / Au (2500$\mathring{A}$) / Ti (250$\mathring{A}$)

19. Spin PR 1827 (5 secs @ 500RPM, 40 secs @ 3000RPM): Use Bridge mask
    a. Bake at 85^{o}C for 20-30 minutes
    b. Expose
    c. Develop (354)

20. (optional) Acetone: Make "window" for electroplating

21. Dilute HF: Etch Ti (5-10 seconds)

22. Measure thickness of metal with profilometer
    a. Gold plating at 8-12 mA
    b. Plate to 1.2-2μm

23. Expose (20 seconds on MA-6, 1.5 minutes on MJB-3)

24. Develop (60 seconds)

25. Dilute HF: Etch Ti

26. Gold Etchent: Etch Au

27. Dilute HF: Etch Ti

28. PR Stripper 1165 (or acetone): Soak over night (or at least 4 hours)

29. Water (2 minutes)

30. IPA

31. Critical Point Dryer: Dehydrate circuit

REFERENCES

[1] 3M^{TM}, "3m^{TM} Super 77^{TM} multipurpose adhesive." Internet, http://solutions.3m.com/wps/portal/3M/en_US/3M-Super-77, Dec 2006.

[2] Aerocomm, "Ac4424 transceiver." Internet, http://www.aerocomm.com, May 2007.

[3] Anagnostou, D. E., Zheng, G., Chryssomallis, M., Papapolymerou, J., Christodoulou, C. G., Lyke, J., and Ponchak, G., "Design, fabrication and measurements of a self-similar re-configurable antenna with RF MEMS switches," *IEEE Transactions on Antennas & Propagation, Special Issue on Multifunction Antennas and Antenna Systems*, vol. 54, Feb 2006.

[4] Anguera, J., Martnez-Ortigosa, E., Puente, C., C. Borja, C., and Soler, J., "Broadband triple-frequency microstrip patch radiator combining a dual-band modified sierpinski fractal and a monoband antenna," *IEEE Transactions on Antennas and Propagation*, vol. 54, pp. 3367–3373, Nov 2006.

[5] Bairavasubramanian, R., Thompson, D., DeJean, D., Ponchak, G., Tentzeris, M., and Papapolymerou, J., "Development of mm-wave dual-frequency multilayer antenna arrays on liquid crystal polymer (LCP) substrate," *IEEE International Antennas and Propagation Symposium*, July 2005.

[6] Balanis, C., *Antenna Theory: Analysis and Design.* John Wiley and Sons, Inc, 2 ed., 1982.

[7] Brown, E., "RF MEMS for digitally-controlled front-end components," *Second Annual IEEE International Conference on Innovative Systems in Silicon*, p. 338, Oct. 1997.

[8] Brown, S. and Jansen, E., "Reliability and long term stability of MEMS," *Advanced Applications of Lasers in Materials Processing*, pp. 9–10, Aug. 1996.

[9] Brownlee, K., Raj, P., Bhattacharya, S., Shinotani, K., Wong, C., and Tummala, R., "Evaluation of liquid crystal polymers for high performance SOP application," *Electronic Components and Technology Conference*, pp. 676–680, May 2002.

[10] Bushyager, N., Lange, K., Tentzeris, M., and Papapolymerou, J., "Modeling and optimization of RF-MEMS reconfigurable tuners with computationally efficient time-domain techniques," in *Proc. of the 2002 IEEE-IMS Symposium*, pp. 883–886, Jun 2002.

[11] CADopia Inc., "The intelliCAD source for CAD users." Internet, http://www.cadopia.com, May 2005.

[12] Cafe, R., "Dielectric constant, strength, and loss tangent." Internet, http://www.rfcafe.com/references/electrical/dielectric_constants_strengths.htm, May 2005.

[13] Campbell, S., *The Science and Engineering of Microelectronic Fabrication*. New York: Oxford University Press, 2 ed., 2001.

[14] Campbell, S., *The Science and Engineering of Microelectronic Fabrication*. Oxford University Press, 2001.

[15] Center", G. T. M. R., "Equipment." Internet, http://grover.mirc.gatech.edu, May 2006.

[16] Comsol, I., "Femlab multiphysics modeling." Internet, http://www.comsol.com/products/femlab, Nov 2004.

[17] Corbin, M., "A unified security budget for the united states, 2006." Internet, http://www.fpif.org/papers/0505usb.html, May 2005.

[18] Corporations, R., "RO3000 series high frequency circuit materials." Internet, http://www.rogerscorporation.com/mwu/pdf/3000data.pdf, May 2005.

[19] Coventor, I., "MEMCAD and FlumeCAD." Internet, http://www.cmf.rl.ac.uk/cad/memcad.html, May 2005.

[20] Culbertson, E., "A new laminate material for high performance PCBs: Liquid crystal polymer copper clad films," *IEEE*, pp. 520–533, 1995.

[21] DeJean, G., Bairavasubramanian, R., Thompson, D., Ponchak, G., Tentzeris, M., and Papapolymerou, J., "Liquid crystal polymer (LCP): a new organic material for the development of multilayer dual-frequency/dual-polarization flexible antenna arrays," *Antennas and Wireless Propagation Letters*, vol. 4, pp. 22–26, 2005.

[22] Du, G., Zhang, Y., Ma, Y., Yang, X., Zhao, B., and Liu, B., "ZnO thin films grown by plasma-assisted metal-organic vapor phase epitaxy," in *Proceedings of the Sixth Chinese Symposium Optoelectronics*, pp. 292–296, Sept 2003.

[23] Eyring, H., Lin, H., and Lin, S., *Basic Chemical Kinetics*. New York: Wiley, 1980.

[24] Fedder, G., "Structured design methods for MEMS: Essential tools for rapid MEMS development." Internet, http://www.design.caltech.edu/NSF_MEMS_Workshop/fedder.html, May 2005.

[25] Fujita, H., "A decade of MEMS and its future," *Tenth Annual International Workshop on Micro Electro Mechanical Systems*, pp. 1–7, Jan. 1997.

[26] Geller, B., Thaler, B., Fathy, A., Liberatore, M., Chen, H., Ayers, G., Pendrick, V., and Narayan, Y., "LTCC-M: an enabling technology for high performance multilayer RF systems," *IEEE MTT-S Symposium on Technologies for Wireless Applications*, pp. 189–192, Feb. 1999.

[27] Gere, J., *Mechanics of Materials*. Thompson-Engineering, 5 ed., 2003.

[28] Goldsmith, C., Ehmke, J., Malczewski, A., Pillans, B., Eshelman, S., Yao, Z., Brank, J., and Eberly, M., "Lifetime characterization of capacitive rf mems switches," in *2001 IEEE MTT-S International Microwave Symposium Digest*, vol. 1, pp. 227–230, May 2001.

[29] Goldsmith, C., "E-mail correspondance with Dr. Charles Goldsmith, President MEMtronics corporation," Sept 2006.

[30] Google, "Google maps." Internet, http://maps.google.com, May 2007.

[31] Halliberg, D. and Peck, S., "Recent humidity accelerations, a base for testing standards," *Qual. Reliab. Eng. Int.*, vol. 7, pp. 169–180, 1991.

[32] Hayden, J., Malczewski, A., Kleber, J., Goldsmith, C., and Rebeiz, G., "2 and 4-bit DC-18 GHz microstrip MEMS distributed phase shifters," in *IEEE Microwave Symposium Digest*, vol. 1, pp. 219–222, 2001.

[33] Horst, S., Bhattacharya, S., Johnson, S., Tentzeris, E., , and Papapolymerou, J., "Modeling and characterization of thin film broadband resistors on LCP for RF applications," in *Proc. 56th Electronic Components and Technology Conf.*, pp. 1751–1755, June 2006.

[34] Hung, J.-J., Dussopt, L., and Rebeiz, G., "A low-loss distributed 2-bit w-band MEMS phase shifter," in *33rd European Microwave Conference*, vol. 3, pp. 983–985, Oct 2003.

[35] Hung, J.-J., Dussopt, L., and Rebeiz, G., "Distributed 2- and 3-bit w-band MEMS phase shifters on glass substrates," *IEEE Transactions on Microwave Theory and Techniques*, vol. 52, pp. 600–606, Feb 2004.

[36] IE3D^{TM}, "Zeland software."

[37] Imhof, H. and Johnson, W., "Interconnection substrates – ceramic," *IMAPS-CII / NEMI Technology Roadmaps*, Dec. 2002.

[38] Inc.", E. P., "Products." Internet, http://www.elmers.com/product/prod_list.asp?prodCat=5, Dec 2006.

[39] Kheng, L., Chai, L., Ming, C., and Hong, N., "Enhancement of moisture sensitivity performance of a FBGA," in *2000 Int'l Symp on Electronic Materials & Packaging*, pp. 470–475, 2000.

[40] Kim, H.-T., Park, J.-H., Yim, J., Kim, Y.-K., and Kwon, Y., "A compact V-band 2-bit reflection-type MEMS phase shifter," *IEEE Microwave and Wireless Components Letters*, vol. 12, pp. 324–326, Sept 2002.

[41] Kingsley, N., Kirby, P., Ponchak, G., and Papapolymerou, J., "14GHz MEMS 4-bit phase shifter on silicon," *Topical Meeting on Silicon Monolithic Integrated Circuits in RF Systems*, pp. 326–328, Sept. 2004.

[42] Kingsley, N. and Papapolymerou, J., "Organic 'wafer-scale' packaged miniature four-bit RF MEMS phase shifter," *IEEE Transactions on Microwave Theory and Technique*, vol. 54, Mar. 2006.

[43] Kingsley, N., Wang, G., and Papapolymerou, J., "14 GHz microstrip MEMS phase shifters on flexible, organic substrate," *35th European Microwave Conference*, Oct. 2005.

[44] Kingsley, N., Wang, G., and Papapolymerou, J., "Comparative study of analytical and simulated doubly-supported RF MEMS switches for mechanical and electrical performance," *Applied Computational Electromatnetics Society (ACES) Journal*, vol. 21, Mar. 2006.

[45] Kingsley, N., Anagnostou, D. E., and Papapolymerou, J., "RF MEMS sequentially-reconfigurable sierpinski antenna on a flexible, organic substrate without the need for DC bias lines," *IEEE Journal of MEMS (submitted Jan. 2007)*, 2007.

[46] Kingsley, N., Bhattacharya, S., and Papapolymerou, J., "Moisture lifetime testing of RF MEMS switches packaged in liquid crystal polymer," *IEEE Transactions on Components, Packaging, and Manufacturing Technology (submitted Jan. 2007)*, 2007.

[47] Ko, Y., Park, J., and Bu, J., "Integrated 3-bit RF MEMS phase shifter with constant phase shift for active phased array antennas in satellite broadcasting systems," in *12th International Conference on Transducers, Solid-State Sensors, Actuators and Microsystems*, vol. 2, pp. 1788–1791, Jun 2003.

[48] Ko, Y., Park, J., and Bu, J., "Integrated RF MEMS phase shifters with constant phase shift," in *IEEE Microwave Symposium Digest*, vol. 3, pp. 1489–1492, Jun 2003.

[49] Ko, Y., Park, J., Kim, H., and Bu, J., "Integrated five-bit RF MEMS phase shifter for satellite broadcasting/communication systems," in *The Sixteenth Annual International Conference on Micro Electro Mechanical Systems*, pp. 144–148, Jan 2003.

[50] Koester, D., Markus, K., and Walters, M., "MEMS: small machines for the microelectronics age," *Computer*, vol. 29, pp. 93–94, Jan. 1996.

[51] Krzysztofik, W., "Fractal monopole antenna for dual-ism-bands applications," in *36th European Microwave Conference*, pp. 1461–1464, Sept 2006.

[52] Lee, S., Park, J.-H., Kim, H.-T., Kim, J.-M., Kim, Y.-K., and Kwon, Y., "A 15-to-45 ghz low-loss analog reflection-type MEMS phase shifter," in *IEEE Microwave Symposium Digest*, vol. 3, pp. 1493–1496, Jun 2003.

[53] Liu, Y., Borgioli, A., Nagra, A. S., and York, R. A., "K-band 3-bit low-loss distributed MEMS phase shifter," *IEEE Microwave and Guided Wave Letters*, vol. 10, pp. 415–417, Oct 2000.

[54] Lou, J., Zhao, Z., Yang, R., Lu, M., and Hu, X., "A DC-to-32ghz 2-bit MEMS phase shifter," in *IEEE Antennas and Propagation Society Symposium*, vol. 3, pp. 2867–2870, Jun 2004.

[55] Luque, N. A., "Telephone conversation with Raytheon MMIC designers," Jan 2007.

[56] Lynes, G., Johnson, G., Huckleberry, B., and Forrest, N., "Design of a broadband 4-bit loaded switched-line phase shifter," *IEEE Transactions on Microwave Theory and Techniques*, vol. 22, pp. 693–697, Jun 1974.

[57] Markus, K., "Developing infrastructure to mass-produce MEMS," *IEEE Computational Science and Engineering*, vol. 4, pp. 49–54, January–March 1997.

[58] Meek, G., "Photograph by Gary Meek. Used with permission."

[59] MEMS, R., "Radant MEMS switch." Internet, http://www.radantmems.com/radantmems/switchoverview.html, May 2007.

[60] MEMtronics Corporation, "RF MEMS switches," *Internet, http://www.memtronics.com*, Dec. 2005.

[61] Mercier, D., Blondy, P., Cros, D., and Guillon, P., "An electromechanical model for MEMS switches," in *IEEE MTT-S Microwave Symposium Digest*, vol. 3, pp. 2123–2126, May 2001.

[62] Mobiledia, "Half the world will use a cell phone by 2009." Internet, http://www.mobiledia.com/news/43104.html, Jan 2006.

[63] Morrison, D. G., "Low-temperature cofired ceramics fuel growth of high-frequency designs." Internet, http://www.elecdesign.com/Articles/Index.cfm?ArticleID=4785, May 2000.

[64] Morton, M. A., Kingsley, N., and Papapolymerou, J., "Low cost method for localized packaging of temperature sensitive capacitive RF MEMS switches in liquid crystal polymer," in *2007 IEEE MTT-S International Microwave Symposium in Honolulu, HI*, June 2007.

[65] Muldavin, J. and Rebeiz, G., "High-isolation CPW MEMS shunt switches - part 1: Modeling," *IEEE Transactions on Microwave Theory and Techniques*, vol. 48, pp. 1045–1052, Jun 2000.

[66] Nejad, M. B., Tenhunen, H., and Zheng, L.-R., "Chip-package and antenna co-design of a tunable uwb transmitter in system-on-package with on-chip versus off-chip passives," in *1st Electronics System Integration Technology Conference*, vol. 1, pp. 291–298, Sept 2006.

[67] Newman, H., "E-mail correspondance with Dr. Harvey Newman, Naval Research Laboratory," June 2006.

[68] of Defense, U. S. D., "Test Method Standard, Microcircuits." MIL-STD-883E, Dec 1996. FSC 5962.

[69] of Homeland Security, D., "U.S. Department of Homeland Security FY 2006 budget." Internet, http://www.dhs.gov/dhspublic/interapp/press_release/press_release_0613.xml, Feb 2005.

[70] Pacheco, S., Katehi, L., and Nguyen, C.-C., "Design of low actuation voltage RF MEMS switch," in *IEEE MTT-S Microwave Symposium Digest*, vol. 1, pp. 165–168, Jun 2000.

[71] Parallax, I., "RF communication modules." Internet, http://www.parallax.com, May 2007.

[72] Peroulis, D., Pacheco, S., Sarabandi, K., and Katehi, L., "Electromechanical considerations in developing low-voltage RF MEMS switches," *IEEE Transactions on Microwave Theory and Techniques*, vol. 51, pp. 259–270, Jan 2003.

[73] Popov, E., *Mechanics of Materials*. Prentice-Hall, Inc, 1976.

[74] Pozar, D., "A review of aperture coupled microstrip antennas: History, operation, development, and applications," May 1996.

[75] Pozar, D., *Microwave Engineering, Second Edition*. New York, NY: John Wiley and Sons, Inc, 2001.

[76] Puente, C., Romeu, J., Pous, R., and Cardama, A., "On the behavior of the sierpinski multiband fractal antenna," *IEEE Transactions on Antennas and Propagation*, vol. 46, pp. 517–524, April 1998.

[77] Qian, J., Li, G., and deFlavis, F., "A parametric model of MEMS capacitive switch operating at microwave frequencies," in *IEEE Microwave Symposium Digest*, vol. 2, pp. 1229–1232, Jun 2000.

[78] Rebeiz, G., Guan-Leng, T., and Hayden, J., "RF MEMS phase shifters: design and applications," *IEEE Microwave Magazine*, vol. 3, pp. 72–81, June 2002.

[79] Rizk, J. and Rebeiz, G., "W-band microstrip RF-MEMS switches and phase shifters," in *IEEE Microwave Symposium Digest*, vol. 3, pp. 1485–1488, Jun 2003.

[80] Rizk, J. and Rebeiz, G., "W-band CPW RF MEMS circuits on quartz substrates," *IEEE Transactions on Microwave Theory and Techniques*, vol. 51, pp. 1857–1862, Jul 2003.

[81] Rung, J., "Verbal conversations about polishing," 2005.

[82] Sandor, E., "Advances in laminates for high frequency cost sensitive commercial applications." Internet, http://www.az-ww.com/2002%20pdf/Sandorpresentation2002.pdf, May 2002.

[83] Sarkar, S., Palazarri, V., Wang, G., Papageorgiou, N., Thompson, D., Lee, J., Pinel, S., Tentzeris, M., Papapolymerou, J., and Laskar, J., "RF and mm-wave SOP module platform using LCP and RF MEMS technologies," in *2004 IEEE MTT-S International Microwave Symposium Digest*, vol. 2, pp. 567–570, June 2004.

[84] Semtech, "Sx1223: Single-chip multi-channel low-power transmitter." Internet, http://www.semtech.com, May 2007.

[85] Senturia, S., *Microsystem Design*. Kluwer Academic Publishers, 2001.

[86] Sigma, S., "Hermeticity testing (fine and gross leak)." Internet, http://www.sixsigmaservices.com/hermeticitytesting.asp, Nov 2006.

[87] Simion, S., "Modeling and design aspects of the MEMS switch," in *Semiconductor Conference*, vol. 1, pp. 125–128, Oct 2003.

[88] Swanberg, N., "LTCC packaging for wireless UWB applications." Internet, http://www.eet.com/article/showArticle.jhtml?articleId=55800631, May 2005.

[89] Tan, G., Mihailovich, R., Hacker, J., DeNatale, J., and Rebeiz, G., "A 4-bit miniature X-band MEMS phase shifter using switched-LC networks," *IEEE MTT-S International Microwave Symposium Digest*, vol. 3, pp. 1477–1480, June 2003.

[90] Tan, T. G.-L., Mihailovich, R., Hacker, J., DeNatale, J., and Rebeiz, G., "Low-loss 2- and 4-bit TTD MEMS phase shifters based on SP4T switches," *IEEE Transactions on Microwave Theory and Techniques*, vol. 51, pp. 297–304, Jan. 2003.

[91] Tentzeris, M., Laskar, J., Papapolymerou, J., Pinel, S., Palazzari, V., Li, R., DeJean, G., Papageorgiou, N., Thompson, D., Bairavasubramanian, R., Sarkar, S., and Lee, J., "3-d-integrated RF and millimeter-wave functions and modules using liquid crystal polymer (LCP) system-on-package technology," *IEEE Transactions on Advanced Packaging*, vol. 27, pp. 332–340, May 2004.

[92] Teo, Y., Wong, E., and Lim, T., "Enhancing moisture resistance of PBGA," in *1998 Electronic Components and Technology Conference*, pp. 930–935, 1998.

[93] Thomas, P., Dwarakanath, K., Sampathkumaran, P., Seetharamu, S., and Kishore, "Influence of moisture absorption on electrical characteristics of glass-epoxy polymer composite system," in *Proceedings of 2005 International Symposium on Electrical Insulating Materials*, pp. 612–615, 2005.

[94] Thompson, D., Kingsley, N., Morton, M., Tentzeris, M., and Papapolymerou, J., "Localized bonding technique for near-hermetic packaging of RF MEMS devices on flexible, organic substrate," *Submission of the invention for patent protection to U.S. Patent and Trademark Office on 5/18/2006 (provisional patent application)*, 2006.

[95] Thompson, D., Kingsley, N., Wang, G., Papapolymerou, J., and Tentzeris, M., "RF characteristics of thin-film liquid crystal polymer (LCP) packages for RF MEMS and MMIC integration," *IEEE MTT-S Int. Microwave Symp. Dig.*, June 2005.

[96] Thompson, D., Tentzeris, M., and Papapolymerou, J., "Experimental analysis of the water absorption effects on RF active/passive circuits packaged in a multilayer organics," *submitted to IEEE Transactions on Advanced Packaging*, 2006.

[97] Thompson, D., Tantot, O., Jallageas, H., Ponchak, G., Tentzeris, M., and Papapolymerou, J., "Characterization of liquid crystal polymer (LCP) material and transmission lines on LCP substrates from 30 to 110 GHz," *IEEE Transactions on Microwave Theory and Techniques*, vol. 52, pp. 1343–1352, Apr. 2004.

[98] Tsachtsiris, G., Soras, C., Karaboikis, M., and Makios, V., "Analysis of a modified sierpinski gasket monopole antenna printed on dual band wireless devices," *IEEE Transactions on Antennas and Propagation*, vol. 52, pp. 2571–2579, Oct 2004.

[99] Tummala, R. R., "SOP: What is it and why? A new microsystem-integration technology paradigm - Moores law for system integration of miniaturized convergent systems of the next decade," *IEEE Trans. Adv. Packag.*, vol. 27, pp. 241–249, May 2004.

[100] Wang, G., Barstow, S., Jeyakumar, A., Papapolymerou, J., and Henderson, C., "Low cost RF MEMS switches using photodefinable mixed oxide dielectrics," in *IEEE MTT-S Microwave Symposium Digest*, vol. 3, pp. 1633–1636, Jun 2003.

[101] Wang, Z., Jensen, B., Volakis, J., Saitou, K., and Kurabayashi, K., "Analysis of RF-MEMS switches using finite element-boundary integration with moment method," in *Antennas and Propagation Society International Symposium*, vol. 2, pp. 173–176, Jun 2003.

[102] Weis, V., "Combining dielectrics in multilayer microwave boards." Internet, http://www.arlon-med.com/Combining%20Dielectrics.pdf, May 1997.

[103] Wikipedia, "Aluminium oxide." Internet, http://en.wikipedia.org/wiki/Alumina, May 2005.

[104] Wikipedia, "Ultrasonic welding." Internet, http://en.wikipedia.org/wiki/Ultrasonic_bonding, May 2006.

[105] Wikipedia, "B-2 spirit." Internet, http://en.wikipedia.org/wiki/B2_Bomber, May 2007.

[106] Wikipedia, "Boeing 777." Internet, http://en.wikipedia.org/wiki/Boeing_777, May 2007.

[107] Wikipedia, "Fatigue (material)." Internet, http://en.wikipedia.org/wiki/Fatigue_%28material%2 May 2007.

[108] Wikipedia, "Strain hardening." Internet, http://en.wikipedia.org/wiki/Strain_hardening, May 2007.

[109] Wikipedia, t. . F. Internet, http://en.wikipedia.org/wiki/FR4, May 2005.

[110] Winter, M., "WebElements periodic table (professional edition)." Internet, http://www.webelements.com, May 2006.

[111] Ziaei, A., Dean, T., and Mancuso, Y., "Lifetime characterization of capacitive power rf mems switches," in *2005 European Microwave Conference*, vol. 3, 2005.